Durham E-Theses

Enrichment of the Boundary Element Method through the Partition of Unity Method for Fracture Analysis using Local and Global Formulations

ROBERT SIMPSON

How to cite:

SIMPSON, ROBERT (2010) Enrichment of the Boundary Element Method through the Partition of Unity Method for Fracture Analysis using Local and Global Formulations. Doctoral thesis, Durham University.

Use policy

The full-text may be used and/or reproduced, and given to third parties in any format or medium, without prior permission or charge, for personal research or study, educational, or not-for-profit purposes provided that:

- a full bibliographic reference is made to the original source
- a https://etheses.durham.ac.uk/id/eprint/305/ is made to the metadata record in Durham E-Theses
- the full-text is not changed in any way

The full-text must not be sold in any format or medium without the formal permission of the copyright holders.

Please consult the full Durham E-Theses policy for further details.

Academic Support Office, The Palatine Centre, Durham University, Stockton Road, Durham, DH1 3LE
e-mail: e-theses.admin@durham.ac.uk Tel: +44 0191 334 6107
https://etheses.durham.ac.uk

Enrichment of the Boundary Element Method through the Partition of Unity Method for Fracture Analysis using Local and Global Formulations

Robert Simpson

PhD thesis

Computational Mechanics Group
School of Engineering and Computing Sciences
Durham University
England
January 2010

Enrichment of the Boundary Element Method through the Partition of Unity Method for Fracture Analysis using Local and Global Formulations

Robert Simpson

Abstract

The present thesis proposes an innovative technique of applying enrichment to the Boundary Element Method to allow accurate analysis of 2D crack problems. An overview of fracture mechanics is given, with particular emphasis given to numerical methods and the techniques used to extract the highly important stress intensity factors - a measure of the singularity of a crack tip. The Boundary Element Method framework is described and later, the implementation of the new technique of enrichment is defined in detail. Finally, several crack problems are used to verify the accuracy of the method where the results are shown to compare very favourably with other well-established numerical methods.

Declaration

The work in this thesis is based on research carried out in the Computational Mechanics Group, School of Engineering and Computing Sciences, England. No part of this report has been submitted elsewhere for any other degree or qualification and it is all my own work unless referenced to the contrary in the text.

Copyright © 2010 by Robert Simpson.
"The copyright of this thesis rests with the author. No quotations from it should be published without the author's prior written consent and information derived from it should be acknowledged".

Acknowledgements

The following project would not be possible without the generous funding from the Engineering and Physical Sciences Research Council[1] and their support is gratefully acknowledged.

Thanks go to my colleagues in the School of Engineering and Computer Sciences at Durham University who have provided me with great insight and have helped provide direction on numerous occasion. Of course, special thanks is extended to my supervisor, Jon Trevelyan, who has provided me with the greatest assistance, particularly at the start of my research. When things have not gone the expected way or computer code just does not seem to work, Jon has guided me through and kept my sanity at a normal level. Other colleagues who have provided endless helpful advice and have helped sustain my motivation must also be mentioned. These include: Gareth Bird, who has been studying alongside me and whose knowledge, particularly in BEM implementation, has been invaluable; Xiaoying Zhuang, whose exceptional knowledge of numerical methods has been obvious ever since she arrived at Durham and has offered endless advice on meshless methods; and Charles Augarde, whose background in finite elements and meshless methods has offered many interesting and insightful recommendations for my work. Thanks also go to Will Coombs, Claire Heaney, Roger Crouch and Paul Jaquin who have all helped assist me in my research and have made my time at Durham very enjoyable.

Two special mentions must be given to Nicolas Moës at Ecole Centrale de Nantes and Ferri Aliabadi at Imperial College, London who have generously provided assistance, particular in the area of fracture mechanics. Nicolas Moës' extensive background in the eXtended Finite Element Method (XFEM) has been invaluable for implementing enrichment in the present work and Ferri Aliabadi, who has vast expertise in the Boundary Element Method (BEM), has aided me on countless occasions in the implementation of the BEM for fracture.

---

[1] Grant number EP/E/12310/1

Programming computer code and writing technical papers often takes its toll on the mind and it is a welcome (and, I believe, necessary) relief when time is taken out for hobbies and pastimes. For me, cycling is, and always has been, a great passion of mine, and throughout my time at Durham I have built up a great deal of friends by my association with the university cycling club. It would take too long to mention everyone, but I extend my thanks to everyone in the club for taking me on some extremely enjoyable and memorable rides and for getting me home when the going got tough.

Last, but of course not least, I must acknowledge Heather who has helped me through the ups and downs of my research. During those tough moments she has guided me through and helped my keep in perspective what is important - something which is all too easy to forget when submersed in the world of academia. In particular, throughout the writing of this thesis she has shown incredible patience and understanding, and for this, I am truly grateful.

Nomenclature

α_{ij}	Jump term for T_{ij} kernel
δ_{ij}	Kronecker delta function
$\Delta(\mathbf{X}-\mathbf{X}')$	Dirac delta function
ε_{ij}	(Mathematical) Strain component
Γ	Domain boundary
Γ^{c}	Crack surface
Γ^{c+}	Upper crack surface
Γ^{c-}	Lower crack surface
Γ_J	J-integral path
Γ_n	Element boundary
κ	Kosolov constant
Λ	Strain energy jump term for J_k-integral
λ	Lamé constant
μ	Shear modulus
ν	Poisson's Ratio
Ω	Volume domain
Φ	Airy stress function
ψ^u_l	Displacement crack tip enrichment function (PUM enrichment)
$\bar{\psi}^u_{lja}$	Displacement crack tip enrichment function evaluated at node a

ψ^{t}_{lj}	Traction crack tip enrichment function (combined basis)
ψ^{u}_{lj}	Displacement crack tip enrichment function (combined basis)
(ρ, θ)	Polar crack-tip coordinates
σ_{ij}	Stress component
ξ	Local 2D boundary coordinate
ξ'	Local coordinate of source point
a	Crack length
A^{na}_{jl}	Enrichment coefficient (PUM enrichment)
a_n	Coefficient of Williams expansion (symmetric terms)
b_i	Body force component
b_n	Coefficient of Williams expansion (antisymmetric terms)
C_{ij}	Jump term
D_{kij}	Differentiated displacement fundamental solution
E	Young's Modulus
e	Volumetric strain
E'	Modified Young's modulus
e_i	Unit load vector component
E^{na}_{kij}	Element integral of S_{kij} kernel
$\tilde{E}^{na}_{kij}$	Element integral of enriched S_{kij} kernel
$F_{-1}(\xi')$, $F_{-2}(\xi')$	Power series functions (subtraction of singularity integration)
F^{na}_{kij}	Element integral of D_{kij} kernel
G	Strain energy release rate
$\mathbf{h}^{a}$	Singular T_{ij} integral matrix
$\bar{\mathbf{h}}^{a}$	Singular S_{kij} integral matrix

$\mathbf{I}$	Identity matrix
J	J-integral (J_1-integral)
J_2	J_2-integral
$J(\xi)$	Jacobian of transformation
K_{I}	Mode I stress intensity factor
K_{II}	Mode II stress intensity factor
$\tilde{K}_{\mathrm{I}}$	Mode I enrichment coefficient
$\tilde{K}_{\mathrm{II}}$	Mode II enrichment coefficient
$\mathbf{m}$	Tangential vector
$\mathbf{n}$	Normal vector
$\mathbf{n}'$	Source point normal matrix
$\bar{n}$	Element containing collocation point (PUM enrichment)
N_a	Shape function for node a
N_e	Number of elements
$\bar{N}_{enr}$	Normalised number of enriched elements
n_i	Normal component
P_{ij}^{na}	Element integral of T_{ij} kernel
$\tilde{P}_{ijl}^{na}$	Element integral of enriched T_{ij} kernel
Q_{ij}^{na}	Element integral of U_{ij} kernel
R	Cutoff radius for J_k-integral evaluation
r	Distance between source and field points
R_c	Curved crack radius
S_{kij}	Differentiated traction fundamental solution
T_{ij}	Traction fundamental solution

T	T-stress
U	Strain energy
$\mathbf{u}$	Displacement vector
U_{ij}	Displacement fundamental solution
u_i	Displacement component
V_{lj}^{na}	Traction crack-tip boundary integral term
W	Strain energy density
W^+	Strain energy on upper crack face
W^-	Strain energy on lower crack face
$[\![W]\!]$	Strain energy jump
W_{lj}^{na}	Displacement crack-tip boundary integral term
$\mathbf{X}$	Domain field point
$\mathbf{x}$	Boundary field point
$\mathbf{X}'$	Domain source point
$\mathbf{x}'$	Boundary source point
x_i	Coordinate component
$-\!\!\!\!\!\!\int$	Cauchy Principal Value integral
$=\!\!\!\!\!\!\!\int$	Hadamard finite part integral
∇^2	Laplacian operator $\left(\text{eg. in 2D } \nabla^2 f = \dfrac{\partial^2 f}{\partial x_1^2} + \dfrac{\partial^2 f}{\partial x_2^2}\right)$

Contents

List of Figures

List of Tables

Chapter 1

Introduction

> "...I heard the noise of an aircraft..but I did not pay any attention to it. Suddenly, however, my attention was caught by a roaring sound in the air in the direction from which the noise of an aircraft was coming, and distinctly noticed, in that direction, two pieces of an aircraft, the smaller in flames, falling in almost parallel line into the sea..." [2]
>
> (eyewitness, de Havilland Comet disaster, 1954)

On the 10th January 1954, Comet G-ALYP departing from Rome's Ciampino airport crashed into the waters near the Mediterranean island of Elba, killing all thirty-five on board. There was no immediate obvious explanation for the cause of the crash, but eventually it was decided that fire was responsible [3], and after some modifications to the aircraft to protect against this, normal passenger service resumed. Approximately two weeks later, the second Comet fatality occured and with immediate effect, the entire Comet fleet was grounded and a full-scale investigation was carried out under the direction of the Royal Aircraft Establishment (RAE). Headed by Sir Arnold Hall, the investigation provided an exceptionally detailed account of the crash and described, during a public inquiry, that:

> [The probable cause of failure was] "a phenomenon known as fatigue. The essence of the phenomenon, is that whereas the structure will stand one application of the load quite satisfactorily, it may not stand many hundreds, thousands or millions of applications of the load satisfactorily, and may in the end fail under a load which it is well capable of bearing when new..." [2]
>
> (Sir Arnold Hall, The Comet Inquiry, 1954)

This marked the start of an intensive period of study into the mechanisms and factors that control fracture and fatigue and formed the birth of a new subject, entitled “fracture mechanics”. The importance of this subject has remained high to the present day and, for the design of components subject to repeated loads, the application of the principles of fracture and fatigue remain an integral part of the engineering process. In particular, it is found that the majority of fatigue calculations are empirical and rely on the use of parameters known as stress intensity factors (SIFs) - a measure of the strength of a crack tip singularity - and accurate determination of these values is vital for efficient design. At present, there are a variety of methods available to the engineer to determine SIFs ranging from handbooks detailing numerous crack geometries to the more recent computational methods that have exploded in popularity, attributable to the abundance and constantly increasing power of the portable computer. But what is especially useful when computational methods are employed, is the ability to model completely arbitrary geometries thus allowing a certain type of “bespoke” analysis to be carried out. For this reason, they represent one of the most popular tools of choice for designing against fracture and a large variety of software packages are available - these implement computational methods ranging from the hugely popular Finite Element Method (FEM) to the less well-known Boundary Element Method (BEM). Each demonstrates certain advantages and disadvantages, but what is common to all, is the difficulty encountered when cracks are modelled and the large inaccuracies that result if special treatment is not applied. A variety of techniques are available to overcome these problems, but the search to find increasingly efficient and accurate methods is ever-present. This thesis concentrates the technique of “enriching” a certain region surrounding the crack tip and how this can be applied to the BEM to allow accurate and efficient modelling of cracks; this is achieved by using functions that are known to capture the required crack-tip behaviour, and once these are included, significant increases in accuracy are seen for a variety of crack geometries. In fact, two variants of implementing enrichment are described where the enrichment functions are included in different ways. Both are assessed for their ability to model a crack tip field and compared against standard methods and reference solutions to verify the high accuracy of the new implementation.

Several key advancements have been made in the field of fracture mechanics and it is the goal of Chapter 2 to give an overview of some of the most important findings, varying from the early work by Griffith in 1921 to the more recent studies into the advancement of computational methods. Since this thesis concentrates on the use of the Boundary Element Method and to allow clear understanding of later work that presents certain modifications to the method, a detailed derivation of the BEM is given in Chapter 3. Furthermore, since problems are sometimes encountered when the Boundary Element Method is applied directly to crack models, the Dual Boundary Element Method (which provides an elegant solution to overcome these difficulties) is described and the mathematical details of the method outlined. Chapter 4 introduces the various integration scenarios that are encountered in BEM/DBEM implementations and the appropriate integration routines that are available. This overview is important since, in contrast to methods such as the FEM, "singular" integrals (which present challenges for conventional integration routines) are commonly encountered and must be evaluated accurately. Next, Chapter 5 outlines the difficulties encountered by conventional implementations of computational methods to crack problems and some of the most popular techniques used to overcome these, with emphasis given to BEM implementations.

Chapters 6 to 8 present the new forms of enrichment applied to the BEM/DBEM with Chapter 6 describing how the Partition of Unity Method (PUM) can be used to apply enrichment functions in a region surrounding the crack tip thereby increasing the accuracy of the approximation. The second form of enrichment is then outlined in Chapter 7 in which the enrichment functions are combined to reduce the number of introduced unknowns with associated benefits on the behaviour of the system. Finally, each method of enrichment is compared and the improvement in accuracy demonstrated by analysing a variety of crack geometries with known reference solutions (Chapter 8) where it is shown that the methods presented in this thesis compare very favourably.

Chapter 2

Fracture Mechanics

Fracture mechanics, a subject which is focused on studying the effects of cracks within materials, is a topic whose beginnings can be traced back to the early 20th century. It is generally regarded that the birth of the subject was due to the pioneering work of Inglis [4] in 1913 and Griffith [5] in 1921. Inglis investigated the problem of an elliptical hole within an infinite plate and considered the limit as the radius of curvature at the ends of the major axis of the ellipse tended to zero, in essence modelling a crack within the material. Griffith took a different approach by considering the energies associated with fracture and demonstrated his theory by performing experiments on glass rods which were subject to brittle fracture. However, little attention was paid towards these early theories and many designs, to prevent failure by fracture, were based on high factors of safety with additional material used in regions of high stress. But, with the start of the Second World War and the rise in demand for structures with large strength-to-weight ratios, the need for more efficient fracture-resistant designs arose. 1940-1960 marked an intense period in the advancement of Linear Elastic Fracture Mechanics (LEFM) where several major failures provided the impetus to develop a unified code for design against fracture. One such example was the series of Liberty ships which were constructed using the relatively new technique of joining sections together by welding, thus allowing for a substantial increase in the rate of construction. What was not understood though, was the ability of welded joints to act as crack propagation sites and, coupled with the effect of increased brittleness in cold water, the potential for catastrophic failure (see Fig. 2.1). Another example of failure by fracture but with greater loss of life was the de Havilland Comet aircraft - the first commercial jet-engined aircraft to be put into service. In the early years of its use several fatal accidents occurred leaving investigators with the destroyed remains of the cabin to determine the cause. The failures were traced to sharp corners in the design of cabin windows where the effect of the corner acted as a stress-raiser. In turn, stresses within the fuselage were able to reach the critical value for crack propagation and catastrophic failure occurred.

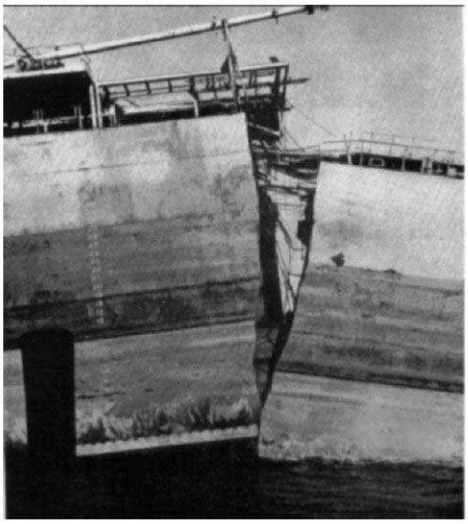

Figure 2.1: Failure due to fracture: Liberty ship

To investigate the inclusion of a crack, Inglis studied the effect of a shallow ellipse and considered the limiting case as the length of the minor axis tended to zero (therefore approaching the crack-tip solution) and found the stresses to be raised significantly along the axis of the ellipse. However, the exact solution of a crack, where the root radius is equal to zero, was not determined. It was the work by Williams in 1952 [6] and 1957 [7] which first considered the solution of a wedge with traction free faces and arbitrary loadings elsewhere (see Fig. 2.2a). The work used an Airy stress function with the semi-inverse method to find a solution but, more significantly, the case for which the apex angle α was equal to π resulting in the edge-crack geometry of Fig. 2.2b was considered. This provided the crack-tip solution which exhibits a theoretically infinite stress at the crack tip but, more importantly, the solution showed that the magnitudes of stress and displacement may vary from one crack geometry to another, but the *distribution* of these parameters would remain the same. In fact, the only change between geometries is the magnitude of certain constants which are now commonly known as stress intensity factors (SIFs) denoted K_{I}, K_{II} and K_{III}. These give a description of the magnitude of the crack-tip singularities in certain orientations defined in Figs 2.3a to 2.3c and, once they have been determined for a crack geometry, a complete description of the stresses and displacements surrounding the crack can be found. For this reason, along with the large accuracy dependence of fatigue crack growth calculations on SIFs, they are regarded as the single most important parameters in design against fracture. However, since analytical solutions exist only for a limited number of cracked geometries, alternative techniques, like the use of handbook solutions and numerical methods, are required to allow engineers to evaluate the ability of designs to resist fracture.

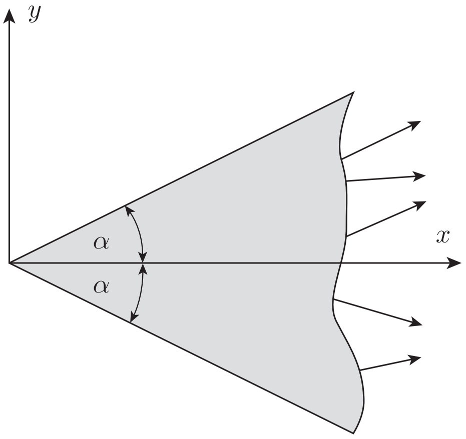

(a) Wedge of angle α subject to arbitrary loading

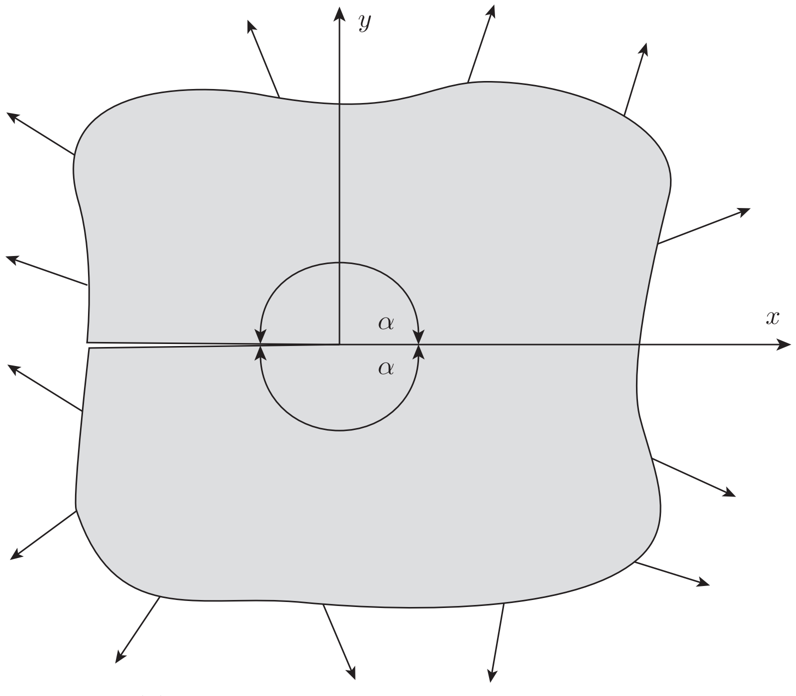

(b) Wedge with $\alpha = \pi$ resulting in edge crack

Figure 2.2: Wedge geometries for Williams solution

The stress intensity factor handbooks such as that by Tada et al. [8] give solutions to a variety of crack geometries and loadings allowing SIFs to be determined quickly and easily. During design, since the geometry and loading of a certain component

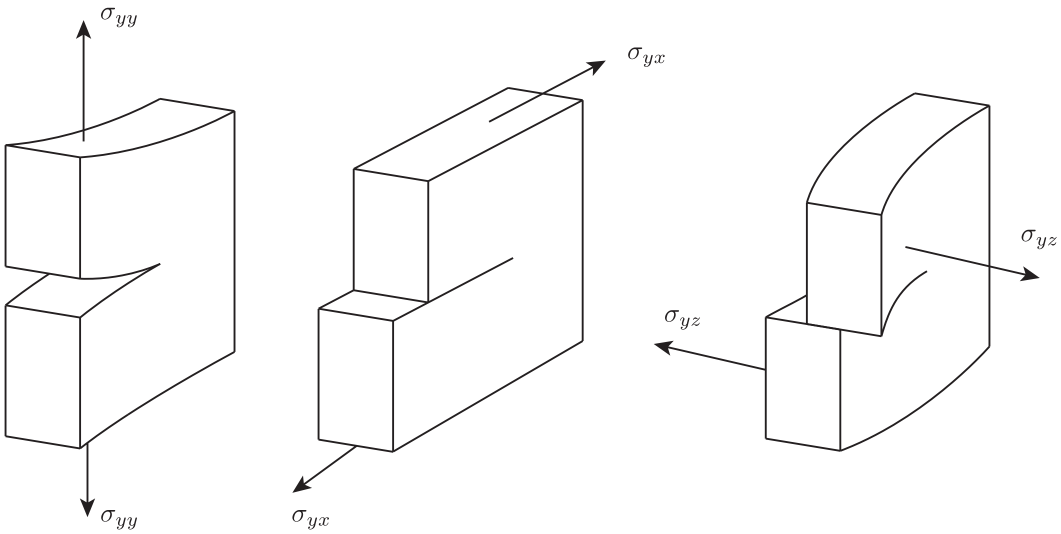

(a) Mode I (b) Mode II (c) Mode III

Figure 2.3: Fracture mode definitions

may not be given by handbook solutions, it is sometimes possible to combine several known solutions into one by the process of superposition. In some circumstances though, a solution is unobtainable by these means and it is necessary to make use of numerical methods. These rely heavily on the processing power of computers but offer significant advantages to the engineer. In particular, for the analysis of 3D cracks where very few analytical solutions exist, it is almost always necessary to use numerical methods to find SIFs. At present, the most widely used methods are the Boundary Collocation Method (BCM), the Finite Element Method (FEM) and the Boundary Element Method (BEM). Each of these exhibits certain advantages over each other, but what is common to all numerical methods used for fracture analysis are the problems created by the singular field around a crack tip. Chapter 4 outlines some of the methods used to overcome these problems for both the FEM and BEM while chapter 6, which is the basis of the present thesis, describes a new method for enriching the BEM to allow SIFs to be determined accurately and efficiently.

The present chapter gives an overview of the important advancements in the field of fracture mechanics with particular attention paid to analytical solutions since these play an important role in later work. Overviews of the most popular numerical methods used in fracture mechanics are given and finally, the techniques which are used as post-processing tools to determine stress intensity factors are described.

2.1 Energy approaches - Griffith's law

The first approach to determine whether unstable crack growth would occur in a material under load was carried out by A.A. Griffith in 1921 [5]. He first noticed that glass rods fractured at stresses significantly lower than those predicted by conventional failure laws and postulated that the presence of cracks (and the associated local increase in stress) was the cause. To prove this, tests were carried out on glass rods which varied in age and in diameter and the results suggested that the lowest failure stresses were seen in older rods and those with larger diameters. Griffith explained that the aging process introduced flaws and defects to the material while larger rods, due to their increased surface area, were more likely to contain flaws compared to similar thin rods. But the most important feature of the work was the introduction of a law, now known as Griffith's law, which governs crack growth in a brittle material.

Before this is stated, we consider the problem of a crack of length $2a$ within an infinite body and define a quantity known as the strain energy release rate G as

$$G = -\frac{\partial U}{\partial a} \tag{2.1}$$

where U is the stored strain energy of the system and a negative sign is introduced to make G a positive quantity. Then, for unstable crack growth to occur, the rate at which strain energy is released must be greater than or equal to the rate of energy required to create new crack surfaces. Mathematically, this can be written as

$$G \geq \frac{\partial W_s}{\partial a} \tag{2.2}$$

where W_s is the surface energy required to propagate the crack. By comparing the elastic strain energy of an infinite plate under a stress σ with that of a similar plate with a crack of length $2a$, it can be shown that the change in energy is given by

$$U = -\frac{\pi a^2 \sigma^2}{E} \tag{2.3}$$

where E is the Young's modulus of the material. Also, by defining a quantity γ_s known as the surface energy per unit area, the quantity W_s can be written as

$$W_s = 2.\gamma_s.2a \tag{2.4}$$

This is the energy required to create two crack surfaces (upper and lower) of length $2a$ and it has been assumed that the plate is of unit thickness. Now, by inspecting the condition (2.2) which governs crack growth, it is clear that crack growth *just* occurs when the strain energy release rate is equal to the rate of energy required to create new crack surfaces. ie.

$$G = \frac{\partial W_s}{\partial a}. \tag{2.5}$$

By substituting (2.3) into (2.1) and differentiating to give G and then differentiating (2.4) to obtain $\partial W_s/\partial a$, the following is given

$$\frac{\pi 2a\sigma^2}{E} = 4\gamma_s \tag{2.6}$$

Since this is the condition at which crack growth just occurs, the stress σ is replaced by σ_c which denotes the critical stress for crack growth and the equation is rearranged:

$$\sigma_c = \sqrt{\frac{2E\gamma_s}{\pi a}} \tag{2.7}$$

The law proposed by Griffith was largely ignored for many years, mainly due to the restriction of the law to brittle materials, and it was not until the work of Orowan [9] and Irwin [10] who considered the energy due to plastic deformation that the original work was more widely recognised. Orowan showed that significant plastic deformation occurred along the crack surfaces and this plastic work was many orders of magnitude greater than the surface energy γ_s. Therefore, by introducing a term known as the plastic work per unit area γ_p and replacing γ_s with the combined term $\gamma_s + \gamma_p$ in Eq. (2.7), the critical stress for crack growth can be extended to metals in plane strain by

$$\sigma_c = \sqrt{\frac{2E(\gamma_s + \gamma_p)}{\pi a}} \tag{2.8}$$

Irwin also recognised the importance of including an additional term to account for the plastic work done but in addition, he provided a relation between the strain energy release rate G and stress intensity factors. Irwin showed, by considering a crack in an infinite plate extending by an infinitesimal distance and calculating the energy required to close the crack, that the following relations could be defined

$$G_{\mathrm{I}} = \begin{cases} \dfrac{K_{\mathrm{I}}^2}{E} & \text{plane stress} \\ \dfrac{K_{\mathrm{I}}^2(1-\nu^2)}{\pi E} & \text{plane strain} \end{cases} \tag{2.9a}$$

$$G_{\mathrm{II}} = \begin{cases} \dfrac{K_{\mathrm{I}}^2}{E} & \text{plane stress} \\ \dfrac{K_{\mathrm{I}}^2(1-\nu^2)}{\pi E} & \text{plane strain} \end{cases} \tag{2.9b}$$

where the strain release rate components are related by

$$G = G_{\mathrm{I}} + G_{\mathrm{II}} \tag{2.10}$$

These equations are extremely important in fracture since they relate the energy release rates G_{I} and G_{II} which are based on global energy concepts to those of the stress intensity factors K_{I} and K_{II} which are based on local stress fields. Therefore, even though the Griffith crack growth laws are based on the solution of an infinite plate, they can be used (through Eqns (2.9a) (2.9b)) to provide the solution for any crack geometry. The most widely used method which makes heavy use of this principle is the J-integral which allows calculation of stress intensity factors through a path/domain integral. It can be shown the value obtained from this integral J is in fact related to the strain energy release rate (in the case of linear elasticity) by

$$J = G \tag{2.11}$$

Further details of this method are given in Secs 2.6.2 and 2.6.3 with a full derivation in App D.3.

The Griffith law, due to its basis on energy principles, gives no solution for displacements or stresses surrounding the crack - it can only determine whether or not failure due to fracture will occur. Instead, we require a solution which is capable of providing expressions for these parameters. This solution is very well-known within fracture mechanics and in fact, many numerical methods are reliant on it. The next section outlines two mathematical methods which have been used to arrive at the solution of a domain containing a crack tip and emphasises the importance of the stress intensity factors (briefly mentioned here) in their use for fracture design.

2.2 Williams solution

As described in Sec. 2, the first solution to the problem of a crack within a material subject to arbitrary loadings on the boundary was given by Williams [6]. Since fracture mechanics relies heavily on this solution (the Williams solution is recalled on numerous occasions in this thesis), it is instructive to follow through the derivation to prevent any gaps in understanding. The solution is dependent on an appropriate choice of Airy stress function and the application of the semi-inverse method (see [11] for an overview of these topics) which ensures the initial choice of Airy stress function is correct by verifying boundary conditions. Williams considered the problem of a wedge of apex angle 2α (see Fig. 2.2a), and chose the the following Airy stress function

$$\Phi(\rho,\theta) = \rho^{\lambda+1}.f(\theta) \tag{2.12}$$

where (ρ,θ) is the polar coordinate system defined in Fig. 2.4 while the eigenvalue λ and the function $f(\theta)$ are yet to be determined as part of the solution. Using the expressions relating stresses in polar coordinates to the Airy stress function (see Eq. B.1.2 in Appendix B.1), the crack-tip stresses can be expressed as

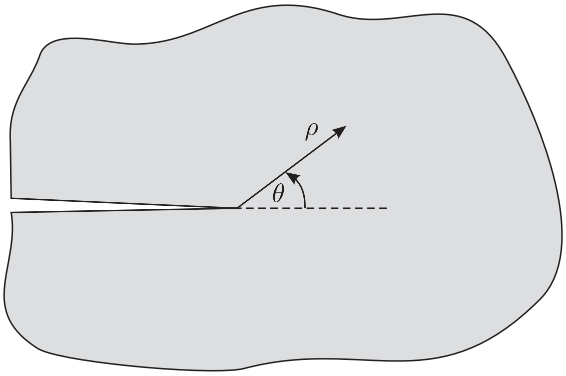

Figure 2.4: Definition of crack-tip polar coordinates

$$\sigma_{\rho\rho} = \rho^{\lambda-1}[(\lambda+1)f(\theta) + f''(\theta)] \tag{2.13a}$$

$$\sigma_{\theta\theta} = \lambda(\lambda+1)\rho^{\lambda-1}f(\theta) \tag{2.13b}$$

$$\sigma_{\rho\theta} = -\lambda\rho^{\lambda-1}f'(\theta). \tag{2.13c}$$

where $'$ implies differentiation of a function. Using the imposed boundary conditions of traction free faces

$$\sigma_{\rho\rho} = 0, \quad \sigma_{\rho\theta} = 0 \quad \text{for} \quad \theta = \pm\alpha, \quad \rho \geq 0 \tag{2.14}$$

certain conditions on the function $f(\theta)$ can be written

$$f(\alpha) = f(-\alpha) = 0 \tag{2.15a}$$

$$f'(\alpha) = f'(-\alpha) = 0 \tag{2.15b}$$

assuming that $\lambda \neq 0$. If the assumed Airy stress function Φ is then substituted into the biharmonic equation in polar form (B.1.5), the ordinary differential equation can be written as

$$\left[\frac{d^2}{d\theta^2} + (\lambda-1)^2\right] \cdot \left[\frac{d^2}{d\theta^2} + (\lambda+1)^2\right] f(\theta) = 0 \tag{2.16}$$

with the general solution of

$$f(\theta) = a\cos(\lambda-1)\theta + b\sin(\lambda-1)\theta + c\cos(\lambda+1)\theta + d\sin(\lambda+1)\theta. \tag{2.17}$$

where a, b, c and d are constants. By substituting into (2.17) the boundary conditions of (2.15), four simultaneous equations are formed

$$a\cos(\lambda-1)\alpha + b\sin(\lambda-1)\alpha + c\cos(\lambda+1)\alpha + d\sin(\lambda+1)\alpha = 0 \tag{2.18a}$$

$$a\cos(\lambda-1)\alpha - b\sin(\lambda-1)\alpha + c\cos(\lambda+1)\alpha - d\sin(\lambda+1)\alpha = 0 \tag{2.18b}$$

$$\begin{aligned} &-a(\lambda-1)\sin(\lambda-1)\alpha + b(\lambda-1)\cos(\lambda-1)\alpha \\ &\qquad -c(\lambda+1)\sin(\lambda+1)\alpha + d(\lambda+1)\cos(\lambda+1)\alpha = 0 \end{aligned} \tag{2.18c}$$

$$\begin{aligned} &a(\lambda-1)\sin(\lambda-1)\alpha + b(\lambda-1)\cos(\lambda-1)\alpha \\ &\qquad +c(\lambda+1)\sin(\lambda+1)\alpha + d(\lambda+1)\cos(\lambda+1)\alpha = 0 \end{aligned} \tag{2.18d}$$

which, after some simple manipulations, can be written more succinctly as

$$\begin{pmatrix} \cos(\lambda-1)\alpha & \cos(\lambda+1)\alpha \\ (\lambda-1)\sin(\lambda-1)\alpha & (\lambda+1)\sin(\lambda+1)\alpha \end{pmatrix} \begin{pmatrix} a \\ c \end{pmatrix} = \begin{pmatrix} 0 \\ 0 \end{pmatrix} \tag{2.19a}$$

$$\begin{pmatrix} \sin(\lambda-1)\alpha & \sin(\lambda+1)\alpha \\ (\lambda-1)\cos(\lambda-1)\alpha & (\lambda+1)\cos(\lambda+1)\alpha \end{pmatrix} \begin{pmatrix} b \\ d \end{pmatrix} = \begin{pmatrix} 0 \\ 0 \end{pmatrix} \tag{2.19b}$$

For non-trivial solutions the determinant for each of these matrices must be zero, giving, after simplification,

$$\sin(2\lambda\alpha) = 0 \tag{2.20a}$$

$$\lambda\sin(2\alpha) = 0 \tag{2.20b}$$

In the case of a crack where $\alpha = \pi$, the second of these equations is automatically satisfied. The first equation is satisfied if

$$\lambda = \frac{n}{2} \quad \text{where} \quad n = \pm 0, \pm 1, \pm 2, \pm 3 \ldots \tag{2.21}$$

But before we can proceed, some comments need to be made on the choice of the values λ and n. Considering first the relations for stresses around the crack tip (Eqns. (2.13)) which are of $O(\rho^{\lambda-1})$, it is found that strains, which will be shown to be related to stresses by relations (3.5), will also be of $O(\rho^{\lambda-1})$. Since displacements are obtained through integration of strain components, these will be of $O(\rho^{\lambda})$ which places some restrictions on the choice of λ. If λ is negative then infinite displacements are experienced at the crack tip where $\rho = 0$ - this discounts any negative values of λ from the solution. If λ is equal to zero, displacements are finite but, due to the inclusion of functions which are dependent on θ, the displacements at the crack tip become multi-valued when in fact we know displacements are equal to zero. The only feasible values of λ are therefore

$$\lambda = \frac{n}{2}, n > 0 \tag{2.22}$$

Once these eigenvalues are substituted into Eqns (2.19) and denoting the coefficients a_n, b_n, c_n and d_n to correspond to the eigenvalue n, it can be shown that these coefficients are related as follows

$$c_n = -\frac{n-2}{n+2}a_n, \qquad d_n = -b_n, n = 1, 3, 5 \ldots \tag{2.23a}$$

$$c_n = -a_n, \qquad d_n = -\frac{n-2}{n+2}b_n, n = 2, 4, 6 \ldots \tag{2.23b}$$

allowing the final expression for the Airy stress function to be written as

$$\begin{aligned}\Phi(\rho, \theta) = \sum_{n=1,3\ldots} \rho^{1+\frac{n}{2}} \Bigg[a_n \left(\cos\frac{n-2}{2}\theta - \frac{n-2}{n+2}\cos\frac{n+2}{2}\theta \right) \\ + b_n \left(\sin\frac{n-2}{2}\theta - \sin\frac{n+2}{2}\theta \right) \Bigg] \\ + \sum_{n=2,4,\ldots} \rho^{1+\frac{n}{2}} \Bigg[a_n \left(\cos\frac{n-2}{2}\theta - \cos\frac{n+2}{2}\theta \right) \\ + b_n \left(\sin\frac{n-2}{2}\theta - \frac{n-2}{n+2}\sin\frac{n+2}{2}\theta \right) \Bigg]\end{aligned} \tag{2.24}$$

By inspecting the terms related to a_n, it can be seen in each case the cosine function is present. Since this is a symmetric function, we regard the coefficient a_n to relate to the opening fracture mode as illustrated in Fig. 2.3a. Similarly, since the sine function (which is antisymmetric) is present in each b_n term, we regard this coefficient to correspond to the forward shear mode shown in Fig. 2.3b. Later, it will be shown that certain coefficients in the expansion are related to the stress intensity factors while any higher order terms are usually omitted. But before expression (2.24) is of any practical use, it must first be substituted into Eqns (B.1.1) to obtain expressions for crack-tip stresses

$$\begin{aligned}\sigma_{xx} = \sum_{n=1}^{\infty} \frac{n}{2}\rho^{n/2-1}\Bigg\{ & a_n \left[\left(2+\frac{n}{2}+(-1)^n\right)\cos\left(\frac{n}{2}-1\right)\theta+\left(\frac{n}{2}-1\right)\cos\left(\frac{n}{2}-3\right)\theta\right] \\ & -b_n\left[\left(2+\frac{n}{2}-(-1)^n\right)\sin\left(\frac{n}{2}-1\right)\theta-\left(\frac{n}{2}-1\right)\sin\left(\frac{n}{2}-3\right)\theta\right]\Bigg\}\end{aligned} \tag{2.25a}$$

$$\begin{aligned}\sigma_{yy} = \sum_{n=1}^{\infty} \frac{n}{2}\rho^{n/2-1}\Bigg\{ & a_n \left[\left(2-\frac{n}{2}-(-1)^n\right)\cos\left(\frac{n}{2}-1\right)\theta+\left(\frac{n}{2}-1\right)\cos\left(\frac{n}{2}-3\right)\theta\right] \\ & -b_n\left[\left(2-\frac{n}{2}+(-1)^n\right)\sin\left(\frac{n}{2}-1\right)\theta+\left(\frac{n}{2}-1\right)\sin\left(\frac{n}{2}-3\right)\theta\right]\Bigg\}\end{aligned} \tag{2.25b}$$

$$\begin{aligned}\sigma_{xy} = \sum_{n=1}^{\infty} \frac{n}{2}\rho^{n/2-1}\Bigg\{ & a_n \left[\left(\frac{n}{2}-1\right)\sin\left(\frac{n}{2}-3\right)\theta-\left(\frac{n}{2}+(-1)^n\right)\sin\left(\frac{n}{2}-1\right)\theta\right] \\ & +b_n\left[\left(\frac{n}{2}-1\right)\cos\left(\frac{n}{2}-3\right)\theta-\left(\frac{n}{2}-(-1)^n\right)\cos\left(\frac{n}{2}-1\right)\theta\right]\Bigg\}\end{aligned} \tag{2.25c}$$

where the global Cartesian coordinate system xy is used. In this coordinate system the x-axis lies in the plane $\theta = 0$ (Fig. 2.4). Finally, by using the constitutive equations to obtain strains and then integrating to find displacements (these relations will be described in Sec. 3.1.1), the following series expressions can be written for crack-tip displacements

$$\begin{aligned}u_x = \sum_{n=0}^{\infty} \frac{\rho^{n/2}}{2\mu}\Bigg\{ & a_n \left[\left(\kappa+\frac{n}{2}+(-1)^n\right)\cos\frac{n}{2}\theta-\frac{n}{2}\cos\left(\frac{n}{2}-2\right)\theta\right] \\ & -b_n\left[\left(\kappa+\frac{n}{2}-(-1)^n\right)\sin\frac{n}{2}\theta-\frac{n}{2}\sin\left(\frac{n}{2}-2\right)\theta\right]\Bigg\}\end{aligned} \tag{2.26a}$$

$$\begin{aligned}u_y = \sum_{n=0}^{\infty} \frac{\rho^{n/2}}{2\mu}\Bigg\{ & a_n \left[\left(\kappa-\frac{n}{2}-(-1)^n\right)\sin\frac{n}{2}\theta+\frac{n}{2}\sin\left(\frac{n}{2}-2\right)\theta\right] \\ & +b_n\left[\left(\kappa-\frac{n}{2}+(-1)^n\right)\cos\frac{n}{2}\theta+\frac{n}{2}\cos\left(\frac{n}{2}-2\right)\theta\right]\Bigg\}.\end{aligned} \tag{2.26b}$$

where μ is defined as the shear modulus and κ is known as the Kosolov constant. The solutions for stresses and displacements given by (2.25) and (2.26) are fundamental to linear elastic fracture mechanics since they give an exact analytical solution to which other methods can be compared against. But what is important to note is the form each of these expressions take. Taking first the crack-tip stresses, we see that a singularity of $\mathcal{O}(1/\rho^{1/2})$ is experienced at the crack-tip creating a theoretically infinite stress while displacements, of $\mathcal{O}(\rho^{1/2})$, exhibit an infinite-gradient at the crack-tip. As will be seen later, these singularities in the crack solution create problems for numerical methods since, most often, polynomial expressions are used for the interpolation of stresses and displacements. In fact, this thesis is centred on a method of overcoming this difficultly for implementation of cracks in the Boundary Element Method.

2.3 Westergaard solution

Another very successful technique used to provide solutions to crack problems is the approach developed by Westergaard in 1939 [12]. The method makes use of the complex analysis technique originally developed by Muskhelishvili [13] which is particularly convenient due to the automatic satisfaction of the biharmonic equation if the complex functions are shown to be analytic (see Appendix B.2 for details). Taking the example of a centre crack with two local polar crack tip coordinate systems, as defined in Fig. 2.5, the complex analysis approach allows the complex variable z to be expressed as

$$z - a = (x - a) + iy = \rho_1 e^{i\theta_1} \tag{2.27a}$$

$$z + a = (x + a) + iy = \rho_2 e^{i\theta_2} \tag{2.27b}$$

In Westergaard's solution, he first proposed a complex function of the form

$$F(z) = \mathrm{Re}\tilde{\tilde{Z}}(z) + y(\mathrm{Im}\tilde{Z}(z) + \mathrm{Im}\tilde{Y}(z)) \tag{2.28}$$

where $Z(z)$ and $Y(z)$ are complex functions which will be defined later and the symbol $\sim$ represents integration with respect to the complex variable z. Therefore

$$\frac{d\tilde{\tilde{Z}}}{dx} = \tilde{Z} \quad \frac{d\tilde{Z}}{dz} = Z \quad \frac{d\tilde{Y}}{dz} = Y \tag{2.29}$$

It is possible, through the use of the Cauchy-Riemann equations, to obtain the following derivative expressions

$$\frac{\partial F}{\partial x} = \mathrm{Re}\tilde{Z} + y(\mathrm{Im}Z + \mathrm{Im}Y) \tag{2.30a}$$

$$\frac{\partial F}{\partial y} = \mathrm{Im}\tilde{Y} + y(\mathrm{Re}Z + \mathrm{Re}Y) \tag{2.30b}$$

which, once differentiated again, and substituted into the expressions relating the Airy stress function to stresses (Eqns B.1.1), give

$$\sigma_{xx} = ReZ - y(ImZ' + Y') + 2ReY \tag{2.31a}$$

$$\sigma_{yy} = ReZ + y(ImZ' + ImY') \tag{2.31b}$$

$$\sigma_{xy} = -ImY - y(ReZ' + ReY') \tag{2.31c}$$

Using the elastic constitutive equations, these expressions can be used to derive strains and, through integration, displacements. The only task then is to make an appropriate choice of the complex functions Z and Y which, through the semi-inverse method, are shown to satisfy the boundary conditions of the problem. Westergaard considered the problem of a central crack in an infinite plate (see Fig. 2.5) and chose the following complex functions

$$Z(z) = \frac{\sigma z}{\sqrt{z^2 - a^2}} \quad Y(z) = 0. \tag{2.32}$$

By substituting relations (2.27) into the functions which relate the stress components to the Airy stress function (Eqns (B.1.1)), the following solution for stresses in a centre crack can be written

$$\sigma_{xx} = \frac{\sigma\rho}{\sqrt{\rho_1\rho_2}} \cos\left(\theta - \frac{\theta_1 + \theta_2}{2}\right) - \frac{\sigma a^2}{(\rho_1\rho_2)^{3/2}} \rho_1 \sin\theta_1 \sin\frac{3}{2}(\theta_1 + \theta_2) \tag{2.33a}$$

$$\sigma_{yy} = \frac{\sigma\rho}{\sqrt{\rho_1\rho_2}} \cos\left(\theta - \frac{\theta_1 + \theta_2}{2}\right) + \frac{\sigma a^2}{(\rho_1\rho_2)^{3/2}} \rho_1 \sin\theta_1 \sin\frac{3}{2}(\theta_1 + \theta_2) \tag{2.33b}$$

$$\sigma_{xy} = \frac{\sigma a^2}{(\rho_1\rho_2)^{3/2}} \rho_1 \sin\theta_1 \cos\frac{3}{2}(\theta_1 + \theta_2) \tag{2.33c}$$

If a point is chosen which lies close to one of the crack tips (here, the crack tip on

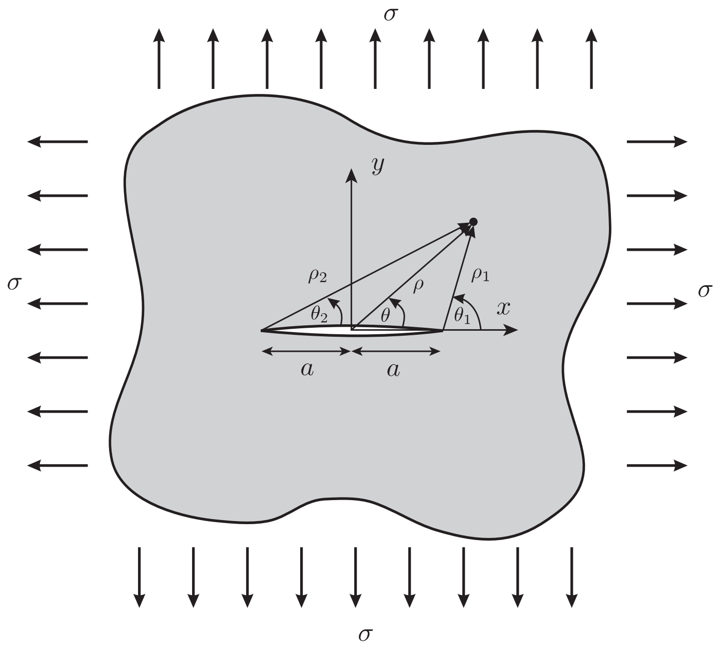

Figure 2.5: Centre crack in infinite plate

the right is chosen) then the following assumptions can be made

$$\rho_2 \approx 2a \quad \rho \approx a \quad \theta_2 \approx \theta \approx 0 \tag{2.34}$$

When these are substituted into Eqns (2.33) the following relations for stresses in the immediate vicinity of one of the crack tips are obtained

$$\sigma_{xx} = \frac{\sigma\sqrt{\pi a}}{\sqrt{2\pi\rho_1}} \cos(\theta/2)\left[1 - \sin(\theta/2)\sin(3\theta/2)\right] \tag{2.35a}$$

$$\sigma_{yy} = \frac{\sigma\sqrt{\pi a}}{\sqrt{2\pi\rho_1}} \cos(\theta/2)\left[1 + \sin(\theta/2)\sin(3\theta/2)\right] \tag{2.35b}$$

$$\sigma_{xy} = \frac{\sigma\sqrt{\pi a}}{\sqrt{2\pi\rho_1}} \cos(\theta/2)\sin(\theta/2)\cos(3\theta/2) \tag{2.35c}$$

Since the term $\sigma\sqrt{\pi a}$ is a constant for a given geometry and loading, we can replace this with the constant K_I and compare the relation with those given by the first-order terms of the Williams expansion for an edge crack (Eqns (2.25)). What can be seen is that, if the constant $K = a_1\sqrt{2\pi}$, the two equations are *exactly the same.* This proves that the equations relating stresses and displacements around a crack are of the same form regardless of the geometry and loading while the constant K_I, known as the mode I *stress intensity factor*, is the sole governing parameter for determining the magnitudes of stresses and displacements. In a similar fashion, expressions for mode II loading can be obtained which can be combined with those of (2.35) to give the general expressions for stresses around a crack tip

$$\begin{aligned}\sigma_{xx} =& \frac{K_{\mathrm{I}}}{\sqrt{2\pi\rho}} \cos(\theta/2)\,[1 - \sin(\theta/2)\sin(3\theta/2)] \\ & - \frac{K_{\mathrm{II}}}{\sqrt{2\pi\rho}} \sin(\theta/2)\,[2 + \cos(\theta/2)\cos(3\theta/2)] + H.O.T.\end{aligned} \tag{2.36a}$$

$$\begin{aligned}\sigma_{yy} =& \frac{K_{\mathrm{I}}}{\sqrt{2\pi\rho}} \cos(\theta/2)\,[1 + \sin(\theta/2)\sin(3\theta/2)] \\ & + \frac{K_{\mathrm{II}}}{\sqrt{2\pi\rho}} \sin(\theta/2)\cos(\theta/2)\sin(3\theta/2) + H.O.T.\end{aligned} \tag{2.36b}$$

$$\begin{aligned}\sigma_{xy} =& \frac{K_{\mathrm{I}}}{\sqrt{2\pi\rho}} \cos(\theta/2)\sin(\theta/2)\cos(3\theta/2) \\ & + \frac{K_{\mathrm{II}}}{\sqrt{2\pi\rho}} \cos(\theta/2)\,[1 - \sin(\theta/2)\sin(3\theta/2)] + H.O.T.\end{aligned} \tag{2.36c}$$

Then, by use of the constitutive equation to obtain strains which can then be integrated, displacements around a crack tip are written as

$$\begin{aligned}u_x =& \frac{K_{\mathrm{I}}}{2\mu}\sqrt{\frac{\rho}{2\pi}} \cos(\theta/2)[\kappa - 1 + 2\sin^2(\theta/2)] \\ & + \frac{K_{\mathrm{II}}}{2\mu}\sqrt{\frac{\rho}{2\pi}} \sin(\theta/2)[\kappa + 1 + 2\cos^2(\theta/2)]\end{aligned} \tag{2.37a}$$

$$\begin{aligned}u_y =& \frac{K_{\mathrm{II}}}{2\mu}\sqrt{\frac{\rho}{2\pi}} \sin(\theta/2)[\kappa + 1 - 2\cos^2(\theta/2)] \\ & - \frac{K_{\mathrm{II}}}{2\mu}\sqrt{\frac{\rho}{2\pi}} \cos(\theta/2)[\kappa - 1 - 2\sin^2(\theta/2)]\end{aligned} \tag{2.37b}$$

These expressions are extremely important in fracture mechanics since, once the parameters K_{I} and K_{II} are determined, the stress and displacement at any point surrounding the crack can be calculated. The importance of accurate stress intensity factors cannot be overemphasized and in fact, as will be discussed in the next section, it is generally accepted that these are the *sole* governing parameters that dictate fracture for linear elasticity.

2.4 Stress intensity factors as governing parameters

The equations which describe the stresses and displacements around a crack tip have been shown to follow the same dependence on the crack-tip coordinates ρ and θ regardless of the geometry or applied loading. Rather, it is the magnitude of the constants K_{I}, K_{II} (and K_{III} in 3D) which change and in fact, as will be argued in this section, a complete description of the region surrounding the crack tip can be described by these parameters. Therefore, what is paramount, and provides the main impetus for this thesis, is the accurate determination of these constants.

One application which illustrates clearly the need for accurate SIFs is in macro crack growth assessments and damage tolerant design. One fundamental equation which might often be used is the Paris law [14] which is probably the simplest of many crack growth laws. It dictates that the rate of crack growth da/dN (where N is the number of loading cycles) is given by

$$\frac{da}{dN} = C(\Delta K)^n \tag{2.38}$$

where C and n represent material constants and ΔK, related to the maximum difference in applied stresses, is the range of the stress intensity factor encountered in the cyclical loading regime. Taking for example 7075-T6 aluminum with a value of $n = 4$ [1], it is clear from (2.38) that any inaccuracy in K will be magnified greatly in the crack growth rate estimation.

However, some researchers have postulated that higher order terms in the crack solution must be included to provide an accurate representation of stresses and displacements surrounding the crack tip. Karihaloo and Xiao [16] implemented a “hybrid” crack element which is capable of calculating higher-order terms seen in Eqns (2.25) and (2.26) and found that the inclusion of these additional terms was beneficial to convergence. However, studies were also carried out by Chona et al. [1] using photoelastic experiments combined with the boundary collocation method (BCM). The formulation of the BCM incorporated a truncated form of the series

---

[1] in some ceramic materials n can be found to be as high as 24 to 131 [15]

given by (2.25) allowing higher-order terms to be included in the solution. Then, by comparing the stresses obtained through experiments with those calculated using only the first-order terms (ie. those including K_{I} and K_{II}) and those calculated using higher-order terms, they were able to define regions in which the singularity is most dominant. Fig. 2.6 illustrates one such plot in which the regions where the single-parameter solution differs from the series solution by 2% and 5% are defined for a specific crack length ratio. However, one of the most important features of their findings was the proof that there exists a region in which the stresses and displacements are governed by the singular terms and are *completely* described by the terms K_{I} and K_{II} - it is only a matter of substituting these values into expressions (2.36) and (2.37) to obtain stresses and displacements at any point within this zone. It becomes clear then, that in order to describe the singular field surrounding a crack tip with high accuracy, effort must be focused on finding accurate values of K_I and K_{II}. To achieve this, several methods are available to the engineer where more recently, due to their flexibility and ability to model arbitrary crack geometries, numerical methods have grown in popularity. A few methods in particular have seen extensive development and it is these, along with with some of the more recent advancements, that are described in the next section.

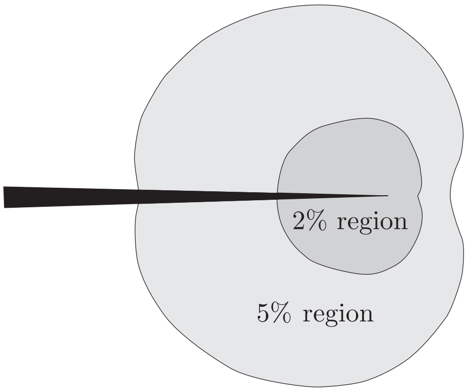

Figure 2.6: Singularity dominated zone for modified-compact-tension specimen, $a/w = 0.7$ (figure reproduced from [1])

2.5 Numerical methods for fracture

Analytical solutions like those given by Williams and Westergaard are limited in their practical application due to specified loadings on the boundary and the added assumption that cracks lie in an infinite domain. This clearly is an unreasonable assumption to make for cracked bodies in finite plates (see Figs. 2.7a and 2.7b) since the proximity of the boundary to the crack plays an important role in the distribution of stresses. By considering certain infinite plate problems (such as a the problem of an infinite array of collinear cracks) and making certain assumptions on the distribution of stress, it is possible to derive solutions for a certain number of finite plate problems (see [17] for a comprehensive review). In addition, since materials are considered to be linear elastic, the principle of superposition can be used to combine certain problems and solve a greater number of problems. However, when geometries and loadings are considered that do not follow any solution given in handbooks, then the situation is made more complicated. It is in these scenarios that the use of numerical methods, which make no restrictions on the geometry and loading of the cracked body, prove most useful.

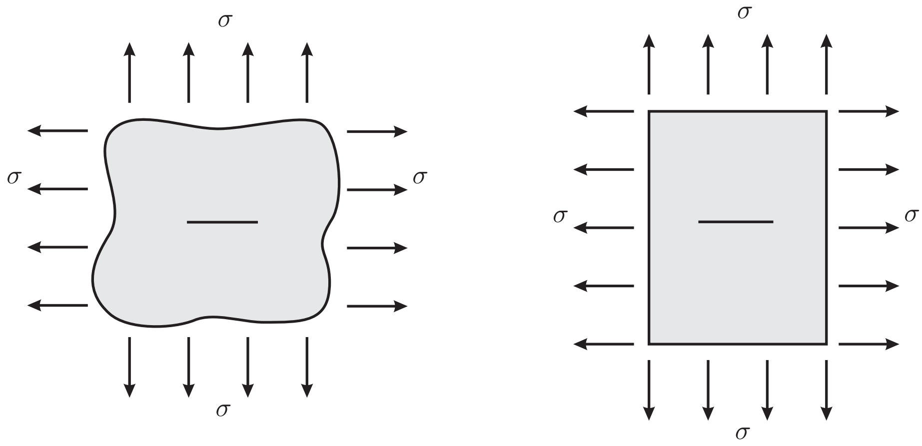

(a) Centre crack in infinite plate (b) Centre crack in finite plate

Figure 2.7: Comparison of infinite and finite boundaries

2.5.1 Boundary Collocation Method

One of the earliest numerical methods developed for use in fracture mechanics is the boundary collocation method (BCM) with the preliminary development of the method attributable to Gross et al. [18]. Use is made of the complex stress functions introduced by Westergaard (see Sec. 2.3) but, in the case of finite boundaries, complications arise due to the need to satisfy boundary conditions. To allow for this, complex functions in the form a truncated series can be used in which the first term corresponds to the singular solution of the crack tip and higher-order terms are included to satisfy the remote boundary conditions. One possible set of complex functions which can be used for the case of a single-ended traction-free crack is expressed as

$$Z(z) = \sum_{j=0}^{\infty} A_j z^{-1/2} \tag{2.39a}$$

$$Y(z) = \sum_{m=0}^{\infty} B_m z^m. \tag{2.39b}$$

Then, by using the above complex functions with Eqns (2.30) and (2.31), it is possible to write the following general expression for stress at any point with the complex coordinate $z = x + iy$

$$\sigma = \sum_{j=0}^{\infty} A_j f_j(z) + \sum_{m=0}^{\infty} B_m g_m(z) \tag{2.40}$$

where $f_j(z)$ and $g_m(z)$ are known, real functions. In fact, for the case of an edge crack, it can be shown that these functions are equivalent to those given by the Williams' expansion (Eqns 2.25 and Eqns 2.26). For other crack geometries, like that of a curved crack [19], the functions $f_j(z)$ and $g_m(z)$ can be derived through complex analysis methods. The task then is to find the values of the coefficients A_j and B_m. The BCM achieves this by evaluating expression (2.40) at a discrete number of points around the boundary in a process known as collocation. Then, if the number of collocation points is equal to to the number of unknown coefficients, the system is square and can be solved. In partitioned matrix form, the system of equations can be written as

$$\left[\begin{array}{c|c} f_j(\rho_i, \theta_i) & g_m(\rho_i, \theta_i) \end{array}\right] \left[\begin{array}{c} A_j \\ \hline B_m \end{array}\right] = [\sigma_i] \tag{2.41}$$

where i represents the row number of the matrix corresponding to a particular collocation point and polar coordinates have been assumed. If the matrix expression (2.41) is written more succinctly as

$$[f \mid g] \left[\begin{array}{c} A \\ \hline B \end{array}\right] = [\sigma] \tag{2.42}$$

then the coefficients can be solved simply by

$$\left[\begin{array}{c} A \\ \hline B \end{array}\right] = [f \mid g]^{-1} [\sigma]. \tag{2.43}$$

However, in the straightforward implementation of (2.43), large differences between required boundary values and those given by (2.42) at points in between collocation points lead to inaccuracies in the method. A simple least-squares procedure is often used [20] which uses a greater number of collocation points to produce an over-determined system. If we define the matrix $[C]$ as

$$[C] = [f \ | \ g]^T \, [f \ | \ g] \tag{2.44}$$

then the least squares solution for the over-determined system is written as

$$\left[\frac{A}{B}\right] = [C]^{-1} \, [f \ | \ g]^T \, [\sigma] \tag{2.45}$$

The BCM is one of the first numerical methods to be applied to fracture problems with finite, general geometries and it has been shown that high accuracies are seen in the implementation of the method, with errors of less than 0.2% found in K_{I} [21]). However, as briefly described here, the method suffers from the limitation that the complex functions $Z(z)$ and $Y(z)$ must be known *a priori* and, as seen in the case of a curved crack in a finite domain [19], the derivation of these can lead to rather complicated expressions. It must be noted though, that in many of the implementations of new numerical methods and variations thereof, solutions provided by the BCM for fracture problems are often used since they give a benchmark for problems that have no analytical solution. In fact, as will be shown in Chapter 8, the BCM is used for comparison of the new method outlined in this thesis for certain crack geometries.

2.5.2 Finite Element Method

Without doubt, the most popular numerical method at present is the Finite Element Method (FEM) [22] shown by its proven success in numerous applications. Within the field of fracture mechanics it too has shown a dominance over other methods, mainly due to its well-understood technologies and accepted use rather than its suitability for problems containing singularities. However, numerous methods have been developed to overcome the problem of a singularity created by a crack, with the eXtended Finite Element Method (XFEM) representing the most recent significant advance. Chapter 4 gives an overview of the these techniques along with a detailed description of the XFEM.

Before we consider how the FEM is able to model singularities, it is beneficial to give an overview of the method introducing the basic concepts that will be used in later chapters. The derivation of the method can be achieved by different routes, but all may be shown to be equivalent. For simplicity, the method which uses the principle of virtual work is adopted here. First, we consider a domain Ω with boundary Γ subject to a set of body forces b_i and tractions t_i which allows the principle of virtual work to be expressed as (assuming the index summation convention)

$$\int_{\Omega} \sigma_{ij}\delta\varepsilon_{ij}\mathrm{d}\Omega = \int_{\Omega} b_i\delta u_i\mathrm{d}\Omega + \int_{\Gamma} t_i\delta u_i\mathrm{d}\Gamma \tag{2.46}$$

where σ_{ij} and $\delta\varepsilon_{ij}$ are components of stress and virtual strain and u_i and δu_i are the components of displacements and virtual displacement respectively. Expression (2.46) can also be written in matrix notation as

$$\int_{\Omega} \boldsymbol{\delta\varepsilon}^{\mathbf{T}}\boldsymbol{\sigma}\mathrm{d}\Omega = \int_{\Omega} \boldsymbol{\delta}\mathbf{u}^{\mathbf{T}}\mathbf{b}\mathrm{d}\Omega + \int_{\Gamma} \boldsymbol{\delta}\mathbf{u}^{\mathbf{T}}\mathbf{t}\mathrm{d}\Gamma \tag{2.47}$$

The next step relies on what is arguably one of the most important concepts of the method, which is that an integral taken over the entire domain is equivalent to the sum of the integrals taken over the smaller sub-domains known as “elements”. This is shown in Figs 2.8a and 2.8b where an arbitrary global domain Ω with boundary Γ can be split into elements with local sub-domains Ω_e, $e = 1, ...N_e$. Regarding displacements over one of these elements and mapping from a global coordinate system (x, y) to a local coordinate system (ξ, η) (see Fig. 2.8c), it is possible to formulate an expression which gives the displacement at any point within the element by interpolation. The displacement components can then be written as

$$\mathbf{u} = [\mathbf{N^e}]\{\mathbf{u^e}\} \tag{2.48a}$$

$$\boldsymbol{\delta}\mathbf{u} = [\mathbf{N^e}]\{\boldsymbol{\delta}\mathbf{u^e}\} \tag{2.48b}$$

where in both cases $[\mathbf{N^e}]$ represents a matrix containing the local shape functions and $\{\boldsymbol{\delta}\mathbf{u^e}\}$ and $\{\mathbf{u^e}\}$ represent vectors of nodal displacements and virtual displacements respectively. In most cases the functions used for interpolation in $[\mathbf{N^e}]$ are chosen to be quadratic polynomials due to their relative accuracy and computational efficiency and depend on the local coordinates ξ and η. Using the above expressions, it is then

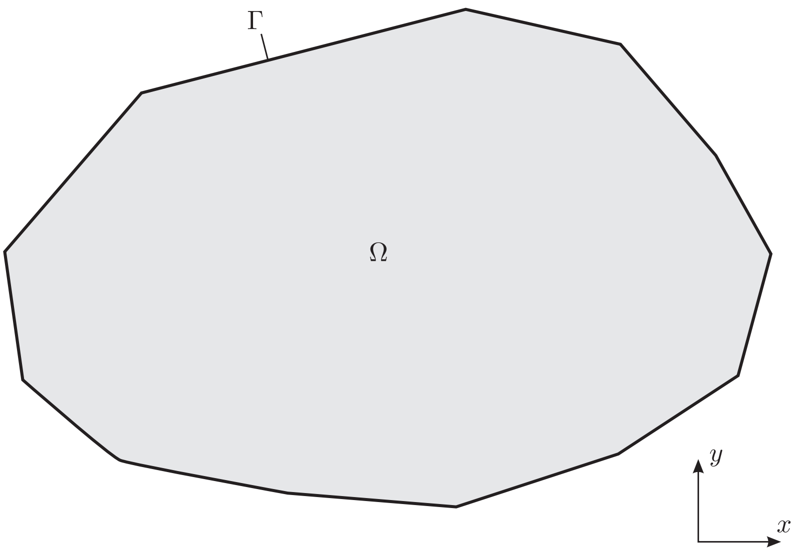

(a) Global domain Ω

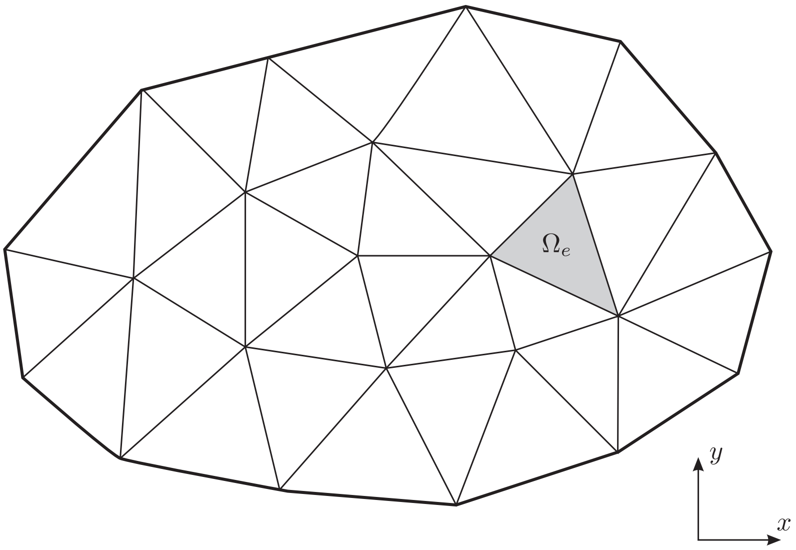

(b) Sub-domain Ω_e defining a particular “element”

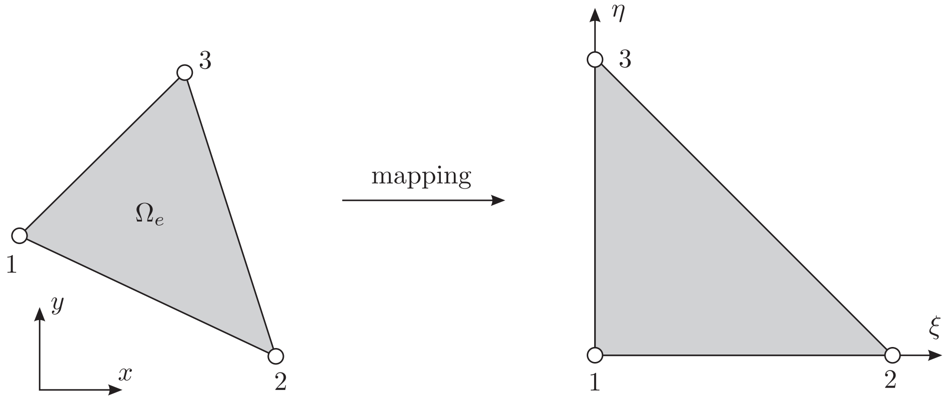

(c) Element in global and local coordinate systems

Figure 2.8: Global and local domains for FEM

possible to define strains and virtual strains as

$$\boldsymbol{\varepsilon} = [\mathbf{B^e}]\{\mathbf{u^e}\} \tag{2.49a}$$

$$\delta\boldsymbol{\varepsilon} = [\mathbf{B^e}]\{\delta\mathbf{u^e}\} \tag{2.49b}$$

where the matrix $[\mathbf{B^e}]$ is defined as

$$[\mathbf{B^e}] = \begin{bmatrix} \dfrac{\partial}{\partial x} & 0 \\ 0 & \dfrac{\partial}{\partial y} \\ \dfrac{\partial}{\partial y} & \dfrac{\partial}{\partial x} \end{bmatrix} [\mathbf{N^e}] \tag{2.50}$$

where engineering strain has been assumed. Having found the strains, stresses can be derived by using an appropriate set of constitutive equations through the relation

$$\boldsymbol{\sigma} = [\mathbf{D}]\boldsymbol{\varepsilon} = [\mathbf{D}][\mathbf{B^e}]\{\mathbf{u^e}\} \tag{2.51}$$

where, for a linear elastic body under plane stress, for example,

$$[\mathbf{D}] = \frac{E}{1-\nu^2} \begin{bmatrix} 1 & \nu & 0 \\ \nu & 1 & 0 \\ 0 & 0 & \dfrac{1-\nu}{2} \end{bmatrix} \tag{2.52}$$

Since displacements, strains and stresses are now defined by Eqns (2.48), (2.49) and (2.51) over a particular element e, substitution of these expressions into (2.47) gives the following integral over the local sub-domain for virtual work

$$\{\delta\mathbf{u^e}\}^{\mathbf{T}} \left\{ \int_{\Omega_e} [\mathbf{B^e}]^{\mathbf{T}}[\mathbf{D}][\mathbf{B^e}]\{\mathbf{u^e}\}\,\mathrm{d}\Omega_e - \int_{\Omega_e} [\mathbf{N^e}]^{\mathbf{T}}\{\mathbf{b^e}\}\,\mathrm{d}\Omega_e - \int_{\Omega_e} [\mathbf{N^e}]^{\mathbf{T}}\{\mathbf{t^e}\}\,\mathrm{d}\Omega_e \right\} = 0 \tag{2.53}$$

Since this must be true for any virtual displacement $\{\delta\mathbf{u^e}\}$, the second term of (2.53) must be equal to zero. Defining the element stiffness matrix as

$$[\mathbf{K^e}] = \int_{\Omega_e} [\mathbf{B^e}]^{\mathbf{T}}[\mathbf{D}][\mathbf{B^e}]\,\mathrm{d}\Omega_e \tag{2.54}$$

and the local body force and traction vectors as

$$\{\mathbf{F^e_b}\} = \int_{\Omega_e} [\mathbf{N^e}]^{\mathbf{T}}\{\mathbf{b^e}\}\,\mathrm{d}\Omega_e \tag{2.55a}$$

$$\{\mathbf{F^e_t}\} = \int_{\Omega_e} [\mathbf{N^e}]^{\mathbf{T}}\{\mathbf{t^e}\}\,\mathrm{d}\Omega_e \tag{2.55b}$$

which can be expressed in terms of a single vector known as the nodal force vector

$$\{\mathbf{F^e}\} = \{\mathbf{F^e_b}\} + \{\mathbf{F^e_t}\} \tag{2.56}$$

the FEM formulation can be reduced, for a particular element, to

$$[\mathbf{K^e}]\{\mathbf{u^e}\} = \{\mathbf{F^e}\} \tag{2.57}$$

Now, referring back to the concept described earlier where an integral over a domain Ω is equivalent to the sum of the integrals taken over all the sub-domains Ω_e, expression (2.57) can be found for all elements and combined to form a global stiffness matrix $[\mathbf{K}]$ and generalised nodal force vector $\{\mathbf{F}\}$. This allows the following global system of equations to be written

$$[\mathbf{K}]\{\mathbf{u}\} = \{\mathbf{F}\} \tag{2.58}$$

Once sufficient boundary conditions are imposed on the domain, it is possible to solve the above equation and find all unknown nodal displacements and forces for any arbitrary problem. This flexibility makes the method extremely powerful for solving a wide variety of problems but, in the case of problems containing singularities or discontinuities, problems arise. A domain containing a crack is one such problem since, as described in Sec. 2.2, a singular stress of $\mathcal{O}(1/\rho^{1/2})$ is seen at the crack tip. It is clear then that if conventional quadratic shape functions are used to interpolate this singular stress, large errors will occur if relatively coarse meshes are used. In order to overcome this problem using conventional elements, very refined meshes are required in the region surrounding the crack tip (see Fig. 2.9) and even with this refinement, convergence is not guaranteed [23]. Various methods are available to overcome this problem including special elements that can capture the crack-tip singularity and the more recently developed eXtended Finite Element Method (XFEM), but in certain circumstances other alternative numerical methods are available which provide more economical solutions.

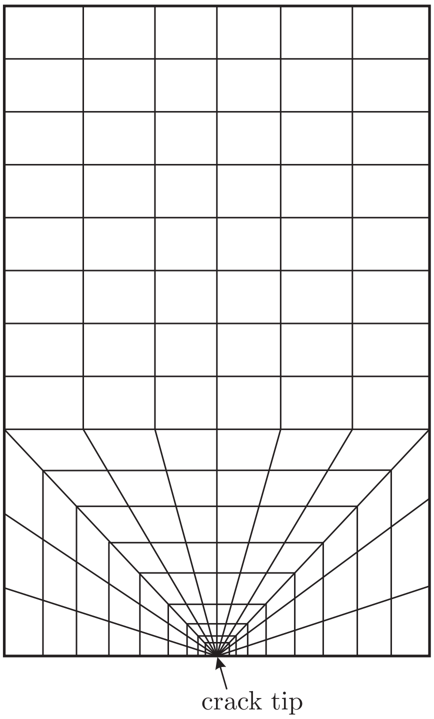

Figure 2.9: Mesh refinement for FEM using conventional, non-singular elements

2.5.3 Boundary Element Method

The Boundary Element Method (BEM) is another numerical technique which has seen success in a wide variety of applications and, as shown by numerous researchers (eg. [24] and [25]), the method demonstrates particular advantages in problems containing singularities. For various reasons, the BEM has not been popularised to the same extent as the FEM, but recent developments have shown that in many cases the BEM provides a more economical implementation. The case of Linear Elastic Fracture Mechanics (LEFM) is one such example.

The inherent advantage of the BEM over domain-discretisation methods such as the FEM is that only the *boundary* need be discretised. Therefore, to model the same crack problem as that shown in Fig. 2.9 for a BEM analysis, the mesh shown in Fig. 2.10 could be used. Clearly, far fewer elements are required which, even if mesh-grading is used around the crack tip, leads to a more efficient solution. Of course, as with any numerical method, there are some drawbacks to the BEM such as the creation of fully populated matrices (in comparison to the diagonally dominant matrices seen in the FEM) and difficulties in implementing non-linear materials. But for models which are linear elastic and exhibit high stress gradients, the BEM is an extremely strong contender for the most efficient computational method available to the engineer. In fact, for a model which includes a crack, the method is particularly suitable not only due to its ability to model high stress gradients, but also due to the fact that fracture analysis is mostly concerned with parameters on the boundary.

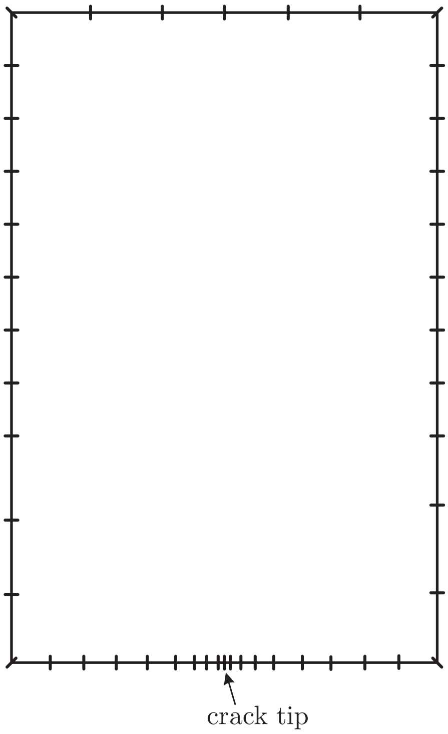

Figure 2.10: Example BEM mesh for crack problem

A much more detailed description of the method could be given here but, in keeping with previous sections, only a brief overview of the method rather than a complete derivation is outlined. Instead, Chapter 3 is devoted to a much more detailed description of the method since extensive use is made of the BEM in this thesis.

2.5.4 Meshless methods

In both the FEM and BEM meshes are constructed which divide the domain and boundary into discrete elements over which parameters are interpolated. A relatively new approach which has seen rapid growth within the academic community precludes the use of meshes but instead relies on an interpolation scheme using the method of moving least squares (MLS). These methods fall under the general name of meshless methods. The first use of a meshless method within the context of elastostatics can be attributed to Belytschko et al. [26] which is now known as the Element Free Galerkin (EFG) method. Instead of dividing the domain into a grid made up of elements, nodes are spaced throughout the domain which can be spaced arbitrarily (within reason) and each is contained with a region known as the nodal support (shown in Fig. 2.11). Within this region a weight function is defined such that any point within the domain is covered by at least three distinct weight functions. There are several common weight functions including quartic splines and exponential functions (see Fig. 2.12) which are defined over this nodal support. The shape functions can then be created using a weighted MLS routine and are usually expressed in the following manner

$$N_a(\mathbf{x}) = \mathbf{p}^{\mathrm{T}}(\mathbf{x})\mathbf{A}^{-1}(\mathbf{x})\mathbf{C}_a(\mathbf{x}) \tag{2.59}$$

where $\mathbf{p}^{\mathrm{T}}(\mathbf{x})$ is a basis vector that, for a linear basis, is denoted by

$$\mathbf{p}^{\mathrm{T}}(\mathbf{x}) = [1, x, y] \tag{2.60}$$

and the terms $\mathbf{A}^{-1}(\mathbf{x})$ (often called the moment matrix) and $\mathbf{C}_a(\mathbf{x})$ are made up of combinations of the basis vector and the chosen weight functions. Displacements can then be interpolated in the conventional manner as

$$u_j = \sum_{a=1}^{n} N_a u_j^a \tag{2.61}$$

where n is the number of neighbours to the point a and u_j^a is a nodal displacement. However, as is well-known in mesh-free methods, if the shape functions are formulated in this way then they do not possess the kronecker delta property and alternative ways of enforcing boundary conditions have to be employed. The two most popular methods are the use of Lagrange multipliers and penalty methods where additional terms, included in the variational equation, are used to satisfy the required boundary conditions.

The EFG method has been applied successfully to fracture problems where the absence of a mesh is found to be particularly useful, especially for crack propagation. One of the first implementations of crack problems in EFG can be attributed to Belytschko et al. [27] who showed that accurate SIFs (∼1% error) could be obtained using the method[2]. Of course, with high stress gradients surrounding the crack tip, high densities of nodes were required in this region (such as those shown in Fig. 2.11),

---

[2] Compared to ∼0.1% seen using local PUM enrichment illustrated in this thesis.

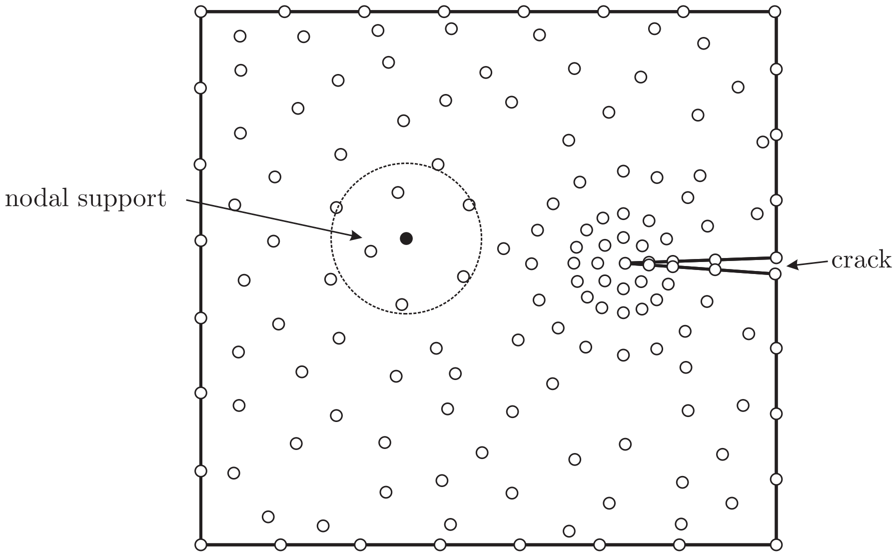

Figure 2.11: Example of arbitrary nodal arrangement for the Element Free Galerkin Method

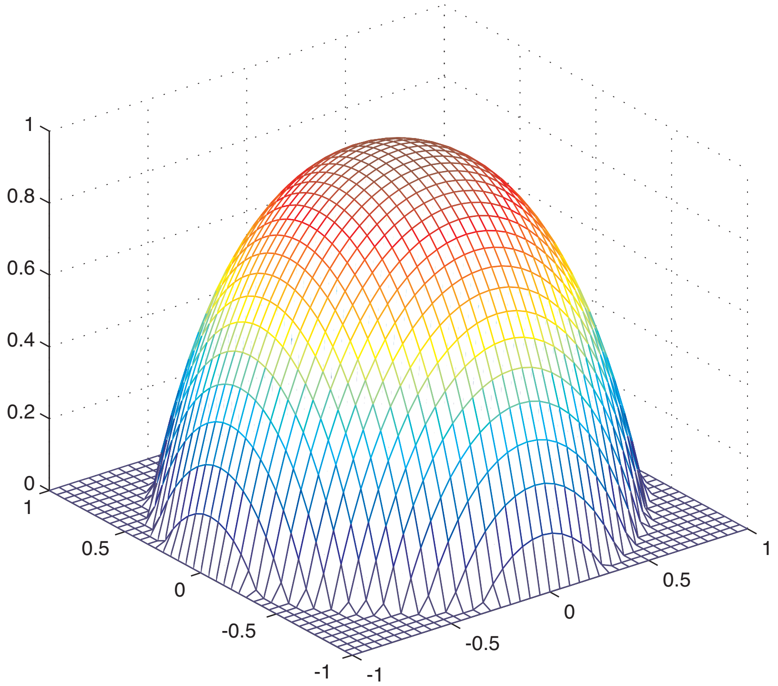

Figure 2.12: Exponential weight function defined over nodal support

but the relative ease of advancing the crack represented a significant advantage over the FEM. The EFG method has since been developed to incorporate functions which "enrich" certain nodes surrounding the crack tip [28] and therefore reduce the required number of nodes for a given accuracy. In addition, several techniques which overcome the problems of defining nodal supports around discontinuities have been outlined and these have helped to make meshless methods recognised as a key method in numerical fracture mechanics.

2.6 Methods for evaluating stress intensity factors

As described in Sec. 2.4, fracture mechanics is centred around the task of finding accurate SIFs and since most numerical methods do not output SIFs directly,[3] it is necessary to carry out post-processing routines. The techniques which can achieve this fall into two categories: those which use either stresses or displacements surrounding the crack tip to calculate SIFs which are then extrapolated to the crack tip, and the use of energy methods requiring path/domain integrals.

2.6.1 Displacement extrapolation

Since displacements within a certain region surrounding the crack tip are known to be described by the singular terms given by both the Williams and Westergaard expressions (Eqns (2.26) and (2.37)), it is possible, through rearrangement of these expressions and values of displacements from a numerical analysis, to determine SIFs. These values can then be plotted against the distance ρ to the crack tip and, by extrapolation, a single value for the SIF can be found. To illustrate how this can be achieved, 2D boundary elements such as those illustrated in Fig. 2.13 can be used where, for illustration purposes, the elements on each of the crack surfaces have been drawn with a finite separation when in reality these will be coincident. Therefore, by making the assumption that the elements are flat, the crack angle θ will be equal to π and $-\pi$ along the top and bottom crack surfaces respectively. By substituting these values into the expressions for crack tip displacements (Eqns 2.37a and 2.37b),

---

[3] There are, however, some methods that do and these will be described in Chapter 4. In addition, one of the enrichment formulations for the BEM presented in this thesis is capable of direct SIF output and is shown in Chapter 6.

the following can be written

$$u_y^T - u_y^B = \frac{\kappa+1}{\mu} K_{\mathrm{I}} \sqrt{\frac{\rho}{2\pi}} \tag{2.62a}$$

$$u_x^T - u_x^B = \frac{\kappa+1}{\mu} K_{\mathrm{II}} \sqrt{\frac{\rho}{2\pi}} \tag{2.62b}$$

where the superscripts T and B denote the top and bottom crack faces respectively. These could be used directly with one set of adjacent nodes (eg. nodes 2 and 3 or 4 and 5 in Fig. 2.13) where the formula is known as the one-point displacement formula. Instead, SIFs can be determined at each of the nodal pairs and then extrapolated to the crack tip to produce a two-point displacement formula. This can be derived by first noting that in Fig. 2.13 the nodes 2 and 3 are positioned at a distance $l/2$ from the crack tip. Substituting this for ρ in Eqns (2.62a) and (2.62b) gives

$$K_{\mathrm{I}}^{23} = \frac{2\mu}{\kappa+1} \sqrt{\frac{\pi}{l}} (u_y^2 - u_y^3) \tag{2.63a}$$

$$K_{\mathrm{II}}^{23} = \frac{2\mu}{\kappa+1} \sqrt{\frac{\pi}{l}} (u_x^2 - u_x^3) \tag{2.63b}$$

and likewise, by substituting l for ρ a similar set of equations are given for nodes 4 and 5

$$K_{\mathrm{I}}^{23} = \frac{\mu}{\kappa+1} \sqrt{\frac{2\pi}{l}} (u_y^4 - u_y^5) \tag{2.64a}$$

$$K_{\mathrm{II}}^{23} = \frac{\mu}{\kappa+1} \sqrt{\frac{2\pi}{l}} (u_x^4 - u_x^5). \tag{2.64b}$$

Finally, using linear extrapolation to the crack tip, a single value for each of the SIFs can be obtained from

$$K_{\mathrm{I}} = 2K_{\mathrm{I}}^{23} - K_{\mathrm{I}}^{45} \tag{2.65a}$$

$$K_{\mathrm{II}} = 2K_{\mathrm{II}}^{23} - K_{\mathrm{II}}^{45}. \tag{2.65b}$$

These expressions are extremely simple to implement as a post-processing procedure and are probably the fastest way to obtains SIFs from a numerical analysis. However, before other more complex SIF evaluation techniques are disregarded, some significant drawbacks of the present approach must be outlined. Perhaps the most prominent of these is the failure of the crack-tip elements to account for the $\sqrt{\rho}$ variation seen at a crack tip. When the above formulae are used for these types of elements, inaccurate SIFs are often produced. For example, Fig. 2.14 illustrates displacement extrapolation of SIFs using conventional quadratic elements and special "enriched" elements which are capable of capturing the singularity seen at the crack tip. This figure was obtained for a mode I centre crack using the Dual Boundary Element Method (unenriched) and local PUM enriched formulation outlined in Chapter 6. Clearly in the unenriched case an extrapolation of nodal values closest to the crack tip produces highly inaccurate results whereas the "enriched" elements much more closely approximate the solution. Therefore special elements or shape functions must be used in conjunction with the displacements extrapolation method if reasonably accurate results are to be obtained. Even so, Martínez and Domínguez [29] showed that the displacement extrapolation method used with quarter-point elements (these are described in Sec. 5.1.1) was unreliable due to a dependence on crack-tip element length and errors greater than 5% in SIFs were not uncommon. However, it must not be forgotten that the method is one of the simplest and quickest techniques to obtain SIFs and therefore, if the limitations in accuracy are acknowledged, the displacement extrapolation method provides a quick, rough estimate of SIFs for the engineer.

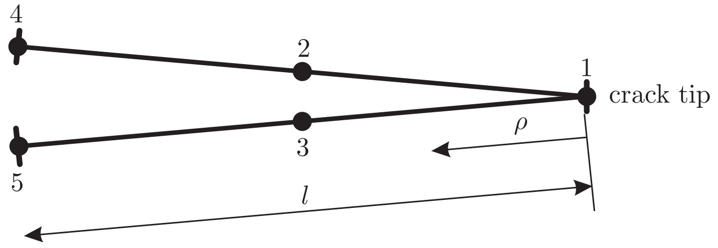

Figure 2.13: Crack tip elements used for displacement extrapolation

2.6.2 J-integral for flat cracks

The J-integral is the most popular technique used to evaluate SIFs, especially for FEM and BEM implementations, and is attributed to the work carried out by Rice [30]. The integral is based on energy methods and has the important property of path-independence, a particularly useful feature in fracture problems since an integration path, positioned far from the high stress gradients seen at the crack

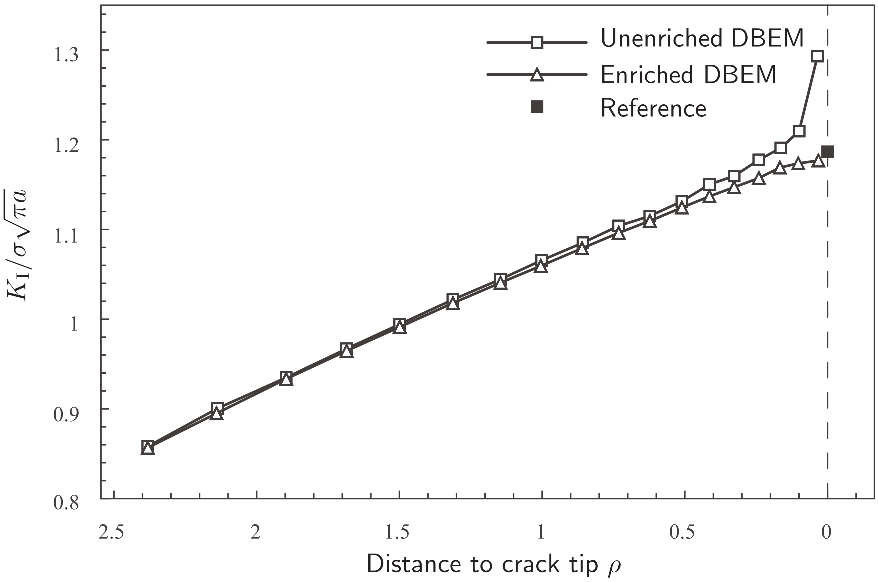

Figure 2.14: Comparison of SIF extrapolation using quadratic elements and "enriched" elements

tip, can be used. However, as will be shown shortly, the direct implementation of the J-integral for mixed-mode problems does not allow the SIF components to be determined - instead, certain decomposition routines or modified forms of the integral must be used. Once implemented though, the method presents one of the most accurate techniques for evaluation of SIFs and for this reason, it is used routinely for the numerical examples presented in this thesis.

To begin with, we consider a flat crack within a domain with local crack-tip coordinates (x,y) and take a path Γ_J starting at one crack face and ending at the other (see Fig. 2.15). We can then define the J-integral as

$$J = \int_{\Gamma_J} \left(W n_x - t_i \frac{\partial u_i}{\partial x} \right) \mathrm{d}\Gamma \tag{2.66}$$

where W is the strain energy density defined as

$$W = \frac{1}{2}\sigma_{ij}\varepsilon_{ij}, \tag{2.67}$$

n_x is the x-component of the normal vector $\mathbf{n}$ and (u_i,t_i) are displacement and traction components. In the strict sense, the J-integral path should be the closed contour formed by the union of Γ_J with the portions of the upper and lower crack surfaces lying between the crack tip and the end points of Γ_J. It should be noted that, for the case of a flat crack subject to zero tractions on the crack surfaces, the

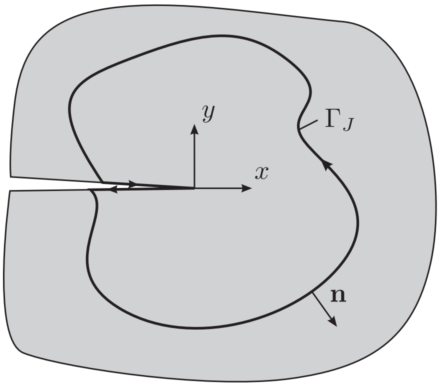

Figure 2.15: Definition of J-integral path

situation is simplified and the path Γ_J is sufficient, because no contribution is made to the J-integral along each of the surfaces since $n_x = 0$ and $t_i = 0$. The direct implementation of Eq. (2.66) is simple, but, for the J-integral to be of practical use, it is necessary to express it in terms of the SIFs. By noting that J is related to the strain energy release rate (see Sec. 2.1), it is possible to write the following equation which expresses J in terms of the Mode I and II SIFs for 2D plane stress problems

$$J = \frac{K_{\mathrm{I}}^2 + K_{\mathrm{II}}^2}{E'} \tag{2.68}$$

where E' is the modified Young's modulus defined as

$$E' = \begin{cases} E & \text{plane stress} \\ \dfrac{E}{1-\nu^2} & \text{plane strain} \end{cases} \tag{2.69}$$

In the case of pure Mode I problems where K_{II} equals zero, a simple rearrangement of the equation will return K_{I} directly. However, for mixed-mode fracture, problems arise due to the summation of K_{I} and K_{II} terms. Several researchers have studied this problem [31], [32], [33], [34], [35] while all achieve the same goal - decomposition of the J-integral into individual SIF components. In the present work, use is made of the decomposition technique using symmetric points [31]. An outline of the technique is given presently.

Ishikawa et al. [31] showed that, if the internal points used for the numerical integration of the J-integral are located symmetrically about the crack (assuming it is flat), then it is possible to derive two integral expressions which allow evaluation of the SIF components. If a circular integration path is used, then the points may be positioned in a manner such as those in Fig. 2.16. Considering two points $P(x,y)$ and $P'(x,-y)$ with displacements, strains and stresses at each of these defined by $(u_i,\ \varepsilon_{ij},\ \sigma_{ij})$ and $(u'_i,\ \varepsilon'_{ij},\ \sigma'_{ij})$ respectively (while noting that $t_i = \sigma_{ij} n_j$), then the following symmetric and anti-symmetric components can be defined as

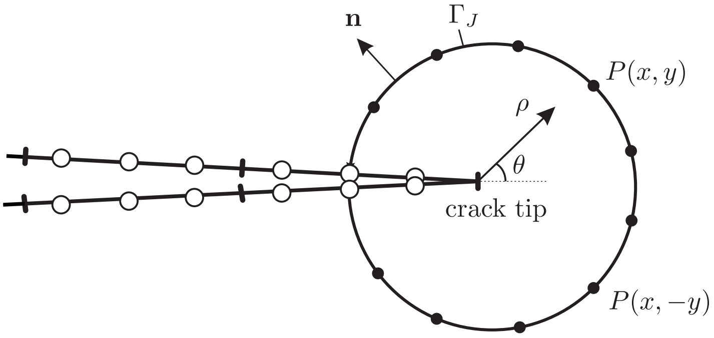

Figure 2.16: Circular J-integral path with symmetric internal points

$$\begin{Bmatrix}\sigma^{\mathrm{I}}_{xx}\\ \sigma^{\mathrm{I}}_{yy}\\ \sigma^{\mathrm{I}}_{xy}\end{Bmatrix} = \frac{1}{2}\begin{Bmatrix}\sigma_{xx}+\sigma'_{xx}\\ \sigma_{yy}+\sigma'_{yy}\\ \sigma_{xy}-\sigma'_{xy}\end{Bmatrix} \qquad \begin{Bmatrix}\sigma^{\mathrm{II}}_{xx}\\ \sigma^{\mathrm{II}}_{yy}\\ \sigma^{\mathrm{II}}_{xy}\end{Bmatrix} = \frac{1}{2}\begin{Bmatrix}\sigma_{xx}-\sigma'_{xx}\\ \sigma_{yy}-\sigma'_{yy}\\ \sigma_{xy}+\sigma'_{xy}\end{Bmatrix} \tag{2.70a}$$

$$\begin{Bmatrix}\varepsilon^{\mathrm{I}}_{xx}\\ \varepsilon^{\mathrm{I}}_{yy}\\ \varepsilon^{\mathrm{I}}_{xy}\end{Bmatrix} = \frac{1}{2}\begin{Bmatrix}\varepsilon_{xx}+\varepsilon'_{xx}\\ \varepsilon_{yy}+\varepsilon'_{yy}\\ \varepsilon_{xy}-\varepsilon'_{xy}\end{Bmatrix} \qquad \begin{Bmatrix}\varepsilon^{\mathrm{II}}_{xx}\\ \varepsilon^{\mathrm{II}}_{yy}\\ \varepsilon^{\mathrm{II}}_{xy}\end{Bmatrix} = \frac{1}{2}\begin{Bmatrix}\varepsilon_{xx}-\varepsilon'_{xx}\\ \varepsilon_{yy}-\varepsilon'_{yy}\\ \varepsilon_{xy}+\varepsilon'_{xy}\end{Bmatrix} \tag{2.70b}$$

$$\begin{Bmatrix}u^{\mathrm{I}}_{x}\\ u^{\mathrm{I}}_{y}\end{Bmatrix} = \frac{1}{2}\begin{Bmatrix}u_x+u'_x\\ u_y-u'_y\end{Bmatrix} \qquad \begin{Bmatrix}u^{\mathrm{II}}_{x}\\ u^{\mathrm{II}}_{y}\end{Bmatrix} = \frac{1}{2}\begin{Bmatrix}u_x-u'_x\\ u_y+u'_y\end{Bmatrix} \tag{2.70c}$$

where

$$\sigma_{ij} = \sigma^{\mathrm{I}}_{ij} + \sigma^{\mathrm{II}}_{ij} \tag{2.71a}$$

$$\varepsilon_{ij} = \varepsilon^{\mathrm{I}}_{ij} + \varepsilon^{\mathrm{II}}_{ij} \tag{2.71b}$$

$$u_i = u^{\mathrm{I}}_{i} + u^{\mathrm{II}}_{i} \tag{2.71c}$$

When the above equations are substituted into the original J-integral expression (Eq. 2.66), and the following expression relating normal components is used

$$(n'_x, n'_y) = (n_x, -n_y) \tag{2.72}$$

then the J-integral can be written as

$$J = J_{\mathrm{I}} + J_{\mathrm{II}} \tag{2.73}$$

where

$$J_{\mathrm{I}} = \int_{\Gamma_J} \left(\frac{1}{2} \sigma_{ij}^{\mathrm{I}} \varepsilon_{ij}^{\mathrm{I}} n_x - \sigma_{ij}^{\mathrm{I}} n_j u_{i,y}^{\mathrm{I}} \right) \mathrm{d}\Gamma \tag{2.74a}$$

$$J_{\mathrm{II}} = \int_{\Gamma_J} \left(\frac{1}{2} \sigma_{ij}^{\mathrm{II}} \varepsilon_{ij}^{\mathrm{II}} n_x - \sigma_{ij}^{\mathrm{II}} n_j u_{i,y}^{\mathrm{II}} \right) \mathrm{d}\Gamma \tag{2.74b}$$

Therefore, once these components are known, is it possible to extract SIFs through the relations

$$J_{\mathrm{I}} = \frac{K_{\mathrm{I}}^2}{E'} \qquad J_{\mathrm{II}} = \frac{K_{\mathrm{II}}^2}{E'} \tag{2.75}$$

The technique is simple to implement making it very attractive for FEM and BEM formulations and, as shown by Portela et al. [24], the accuracy of the SIFs is shown to be very high. However, as is the case with many other J-integral decomposition routines, the method breaks-down when non-flat cracks are considered. Further details on why this is the case, along with alternative techniques to overcome this problem, will be outlined shortly, but the present method, due to its ease of implementation and high accuracy, is favoured in problems with flat cracks.

2.6.3 J-integral for non-flat cracks

The majority of fracture problems analysed using numerical techniques are modelled with flat cracks which, in many cases, is a valid assumption. However, there are scenarios where this assumption cannot be made and alternative techniques to model the crack must be employed. In addition, the straightforward application of the J-integral described previously to non-flat cracks is no longer valid requiring certain modifications in the implementation. This section aims to describe, by taking the case of a curved crack, why the conventional J-integral expression presents difficulties for numerical implementation and how the use of an additional integral, termed the J_2 integral, can be used to provide a complete description of the crack behaviour.

Fig. 2.17 illustrates a curved, traction-free crack with local Cartesian crack-tip coordinates and a normal vector $\mathbf{n}$ defined for the upper crack surface. If the technique illustrated in Sec. 2.6.2 is used for this example, then the results will no longer be valid. This is because the assumption that along the crack surfaces the normal component $n_x = 0$ is no longer true, and an additional component Wn_x must be included. But before this is evaluated, it is important to observe the behaviour of the strain energy W as the crack tip is approached. We know that Eq. (2.67) is used to calculate W where, from the expressions describing stresses around a crack tip, the terms ε_{ij} and σ_{ij} are both of $\mathcal{O}(1/\rho^{1/2})$. This gives a strain energy of $\mathcal{O}(1/\rho)$ but, since the normal component $n_x \to 0$ as the crack tip is approached, the product Wn_x is non-singular and can be evaluated using standard numerical integration routines. Therefore the evaluation of the J-integral does not present undue difficulties for curved cracks. But what presents a problem is the decomposition of the integral into separate components that will allow the determination of SIFs.

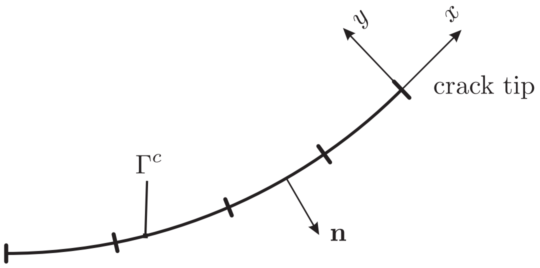

Figure 2.17: Traction-free curved crack

To address this, it is necessary to introduce a more general form of the J-integral expression which is written as

$$J_k = \int_{\Gamma_J} (Wn_k - t_i u_{i,k})\, \mathrm{d}\Gamma, \quad k = 1, 2 \tag{2.76}$$

where, in keeping with other common notation, the component directions 1 and 2 are used which are equivalent to the local crack tip coordinates x and y. What this expression shows is that the J-integral is in fact the J_1 component while a new integral, known as the J_2-integral, is introduced. By evaluating both of these components and noting that J_1 is related to the SIFs by Eq. (2.68) and J_2 is expressed likewise as

$$J_2 = -\frac{2K_\mathrm{I}K_\mathrm{II}}{E'}, \tag{2.77}$$

the mode I and II SIFs can be found. However, in contrast to the J_1 integral where the component Wn_k is regular, the normal component n_2 (n_y) tends to unity as the crack tip is approached and therefore the term Wn_2 is singular of $\mathcal{O}(1/\rho)$. Integration of this term using a standard integration routine would introduce large errors and so an alternative procedure which can account for this singularity must be used. Eischen [36] first introduced a technique that defines a certain region with radius R which is regarded as being dominated by the singular term (see Fig. 2.18). By defining a strain energy jump across the crack faces in the region R as

$$[\![W]\!] = W^+ - W^- \tag{2.78}$$

where W^+ and W^- are the strain energies on the upper and lower crack faces respectively, it is possible, through the use of Eqns (2.36) (and similar expressions for strain), to show that the strain energy jump can be rewritten as

$$[\![W]\!] \approx \Lambda \rho^{-1/2} + \mathcal{O}(1) \tag{2.79}$$

where the constant Λ is an invariant for a given problem. Using this definition, along with the integration paths defined in Fig. 2.18, the J_k-integral can then be rewritten as

$$J_k = \int_{\Gamma_J} \left(W n_k - \sigma_{ij} n_j \left(\frac{\partial u_i}{\partial x_k} \right) \right) d\Gamma + \int_{(\Gamma_J^{c+} - R) + (\Gamma_J^{c-} - R)} W n_k d\Gamma + 2\Lambda \delta_{k2} R^{1/2} \tag{2.80}$$

where δ denotes the kronecker delta function. Therefore, in the evaluation of the J_1 integral, the third term of (2.80) is simply omitted. In the case of the J_2 integral, it is necessary to make an appropriate choice of R and in fact, since both J_2 and Λ are both unknowns, it is necessary to choose multiple values of R to allow both values to be determined by a least-squares scheme [37]. This is possible since both values are invariant for a given problem.

It can be seen, by comparing this technique to that described for flat cracks in Sec. 2.6.2, that the introduction of non-flat cracks creates certain complications for the evaluation of fracture parameters. These can not be avoided if an accurate representation of the problem is required, but it is convenient that in most cases - and in fact, for most standard testing specimens - flat cracks are seen.

2.6.4 Contour integral method

In addition to the popularised J-integral approach, there are a variety of integral approaches proposed which are capable of producing decomposed SIFs. One of the original methods, proposed by Stern et al. [33], uses Betti's reciprocal theorem with an appropriate auxiliary equilibrium state which allows, after carrying out

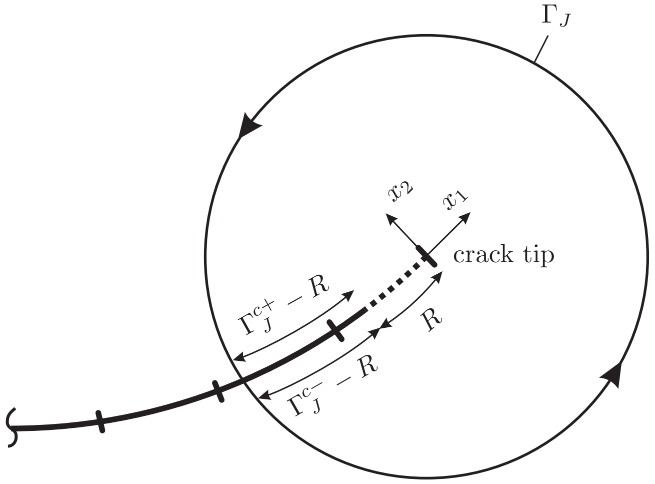

Figure 2.18: Definition of integral paths used for evaluation of J_1 and J_2 integrals

an appropriate path integral, K_{I} and K_{II} to be determined separately. Since this method is used in later work, an outline of the derivation and implementation is given here.

Betti's reciprocal theorem [38] states that two equilibrium states (u_i, t_i) and (u_i^*, t_i^*) for a domain with boundary Γ can be related by the following integral equation

$$\int_\Gamma (u_i t_i^* - u_i^* t_i)\mathrm{d}\Gamma = 0. \tag{2.81}$$

Considering a body with a flat crack, a region with an arbitrarily small radius ε is removed from the domain leaving the boundaries Γ, Γ_ε,Γ_c^+ and Γ_c^- (see Fig. 2.19). Applying Eq. (2.81) to these boundaries and assuming traction-free cracks[4], Eq. (2.81) can be rewritten as

$$-\int_{\Gamma_\varepsilon} (u_i t_i^* - u_i^* t_i)\mathrm{d}\Gamma = \int_\Gamma (u_i t_i^* - u_i^* t_i)\mathrm{d}\Gamma. \tag{2.82}$$

Since the integral on the LHS of (2.82) is evaluated at a small distance from the crack tip, the equilibrium state (u_i, t_i) can be represented by Eqns (2.37) and (2.36) (while noting that $t_i = \sigma_{ij} n_j$) which describe displacements and stresses surrounding a crack. The equilibrium state (u_i^*, t_i^*) however is chosen in such a way that when it is substituted into (2.82) and combined with the exact crack tip displacements and

---

[4] Therefore no contribution is made to the integral from the crack surfaces $\Gamma c+$ and $\Gamma c-$

tractions u_i and t_i, the integral equation reduces to the following

$$c_1 K_{\mathrm{I}} + c_2 K_{\mathrm{II}} = \int_{\Gamma} (u_i t_i^* - u_i^* t_i) \mathrm{d}\Gamma \tag{2.83}$$

where c_1 and c_2 are constants included in the expressions for the state $(u_i^*,\ t_i^*)$. These "auxiliary" solutions are derived through a complex analysis method where the Cartesian form of the equations are given in Appendix D.4. Then, by performing an integral around the crack using these auxiliary solutions along with displacements and tractions obtained from a numerical analysis, it is possible, by combing all those terms relating to c_1 and c_2, to determine the SIFs K_{I} and K_{II}.

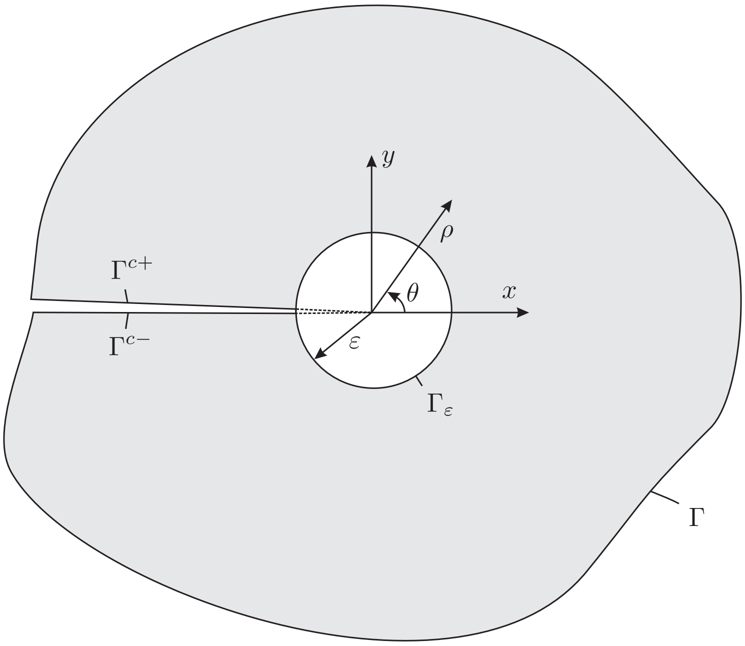

Figure 2.19: Definition of boundaries about crack tip used for contour integral

Since the introduction of the method by Stern et al. [33], the method has since been extended to 3D problems [39], [35] where the integral is now taken over a domain such as that shown in Fig. (2.20). It is found, however, that much of the effort required in implementing the method is centred on the definition of a suitable 3D coordinate system which can, for cracks that are non-planar (ie. curved) and have a curved crack front, become even more complicated.

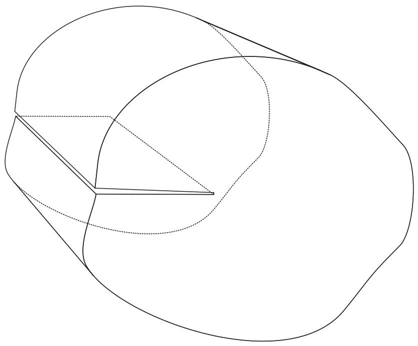

Figure 2.20: Example integration domain used for 3D implementation of contour integral

Chapter 3

The Boundary Element Method

The history of the Boundary Element Method (BEM) dates back to the 1960s when, with the introduction of computers that could handle thousands of calculations per second, numerical methods became feasible analytical tools. It is generally regarded that Jaswon [40] and Symm [41] were the first to utilise this power with the BEM and carry out computational analyses for 2D potential problems. However, with the introduction of the FEM and its broad acceptance amongst engineers, the original work on the BEM was slow in development and remained relatively dormant for a period of time. Some key advances that did appear in this period though included an extension of the method to elastostatics by Rizzo [42] which was later adapted for 3D problems by Cruse [43], but the lack of active research in the field made progress slow. Eventually, a group of determined researchers emerged who were convinced of the benefits the BEM could provide and rapid development of the method ensued. Some of the most important work is attributed to Lachat [44] and later Lachat and Watson [45] who were the first to explain the benefits of using quadratic isoparametric elements and outlined a very effective and simple technique to calculate singular integrals - thus only integrals of, at most, weak singularity needed to be evaluated. The 1980s marked a peak in activity for the method and several BEM packages, most notably the software BEASY, were developed for commercial use while advances were made in particular areas such as fracture mechanics and efficient numerical solvers. Unfortunately, the continued success of the FEM stifled widespread use of the BEM, even with significant advantages in particular areas of application - this remains true to the present day. There are however, active research groups who are presently making significant advances in the method demonstrating the efficiency and superior accuracy of the method for certain applications, but engineers are slow to accept new technologies and it will take some time yet for the method to become widespread throughout the industry.

This chapter presents a derivation of the BEM which is based on a collocation procedure - other forms such as the Galerkin method and indirect BEM are not used here, but the interested reader should consult [46] and [47] for further details. Furthermore, details on how the mathematical formulation can be used to generate a system of equations for computer implementation are given. The more recent development known as the Dual Boundary Element Method - a technique used to overcome the difficulties encountered when the conventional BEM is applied to fracture problems - is also outlined.

3.1 BEM formulation

The derivation of the BEM is often regarded as too complicated by engineers and many are left with puzzling questions such as how, if only parameters on the boundary are required, internal displacements and stresses can be found? This section aims to provide a comprehensive yet understandable discussion on the BEM derivation and hopes to alleviate any misunderstandings and misconceptions that often are associated with the method. The boundary value problem considered throughout is an elastostatic problem assuming linear elasticity.

3.1.1 Equations of elasticity

Before consideration is given to any boundary integrals, it is necessary to provide the equations of elasticity that underpin the framework of the BEM. These are well-known within the field of computational mechanics but are stated here for future reference. The first of these comes from consideration of equilibrium on an infinitesimal cube (see Fig. 3.1) with sides Δx, Δy and Δz and contains a body force per unit volume represented by the components b_i. If stresses on this cube are defined as σ_{ij} where i is the direction of the normal component on that face and j is the direction the stress acts in, then by equating forces, the following differential equation can be written

$$\frac{\partial \sigma_{ij}}{\partial x_i} + \frac{\partial \sigma_{ij}}{\partial x_j} + \frac{\partial \sigma_{ij}}{\partial x_k} + b_i = 0 \qquad i, j, k = x, y, z \tag{3.1}$$

or in indicial notation, where repeated indices imply summation and a comma implies differentiation

$$\sigma_{ij,j} + b_i = 0 \tag{3.2}$$

Denoting displacement components as u_i, tensorial strains can then be defined as

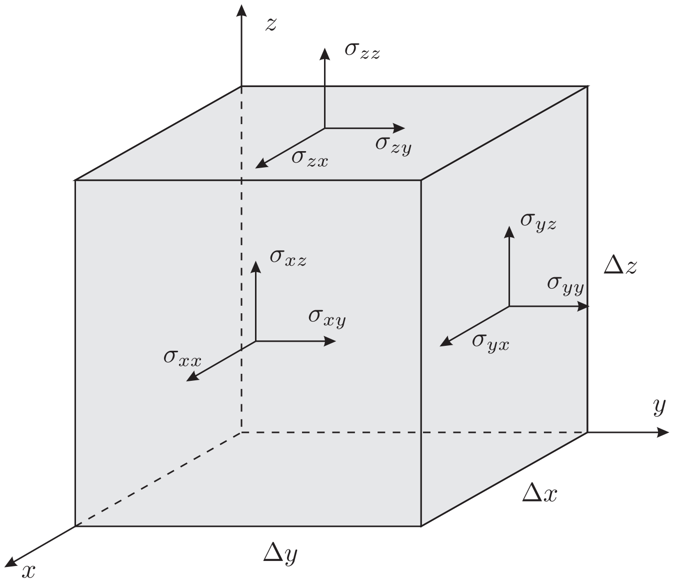

Figure 3.1: Definition of stress component directions on infinitesimal cube

$$\varepsilon_{ij} = \frac{1}{2}\left(\frac{\partial u_i}{\partial x_j} + \frac{\partial u_j}{\partial x_i}\right) \tag{3.3}$$

To find a valid solution it is necessary to define additional relations known as compatibility equations[1] defined in indicial notation as

$$\frac{\partial^2 \varepsilon_{ii}}{\partial x_j^2} + \frac{\partial^2 \varepsilon_{jj}}{\partial x_i^2} - 2\frac{\partial^2 \varepsilon_{ij}}{\partial x_i \partial x_j} = 0 \tag{3.4a}$$

$$\frac{\partial \varepsilon_{ij}}{\partial x_j \partial x_k} - \frac{\partial}{\partial x_i}\left(-\frac{\partial \varepsilon_{jk}}{\partial x_i} + \frac{\partial \varepsilon_{ik}}{\partial x_j} + \frac{\partial \varepsilon_{ij}}{\partial x_k}\right) = 0 \quad i \neq j \neq k \tag{3.4b}$$

---

[1] These ensure that the body will remain continuous under an arbitrary set of forces

For an elastic, isotropic material strains and stresses are related by Hooke's law allowing the strain components to be expressed as

$$\begin{aligned}
\varepsilon_{xx} &= \frac{1}{E}[\sigma_{xx} - \nu(\sigma_{yy} + \sigma_{zz})], & \varepsilon_{xy} &= \frac{1+\nu}{E}\sigma_{xy}, \\
\varepsilon_{yy} &= \frac{1}{E}[\sigma_{yy} - \nu(\sigma_{xx} + \sigma_{zz})], & \varepsilon_{yz} &= \frac{1+\nu}{E}\sigma_{yz}, \\
\varepsilon_{zz} &= \frac{1}{E}[\sigma_{zz} - \nu(\sigma_{xx} + \sigma_{yy})], & \varepsilon_{zx} &= \frac{1+\nu}{E}\sigma_{zx}
\end{aligned} \tag{3.5}$$

where E and ν are the Young's modulus and Poisson's ratio respectively. Likewise, expressions for stress in terms of strain can be stated

$$\begin{aligned}
\sigma_{xx} &= \lambda e + 2\mu\varepsilon_{xx}, & \sigma_{xy} &= 2\mu\varepsilon_{xy}, \\
\sigma_{yy} &= \lambda e + 2\mu\varepsilon_{yy}, & \sigma_{yz} &= 2\mu\varepsilon_{yz}, \\
\sigma_{zz} &= \lambda e + 2\mu\varepsilon_{zz}, & \sigma_{zx} &= 2\mu\varepsilon_{zx}
\end{aligned} \tag{3.6}$$

where μ is the shear modulus defined as

$$\mu = \frac{E}{2(1+\nu)} \tag{3.7}$$

λ is the Lamé constant

$$\lambda = \frac{2\mu\nu}{(1-2\nu)} \tag{3.8}$$

and e is the volumetric strain

$$e \equiv \varepsilon_{xx} + \varepsilon_{yy} + \varepsilon_{zz} \tag{3.9}$$

The previous equations are completely general in nature since they apply to a three-dimensional body under an arbitrary set of forces, but in many cases certain assumptions can be made to simplify the problem into that of a two-dimensional body. There are two scenarios in which this may occur - that of plane strain and plane stress. Plane strain conditions occur for example in thick plates where the geometry and loading does not vary significantly in the z direction and it can be assumed that $\varepsilon_{zz} = \varepsilon_{zx} = \varepsilon_{zy} = 0$. Likewise, plane stress conditions can occur in thin plates where, since stresses in the z direction cannot reach any appreciable value, they can be assumed to be zero (ie. $\sigma_{zz} = \sigma_{zx} = \sigma_{zy} = 0$). Using these assumptions, it is possible to express strains for plane strain as

$$\begin{aligned}
\varepsilon_{xx} &= \frac{1-\nu^2}{E}\left(\sigma_{xx} - \frac{\nu}{1-\nu}\sigma_{yy}\right), \\
\varepsilon_{yy} &= \frac{1-\nu^2}{E}\left(\sigma_{yy} - \frac{\nu}{1-\nu}\sigma_{xx}\right), \\
\varepsilon_{xy} &= \frac{1+\nu}{E}\sigma_{xy}
\end{aligned} \tag{3.10}$$

and for the case of plane stress

$$\begin{aligned}
\varepsilon_{xx} &= \frac{1-\nu^2}{E}\left(\sigma_{xx} - \frac{\nu}{1-\nu}\sigma_{yy}\right), \\
\varepsilon_{yy} &= \frac{1-\nu^2}{E}\left(\sigma_{yy} - \frac{\nu}{1-\nu}\sigma_{xx}\right), \\
\varepsilon_{xy} &= \frac{1+\nu}{E}\sigma_{xy}, \\
\varepsilon_{zz} &= -\frac{\nu}{1-\nu}\left(\varepsilon_{xx} + \varepsilon_{yy}\right)
\end{aligned} \tag{3.11}$$

A much more convenient way of expressing both of these equations is to take the plane strain case as the general case and substitute modified values of Young's modulus, Poisson's ratio and Shear Modulus as given in Table 3.1 where, for completion, the plane strain expressions are stated again but with modified material properties

Table 3.1: Effective material properties

Plane strain	$E^* = E$	$\nu^* = \nu$	$\mu^* = \mu$
Plane stress	$E^* = \dfrac{E(1+2\nu)}{(1+\nu)^2}$	$\nu^* = \dfrac{\nu}{1+\nu}$	$\mu^* = \mu$

$$\begin{aligned}
\varepsilon_{xx} &= \frac{1-\nu^2}{E^*}\left(\sigma_{xx} - \frac{\nu^*}{1-\nu^*}\sigma_{yy}\right), \\
\varepsilon_{yy} &= \frac{1-\nu^2}{E^*}\left(\sigma_{yy} - \frac{\nu^*}{1-\nu^*}\sigma_{xx}\right), \\
\varepsilon_{xy} &= \frac{1+\nu^*}{E^*}\sigma_{xy}
\end{aligned} \tag{3.12}$$

Finally, although technically not an equation of elasticity, a definition of traction components is given since they are used on numerous occasions in future work. Considering a tetrahedron under a state of stress σ_{ij} such as that in Fig. 3.2a, it is possible to imagine a face with a normal vector $\mathbf{n}$ which must be acted on by a force to ensure equilibrium of the body. This force is known as a traction and it can be shown, by consideration of equilibrium, that the components of this traction are related to the stresses by

$$\begin{aligned} t_x &= \sigma_{xx} n_x + \sigma_{xy} n_y + \sigma_{xz} n_z, \\ t_y &= \sigma_{yx} n_x + \sigma_{yy} n_y + \sigma_{yz} n_z, \\ t_z &= \sigma_{zx} n_x + \sigma_{zy} n_y + \sigma_{zz} n_z \end{aligned} \tag{3.13}$$

with the normal components defined in Fig. 3.2b. The Eqns in (3.13) are more often written in indicial notation as

$$t_i = \sigma_{ij} n_j \tag{3.14}$$

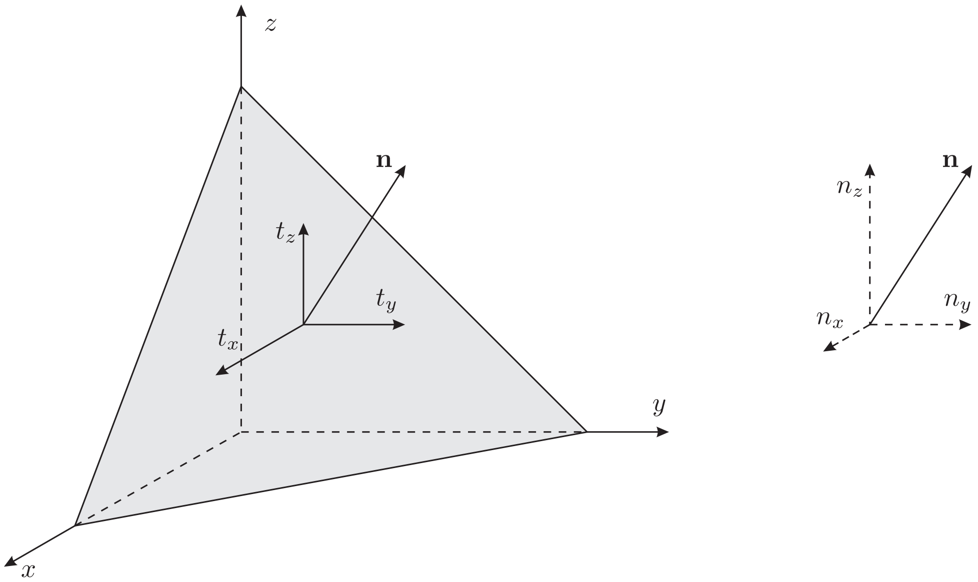

(a) Traction components on tetrahedron

(b) Normal components

Figure 3.2: Tractions definition

3.1.2 Betti's reciprocal theorem

The previous section outlined the underlying equations of elasticity which apply to any numerical method which considers elastostatic problems, but the theory now specialises towards the derivation of the BEM with the relation known as Betti's reciprocal theorem, which is fundamental to the BEM, now described in detail.

Betti's reciprocal theorem states that if there are two systems (a) and (b) where the stresses and strains associated with each of these systems are $(\sigma_{ij}, \varepsilon_{ij})$ and $(\sigma^*_{ij}, \varepsilon^*_{ij})$ respectively, then the work done by the stresses of (a) on the strains of (b) is equal to the work done by the stresses of (b) on the strains of (a). This can be written mathematically as:

$$\int_\Omega \sigma_{ij}\varepsilon^*_{ij}\,\mathrm{d}\Omega = \int_\Omega \sigma^*_{ij}\varepsilon_{ij}\,\mathrm{d}\Omega \tag{3.15}$$

where Ω is an arbitrary domain. Clearly this is not in a form sufficient for a "boundary only" method since both terms involve domain integrals. What will be shown now is that, by utilising the divergence theorem and carrying out certain manipulations, it is possible to arrive at a boundary integral expression. First, expression (3.3) is written in indicial notation and substituted into Eq. (3.15) replacing both ε^*_{ij} and ε_{ij}

$$\int_\Omega \frac{1}{2}\sigma_{ij}(u^*_{i,j} + u^*_{j,i})\,\mathrm{d}\Omega = \int_\Omega \frac{1}{2}\sigma^*_{ij}(u_{i,j} + u_{j,i})\,\mathrm{d}\Omega \tag{3.16}$$

But, by noting that the terms σ_{ij} and σ^*_{ij} are symmetric (ie. $\sigma_{ij} = \sigma_{ji}$, $\sigma^*_{ij} = \sigma^*_{ji}$), the following simplification can be made

$$\begin{aligned}
\frac{1}{2}\sigma_{ij}(u^*_{i,j} + u^*_{j,i}) &= \frac{1}{2}(\sigma_{ij}u^*_{i,j} + \sigma_{ij}u^*_{j,i}) \\
&= \frac{1}{2}(\sigma_{ij}u^*_{i,j} + \sigma_{ji}u^*_{j,i}) \\
&= \sigma_{ij}u^*_{i,j} \qquad (3.17)
\end{aligned}$$

Therefore Eq. (3.16) can be written as

$$\int_\Omega \sigma_{ij}u^*_{i,j}\,\mathrm{d}\Omega = \int_\Omega \sigma^*_{ij}u_{i,j}\,\mathrm{d}\Omega \tag{3.18}$$

We now focus our attention to the left hand side of this equation where we find that the integral term can be expressed as

$$\int_{\Omega} \sigma_{ij} u^*_{i,j} \, \mathrm{d}\Omega = \int_{\Omega} [(\sigma_{ij} u^*_i)_{,j} - \sigma_{ij,j} u^*_i] \, \mathrm{d}\Omega \tag{3.19}$$

This can be explained by considering the product rule on the integral $\int_{\Omega} (\sigma_{ij} u^*_i)_{,j} \, \mathrm{d}\Omega$

$$\int_{\Omega} (\sigma_{ij} u^*_i)_{,j} \, \mathrm{d}\Omega = \int_{\Omega} \sigma_{ij} u^*_{i,j} \, \mathrm{d}\Omega + \int_{\Omega} \sigma_{ij,j} u^*_i \, \mathrm{d}\Omega \tag{3.20}$$

which can be rearranged to give expression 3.19. We note that the term $\sigma_{ij,j}$ is related to the body force term b_i by Eq. (3.2) which gives, after substitution into (3.19)

$$\int_{\Omega} \sigma_{ij} u^*_{i,j} \, \mathrm{d}\Omega = \int_{\Omega} (\sigma_{ij} u^*_i)_{,j} \, \mathrm{d}\Omega + \int_{\Omega} b_i u^*_i \, \mathrm{d}\Omega \tag{3.21}$$

At this point it is necessary to introduce the divergence theorem - a crucial step in the BEM formulation, since it allows a domain integral to be transformed into a boundary integral. Denoting f as an arbitrary function, the theorem can be expressed as

$$\int_{\Omega} f_{i,i} \, \mathrm{d}\Omega = \int_{\Gamma} f_i n_i \, \mathrm{d}\Gamma \tag{3.22}$$

where Γ is the boundary of the domain and n_i is a component of the outward pointing normal vector $\mathbf{n}$ as shown in Fig. 3.3. Applying this to the second term of (3.21), we have

$$\int_{\Omega} \sigma_{ij} u^*_{i,j} \, \mathrm{d}\Omega = \int_{\Gamma} (\sigma_{ij} u^*_i) n_j \, \mathrm{d}\Gamma + \int_{\Omega} b_i u^*_i \, \mathrm{d}\Omega \tag{3.23}$$

and, by noting that $t_i = \sigma_{ij} n_j$, this can be further simplified to

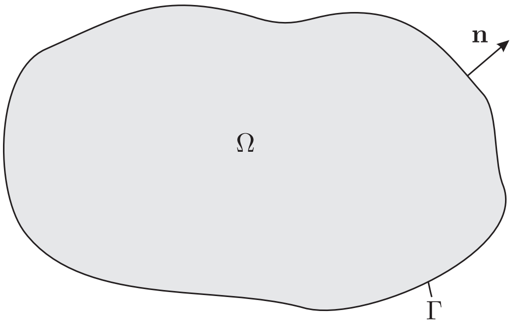

Figure 3.3: Arbitrary domain Ω with boundary Γ

$$\int_{\Omega} \sigma_{ij} u^*_{i,j} \, \mathrm{d}\Omega = \int_{\Gamma} t_i u^*_i \, \mathrm{d}\Gamma + \int_{\Omega} b_i u^*_i \, \mathrm{d}\Omega \tag{3.24}$$

Remembering that this equation applies to the left hand side of Eq. (3.18), and following exactly the same procedure for the right hand side, the final expression for the integral equation is written

$$\int_{\Gamma} t_i u_i^* \, \mathrm{d}\Gamma + \int_{\Omega} b_i u_i^* \, d\Omega = \int_{\Gamma} t_i^* u_i \, d\Gamma + \int_{\Omega} b_i^* u_i \, d\Omega \tag{3.25}$$

This is known as Betti's reciprocal work theorem. It should be noted that there still exist integral terms which which are taken over the domain Ω, but in many cases these can either ignored (zero body force assumption) or can be transformed into boundary integrals. Therefore we are well on our way to the goal of a boundary-only formulation that will allow displacements and tractions to be found for a body under an arbitrary set of loads. But before it is complete, our attention is now drawn to the expressions for u_i^* and t_i^* which will be shown shortly to take the form of fundamental solutions.

3.1.3 Fundamental solutions

A well-known feature of the BEM formulation is the heavy dependence on appropriate fundamental solutions specific to the problem being solved. These can be regarded as a two-edged sword - on the one hand, the use of exact fundamental solutions allows extremely accurate resolution of parameters throughout the domain but on the other, since the fundamental solutions are specific to the problem being considered (eg. linear elastic materials), there are restrictions on the applicability of the boundary integral equation. The problem of applying the BEM to problems containing plasticity is one such example where the integral terms can no longer be evaluated entirely on the boundary but instead, additional domain integrals must be computed. There are methods such as the Dual-Reciprocity Method [48] which overcome this problem, but the implementation quickly becomes complicated and other methods are sought. Fortunately, within the context of fracture mechanics where the assumption of linear elasticity is valid for most problems, fundamental solutions can be found and implemented easily with the boundary integral equations. These relations are now presented for both two-dimensional and three-dimensional problems.

The first necessary step in the derivation of the fundamental solutions for linear elasticity is to state the partial differential equation for displacements - more commonly known as Navier's equation. Before this can be done, Eqns (3.6), (3.8) and

(3.9) are first expressed in indicial notation as

$$\sigma_{ij} = \frac{2\mu\nu}{1-2\nu}\delta_{ij}\varepsilon_{mm} + 2\mu\varepsilon_{ij} \tag{3.26}$$

If the relation between displacements and strains (Eq. 3.3) is then substituted into this equation, we have

$$\sigma_{ij} = \frac{2\mu\nu}{1-2\nu}\delta_{ij}\left(\frac{\partial u_m}{\partial x_m}\right) + \mu\left(\frac{\partial u_i}{\partial x_j} + \frac{\partial u_j}{\partial x_i}\right) \tag{3.27}$$

which, once substituted into the equilibrium equation of (3.2), the final expression (Navier's equation) for the auxiliary state (u_i^*, t_i^*, b_i^*) can be written as

$$\frac{\partial^2 u_i^*}{\partial x_j \partial x_j} + \frac{1}{1-2\nu}\frac{\partial^2 u_j^*}{\partial x_i \partial x_j} = -\frac{b_i^*}{\mu} \tag{3.28}$$

or

$$u_{i,jj}^* + \frac{1}{1-2\nu}u_{j,ji}^* = -\frac{b_i^*}{\mu} \tag{3.29}$$

An important step is now made to substitute the body force term b_i^* with that of an infinite point force

$$b_i^* = \Delta(\mathbf{X} - \mathbf{X}')e_i \tag{3.30}$$

where Δ is the Dirac delta function defined as

$$\Delta(\mathbf{X} - \mathbf{X}') = \begin{cases} +\infty & \mathbf{X} = \mathbf{X}' \\ 0 & \mathbf{X} \neq \mathbf{X}' \end{cases} \tag{3.31}$$

and e_i is a unit load vector in direction i. It will be shown in the next section that the solution to the PDE when the right hand side is equal to a Dirac delta function (as is the case when (3.30) is used) defines a fundamental solution. For now, we introduce two points $\mathbf{X}'$ and $\mathbf{X}$ which both lie within the domain $(\mathbf{X}, \mathbf{X}' \in \Omega)$ and are known as the source and field points respectively (see Fig. 3.4a) . If the point $\mathbf{X}'$ corresponds to the location of the infinite point force (Fig. 3.4b), Navier's equation can be written for u_i^* as

$$\mu u_{i,jj}^* + \frac{\mu}{1-2\nu}u_{j,ji}^* + \Delta(\mathbf{X} - \mathbf{X}')e_i = 0 \tag{3.32}$$

More commonly though, this equation is expressed in terms of a relation known as

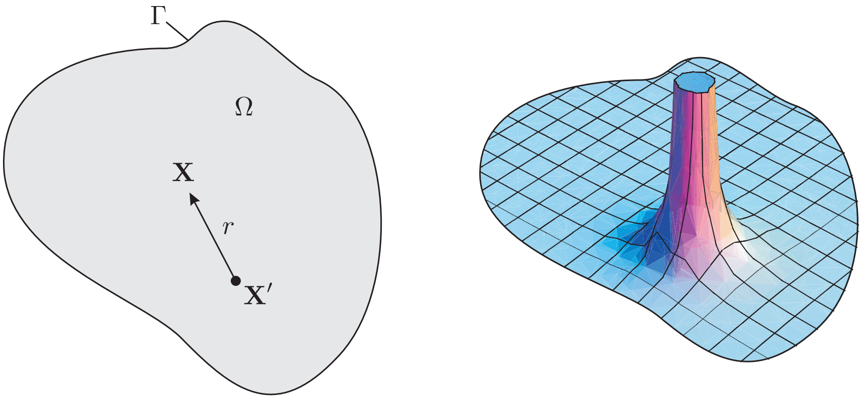

(a) 2D domain with point force at $\mathbf{X}'$

(b) 3D representation of point force

Figure 3.4: Definition of domain with point force

the Galerkin vector which allows the displacements u_i^* to be expressed as

$$u_i^* = G_{i,kk} - \frac{1}{2(1-\nu)} G_{k,ik} \tag{3.33}$$

If this is now substituted into (3.32), Navier's equation can be rewritten as

$$\mu G_{i,kkjj} - \frac{\mu}{2(1-\nu)} G_{k,ikjj} + \frac{\mu}{(1-2\nu)} \left(G_{j,kkij} - \frac{1}{2(1-\nu)} G_{k,jkij} \right) + \Delta(\mathbf{X} - \mathbf{X}') e_i = 0 \tag{3.34}$$

and, since $G_{k,ikjj} = G_{j,kkij} = G_{k,jkij}$, the second and third terms disappear giving

$$\mu G_{i,kkjj} + \Delta(\mathbf{X} - \mathbf{X}') e_i = 0 \tag{3.35}$$

or, by expressing $G_{i,kkjj}$ as $\nabla^2(\nabla^2 G_i)$ (where ∇^2 is the Laplacian operator),

$$\nabla^2(\nabla^2 G_i) + \frac{1}{\mu} \Delta(\mathbf{X} - \mathbf{X}') e_i = 0 \tag{3.36}$$

The solution to this problem is well-known from potential theory and is commonly referred to as Kelvin's point force solution [49]. For two-dimensional problems the solution is given by

$$G_i = -\frac{1}{8\pi\mu} r^2 \ln(r) e_i \tag{3.37}$$

where r denotes the distance between the source and field points. By substituting this solution into (3.33) to obtain displacements and then using relations (3.27) and

(3.14) to obtain tractions, the components u_i^* and t_i^* can be written as

$$u_i^* = U_{ij} e_j \qquad t_i^* = T_{ij} e_j \tag{3.38}$$

where the terms U_{ij} and T_{ij}, defined as the *fundamental solutions*, are given by

$$U_{ij}(\mathbf{X}', \mathbf{X}) = \frac{1}{8\pi\mu(1-\nu)} \left\{ (3-4\nu) \ln\left(\frac{1}{r}\right) \delta_{ij} + r_{,i} r_{,j} \right\} \tag{3.39a}$$

$$T_{ij}(\mathbf{X}', \mathbf{X}) = -\frac{1}{4\pi(1-\nu)r} \left\{ \frac{\partial r}{\partial n} [(1-2\nu)\delta_{ij} + 2r_{,i} r_{,j}] - (1-2\nu)(r_{,i} n_j - r_{,j} n_i) \right\} \tag{3.39b}$$

In a similar manner, solutions can be found for 3D domains with the expressions for U_{ij} and T_{ij} given in Appendix A.1.2. What will be shown next is that, by substituting these equations for u_i^* and t_i^* and making note of the choice for the body force function b_i^*, the expression known as the displacement boundary integral equation (DBIE), which allows displacements to be found at any point within the domain, can be derived.

3.1.4 Displacement Boundary Integral Equation

The DBIE, which is the fundamental underlying equation of the BEM, marks the final point in the mathematical derivation of the method in this thesis. The first step required is to substitute the auxiliary state u_i^*, t_i^*, b_i^* given by Eqns (3.38), (3.39) and (3.30) into Betti's reciprocal work theorem Eq. (3.25)

$$\int_\Gamma t_i U_{ij}(\mathbf{X}', \mathbf{X}) e_j \, \mathrm{d}\Gamma + \int_\Omega b_i U_{ij}(\mathbf{X}', \mathbf{X}) e_j \, d\Omega = \int_\Gamma T_{ij}(\mathbf{X}', \mathbf{X}) e_j u_i \, d\Gamma + \int_\Omega \Delta(\mathbf{X} - \mathbf{X}') e_i u_i \, d\Omega \tag{3.40}$$

Particular attention is paid to the last term of this expression since it can be simplified using a property of the Dirac-delta function. That is,

$$\int_\Omega f(\mathbf{X}) \Delta(\mathbf{X} - \mathbf{X}') \, \mathrm{d}\Omega = f(\mathbf{X}') \tag{3.41}$$

and therefore

$$\int_\Omega \Delta(\mathbf{X} - \mathbf{X}') e_i u_i \, d\Omega = u_i(\mathbf{X}') e_i \tag{3.42}$$

Simplifications can also be made to the other three terms with simple rearrangement and cancellation of the unit vector component e_i giving

$$u_i(\mathbf{X}') = \int_\Gamma U_{ij}(\mathbf{X}',\mathbf{X})t_j(\mathbf{X})\,\mathrm{d}\Gamma - \int_\Gamma T_{ij}(\mathbf{X}',\mathbf{X})u_j(\mathbf{X})\,\mathrm{d}\Gamma + \int_\Omega U_{ij}(\mathbf{X}',\mathbf{X})b_j(\mathbf{X})\,\mathrm{d}\Omega \tag{3.43}$$

Since the goal is to formulate a boundary-only method, the field point is now positioned on the boundary ($\mathbf{x} \in \Gamma$). This does not present any restrictions or difficulties, but if the same procedure is applied to the source point $\mathbf{X}'$, some complications occur. This can be explained with the aid of Fig. 3.5 and Eqns (3.39) which show the dependence the fundamental solutions have with the distance r. First, the case in which the source and field points lie far apart is considered where, since the distance r is large, the functions $U_{ij}(\mathbf{x}',\mathbf{x})$ and $T_{ij}(\mathbf{x}',\mathbf{x})$ are well-behaved and present little difficulties for integration. However, in the case when the source and field points become close and eventually coincide, difficulties arise. The fundamental solutions become singular and, in the limit where $\mathbf{x}' = \mathbf{x}$, there is a requirement to integrate a function that becomes infinite. Fortunately, it is possible to evaluate these terms by considering them in a limiting process and, as will be shown in the section for numerical implementation (Sec. 3.1.6), the explicit evaluation of singular integrals can often be avoided.

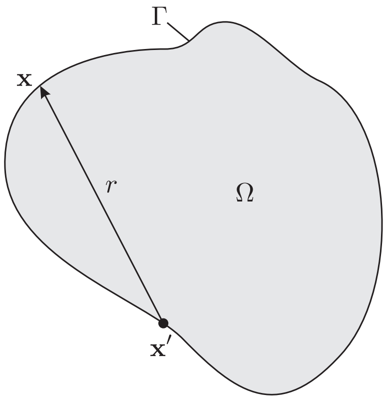

Figure 3.5: Source and field points located on the boundary

Mathematically speaking, we want to know the limit of the integral terms as $\mathbf{X}' \to \mathbf{x}'$ where $\mathbf{x}' \in \Gamma$ and for this to be achieved, an additional semi-circular boundary segment centred at the point $\mathbf{x}'$ and with radius ε is defined (Fig. 3.6). The integrals are then taken over two segments - the non-singular part of the boundary $\Gamma - \Gamma_\varepsilon$ and the singular part Γ_ε. Then, by considering the limit as $\varepsilon \to 0$ for each of the terms in (3.43), the displacement boundary integral equation can be written

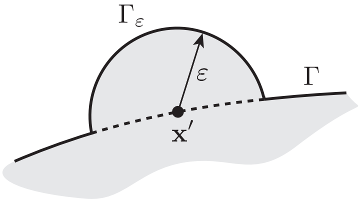

Figure 3.6: Definition of boundaries for CPV limiting process

in terms of parameters which are *entirely* on the boundary. Considering the first integral term, this can be written as

$$\int_{\Gamma} U_{ij}(\mathbf{X}', \mathbf{x}) t_j(\mathbf{x}) \, \mathrm{d}\Gamma = \lim_{\varepsilon \to 0} \int_{\Gamma - \Gamma_\varepsilon} U_{ij}(\mathbf{x}', \mathbf{x}) t_j(\mathbf{x}) \, \mathrm{d}\Gamma + \lim_{\varepsilon \to 0} \int_{\Gamma_\varepsilon} U_{ij}(\mathbf{x}', \mathbf{x}) t_j(\mathbf{x}) \, \mathrm{d}\Gamma \tag{3.44}$$

The first term on the right hand side of this equation contains a singularity of $\mathcal{O}(\ln(1/r))$ in two-dimensions and can be evaluated using an appropriate numerical integration scheme (Chapter 5 provides an overview of these methods) while the second is found to disappear in the limit as $\varepsilon \to 0$ (further details on this can be found in Appendix C.3).

Our attention now turns to the second integral in (3.43) and its behaviour in the limit as $\varepsilon \to 0$. It can be written, in the same manner as before, as

$$\int_{\Gamma} T_{ij}(\mathbf{X}', \mathbf{x}) u_j(\mathbf{x}) \, \mathrm{d}\Gamma = \lim_{\varepsilon \to 0} \int_{\Gamma - \Gamma_\varepsilon} T_{ij}(\mathbf{x}', \mathbf{x}) u_j(\mathbf{x}) \, \mathrm{d}\Gamma + \lim_{\varepsilon \to 0} \int_{\Gamma_\varepsilon} T_{ij}(\mathbf{x}', \mathbf{x}) u_j(\mathbf{x}) \, \mathrm{d}\Gamma \tag{3.45}$$

where the integrands now contain singularities of $\mathcal{O}(1/r)$ (2D). Before, it was stated that the U_{ij} integral over the boundary $\Gamma - \Gamma_\varepsilon$ could be evaluated using special numerical integration routines. In this case, the stronger singularity precludes the use of these techniques and it is necessary to evaluate the integral in a limiting process known as the Cauchy Principal Value (CPV) integral. If we imagine a function $f(x)/(x - x_p)$ in an interval $[a, c]$ with $a < x_p < b$, then this function is undefined at the point x_p. Therefore the integral of this function is undefined and is classed as improper. The CPV integral considers this improper integral and evaluates it in a limiting sense as

$$⨍_a^c \frac{f(x)}{x - x_p} \, \mathrm{d}x = \lim_{\varepsilon \to 0} \left\{ \int_a^{x_p - \varepsilon} \frac{f(x)}{x - x_p} \, \mathrm{d}x + \int_{x_p + \varepsilon}^c \frac{f(x)}{x - x_p} \, \mathrm{d}x \right\} \tag{3.46}$$

where the integral sign $⨍$ denotes that the integral is evaluated in a CPV sense. Therefore, returning to Eq. (3.45), it is possible to express the first integral on the right hand side as

$$\lim_{\varepsilon \to 0} \int_{\Gamma - \Gamma_\varepsilon} T_{ij}(\mathbf{x}', \mathbf{x}) u_j(\mathbf{x}) \, \mathrm{d}\Gamma = \fint_{\Gamma} T_{ij}(\mathbf{x}', \mathbf{x}) u_j(\mathbf{x}) \, \mathrm{d}\Gamma \tag{3.47}$$

There are particular integration routines which are capable of evaluating this integral - and in fact, a large section of this thesis concentrates on the use of one of these to allow certain enriched integrals to be calculated - but in most cases a very simple technique, which actually precludes the need to evaluate the term altogether, can be used. The only integral which now remains is that given by the last term in Eq. (3.45). Assuming that the displacements $u_j(x)$ are differentiable, this can be regularised by the first term of a Taylor series expansion as

$$\begin{aligned} \lim_{\varepsilon \to 0} \int_{\Gamma_\varepsilon} T_{ij}(\mathbf{x}', \mathbf{x}) u_j(\mathbf{x}) \, \mathrm{d}\Gamma &= \lim_{\varepsilon \to 0} \int_{\Gamma_\varepsilon} T_{ij}(\mathbf{x}', \mathbf{x}) \left[u_j(\mathbf{x}) - u_j(\mathbf{x}') \right] \, \mathrm{d}\Gamma \\ &+ u_j(\mathbf{x}') \lim_{\varepsilon \to 0} \int_{\Gamma_\varepsilon} T_{ij}(\mathbf{x}', \mathbf{x}) \, \mathrm{d}\Gamma \end{aligned} \tag{3.48}$$

Since displacements must be continuous, the first term is equal to zero while the second can be written as

$$u_j(\mathbf{x}') \lim_{\varepsilon \to 0} \int_{\Gamma_\varepsilon} T_{ij}(\mathbf{x}', \mathbf{x}) \, \mathrm{d}\Gamma = \alpha_{ij}(\mathbf{x}') u_j(\mathbf{x}') \tag{3.49}$$

where α_{ij} is a jump term that is dependent on the geometry at the source point $\mathbf{x}'$. If the source point lies on a smooth surface then $\alpha_{ij} = -\delta_{ij}/2$ (a full derivation of the limiting procedure along with this result is given in Appendix C.4).

Since each of the boundary integral terms given by Eqns (3.44), (3.47) and (3.49) is now expressed in terms of the boundary points $\mathbf{x}'$ and $\mathbf{x}$, by substituting these equations into the original integral equation (3.43) the DBIE can be written in terms of boundary parameters as

$$\begin{aligned} u_i(\mathbf{x}') + \alpha_{ij}(\mathbf{x}') u_j(\mathbf{x}') + \fint_{\Gamma} T_{ij}(\mathbf{x}', \mathbf{x}) u_j(\mathbf{x}) \, \mathrm{d}\Gamma &= \int_{\Gamma} U_{ij}(\mathbf{x}', \mathbf{x}) t_j(\mathbf{x}) \, \mathrm{d}\Gamma \\ &+ \int_{\Omega} U_{ij}(\mathbf{x}', \mathbf{X}) b_j(\mathbf{X}) \, \mathrm{d}\Omega \end{aligned} \tag{3.50}$$

The first two terms of these equations can be combined as

$$\begin{aligned} u_i(\mathbf{x}') + \alpha_{ij}(\mathbf{x}')u_j(\mathbf{x}') &= u_i(\mathbf{x}') - \frac{\delta_{ij}}{2}u_j(\mathbf{x}') \\ &= \delta_{ij}u_j(\mathbf{x}') - \frac{\delta_{ij}}{2}u_j(\mathbf{x}') \\ &= C_{ij}(\mathbf{x}')u_j(\mathbf{x}') \end{aligned} \tag{3.51}$$

where $C_{ij} = 0.5\delta_{ij}$ (for smooth boundaries) is a jump term. This coefficient varies for different geometries at the source point - Fig. 3.7 illustrates three common boundary geometries with the associated jump terms. And finally, by substituting the simplification given by (3.51) and assuming zero body forces, the expression for the DBIE which is expressed entirely of boundary parameters, can be written as

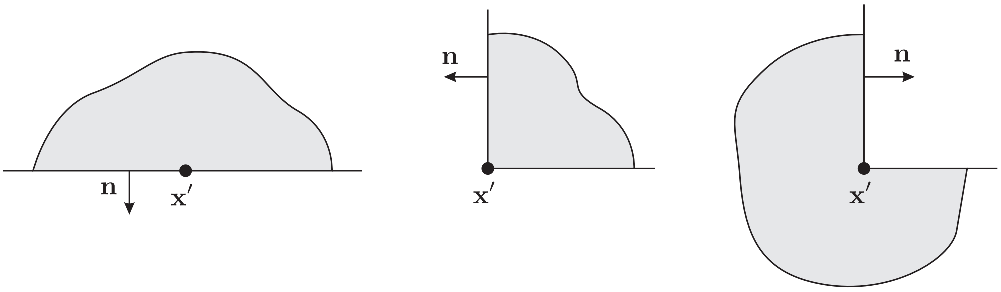

(a) $C_{ij} = 0.5\delta_{ij}$ (b) $C_{ij} = 0.25\delta_{ij}$ (c) $C_{ij} = 0.75\delta_{ij}$

Figure 3.7: Jump terms for various boundary geometries

$$C_{ij}(\mathbf{x}')u_j(\mathbf{x}') + \fint_\Gamma T_{ij}(\mathbf{x}', \mathbf{x})u_j(\mathbf{x})\,\mathrm{d}\Gamma = \int_\Gamma U_{ij}(\mathbf{x}', \mathbf{x})t_j(\mathbf{x})\,\mathrm{d}\Gamma \tag{3.52}$$

This equation is important since it provides a relation between displacements and tractions around the boundary for an arbitrary body. Therefore, with appropriate boundary conditions imposed and sufficiently accurate evaluation of the boundary integrals[2], it is possible to determine unknown boundary displacements and tractions. Of course, for the numerical implementation of the method the DBIE cannot be used in this form but instead, the boundary must be split into segments (elements) and certain assumptions are made for the variation of displacements and tractions. This process of discretisation to allow numerical implementation of the BEM is given in detail in Sec. 3.1.6.

The preceding discussion has been focused on the process of moving all parame-

---

[2] Note that there are *no* domain integrals

ters to the boundary, but no mention has been made to the calculation of parameters which are interior to the boundary ($\mathbf{X}' \in \Omega \backslash \Gamma$). In fact, to find interior displacements no new expression is necessary since Eq. (3.43) is in the required form. First, a BEM analysis can be performed to find all boundary displacements and tractions and then, by positioning the source point $\mathbf{X}'$ at the point of interest and evaluating the non-singular boundary integrals, the displacements $u_i(\mathbf{X}')$ can be found. In the case of strains and stresses, however, further manipulation of this equation is required.

3.1.5 Stresses at interior points

If we recall Hooke's law (Eq. 3.27) which relates stress components to displacement derivatives, then it becomes clear that the task of finding the BIE for interior stresses involves substituting the displacement components in this expression with those given by the DBIE of (3.43). The first step required then is to differentiate Eq. (3.43) with respect to the source point $\mathbf{X}'$ to obtain displacement derivatives. This can be written in indicial notation as

$$\frac{\partial u_i(\mathbf{X}')}{\partial \mathbf{X}'_k} = \int_\Gamma U_{ij,k}(\mathbf{X}', \mathbf{x}) t_j(\mathbf{x}) \, \mathrm{d}\Gamma - \int_\Gamma T_{ij,k}(\mathbf{X}', \mathbf{x}) u_j(\mathbf{x}) \, \mathrm{d}\Gamma + \int_\Omega U_{ij,k}(\mathbf{X}', \mathbf{X}) b_j(\mathbf{X}) \, \mathrm{d}\Omega \tag{3.53}$$

where, for the 2D case, the terms $U_{ij,k}$ and $T_{ij,k}$ are given by

$$U_{ij,k}(\mathbf{X}', \mathbf{x}) = -\frac{1-\nu}{4\pi(1-\nu)E}\frac{1}{r}\left[(3-4\nu)\delta_{ij}r_{,k} - \delta_{jk}r_{,i} - \delta_{ik}r_{,j} + 2r_{,i}r_{,j}r_{,k}\right] \tag{3.54a}$$

$$\begin{aligned} T_{ij,k}(\mathbf{X}', \mathbf{x}) = -\frac{1}{4\pi(1-\nu)}\frac{1}{r^2}\Big\{ & 2\frac{\partial r}{\partial n}[\delta_{ik}r_{,j} + \delta_{jk}r_{,i} - r_{,k}((1-2\nu)\delta_{ij} + 4r_{,i}r_{,j})] \\ & + n_k[(1-2\nu)\delta_{ij} + 2r_{,i}r_{,j}] - n_j(1-2\nu)[\delta_{ik} - 2r_{,i}r_{,k}] \\ & + n_i(1-2\nu)[\delta_{jk} - 2r_{,j}r_{,k}]\Big\} \end{aligned} \tag{3.54b}$$

These equations are valid for both plane strain and plane stress since it is only a matter of substituting in the effective material properties shown in Table 3.1 to obtain the required relation. To aid in the derivation, Eq. (3.27) which expresses stress components in terms of displacement derivatives is restated making use of the Lamé constant λ given by (3.8)

$$\sigma_{ij} = \lambda\delta_{ij}u_{m,m} + \mu(u_{i,j} + u_{j,i}) \tag{3.55}$$

By substituting the displacement derivatives given by (3.53) into this equation, the stress components at the point $\mathbf{X}'$ can be written in terms of boundary integrals as

$$\begin{aligned}\sigma_{ij}(\mathbf{X}') &= \int_\Gamma \left[\lambda\delta_{ij}U_{mk,m} + \mu(U_{ik,j} + U_{jk,i})\right] t_k(\mathbf{x})\,\mathrm{d}\Gamma(\mathbf{x}) && (3.56)\\ &- \int_\Gamma \left[\lambda\delta_{ij}T_{mk,m} + \mu(T_{ik,j} + T_{jk,i})\right] u_k(\mathbf{x})\,\mathrm{d}\Gamma(\mathbf{x}) && (3.57)\\ &+ \int_\Omega \left[\lambda\delta_{ij}U_{mk,m} + \mu(U_{ik,j} + U_{jk,i})\right] b_k(\mathbf{x})\,\mathrm{d}\Gamma(\mathbf{x}) && (3.58)\end{aligned}$$

and, if the terms within brackets are combined into a single term, this can be simplified to

$$\begin{aligned}\sigma_{ij}(\mathbf{X}') &= \int_\Gamma D_{kij}(\mathbf{X}',\mathbf{x})t_k(\mathbf{x})\,\mathrm{d}\Gamma(\mathbf{x}) - \int_\Gamma S_{kij}(\mathbf{X}',\mathbf{x})u_k(\mathbf{x})\,\mathrm{d}\Gamma(\mathbf{x})\\ &\quad + \int_\Omega D_{kij}(\mathbf{X}',\mathbf{x})b_k(\mathbf{x})\,\mathrm{d}\Gamma(\mathbf{x}) \qquad (3.59)\end{aligned}$$

with the expressions for D_{kij} and S_{kij} given in Appendix A.1.1. Therefore, once displacements and tractions are known for all boundary points, Eq. (3.59) can be used to determine the stress at any point within the domain. However, by inspecting the expressions for D_{kij} and S_{kij} (Eqns (A.1.1) and (A.1.2)), it can be seen that as the source point approaches the boundary ($\mathbf{X}' \to \Gamma$) the first two integral terms encounter singularities of $\mathcal{O}(1/r)$ and $\mathcal{O}(1/r^2)$ respectively. There are integration techniques which are capable of evaluating these integrals - and in fact, as will be shown shortly, the Dual Boundary Element Method requires the use of these methods - but often the simplest way to evaluate boundary stresses is through consideration of boundary tractions. This process is illustrated in Appendix A.2, but the reader is strongly encouraged to first understand the process of discretising the DBIE to allow for computer implementation.

3.1.6 Discretisation

The DBIE given by Eq. (3.52) is, in its present form, unsuitable for computer implementation since it can only be solved for very simple geometries. A much more general procedure that is conducive for computation involves the process of discretisation where the boundary of the problem is split into "elements" over which both the geometry and parameters u_j,t_j can be described in terms of certain predetermined functions - these are commonly referred to as “shape functions”. To illustrate the process Fig. 3.8a shows an arbitrary domain with a boundary $\Gamma = \Gamma^u \cup \Gamma^t$ over which the boundary conditions $\mathbf{u} = \bar{\mathbf{u}}$ and $\mathbf{t} = \bar{\mathbf{t}}$ are prescribed over Γ^u and Γ^t respectively. Fig. 3.8b shows the same problem after discretisation where the boundary is now split into much smaller sub-boundaries (elements) denoted by Γ_n. Fig. 3.9 illustrates one such element with three nodal points 1,2 and 3 and a local-coordinate system ξ. If the element is defined in this way, then the coordinates of a general

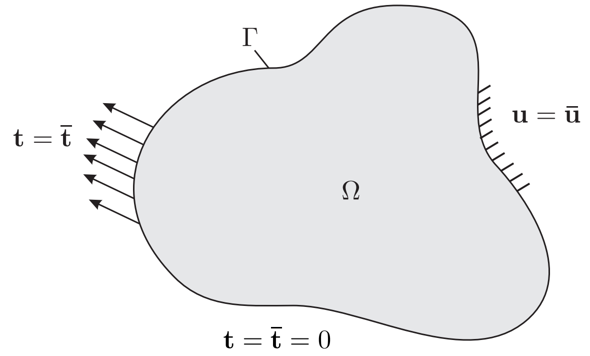

(a) Problem definition with boundary conditions imposed

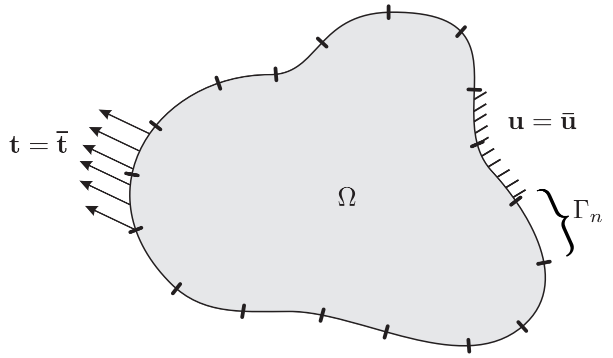

(b) Discretised boundary

Figure 3.8: Boundary discretisation

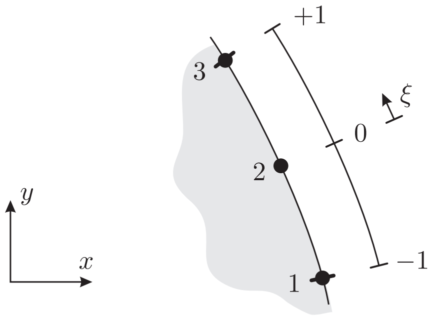

Figure 3.9: Local coordinate system over a continuous boundary element

point on this element can be written as

$$x_i(\xi) = \sum_{a=1}^{3} N_a(\xi) x_i^a \tag{3.60}$$

where $N_a(\xi)$ is the shape function associated with node a and x_i^a is the global coordinate in direction i. The shape functions allow interpolation between nodal values and therefore demonstrate the kronecker delta property. That is, if ξ_b denotes the local coordinate of nodal point b, then

$$N_a(\xi_b) = \delta_{ab} \tag{3.61}$$

Here, three nodal points have been used over the boundary element and, as can be shown relatively easily, the shape functions must vary quadratically. For the case where the nodal points are positioned at the local coordinates $\xi = -1, 0, 1$ and using the kronecker-delta property of (3.61), the shape functions take the form

$$N_1(\xi) = -\frac{\xi}{2}(1-\xi) \tag{3.62a}$$

$$N_2(\xi) = (1+\xi)(1-\xi) \tag{3.62b}$$

$$N_3(\xi) = \frac{\xi}{2}(1+\xi) \tag{3.62c}$$

These are also shown graphically in Fig. 3.10 which demonstrates more clearly the kronecker-delta property at each of the nodal positions. It should be noted that this nodal arrangement and the associated shape functions of (3.62) is not the only element configuration choice; it is entirely possible to choose different nodal coordinates with simple calculations to achieve the required shape functions. As will be shown in Sec. 4.4.3, the integration of the kernels in the Dual Boundary Element Method is greatly simplified by the use of discontinuous elements where nodes are positioned at points inside the element. A common configuration for this type of element is to position nodes at local coordinates $\xi = -2/3, 0, 2/3$ since this allows an even distribution of nodes along the boundary. Bearing in mind that shape functions must be equal to unity at the appropriate node and zero elsewhere, the following shape functions can be written for a discontinuous element with this nodal

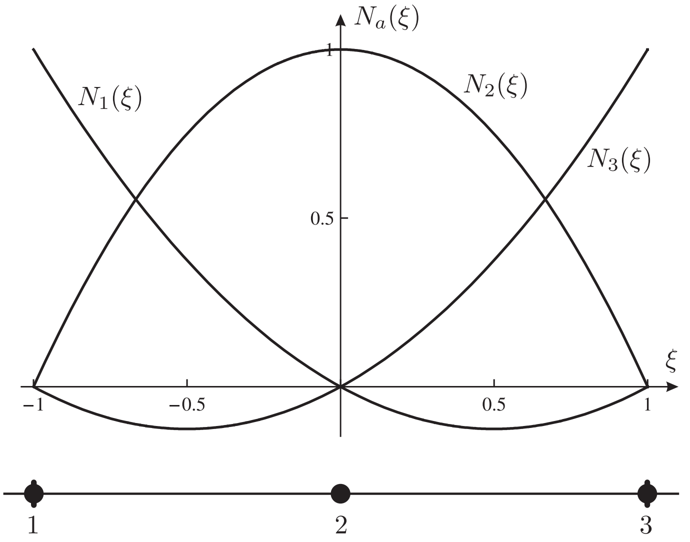

Figure 3.10: Continuous element with quadratic shape functions

configuration:

$$N_1(\xi) = \frac{9}{8}\xi\left(\xi - \frac{2}{3}\right) \tag{3.63a}$$

$$N_2(\xi) = \left(1 - \frac{3}{2}\xi\right)\left(1 + \frac{3}{2}\xi\right) \tag{3.63b}$$

$$N_3(\xi) = \frac{9}{8}\xi\left(\xi + \frac{2}{3}\right) \tag{3.63c}$$

where, as before, these functions can be plotted and are shown in Fig. 3.11.

Attention is now drawn to the interpolation of displacements and tractions over the element boundary where, most often, exactly the same form of interpolation is used as for the geometry, commonly referred to as isoparametric interpolation. Most BEM implementations use quadratic isoparametric elements since they are generally accepted as giving the best compromise between accuracy and efficiency [45]. Using this strategy, the displacements and tractions can be interpolated over a boundary element as

$$u_i(\xi) = \sum_{a=1}^{3} N_a(\xi) u_i^a \tag{3.64a}$$

$$t_i(\xi) = \sum_{a=1}^{3} N_a(\xi) t_i^a \tag{3.64b}$$

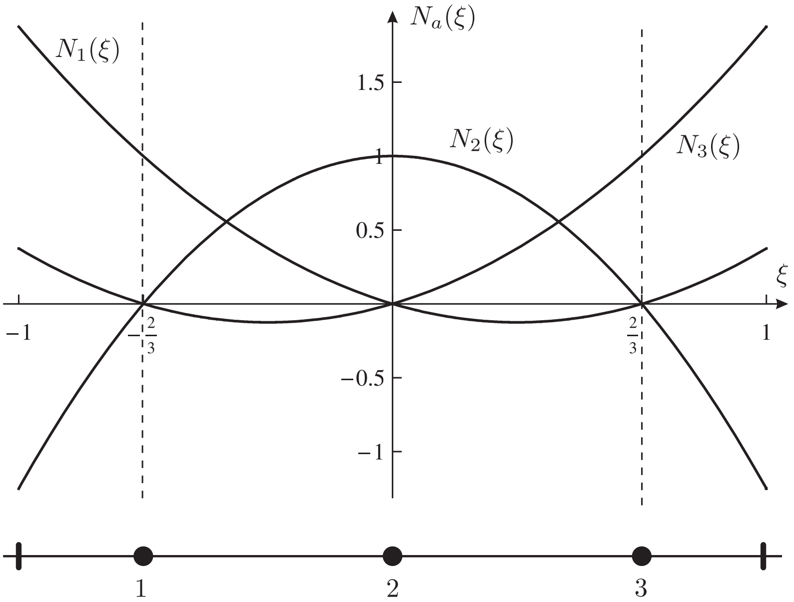

Figure 3.11: Discontinuous element with quadratic shape functions

where u_i^a and t_i^a are the nodal displacements and nodal tractions respectively. Using these interpolations and summing the contribution of each element integration over the entire boundary, the discretised DBIE can now be written as

$$C_{ij}(\mathbf{x}')u_j(\mathbf{x}')+\sum_{n=1}^{N_e}\int_{\Gamma_n} T_{ij}(\mathbf{x}',\mathbf{x})\sum_{a=1}^{3} N_a(\xi)u_j^{na}\,\mathrm{d}\Gamma_n = \sum_{n=1}^{N_e}\int_{\Gamma_n} U_{ij}(\mathbf{x}',\mathbf{x})\sum_{a=1}^{3} N_a(\xi)t_j^{na}\,\mathrm{d}\Gamma_n \tag{3.65}$$

where n is the element number, N_e is the number of elements and u_j^{na},t_j^{na} are the displacements and tractions on element n at local node a. The integral terms are taken over the element boundaries Γ_n, but for numerical implementation is it more convenient to express these integrals in terms of the local coordinate ξ. The Jacobian of transformation - which relates one coordinate system to another - is therefore used. It is stated as

$$J(\xi) = \frac{\mathrm{d}\Gamma}{\mathrm{d}\xi} = \sqrt{\left(\frac{\mathrm{d}x}{\mathrm{d}\xi}\right)^2 + \left(\frac{\mathrm{d}y}{\mathrm{d}\xi}\right)^2} \tag{3.66}$$

Substituting this into the integral expressions in (3.65) and noting that the terms u_j^{na} and t_j^{na} are constants which can be taken outside the integral, the discretised

DBIE is now expressed as

$$C_{ij}(\mathbf{x}')u_j(\mathbf{x}') + \sum_{n=1}^{N_e}\sum_{a=1}^{3}\left[\int_{-1}^{+1} T_{ij}(\mathbf{x}', \mathbf{x}(\xi))N_a(\xi)J^n(\xi)\,\mathrm{d}\xi\right] u_j^{na}$$
$$= \sum_{n=1}^{N_e}\sum_{a=1}^{3}\left[\int_{-1}^{+1} U_{ij}(\mathbf{x}', \mathbf{x}(\xi))N_a(\xi)J^n(\xi)\,\mathrm{d}\xi\right] t_j^{na} \tag{3.67}$$

where $J^n(\xi)$ corresponds to the Jacobian taken over element n. Eq. (3.67) can be written more compactly as

$$C_{ij}(\mathbf{x}')u_j(\mathbf{x}') + \sum_{n=1}^{N_e}\sum_{a=1}^{3} P_{ij}^{na}u_j^{na} = \sum_{n=1}^{N_e}\sum_{a=1}^{3} Q_{ij}^{na}t_j^{na} \tag{3.68}$$

where

$$P_{ij}^{na} = \int_{-1}^{+1} T_{ij}(\mathbf{x}', \mathbf{x}(\xi))N_a(\xi)J^n(\xi)\,\mathrm{d}\xi \tag{3.69a}$$

$$Q_{ij}^{na} = \int_{-1}^{+1} U_{ij}(\mathbf{x}', \mathbf{x}(\xi))N_a(\xi)J^n(\xi)\,\mathrm{d}\xi \tag{3.69b}$$

By formulating the DBIE in this fashion, the task of implementing the BEM becomes clearer, but there still remain a few unanswered questions. The integral expressions of (3.69a) and (3.69b) must be evaluated numerically, but we know that in certain cases these contain singular functions, so what integration routines must be used? The discretised DBIE of (3.68) gives a relation between boundary displacements and tractions, but how will this create a system of equations that will allow all boundary unknowns to be found? Also, the method must be capable of enforcing arbitrary boundary conditions, but how will these be applied? The answer to the first of these questions is devoted an entire chapter since it plays a crucial role in the BEM implementation but the latter two, which can be explained relatively easily, are considered in the next section.

3.1.7 Equation assembly and enforcement of boundary conditions

By inspecting the discretised form of the DBIE given by (3.65) it can be seen that this relation gives two sets of equations (one for each direction of the source point) which relate boundary displacements and tractions. Of course, this single set is insufficient to allow a solution to be found for all unknown boundary parameters and therefore additional relations must be found. In most BEM implementations this is achieved through *nodal collocation*. This process involves placing the source point $\mathbf{x}'$ at each nodal point in turn (see Fig. 3.12) while at each, the DBIE of (3.65) is evaluated. Since the integral terms (3.69a) and (3.69b) contain functions that depend on the distance r between the source and field points, each collocation point provides a unique relation between boundary displacements and tractions. Therefore, if there exist N nodal points, nodal collocation will obtain $2N$ boundary integral equations. Bearing in mind that at each node there exist four degrees of freedom (u_x, u_y, t_x and t_y) and that two of these must be prescribed (appropriate boundary conditions), then the entire problem contains $2N$ unknowns. With $2N$ unknowns and $2N$ equations, the system can then be solved.

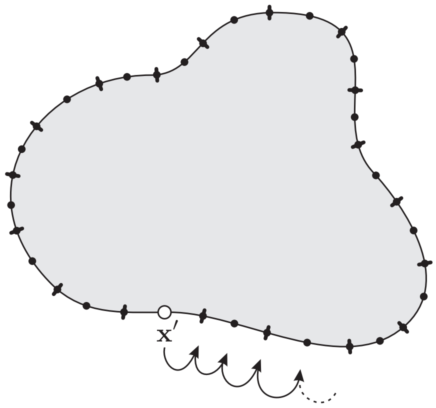

Figure 3.12: Nodal collocation procedure

Our attention is now diverted slightly to give a matrix formulation of the BEM since this often makes the process of computer implementation much simpler. In addition, the process of applying boundary conditions is greatly simplified since it is merely a task of swapping matrix columns and vector rows to achieve the desired result. But before the matrix form can be written, a few manipulations of Eq. (3.68) are required. We begin by letting $\mathbf{x^c}$ denote the location of the collocation point allowing the discretised DBIE to be written for all collocation points as

$$C_{ij}(\mathbf{x^c})u_j(\mathbf{x^c}) + \sum_{n=1}^{N_e}\sum_{a=1}^{3} P_{ij}^{na}(\mathbf{x^c})u_j^{na} = \sum_{n=1}^{N_e}\sum_{a=1}^{3} Q_{ij}^{na}(\mathbf{x^c})t_j^{na} \quad c = 1, N \tag{3.70}$$

where N is the number of nodes. Before this can be generalised any further, a note on displacements and tractions shared between elements must be made[3]. Consider two elements numbered 1 and 2 over which displacement boundary conditions are prescribed (Fig. 3.13a). It is a requirement that displacements must be continuous over the boundary and therefore the displacement components u_i^{13} must equal u_i^{21}. On the other hand, taking the case of tractions applied to each of the two elements, it is entirely feasible for the tractions on one side of a shared node to differ from those on the other side ($t_i^{13} \neq t_i^{21}$). These conditions are important since they have an effect on how the matrices are constructed. More specifically, taking the second term of Eq. 3.70 and noting that shared nodes must have equal displacement values, it can be rewritten as

$$\sum_{n=1}^{N_e}\sum_{a=1}^{3} P_{ij}^{na}(\mathbf{x^c})u_j^{na} = \sum_{\gamma=1}^{N} \bar{H}_{ij}^{c\gamma}u_j^{\gamma} \tag{3.71}$$

where shared nodes are now combined into one term and the summation can now be taken over nodes denoted by γ, a global nodal number. Contrary to this, since tractions can differ on shared nodes, the second summation term is still taken over elements and local nodal numbers with no combining of shared nodes. It is therefore given by

$$\sum_{n=1}^{N_e}\sum_{a=1}^{3} Q_{ij}^{na}(\mathbf{x^c})t_j^{na} = \sum_{n=1}^{N_e}\sum_{a=1}^{3} G_{ij}^{cna}t_j^{na} \tag{3.72}$$

The system of equations can now be expressed as

$$C_{ij}(\mathbf{x^c})u_j(\mathbf{x^c}) + \sum_{\gamma=1}^{N} \bar{H}_{ij}^{c\gamma}u_j^{\gamma} = \sum_{n=1}^{N_e}\sum_{a=1}^{3} G_{ij}^{cna}t_j^{na} \quad c = 1, N \tag{3.73}$$

In Sec. 3.1.4 it was shown that the jump term C_{ij} arises when the source point and field point coincide ($\mathbf{x}' = \mathbf{x}$), therefore the first two terms of(3.73) can be combined as

$$\sum_{\gamma=1}^{N} H_{ij}^{c\gamma} = C_{ij}\delta_{c\gamma} + \sum_{\gamma=1}^{N} \bar{H}_{ij}^{c\gamma} \tag{3.74}$$

to give

$$\sum_{\gamma=1}^{N} H_{ij}^{c\gamma}u_j^{\gamma} = \sum_{n=1}^{N_e}\sum_{a=1}^{3} G_{ij}^{cna}t_j^{na} \quad c = 1, N \tag{3.75}$$

---

[3] This only applies to continuous elements since nodes are not shared between discontinuous elements (Fig. 3.11)

We are now in a position to express the equation in matrix notation as

$$[\mathbf{H}]\{\mathbf{u}\} = [\mathbf{G}]\{\mathbf{t}\} \tag{3.76}$$

which is fundamental to the BEM implementation. **u** and **t** are vectors containing nodal displacements and tractions respectively, **H** is a matrix with dimensions $2N \times 2N$ which, from relation (3.74), contains jump terms down its diagonal and the rectangular matrix **G** is $2N \times M$ where $M = N_e \times 6$ (assuming quadratic elements). Some physical significance can also be given to each of the terms within these matrices: each row of the matrices **H** and **G** corresponds to the source point lying at a particular node and relates to a particular direction. Likewise, each column of the matrices corresponds to a field point which "feels" the effect of the source point in a particular direction. In this way the matrices form a table of coefficients that relate the effects of each of the source points to each of the field points.

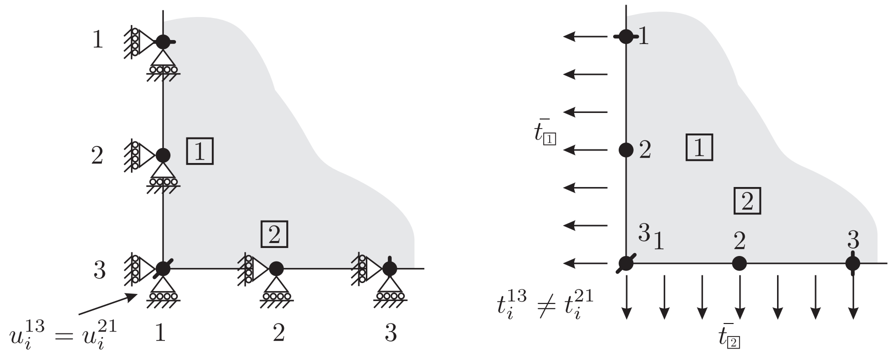

(a) Displacement boundary conditions (b) Traction boundary conditions

Figure 3.13: Boundary conditions for shared nodes with continuous elements

Clearly, Eq. (3.76) is quite restrictive in its current form since displacements and tractions are grouped together into the vectors **u** and **t** on the left hand side and right hand side respectively. In reality, the boundary conditions will usually be prescribed in such a way that there will be both displacement and traction unknowns around the boundary which must be grouped together on the left hand side and all prescribed boundary values must be taken to the right hand side. Once the equations are in this form, the problem can be solved easily using a conventional numerical solver. The actual process to achieve this required matrix form is very simple - it is a simple case of swapping the columns of both the **H** and **G** matrices to take all boundary unknowns to the left hand side and prescribed values to the right hand side. The system of equations can then be written as

$$[\mathbf{A}]\{\mathbf{x}\} = [\mathbf{B}]\{\mathbf{y}\} \tag{3.77}$$

where $\mathbf{x}$ is a vector containing all unknown boundary parameters, $\mathbf{y}$ is a vector containing prescribed boundary parameters and the matrices $\mathbf{A}$ and $\mathbf{B}$ are combinations of $\mathbf{H}$ and $\mathbf{G}$ created by swapping appropriate columns.

3.2 BEM applied to fracture

The power of numerical methods is the ability to analyse problems with arbitrary geometries and loadings where no analytical solutions exist. In the case of the BEM, the use of fundamental solutions (Green's functions) allow extremely accurate displacements and stresses to be obtained throughout the domain where errors are only introduced by discretisation of boundary conditions. For this reason, and the need to only discretise the boundary of the problem (rather than the entire domain), the BEM is one of the most efficient numerical methods for linear elastic fracture analysis. Several researchers have noted this, and as a result, there exist a variety of BEM implementations which demonstrate high accuracies for a variety of crack problems. This section aims to give an overview of some of the most important methods with particular attention given to the Dual Boundary Element Method (DBEM).

3.2.1 BIE degeneracy

Early work by Cruse [50] on applying the conventional BEM formulation to fracture problems discovered that problems are encountered when two surfaces of a boundary mesh coincide (as is the case in crack problems). In fact, the system of equations becomes singular and no sensible solution can be found. This can be easily explained by considering the case of a wedge which, in the limit as the distance between the faces becomes zero, becomes an edge crack problem (Fig. 3.14). Each row of the matrices $\mathbf{H}$ and $\mathbf{G}$ is formed by collocating at each nodal point in turn which presents no serious issues for the wedge problem. However, in the case of the edge crack where the nodal points lie at *coincident* positions, collocation at nodal points will produce *identical* rows for the upper and lower crack surfaces. As a result, it is not possible to use a straightforward application of the BEM to general fracture problems[4] (with coincident surfaces), and alternative techniques must be used.

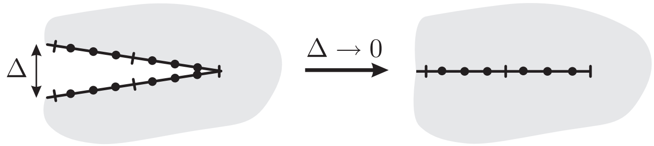

Figure 3.14: Edge crack as limiting case of wedge problem

3.2.2 Multi-region formulation

One of the simplest methods which can be used to overcome the indeterminate system of equations created by coincident crack surfaces is to simply sub-divide the domain along the line of the crack to create two sub-domains. If this procedure is used, then it is necessary to enforce displacement continuity and equilibrium of tractions across the boundary where the domain is split. This can be illustrated with the aid of Fig. 3.15 which denotes the interior boundary along which the domain is split as Γ_{int} and the newly created boundaries on the sub-domains as Γ^1_{int} and Γ^2_{int}. If the displacements and tractions along each of these newly created boundaries are denoted as (u^1_i, t^1_i) and (u^2_i, t^2_i) respectively, then displacement continuity is enforced by

$$u^1_i = u^2_i \tag{3.78}$$

and equilibrium of tractions is enforced through

$$t^1_i = -t^2_i \tag{3.79}$$

Applying these relations to a partitioned form of Eq. (3.76) (which contains the matrices corresponding to each sub-domain) it is possible to evaluate the displacements and tractions for all boundaries.

A major shortcoming of the method is the need to create additional boundaries (Γ^1_{int} and Γ^2_{int}) which incur additional computational costs due to discretisation and extra DOF. In the case of multiple cracks, several sub-domains (with associated boundaries) are required and it is clear that the method is computationally inefficient. The implementation of crack propagation routines presents issues too, since

---

[4] in some simple cases it may be possible to use symmetry. eg. Figs 5.3 and 5.4

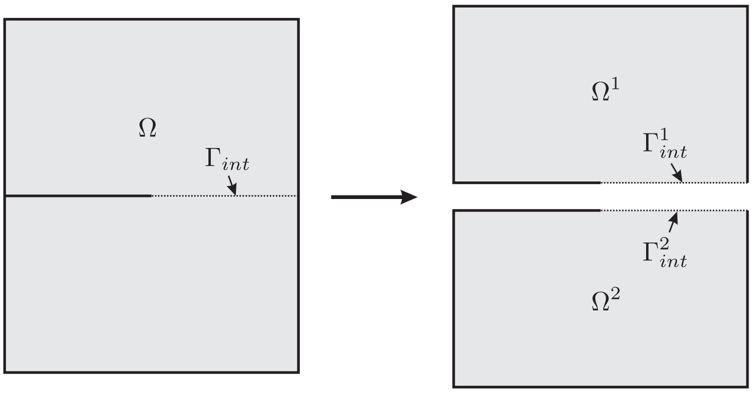

Figure 3.15: Multi-region strategy for crack problems

for each growth increment a new set of sub-domains must be determined and discretised in a rather cumbersome procedure.

3.2.3 Use of special fundamental solutions

The BEM formulation is reliant on the solutions to a point force within an infinite domain (Eqns 3.39), but it was shown by Snyder and Cruse [51] that it is also possible to formulate similar fundamental solutions for an infinite domain containing a flat, traction-free crack. If these are used, then it is only necessary to discretise non-cracked boundaries since the crack is included implicitly within the fundamental solutions. It is also possible to formulate the boundary integral equations in such a way that SIFs are output directly, but, since the fundamental solutions turn out to be complicated algebraic expressions involving complex variables, the method is an unattractive solution for general fracture problems. However, in the case of a 2D fracture problem containing a flat, traction free crack, it is found that the method can be used to find very accurate SIFs with Mews demonstrating the accuracy of the technique for both mode I and II problems [52].

3.2.4 The Dual Boundary Element Method

In recent years the Dual Boundary Element Method (DBEM) [24] has become firmly established as an efficient yet simple to implement method for applying the BEM to fracture problems. It overcomes the problem of a singular system created by the presence of coincident crack surfaces by using an additional, independent boundary integral equation on one of the crack surfaces while the conventional DBIE is used on the other. Therefore, even although collocation will occur twice at nodal points on the crack, the use of this additional equation will prevent identical rows being produced in (3.76).

The idea of using an independent BIE to overcome the problem of coincident crack surfaces actually predates the DBEM with the existence of several other BEM methods which use the same technique. Martha et al. [53] applied the TBIE to 3D fracture problems and used a displacement smoothing technique to ensure sufficient continuity for the hypersingular integration, but the implementation soon became cumbersome. Another method by Watson [54] makes use of three additional hypersingular BIEs that require special "particular solutions" for singular integral evaluation - where rigid body motion is one such solution (Sec. 4.4.2) - and enforced the required continuity by using Hermitian elements. This too ends up presenting complexities during implementation but shows accurate results for a variety of crack geometries. More recently, Domínguez and Ariza [55] have developed a method which uses a hypersingular BIE and overcomes the need to explicitly evaluate the singular integrals by performing a regularisation procedure on the kernels - this leaves only regular and weakly-singular integrals. In addition, the required C^1 continuity at collocation points is ensured by collocating at points internal to elements (rather than the conventional nodal positions). Since all singular integrals are removed the method is attractive, but the absence of an additional BIE on the crack surfaces means that the difference between upper and lower crack displacements is output rather than individual crack displacements. Since some post-processing routines such as the J-integral require these individual components, implementation of these procedures would present unnecessary difficulties.

Returning back to the DBEM, the first step required in the formulation is to derive the Traction Boundary Integral Equation (TBIE) which provides a relation between boundary displacements and tractions that is independent of the DBIE. Eq. (3.59), which allows stress components to be found at any point within the domain, is first recalled. This is only valid for points which do not lie on the boundary ($\mathbf{X}' \notin \Gamma$) and therefore, for the equation to relate to entirely boundary parameters, a limiting process similar to that carried out in Sec. 3.1.4 for the DBIE, is applied. What is found is that in the limit as the source point approaches the field point, the following BIE is obtained

$$\frac{1}{2}\sigma_{ij}(\mathbf{x}') + \,=\!\!\!\!\!\!\int_\Gamma S_{kij}(\mathbf{x}',\mathbf{x})u_k(\mathbf{x})\,\mathrm{d}\Gamma(\mathbf{x}) = -\!\!\!\!\!\!\int_\Gamma D_{kij}(\mathbf{x}',\mathbf{x})t_k(\mathbf{x})\,\mathrm{d}\Gamma(\mathbf{x}) \qquad (3.80)$$

where the first term is a jump term created by the limiting process (assuming the source point lies on a smooth surface) and the integral sign $⨎$ denotes a Hadamard finite part integral. This is similar to the Cauchy Principal Value integral but instead is applicable to integrals containing more strongly singular integrands, termed hypersingular. For instance, the integral of the function $f(x)/(x-x_p)^2$ over an interval $[a,b]$ where $x_p \in [a,b]$ is hypersingular and can be evaluated in a Hadamard finite part sense as

$$⨎_a^b \frac{f(x)}{(x-x_p)^2} = \lim_{\varepsilon\to 0}\left\{\int_a^{x_p-\varepsilon}\frac{f(x)}{(x-x_p)^2}\,\mathrm{d}x + \int_{x_p+\varepsilon}^{b}\frac{f(x)}{(x-x_p)^2}\,\mathrm{d}x - \frac{2f(x_p)}{\varepsilon}\right\} \tag{3.81}$$

Since the third term of Eq. (3.80) is a strongly singular integral, it is evaluated in the CPV sense as described in Sec. 3.1.4. The details of the limiting procedure which allows (3.80) to be written have been omitted, but an important point which was assumed in the process must be mentioned before we proceed. Referring back to the CPV liming process for the integral $\int_\Gamma T_{ij}(\mathbf{x}',\mathbf{x})u_j(\mathbf{x})\,\mathrm{d}\Gamma$, it was assumed that the displacements $u_j(\mathbf{x})$ were continuous at the source point $\mathbf{x}'$. Similarly, for the evaluation of the hypersingular integral $⨎_\Gamma S_{kij}(\mathbf{x}',\mathbf{x})u_k(\mathbf{x})\,\mathrm{d}\Gamma(\mathbf{x})$, it is a requirement that the displacement *derivatives* must be continuous at the point $\mathbf{x}'$. The use of quadratic continuous elements makes the satisfaction of this requirement difficult, so instead, discontinuous quadratic elements are usually applied on surfaces where the TBIE is collocated. In addition, if flat elements are used on the crack surfaces, then both the strongly singular and hypersingular integrals can be calculated using simple analytical expressions (see Sec. 4.4.3).

Eq. (3.80) does not constitute a BIE that can be used to relate displacements and tractions around the boundary since the first term (which is a stress component) is not in the required form. Using the relation which converts stresses to tractions (Eq. 3.14), it is clear that if we multiply (3.80) by the normal component $n_i(\mathbf{x}')$, then we can convert this stress component into a traction

$$\frac{1}{2}t_j(\mathbf{x}') + n_i(\mathbf{x}')⨎_\Gamma S_{kij}(\mathbf{x}',\mathbf{x})u_k(\mathbf{x})\,\mathrm{d}\Gamma(\mathbf{x}) = n_i(\mathbf{x}')⨍_\Gamma D_{kij}(\mathbf{x}',\mathbf{x})t_k(\mathbf{x})\,\mathrm{d}\Gamma(\mathbf{x}) \tag{3.82}$$

This equation can be discretised in the same manner as the DBIE (see Sec. 3.1.6) to give

$$\frac{1}{2}t_j(\mathbf{x}') + n_i(\mathbf{x}')\sum_{n=1}^{N_e}\sum_{a=1}^{3}E_{kij}^{na}u_k^{na} = n_i(\mathbf{x}')\sum_{n=1}^{N_e}\sum_{a=1}^{3}F_{kij}^{na}t_k^{na} \tag{3.83}$$

where quadratic elements have been assumed and the terms E_{kij}^{na} and F_{kij}^{na} are given by

$$E_{kij}^{na} = \int_{-1}^{1} S_{kij}(\mathbf{x}', \mathbf{x}(\xi)) N_a(\xi) J^n(\xi) d\xi \tag{3.84a}$$

$$F_{kij}^{na} = \int_{-1}^{1} D_{kij}(\mathbf{x}', \mathbf{x}(\xi)) N_a(\xi) J^n(\xi) d\xi \tag{3.84b}$$

We are now in a position where the TBIE can be used for collocation to overcome the problem of coincident crack surfaces and any arbitrary crack problem can be analysed using the DBEM. Referring to Figs 3.16 and 3.17, the following crack modelling strategy is used in the implementation of the DBEM:

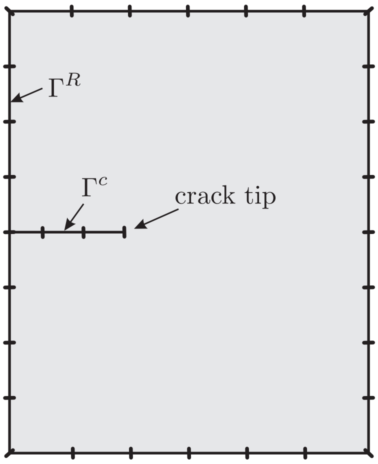

Figure 3.16: Edge-crack problem with boundary mesh for DBEM analysis

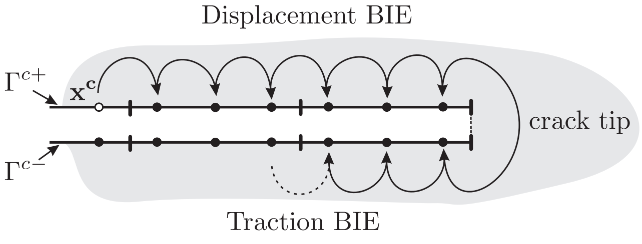

Figure 3.17: DBEM collocation strategy for elements on crack surfaces

- The DBIE is used for collocation on all non-crack surfaces (i.e. when $\mathbf{x^c} \in \Gamma^R$)
- Discontinuous boundary elements are used along all crack surfaces
- The TBIE is used for collocation on one of the crack surfaces ($\mathbf{x^c} \in \Gamma^{c-}$) while the DBIE is used for collocation on the other ($\mathbf{x^c} \in \Gamma^{c+}$)

Chapter 4

Evaluation of Boundary Integrals

The implementation of the Boundary Element Method (BEM) and Dual Boundary Element Method (DBEM) is reliant on the accurate evaluation of boundary integrals given by Eqns (3.69a) and (3.69b) in the case of the Displacement Boundary Integral Equation (DBIE) and Eqns (3.84a) and (3.84b) in the case of the Traction Boundary Integral Equation (TBIE). These integrals are dependent on the distance r between the source point ($\mathbf{x}'$) and field point ($\mathbf{x}$) which varies in value as the integrals are taken around the boundary. For the case when $\mathbf{x}' \neq \mathbf{x}$, the distance r is greater than zero and it is found that in most cases the kernels are regular, presenting few problems for integration. In the case $\mathbf{x}' = \mathbf{x}$, r is equal to zero and the kernels exhibit singularities whose order is dependent on the type of kernel - see Table 4.1 for a summary and Appendix C.1 for formal definitions of singular integrals. To evaluate these singular integrals, several techniques exist which are often developed for the evaluation of a particular order of singularity, and it is the goal of this chapter to present some of the most common methods. Each type of integral that is encountered in a BEM/DBEM implementation is considered - regular, nearly singular, weakly singular, strongly singular and hypersingular integrals - and the scenarios in which each occurs are described. Particular attention is given to the evaluation of the strongly singular and hypersingular integrals since these often present the greatest challenges for any BEM/DBEM implementation.

4.1 Non-singular integration

The first and simplest type of integral to consider is that of regular (non-singular integrals) which occur when the distance r between the source and field points is large. By itself, this statement is imprecise since it is not clear how "large" the

Table 4.1: Degrees of singularity for 2D linear elastic kernels

Kernel	Method[a]	Order	Singularity type
U_{ij}	B/D	$\mathcal{O}\ln(1/r)$	weakly singular
T_{ij}	B/D	$\mathcal{O}(1/r)$	strongly singular
D_{kij}	D	$\mathcal{O}(1/r)$	strongly singular
S_{kij}	D	$\mathcal{O}(1/r^2)$	hypersingular

[a] B=BEM,D=DBEM

distance must be before the integrals become regular. One concept which can help to resolve this is to define the term *field element* which refers to the element on which the field point $\mathbf{x}$ is positioned and over which the boundary integrals are evaluated (see Fig. 4.1). Therefore, by using this definition, the integrals (3.69a), (3.69b), (3.84a) and (3.84b) can be defined as regular if the source point $\mathbf{x}'$ lies at points which are not on or near the field element. In this case the integrals can be evaluated easily by using a numerical quadrature routine, the most common of which is Gauss-Legendre (GL) quadrature. This allows the integral of a function $f(\xi)$ which is defined over an interval $-1 \leq \xi \leq +1$ to be evaluated numerically as

$$\int_{-1}^{+1} f(\xi)\,\mathrm{d}\xi \cong \sum_{g=1}^{N_g} f(\xi_g)w_g \tag{4.1}$$

where ξ_g and w_g are Gauss points and weights that can be found in many textbooks (eg. [56] and [47]) and N_g is the desired number of Gauss points. As an example, Fig. 4.2 illustrates a scenario when the T_{ij} kernel is regular and can be evaluated using Gauss-Legendre quadrature. It shows the positions for an eight point quadrature rule and the corresponding values of the function evaluated at those points. The accuracy of this technique can be improved by increasing the number of Gauss points, but this is at the cost of computational resources. As a compromise, many BEM codes implement adaptive integration routines such as that developed by Gao and Davies [57] which determine the number of Gauss points from the ratio r/l (where l is the field element length)[1].

---

[1] Most commonly values in the range $N_g = 2$ to $N_g = 8$ are used.

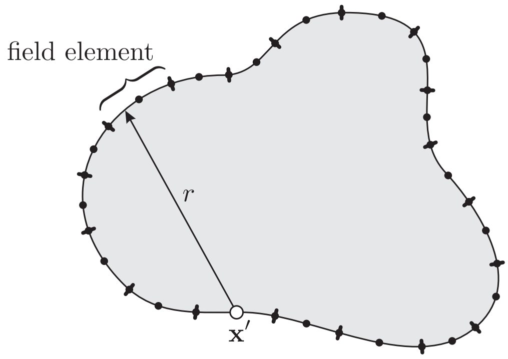

Figure 4.1: Definition of field element

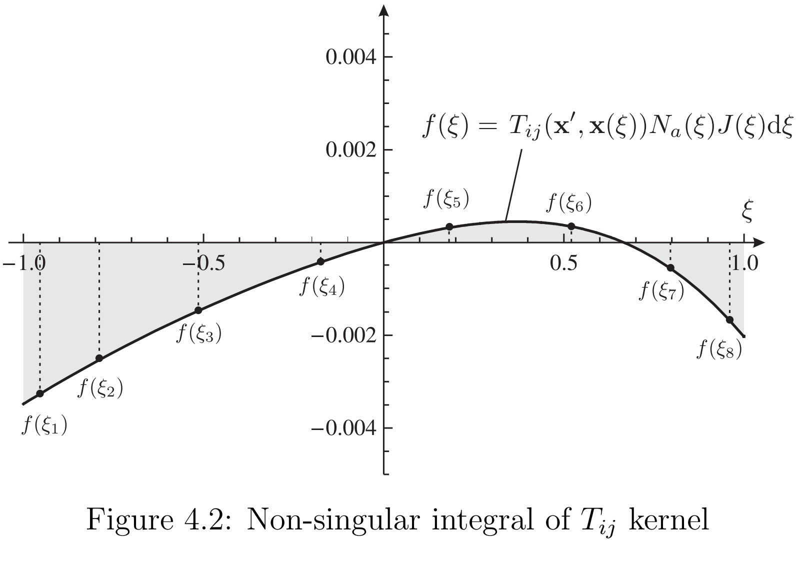

Figure 4.2: Non-singular integral of T_{ij} kernel

4.2 Nearly singular integrals

The previous section described the use of GL quadrature to evaluate integrals that are regular - defined as those integrals where the source point does not lie on or near the field element. As the source point starts to approach the field element, the singularity seen in each of the kernels starts to have an appreciable effect on the accuracy of integration (known as nearly singular integrals) and it becomes necessary to use higher orders of integration. In the case of the kernels U_{ij}, T_{ij} and D_{kij} which exhibit, at most, a singularity of $\mathcal{O}(1/r)$ (in 2D), it is found that high-order GL (ie. ≥ 8 gauss points) is sufficient for their evaluation. In the case of the more strongly singular S_{kij} kernel, however, this is not the case and an alternative integration technique must be employed.

4.2.1 Sub-elements

One of the simplest methods to evaluate nearly singular integrals is to divide the element into "sub-elements" and, by dividing the element appropriately, Gauss points can be concentrated in the location where the near-singularity is seen. Fig. 4.3 illustrates an element where a near singularity is experienced at $\xi = -1$ and, by the use of sub-elements, Gauss points are concentrated around this singular region. One drawback of using this technique is a requirement to perform additional transformations to local sub-element coordinate systems (shown as η_a and η_b in Fig. 4.3) and compute the associated Jacobians for each. Despite this, the method is simple to implement and uses numerical techniques that are readily understood. It is also found that the Telles transformation, which is primarily used for evaluating weakly singular integrals (Sec. 4.3.2 gives an outline of the method), is capable of evaluating nearly singular integrals and provides a very elegant solution to the problem.

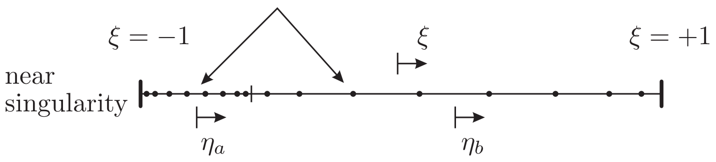

Figure 4.3: Sub-elements for nearly singular integrals

4.3 Weakly singular integrals

The previous discussion dealt with the case when the source point lies outside the field element and the integrals are, at most, nearly singular. But when the source point lies within the field element, the singularities play a large role on the type of numerical integration method required. In the case of the U_{ij} kernel the integral is weakly singular (in 2D elasticity) and the application of conventional GL quadrature, even with a large number of Gauss points, is insufficiently accurate. Two commonly used methods which overcome this problem are the application of a specific logarithmic Gaussian quadrature routine and the use of a coordinate transformation that is formulated in such a way that the singularity is cancelled. An overview of each is given here.

4.3.1 Logarithmic Gaussian quadrature

If a boundary integral contains a logarithmic singularity then often the first choice is to evaluate the integral using logarithmic Gaussian quadrature. This allows the logarithmically singular integrand to be evaluated in much the same manner as conventional GL quadrature but using different Gauss points and weights that are determined in such a way that the logarithmic singularity is accounted for. If the integrand can be expressed in the form $f(\xi)\ln(1/\xi)$, then the integral can be determined from

$$\int_0^1 f(\xi)\ln\left(\frac{1}{\xi}\right)\,\mathrm{d}\xi \cong \sum_{gl=1}^{N_{gl}} f(\xi_{gl})w_{gl} \tag{4.2}$$

where ξ_{gl} and w_{gl} are logarithmic Gauss points and weights respectively (these are tabulated in [47] and [56] for various values of N_{gl}) and, importantly, the integral is taken over the limits $\xi = 0$ to $\xi = 1$. Since the integral we wish to evaluate is expressed with the limits $\xi = -1$ to $\xi = +1$ (Eq. (3.69b)), it is necessary to perform a linear transformation that is dependent on the position of the source point within the element. Referring to the continuous boundary element shown in Fig. 3.9 and taking the source point to lie at each local node in turn, the required linear transformations for each node are given in Table 4.2. where node 2 requires the use of sub-elements to apply the two separate transformations. In the case of a discontinuous quadratic element, sub-elements are required for all three nodes.

Table 4.2: Linear transformations for logarithmic Gaussian quadrature

Local node	Transformation
1	$\eta = 0.5(1+\xi)$
2	$\eta = \begin{cases} -\xi & -1 < \xi < 0 \\ +\xi & 0 < \xi < 1 \end{cases}$
3	$\eta = 0.5(1-\xi)$

4.3.2 Telles transformation

An elegant and simple to implement technique which avoids the use of special logarithmic Gaussian quadrature is the variable transformation technique attributable to Telles [58]. The transformation is formulated in such a way that the Jacobian cancels the singularity and the integral can be evaluated with great accuracy using Gauss-Legendre quadrature. If a function $f(\xi)$ is weakly singular at a point ξ' where $|\xi'| = 1$, and we wish to find the integral

$$\int_{-1}^{+1} f(\xi)\,\mathrm{d}\xi \tag{4.3}$$

then by using the transformation given by Telles, this integral can be expressed as

$$\int_{-1}^{+1} f\left[(1-\gamma^2)\frac{\xi'}{2} + \gamma\right](1-\gamma\xi')\,\mathrm{d}\gamma \tag{4.4}$$

where γ is the new transformed coordinate. Importantly, the term given by $(1-\gamma\xi')$ (which is the Jacobian required to transform into the new coordinate system γ) is equal to zero at the point of singularity. Therefore, the transformation *cancels* the singularity and produces a non-singular function. For example, the function $\ln(1-\xi)$ is singular at the point $\xi = 1$ and if GL quadrature is used to evaluate the integral over the range $[-1, 1]$, then inaccuracies arise due to the singularity (see Fig. 4.4a). If the Telles transformation is used for this function (where $\xi' = 1$), the singularity is removed and there are no difficulties in applying GL quadrature (see Fig. 4.4b). In addition, since the method concentrates Gauss points around the singular point, the integral can be evaluated to a high level of accuracy with a relatively low-order quadrature scheme.

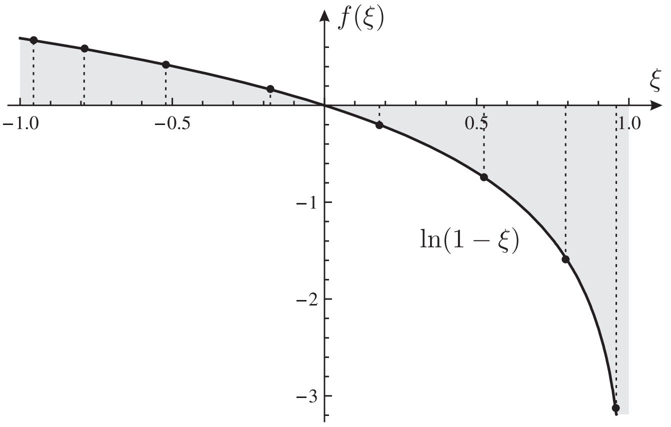

(a) Weakly singular function $\ln(1-\xi)$

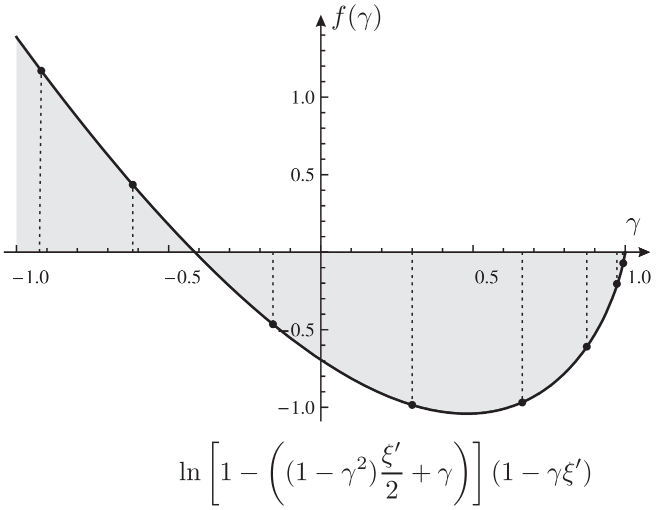

(b) Telles transformation for $\ln(1-\xi)$

Figure 4.4: Telles transformation for weakly singular functions

The astute reader will notice that the condition $|\xi'| = 1$ which allows the use of Eq. (4.4) is restrictive and does not allow the evaluation of integrals where the singularity is found at points within the element[2]. To resolve this, an additional transformation as outlined in Appendix C.2 allows the location of the singular point to lie at any point within the element $(-1 \leq \xi' \leq +1)$. This represents a completely general technique for the evaluation of weakly singular integrals and, in the author's opinion, represents one of most efficient and simple to implement techniques to evaluate integrals of this type.

4.4 Strongly singular and hypersingular integrals

The last types of integral which need to be considered are those which often create the most problems for implementation of the BEM. They are classed as strongly singular and hypersingular which, in 2D problems, correspond to those integrals which show singularities of $\mathcal{O}(1/r)$ and $\mathcal{O}(1/r^2)$ (the last three terms in Table 4.1). Because of these high orders of singularity, GL quadrature cannot be used and other techniques must be employed. As will be shown shortly, there are a variety of methods available which range from the use of analytical expressions to manipulations that avoid the need to calculate the integral altogether, but focus will be given to numerical integration methods which are used in later work on enrichment.

4.4.1 Interaction between shape functions and kernels

Before the various techniques which allow the evaluation of the strongly singular and hypersingular integrals are reviewed, it is beneficial to investigate the form of the functions being evaluated and in particular, the interaction between the shape functions and singular kernels. This is because in some cases the functions behave in such a way that the singularity is cancelled and there is no need to use special integration methods.

If we consider the case of strongly singular integrals first, we find that the situations in which integrals of this type arise are when the source point $\mathbf{x}'$ lies on the field element (Fig. 4.1) and the integrals contain the kernels T_{ij} and D_{kij}. But what is found is that, if quadratic shape functions are used for the interpolation of displacements and tractions, and the shape function within the integral corresponds

---

[2] For example, the middle node of a continuous quadratic element and all three nodes of a discontinuous quadratic element

to a *different* local node to that of the source point[3], then the integral becomes regular. This can be illustrated clearly by an example where the integral containing the T_{ij} kernel (Eq. (3.69a)) is evaluated over a continuous quadratic element which contains the source point at its middle node. If the shape function in the integrand corresponds to a different local node to that of the source point ($a = 1$ is chosen here), then the function we wish to integrate is

$$\int_{-1}^{+1} T_{ij}(\mathbf{x}', \mathbf{x}(\xi)) N_1(\xi) J(\xi) \, \mathrm{d}\xi \tag{4.5}$$

This integrand can be split into two functions - that of the shape function $N_1(\xi)$ and the remaining term $T_{ij}(\mathbf{x}', \mathbf{x}(\xi))J(\xi)$ - and then plotted over the integration interval $[-1, 1]$ (Fig. 4.5a). This illustrates the strong singularity of the T_{ij} kernel around the source point but also demonstrates that the shape function passes through zero at the point of singularity. It can be shown that the rate at which the shape function approaches zero is of $\mathcal{O}(r)$, and therefore, since the kernel is of $\mathcal{O}(1/r)$, the product of these functions contains no singularity (see Fig. 4.5b). Therefore in this case, when it would seem initially that a strong singularity would present difficulties for numerical integration, the integral can actually be evaluated easily using GL quadrature; it is only the case when the local node of the source point and the shape function node coincide that special singular integration techniques are required.

From the reasoning described previously for strongly singular integrals of $\mathcal{O}(1/r)$, it becomes clear that in the case of hypersingular integrals of $\mathcal{O}(1/r^2)$ the interaction between the shape functions and the kernel will not completely cancel the singularity - it will merely reduce the order of the singularity. This can be illustrated in the same manner as before where the hypersingular S_{kij} kernel can be plotted alongside the shape function for a node different to that of the source point (Fig. 4.6). But when the product of the two functions is plotted, a singularity of $\mathcal{O}(1/r)$ still remains. Therefore, unlike before, singular integrals are seen for all three nodes on the element (which in one case is hypersingular) requiring the use of singular integration techniques in each case.

---

[3] both are assumed to lie on the field element

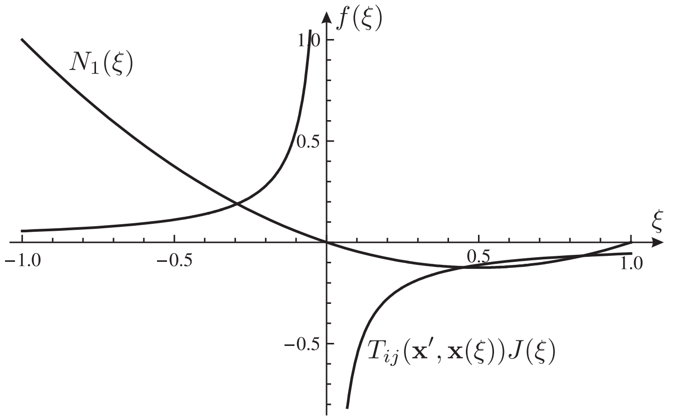

(a) Shape function and strongly singular kernel over a continuous quadratic element

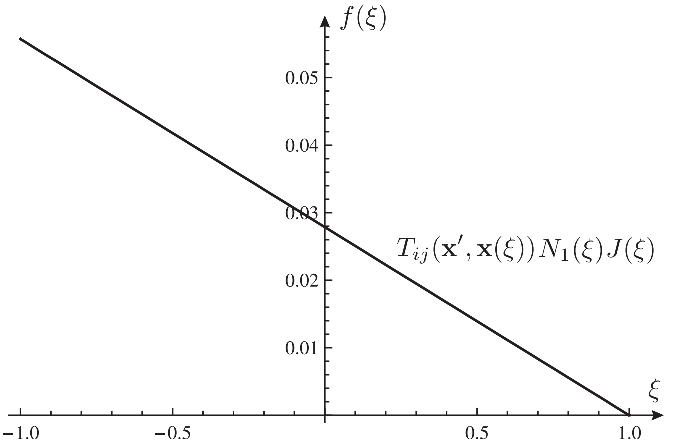

(b) Non-singular function for T_{ij} integrand when local shape function node and source point node are not equal

Figure 4.5: Interaction between strongly singular kernels and quadratic shape functions

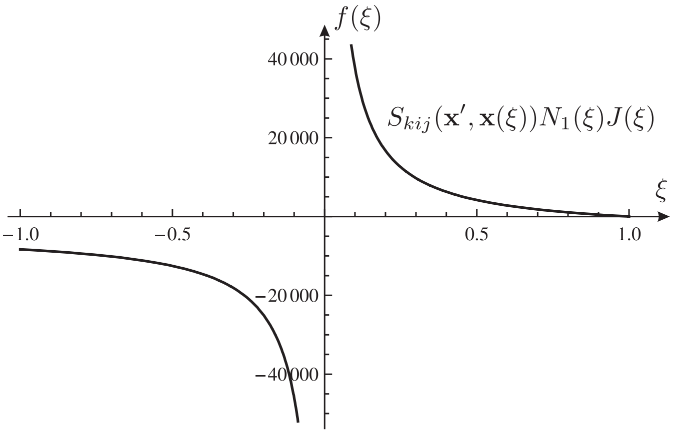

Figure 4.6: Remaining strong singularity for S_{kij} kernel when source point and shape function nodes do not coincide

4.4.2 Rigid body motion

Probably the most common method used to evaluate the strongly singular integrals in a conventional BEM implementation is to use rigid body motion which, through an ingenious procedure, precludes the need to explicitly evaluate the singular terms. As explained in the previous section, if the kernel is strongly singular then only the integral terms which relate to the condition when the source point and field points coincide present problems for GL quadrature. Therefore, in a conventional BEM implementation the only integral terms which cannot be evaluated using one of the quadrature schemes described previously is the strongly singular T_{ij} kernel when $\mathbf{x}' = \mathbf{x}$. Rigid body motion computes these unknown terms by enforcing zero tractions around the boundary and then applying two rigid-body unit translations - one in each of the global coordinate system directions (Fig. 4.7). If Eqn. (3.76) is recalled, then application of rigid-body motion with zero tractions gives the following system of equations

$$[\mathbf{H}]\{\bar{\mathbf{u}}_{RB}\} = 0 \tag{4.6}$$

where $\bar{\mathbf{u}}_{RB}$ is a vector containing unit displacements in either the x or y global directions. For example, applying unit displacements in the x-direction yields the following vector

$$\bar{\mathbf{u}}_{RB} = \begin{Bmatrix} 1 \\ 0 \\ 1 \\ 0 \\ \vdots \end{Bmatrix} \tag{4.7}$$

If all the non-singular terms are evaluated and the rigid-body displacement vector $\bar{\mathbf{u}}_{RB}$ is applied, then the system of equations can be symbolically represented by Fig. 4.8 where a distinction is made between the unknown and known terms. Taking each row of the $\mathbf{H}$ matrix in turn, multiplication with the displacement vector produces an equation where one of the unknown singular terms is expressed in terms of entirely known values. To calculate the second unknown singular term of this row, it is simply a case of applying the displacement vector corresponding to the other global direction (in this case the y direction). Using the notation described in Sec. 3.1.7, this process can be written mathematically as

$$H_{ij}^{cc} = -\sum_{\substack{\gamma=1 \\ \gamma\neq c}}^{N} H_{ij}^{c\gamma} \tag{4.8}$$

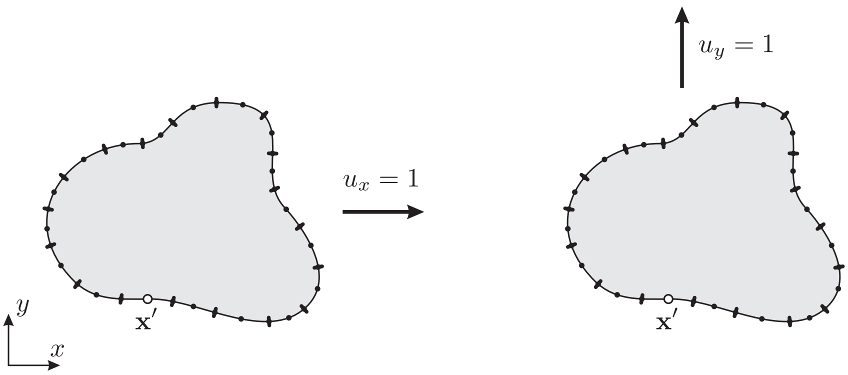

(a) x-direction (b) y-direction

Figure 4.7: Application of rigid-body motion for singular integration

$$
\begin{array}{ccccc}
\mathbf{H} & \bar{\mathbf{u}}_{RB} & & & \\
\begin{bmatrix}
\circ & \circ & \bullet & \bullet & \bullet & \bullet & \cdots \\
\circ & \circ & \bullet & \bullet & \bullet & \bullet & \cdots \\
\bullet & \bullet & \circ & \circ & \bullet & \bullet & \cdots \\
\bullet & \bullet & \circ & \circ & \bullet & \bullet & \cdots \\
\bullet & \bullet & \bullet & \bullet & \circ & \circ & \cdots \\
\bullet & \bullet & \bullet & \bullet & \circ & \circ & \cdots \\
\vdots & \vdots & \vdots & \vdots & \vdots & \vdots & \ddots
\end{bmatrix}
&
\begin{Bmatrix} 1 \\ 0 \\ 1 \\ 0 \\ 1 \\ 0 \\ \vdots \end{Bmatrix}
& = &
\begin{Bmatrix} 0 \\ 0 \\ 0 \\ 0 \\ 0 \\ 0 \\ \vdots \end{Bmatrix}
\end{array}
$$

○ unknown singular term
● known term

Figure 4.8: System of equations with rigid-body motion applied

Due to its simplicity and the avoidance of having to calculate strongly singular integrals altogether, this procedure if favoured for most BEM implementations, but in the case of the DBEM where coincident nodes are seen along crack faces, the technique can no longer be used. There are two reasons for this:

1. Using the DBIE to collocate on a crack face will produce strongly singular integrals for both the upper and lower crack faces. If all non-singular terms are evaluated, then four unknown singular terms will remain for each row of the **H** matrix with only two unique equations given by rigid-body motion.

2. As explained in Sec. 4.4.1, integration of the S_{kij} kernel when the source point lies within the field element will yield not only hypersingular integrals for when the source point and field point coincide, but also strongly singular integrals for when the field point lies at the two other nodes of the element. Since these integrals cannot be evaluated by conventional means, collocation of the TBIE

> will produce twelve unknown singular terms (six for the lower surface and six for the upper) with only two equations provided by rigid-body motion.

Therefore, for the implementation of the DBEM it is necessary to explicitly evaluate the strongly singular and hypersingular integrals.

4.4.3 Analytical integration

In some cases, the need for numerical integration schemes to evaluate strongly singular and hypersingular integrals can be avoided altogether by the use of analytical solutions for both 2D [24] and 3D problems [43]. This is particularly convenient for the implementation of the DBEM since, as explained previously, the use of the rigid-body motion technique can no longer be used. What is shown here is that by assuming flat discontinuous elements along the crack, both the strongly singular and hypersingular integrals are reduced to very simple expressions. Expressions for both type of singularity are outlined here, but more focus is given to the evaluation of the hypersingular terms because, once the derivation is understood for integrals of this type, the task of applying the same procedure to the strongly singular integrals is simple.

Before the analytical integral expressions are given, the conditions which must be enforced to allow the evaluation of hypersingular integrals are recalled (Sec. 3.2.4). The limiting process for integrals of this type requires that the integrand must have a continuous derivative at the limiting point and therefore, in the case of the TBIE (which exhibits hypersingular integrals), the displacement derivatives must be continuous at all collocation points. This is a higher degree of continuity than that required in the DBIE which only requires displacement continuity, presenting no issues for continuous elements. The same is not true for hypersingular integrals since continuity of displacement *derivatives* is required and this cannot be guaranteed with continuous elements. This can be explained by considering the case of a node positioned at a corner where the displacement gradient is allowed to jump from one value to another across the shared node. Therefore, it would seem that applying the TBIE introduces additional complexities due continuity requirements, but by simply using elements where nodes are positioned at interior points of elements (discontinuous elements), the problem is overcome. A technique to allow the use of continuous elements with the TBIE was proposed by Wilde et al. [59], but the method is inordinately complex to implement. Instead, it is much more favourable to use discontinuous elements (which exhibit continuous derivatives at nodal points) on boundaries where the TBIE is collocated.

To allow the strongly singular and hypersingular integrals to be evaluated analytically, it is necessary to make the assumption that flat elements are used. This puts restrictions on the geometry of the problem being analysed, but in the case of fracture problems - which in many cases can be modelled with straight cracks - the assumption is often valid. If this assumption can be made, then in turns out that the strongly singular and hypersingular integrals seen in the DBIE and TBIE reduce to rather simple expressions. In fact, a further simplification to the analytical expressions shown in [24] is given here.

The first integral to consider is that of the strongly singular T_{ij} kernel in the DBIE which occurs when the source point and field point coincide ($\mathbf{x}' = \mathbf{x}$). This can be written as

$$\fint_{-1}^{+1} T_{ij}(\xi', \mathbf{x}(\xi)) N_a(\xi) J^n(\xi)\, \mathrm{d}\xi \; u_j^a = \mathbf{h}^a \mathbf{u}^a \tag{4.9}$$

where ξ' denotes the local coordinate of the source point and $\mathbf{u}^a$ is a vector containing displacements for node a. By noting that the Jacobian is given by $l/2$ and the derivatives $r_{,i}$ are related to the normal components n_i, the matrix $\mathbf{h}^a$ can be written as

$$\mathbf{h}^a = \frac{1-2\nu}{4\pi(1-\nu)} \begin{bmatrix} 0 & -1 \\ 1 & 0 \end{bmatrix} I_a \tag{4.10}$$

where the terms I_a are analytical integral expressions[4] given by

$$I_1 = \fint_{-1}^{+1} \frac{N_1}{\xi - \xi'}\, \mathrm{d}\xi = \frac{3}{4} \left(\frac{\xi'(3\xi' - 2)}{2} \ln \left| \frac{1-\xi'}{1+\xi'} \right| + 3\xi' - 2 \right) \tag{4.11a}$$

$$I_2 = \fint_{-1}^{+1} \frac{N_2}{\xi - \xi'}\, \mathrm{d}\xi = \frac{1}{2} \left(\frac{(3\xi' - 2)(3\xi' + 2)}{2} \ln \left| \frac{1+\xi'}{1-\xi'} \right| - 9\xi' \right) \tag{4.11b}$$

$$I_3 = \fint_{-1}^{+1} \frac{N_3}{\xi - \xi'}\, \mathrm{d}\xi = \frac{3}{4} \left(\frac{\xi'(3\xi' + 2)}{2} \ln \left| \frac{1-\xi'}{1+\xi'} \right| + 3\xi' + 2 \right) \tag{4.11c}$$

and it is assumed that the shape functions given by Eqns (3.63) are used. The next integral to consider is that of the hypersingular S_{kij} integral which can be written,

---

[4] They are obtained by integration through substitution

in the same manner as before, as

$$n_i(\xi')\fint_{-1}^{+1} S_{kij}(\xi', \mathbf{x}(\xi))N_a(\xi)J(\xi)d\xi \; u_k^a = \bar{\mathbf{h}}^a \mathbf{u}^a \tag{4.12}$$

The matrix $\bar{\mathbf{h}}^a$ is given by

$$\bar{\mathbf{h}}^a = \frac{E}{4\pi(1-\nu^2)} \frac{2}{l} \bar{I}_a \mathbf{n}'\mathbf{S} \tag{4.13}$$

where $\mathbf{n}'$ is matrix containing the source point normal components

$$\mathbf{n}' = \begin{bmatrix} n_x' & 0 & n_y' & 0 \\ 0 & n_x' & 0 & n_y' \end{bmatrix} \tag{4.14}$$

and $\mathbf{S}$ contains field point normal components (the derivation of these components is given in Appendix C.5)

$$\mathbf{S} = \begin{bmatrix} +n_x(2n_y^2+1) & +n_y(2n_y^2-1) \\ +n_y(-2n_x^2+1) & +n_x(-2n_y^2+1) \\ +n_y(-2n_x^2+1) & +n_x(-2n_y^2+1) \\ +n_x(2n_x^2-1) & +n_y(2n_x^2+1) \end{bmatrix} \tag{4.15}$$

The integral terms $\bar{I}_a$ are determined, as before, from analytical integration and are written as

$$\bar{I}_1 = \fint_{-1}^{+1} \frac{N_1}{(\xi-\xi)^2} d\xi = \frac{3}{4}\left((3\xi'-1)\log\left|\frac{1-\xi'}{1+\xi'}\right| + \frac{6\xi'^2-2\xi'-3}{\xi'^2-1}\right) \tag{4.16a}$$

$$\bar{I}_2 = \fint_{-1}^{+1} \frac{N_2}{(\xi-\xi)^2} d\xi = \frac{1}{2}\left(9\xi'\log\left|\frac{1+\xi'}{1-\xi'}\right| - \frac{18\xi'^2-13}{\xi'^2-1}\right) \tag{4.16b}$$

$$\bar{I}_3 = \fint_{-1}^{+1} \frac{N_3}{(\xi-\xi)^2} d\xi = \frac{3}{4}\left((3\xi'+1)\log\left|\frac{1-\xi'}{1+\xi'}\right| + \frac{6\xi'^2+2\xi'-3}{\xi'^2-1}\right) \tag{4.16c}$$

Furthermore, by multiplying the matrices $\mathbf{n}'$ and $\mathbf{S}$ and noting that the source point normal $\mathbf{n}'$ and field point normal $\mathbf{n}$ are equal for the case $\mathbf{x}'$ and $\mathbf{x}$ lie on the same element and opposite for the case in which $\mathbf{x}'$ and $\mathbf{x}$ lie on opposite elements, the following simplification can be made

$$\mathbf{n}'\mathbf{S} = (\mathbf{n}'.\mathbf{n}) \begin{bmatrix} 1 & 0 \\ 0 & 1 \end{bmatrix} = (\mathbf{n}'.\mathbf{n})\mathbf{I} \tag{4.17}$$

where **I** is the identity matrix and . denotes the dot product. The matrix $\bar{\mathbf{h}}^a$ can then be expressed simply as

$$\bar{\mathbf{h}}^a = \frac{E}{4\pi(1-\nu^2)}\frac{2}{l}\bar{I}_a(\mathbf{n}'.\mathbf{n})\mathbf{I} \tag{4.18}$$

It should be clear then that the introduction of the TBIE to overcome the problem of coincident crack surfaces presents little difficulties for implementation when flat elements are used; all singular integrals along the crack surfaces can be evaluated analytically using the simple expressions given by (4.10) and (4.18). The use of curved or enriched elements precludes the use of these expressions however, and in these cases other numerical integration techniques are required.

4.4.4 Numerical integration

The evaluation of strongly singular and hypersingular boundary integrals has been studied extensively by BEM researchers and there exist a variety of numerical methods specifically developed for this purpose. Quadrature schemes such as that presented by Kutt [60], [61], Paget [62] and further developed by Ioakimidis [63] use a set of specially constructed integration points and weights that implicitly account for the singularity. Unfortunately, extremely high precision is required since in some cases the magnitude of the weights is as high as 10^{10}. Rudolphi [64] proposed a scheme that uses a particular solution, very similar to that of rigid body motion, capable of evaluating both strongly singular and hypersingular terms, but, as mentioned in [65], the method lacks general applicability. Gray [66] developed a scheme, later implemented for 3D crack problems [53], that enforces continuity of displacement derivatives by introducing a cubic approximation solved using a least-squares scheme. Accurate results are seen, but even the author himself comments on the implementation complexity of the method [67]! A solution to this was therefore proposed [67] by using Hermitian elements which enforce continuity of displacement derivatives at nodal points and the hypersingular integrals are determined directly by considering the limit as the source point approaches the boundary. In the case of flat elements the scheme is simple, but curved elements necessitate the use of extensive symbolic computation [68].

The method which is considered here for the evaluation of *all* singular integrals is a numerical technique commonly referred to as the subtraction of singularity method [69], [70], [71]. This allows the evaluation of the singular integrals through a regularisation process (Hilbert transformation) which removes the singular term(s) from the integrand leaving a regular function that can be evaluated easily using conventional GL quadrature. The singular term is then included back in by an additional integral which, since its form is already known, can be integrated using a simple analytical expression. It is a powerful numerical integration method since it can be used generally for both strongly singular and hypersingular kernels and, as long as displacement derivatives are continuous at the point of singularity, the technique can be used for *any* displacement approximation. This is especially important for the evaluation of singular integrals in the enriched BEM since the standard displacement approximation is replaced by a form that can account for the crack tip singularity.

First, let $F(\xi', \xi)$ define a hypersingular function, infinite at the point ξ', which we wish to integrate over a 2D boundary element. In the case of the DBEM, the integral containing the S_{kij} kernel contains a singularity of this type

$$\mathop{=\!\!\!\!\!\!\int}_{-1}^{+1} S_{kij}(\xi', \mathbf{x}(\xi)) N_a(\xi) J(\xi) d\xi \tag{4.19}$$

Using this integral as an example, we can therefore define the function $F(\xi', \xi)$ as

$$F(\xi', \xi) = S_{kij}(\xi', \mathbf{x}(\xi)) N_a(\xi) J(\xi) \tag{4.20}$$

The key to the method is to represent this function in a series form thus separating it into singular and non-singular components. This is possible through the use of Laurent's theorem (see [72] for a review), allowing $F(\xi', \xi)$ to be written as

$$F(\xi', \xi) = \frac{F_{-2}(\xi')}{(\xi - \xi')^2} + \frac{F_{-1}(\xi')}{(\xi - \xi')} + \mathcal{O}(1) \tag{4.21}$$

The singularities are now made explicit by the expressions $(\xi - \xi')^2$ and $\xi - \xi'$ which are found to be in a convenient form for integration. The non-singular functions $F_{-2}(\xi')$ and $F_{-1}(\xi')$ depend on the first and second derivatives of the shape functions at the singular point ξ' and can be determined using a procedure such as that shown in Appendix C.6.2. By now subtracting this function from the original integrand (Eq. (4.20)) a *regular* function is produced. To illustrate this clearly, Fig. 4.9a shows the hypersingular function given by (4.20) which then subtracts the singular terms to give the function shown in Fig. 4.9b. Of course, if the singular terms are removed from the integrand then they must must be included back in elsewhere. Our attention is now focused towards this task.

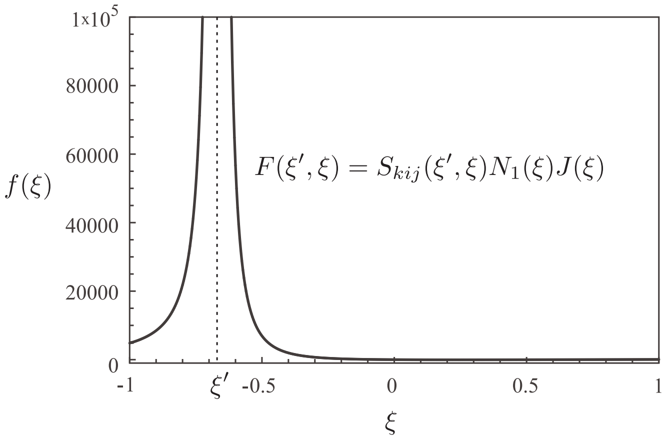

(a) Hypersingular integrand

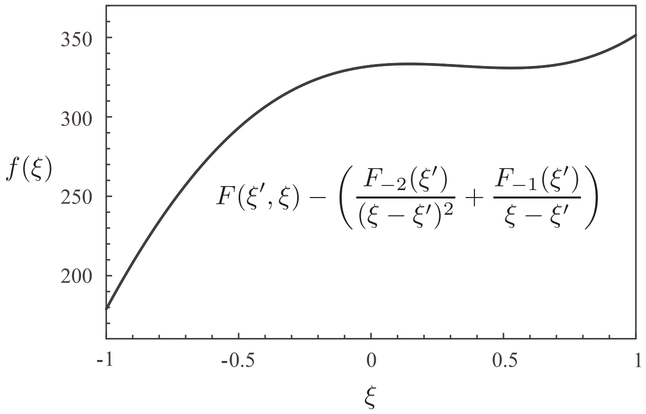

(b) Regularised integrand

Figure 4.9: Regularisation of hypersingular integrand by subtraction of singularity

It is necessary to define the boundary over which the integral is evaluated and to construct a semi-circle (centred at the source point $\mathbf{x}'$) which allows the limiting procedure to be carried out. In the global coordinate system this can be represented by Fig. 4.10a where the integral is taken over the boundary $\Gamma_e \cup \Gamma_\Delta$ (Γ_Δ is represented by the dashed line) and the assumption is made that the source point lies at a point internal to the element[5]. By transforming this into the local coordinate system ξ (Fig. 4.10b), the integral can then be taken over two intervals $[-1, \xi' - \Delta\xi]$ and $[\xi' + \Delta\xi, +1]$ while taking the limit as $\Delta\xi \to 0$.

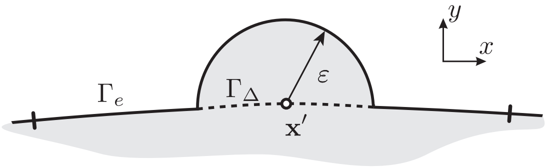

(a) Global coordinate system

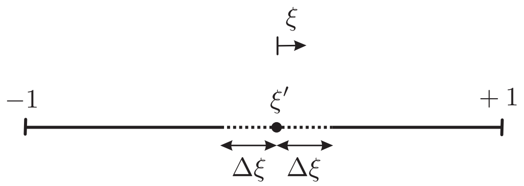

(b) Local coordinate system

Figure 4.10: Limiting procedure for subtraction of singularity method

Now that the integration intervals are defined, it is possible to write the entire integral expression with the singular integrals included as

$$
\begin{aligned}
\mathcal{I} = &\int_{-1}^{+1} \left[F(\xi', \xi) - \left(\frac{F_{-2}(\xi')}{(\xi - \xi')^2} + \frac{F_{-1}(\xi')}{\xi - \xi'} \right) \right] \mathrm{d}\xi \\
&+ \lim_{\varepsilon \to 0} \left\{ \int_{-1}^{\xi' - \Delta\xi} \frac{F_{-1}(\xi')}{\xi - \xi'} \mathrm{d}\xi + \int_{\xi' + \Delta\xi}^{+1} \frac{F_{-1}(\xi')}{\xi - \xi'} \mathrm{d}\xi \right. \\
&\quad \left. + \int_{-1}^{\xi' - \Delta\xi} \frac{F_{-2}(\xi')}{(\xi - \xi')^2} \mathrm{d}\xi + \int_{\xi' + \Delta\xi}^{+1} \frac{F_{-2}(\xi')}{(\xi - \xi')^2} \mathrm{d}\xi + N_a(\xi) \frac{b_{kij}(\xi')}{\varepsilon} \right\}
\end{aligned}
\tag{4.22}
$$

By writing the integral in this way, the natural division of the expression into three components should be made clear: the first consists of the regularised integral which can be evaluated easily using a numerical quadrature scheme, the second contains the singular integral expressions involving F_{-1} while the third contains the singular integrals involving F_{-2} with an introduced jump term $N_a(\xi) b_{kij}(\xi')/\varepsilon$. This term

---

[5] This is a valid assumption if discontinuous elements are used

arises from the limiting procedure, in much the same way that the the jump term C_{ij} arises in the DBIE (Sec. 3.1.4). If the three components are denoted as $\mathcal{I}_0$, $\mathcal{I}_{-1}$ and $\mathcal{I}_{-2}$ respectively, then we can write

$$\mathcal{I}_0 = \int_{-1}^{+1} \left[F(\xi', \xi) - \left(\frac{F_{-2}(\xi')}{(\xi - \xi')^2} + \frac{F_{-1}(\xi')}{\xi - \xi'} \right) \right] \mathrm{d}\xi \tag{4.23a}$$

$$\mathcal{I}_{-1} = \lim_{\varepsilon \to 0} \left\{ \int_{-1}^{\xi' - \Delta\xi} \frac{F_{-1}(\xi')}{\xi - \xi'} \mathrm{d}\xi + \int_{\xi' + \Delta\xi}^{+1} \frac{F_{-1}(\xi')}{\xi - \xi'} \mathrm{d}\xi \right\} \tag{4.23b}$$

$$\mathcal{I}_{-2} = \lim_{\varepsilon \to 0} \left\{ \int_{-1}^{\xi' - \Delta\xi} \frac{F_{-2}(\xi')}{(\xi - \xi')^2} \mathrm{d}\xi + \int_{\xi' + \Delta\xi}^{+1} \frac{F_{-2}(\xi')}{(\xi - \xi')^2} \mathrm{d}\xi + N_a(\xi) \frac{b_{kij}(\xi')}{\varepsilon} \right\} \tag{4.23c}$$

where

$$\mathcal{I} = \mathcal{I}_0 + \mathcal{I}_{-1} + \mathcal{I}_{-2} \tag{4.24}$$

As mentioned previously, the integral $\mathcal{I}_0$ can be integrated easily and requires no further manipulation. The singular integrals $\mathcal{I}_{-1}$ and $\mathcal{I}_{-2}$ are integrated analytically but must be considered in the limit as $\varepsilon \to 0$. Therefore, since Eqns (4.23b) and (4.23c) are written in terms of the infinitesimal boundary $\Delta\xi$, it is necessary to introduce a relation between ε and $\Delta\xi$ by using a Taylor series approximation about the source point ξ'

$$\varepsilon = J(\xi')\Delta\xi + \mathcal{O}(\Delta\xi^2) \tag{4.25}$$

which allows, after ignoring higher order terms, $\Delta\xi$ to be expressed as

$$\Delta\xi = \frac{\varepsilon}{J(\xi')} \tag{4.26}$$

Substituting this into 4.23b we can write

$$\mathcal{I}_{-1} = \lim_{\varepsilon \to 0} \left\{ \int_{-1}^{\xi' - \frac{\varepsilon}{J(\xi')}} \frac{F_{-1}(\xi')}{\xi - \xi'} \mathrm{d}\xi + \int_{\xi' + \frac{\varepsilon}{J(\xi')}}^{+1} \frac{F_{-1}(\xi')}{\xi - \xi'} \mathrm{d}\xi \right\} \tag{4.27}$$

which is integrated analytically[6] to give

$$\mathcal{I}_{-1} = F_{-1}(\xi') \ln \left| \frac{1 - \xi'}{-1 - \xi'} \right| \tag{4.28}$$

---

[6] see Appendix C.6.1 for details of the integration

Likewise, $\mathcal{I}_{-2}$ is given by

$$\mathcal{I}_{-2} = \lim_{\varepsilon \to 0} \left\{ \int_{-1}^{\xi' - \frac{\varepsilon}{J(\xi')}} \frac{F_{-2}(\xi')}{(\xi - \xi')^2} \mathrm{d}\xi + \int_{\xi' + \frac{\varepsilon}{J(\xi')}}^{+1} \frac{F_{-2}(\xi')}{(\xi - \xi')^2} \mathrm{d}\xi + N_a(\xi) \frac{b_{kij}(\xi')}{\varepsilon} \right\} \tag{4.29}$$

which is integrated to give

$$\mathcal{I}_{-2} = F_{-2}(\xi') \left[\frac{1}{-1 - \xi'} - \frac{1}{1 - \xi'} \right] \tag{4.30}$$

where all unbounded terms are cancelled. By combining Eqns (4.23a), (4.28) and (4.30) using relation (4.24), the final expression used to evaluate the hypersingular integral is

$$\begin{aligned} \mathcal{I} = &\int_{-1}^{+1} \left[F(\xi', \xi) - \left(\frac{F_{-2}(\xi')}{(\xi - \xi')^2} + \frac{F_{-1}(\xi')}{\xi - \xi'} \right) \right] \mathrm{d}\xi \\ &+ F_{-1}(\xi') \ln \left| \frac{1 - \xi'}{-1 - \xi'} \right| \\ &+ F_{-2}(\xi') \left[\frac{1}{-1 - \xi'} - \frac{1}{1 - \xi'} \right] \end{aligned} \tag{4.31}$$

which, once the values $F_{-1}(\xi')$ and $F_{-2}(\xi')$ are known, can be implemented easily.

Finally, it is useful to consider the application of the technique to strongly singular integrals where it is found that the terms in (4.31) relating to $F_{-2}(\xi')$ simply equal zero. A procedure specifically formulated to evaluate strongly singular boundary integrals using the same regularisation process was outlined by Guiggiani and Casalini [69], but to allow the use of any displacement approximation (thus allowing the implementation of enriched displacements) the technique outlined here is used.

Chapter 5

Singular Elements, Enrichment and Partition of Unity Methods

From early work on fracture using computational methods (primarily the FEM), many researchers encountered a common problem of large inaccuracies when modelling the singular field seen around a crack tip. For instance, in the work carried out by Chan, Tuba and Wilson [73] to evaluate stress intensity factors (SIFs), accuracies in the region of, at best, 5% were achieved. The problem was more closely examined by Tong et al. [23] who concluded that, if the FEM is used to analyse a model containing a crack with no form of enrichment, the rate of convergence is controlled by the presence of the crack-tip singularity. They showed that, in order to improve the rate of convergence, the singularity must be included within the approximation and that this must be used in a finite region surrounding the crack tip. Since then several methods have been developed to capture the correct singular behaviour of a crack using special elements and displacement approximations which, in many cases, *must* be used if fracture problems are to be modelled with sufficient accuracy. This chapter aims to give an overview of some of these methods but particular attention is paid to the more recent developments that utilise the power of the partition of unity method (PUM).

5.1 Crack tip elements and singular shape functions

The majority of numerical methods use polynomial functions for interpolation and therefore, unless a very refined mesh is used, the singular field experienced at a crack tip cannot be captured. This can be seen clearly in Fig. 5.1 which illustrates the displacement approximation using a discontinuous quadratic element adjacent to the crack tip. The use of a fine mesh in the region surrounding the crack tip can be used (and was the primary technique used to obtain reasonable accuracies in early fracture work), but with the large increase in DOF this is an uneconomical option. Instead, since the form of displacements around a crack is already known, a more appropriate solution is to use this knowledge to make certain modifications to the elements adjacent to the crack and therefore improve accuracy. In this section two types of element modification are outlined: the popular quarter-point element and the use of special singular shape functions.

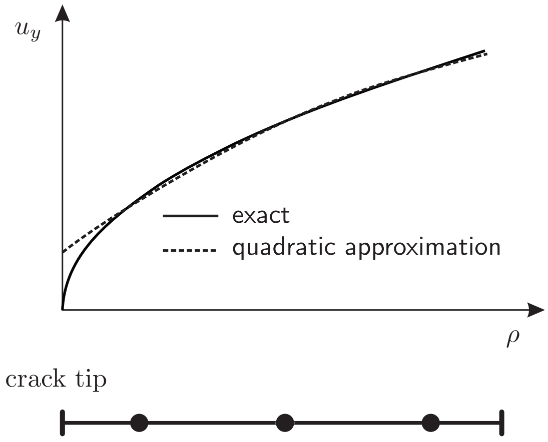

Figure 5.1: Quadratic approximation of crack-tip displacements

5.1.1 Quarter-point elements

In a conventional 2D analysis the most common type of element used in FEM implementations is either the six-noded triangular or eight-noded quadrilateral isoparametric element. Likewise, in the BEM, the three-noded isoparametric elements are most popular (see Fig. 5.2a). Using elements of this type, the correct displacement behaviour of a crack cannot be captured correctly and it was Henshell and Shaw [74] and Barsoum [75] who, almost at exactly the same time, arrived at a simple and elegant solution to the problem. They proposed a special element, now referred to as quarter-point (QP) elements, that captures the required $\sqrt{\rho}$ (where ρ is the distance from the crack tip) variation seen at the crack tip by simply moving the midnode to a quarter-point position on the element. To explain why the correct interpolation is obtained, we can compare the displacement approximation of the three-noded quadratic boundary element in Fig. 5.2a and the corresponding QP element shown in Fig. 5.2b. Denoting l as the element length and letting $y = 0$, the nodal coordinates of the QP element can be expressed as

$$x^1 = l \qquad x^2 = l/4 \qquad x^3 = 0 \tag{5.1}$$

Using the continuous shape functions given by Eqns (3.62) and substituting the above expressions for nodal coordinates, the following relation can be written for the general point x on the element

$$x = \frac{1}{2}\xi(1+\xi)l + (1-\xi^2)\frac{l}{4} \tag{5.2}$$

Rearranging this for ξ and noting that $x = \rho$,

$$\xi = -1 + 2\sqrt{\frac{x}{l}} = -1 + 2\sqrt{\frac{\rho}{l}} \tag{5.3}$$

This can then be substituted into Eq. (3.64a) to arrive at the final expression for displacement interpolation using a QP element

$$\begin{aligned} u_i &= u_i^1 + (-3u_i^1 + 4u_i^2 - u_i^3)\sqrt{\frac{\rho}{l}} + 2(u_i^1 - 2u_i^2 + u_i^3)\frac{\rho}{l} \\ &= c_0 + c_1\sqrt{\frac{\rho}{l}} + c_2\frac{\rho}{l} \end{aligned} \tag{5.4}$$

If the same procedure is applied to an element with no repositioning of the middle node, then the displacement interpolation is expressed as

$$u_i = d_0 + d_1\left(\frac{\rho}{l}\right) + d_2\left(\frac{\rho}{l}\right)^2 \tag{5.5}$$

where d_0, d_1 and d_2 are constants. What should be clear by comparing Eq. (5.4) with Eq. (5.5) is that QP elements are able to account for the known $\sqrt{\rho}$ displacement behaviour while the conventional quadratic polynomial approximation cannot. The particularly attractive feature of the method is the simplicity by which this can be achieved - only the midnode needs to be repositioned and changes to existing FEM or BEM codes are kept to a minimum.

Eq. (5.4) showed that QP elements are capable of capturing the $\sqrt{\rho}$ variation in displacements seen around a crack, but in the BEM, which represents tractions independently of displacements, it is also necessary to account for the singular tractions. For instance, the problem of a double edge crack (Fig. 5.3) can be modelled

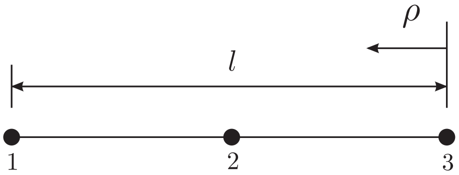

(a) Standard quadratic element

(b) Quarter-point element

Figure 5.2: Comparison of standard and quarter-point boundary elements

with symmetry (Fig 5.4a) resulting in a singular displacement gradient on one side of the crack tip and a singular traction field on the other. The singular displacement gradient can be captured using the QP element outlined previously, but it is also possible to formulate a traction QP element. This is also achieved by shifting the midnode of the element to the quarter-point position and it is then found [76] that the tractions are then interpolated over the element as

$$t_i = t_i^1\sqrt{\frac{l}{\rho}} + (-3t_i^1 + 4t_i^2 - t_i^3) + 2(t_i^1 - 2t_i^2 + t_i^3)\sqrt{\frac{\rho}{l}} \tag{5.6}$$

which, by noting that the stresses around a crack are of $\mathcal{O}(1/\rho^{1/2})$, is the desired interpolation. Using this strategy, both displacement and traction QP elements can be used with a mesh such as that shown in Fig. 5.4b to carry out a BEM fracture analysis with improvements over conventional interpolation. A model very similar to this was used by Martínez et al. [29] to illustrate the individual effects of using displacement and traction QP elements. Tests were also carried out to study the effect of using both displacement and traction extrapolation methods to determine SIFs. Their results concluded that there was a significant dependence on element size when using displacement QP elements while the most consistently accurate results were obtained using traction QP elements with traction nodal value extrapolation to obtain SIFs. They also noted that the best results for displacement QP elements were obtained for small ratios of element length to crack length and concluded that, if the element size was reduced below the optimum length, then the singularity would extend to elements beyond the singular element. Since quadratic interpolation is used in this region, inaccuracies would occur as a result.

Other researchers noted the limitations of QP elements such as Harrop [77] who described the difficulties on obtaining the optimum size of quarter-point elements and concluded that no general strategy could be obtained. This was verified later

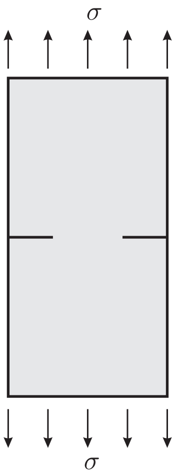

Figure 5.3: Double edge crack problem

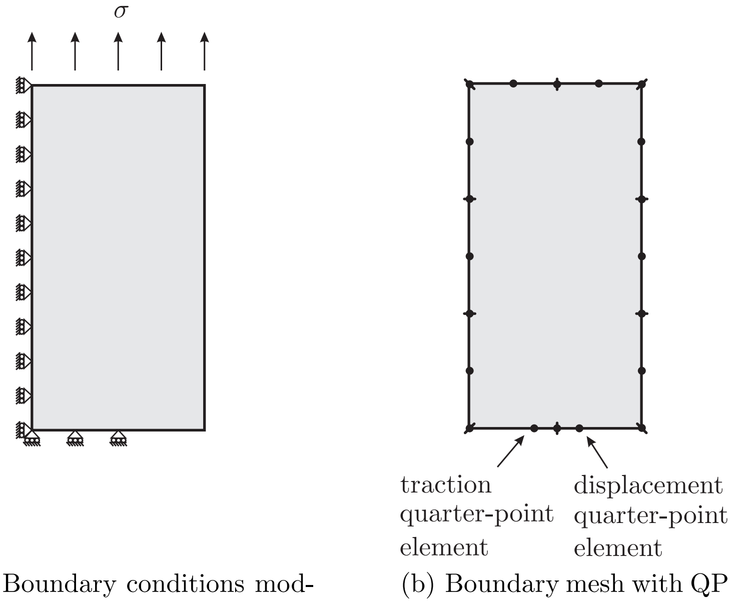

(a) Boundary conditions modelled with symmetry

(b) Boundary mesh with QP elements

Figure 5.4: Double edge crack with displacement and traction quarter-point elements

by Yehia and Shephard [78] who also noted a dependence on the crack propagation angle with QP element size. Furthermore, when the elements were applied to 3D models in the FEM Ingraffea et al. [79] showed that surprisingly, the optimum choice of element size is dependent on Poisson's ratio. But even with these limitations, QP elements still remain one of the simplest and fastest ways to improve crack tip interpolation over standard polynomial functions.

5.1.2 Modified shape functions

Rather than change the nodal positions on the elements to achieve the desired $\rho^{1/2}$ and $\rho^{-1/2}$ variation in displacements and tractions respectively, it is also possible to construct shape functions that achieve the same effect. But before these are given, it is useful to investigate in more detail the polynomial approximation that is most often used for interpolation of these parameters. If we consider an element adjacent to the crack tip (Figs 5.5a and 5.5b) where $\hat{\xi}$ denotes the local coordinate of the crack tip, then it is possible to take a Taylor series expansion about this point allowing the geometry, displacement and traction vectors to be expressed as

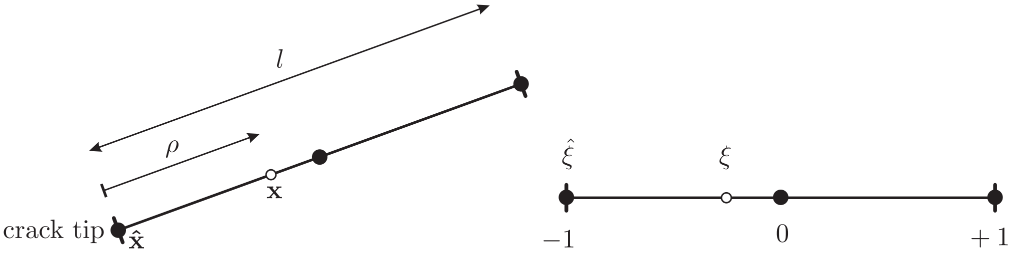

(a) Global coordinate system (b) Local coordinate system

Figure 5.5: Crack tip boundary element for Taylor series expansion

$$\mathbf{x} = \hat{\mathbf{x}} + \hat{\mathbf{x}}^{(1)}(\xi - \hat{\xi}) + \ldots + \frac{1}{(m-1)!}\hat{\mathbf{x}}^{(m-1)}(\xi - \hat{\xi})^{m-1} \tag{5.7a}$$

$$\mathbf{u} = \hat{\mathbf{u}} + \hat{\mathbf{u}}^{(1)}(\xi - \hat{\xi}) + \ldots + \frac{1}{(m-1)!}\hat{\mathbf{u}}^{(m-1)}(\xi - \hat{\xi})^{m-1} \tag{5.7b}$$

$$\mathbf{t} = \hat{\mathbf{t}} + \hat{\mathbf{t}}^{(1)}(\xi - \hat{\xi}) + \ldots + \frac{1}{(m-1)!}\hat{\mathbf{t}}^{(m-1)}(\xi - \hat{\xi})^{m-1} \tag{5.7c}$$

where the symbol ˆ refers to the value of a parameter at the crack tip and a number in brackets denotes the order of differentiation with respect to ξ. For the simple case of a flat element, $\mathbf{x}$ can be approximated as

$$\mathbf{x} = \hat{\mathbf{x}} + \hat{\mathbf{x}}^{(1)}(\xi - \hat{\xi}) \tag{5.8}$$

(since any higher order derivatives are simply zero). Using this relation and noting that the distance between the points $\hat{\mathbf{x}}$ and $\mathbf{x}$ is equal to the polar crack coordinate ρ, we can write

$$|\mathbf{x} - \hat{\mathbf{x}}| = \rho = |\hat{\mathbf{x}}^{(1)}|.|(\xi - \hat{\xi})| \tag{5.9}$$

It can be shown that $|\hat{\mathbf{x}}^{(1)}| = l/2$ (where l is the element length) for a flat element giving

$$\rho = \frac{l}{2}|(\xi - \hat{\xi})| \tag{5.10}$$

It is also necessary to determine the parameters $\hat{\mathbf{x}}$, $\hat{\mathbf{u}}$ and $\hat{\mathbf{t}}$ which can be expressed in terms of Lagrangian shape functions as

$$\hat{\mathbf{x}} = \sum_{a=1}^{M} N_a(\xi_0)\mathbf{x}^a, \qquad \hat{\mathbf{u}} = \sum_{a=1}^{M} N_a(\xi_0)\mathbf{u}^a, \qquad \hat{\mathbf{t}} = \sum_{a=1}^{M} N_a(\xi_0)\mathbf{t}^a \tag{5.11}$$

and, by differentiating these expressions, the derivatives $\hat{\mathbf{x}}^{(n)}$, $\hat{\mathbf{u}}^{(n)}$ and $\hat{\mathbf{t}}^{(n)}$ are given by

$$\hat{\mathbf{x}}^{(n)} = \sum_{a=1}^{M} \frac{d^{(n)}N_a(\hat{\xi})}{d\xi^{(n)}}\mathbf{x}^a, \qquad \hat{\mathbf{u}}^{(n)} = \sum_{a=1}^{M} \frac{d^{(n)}N_a(\hat{\xi})}{d\xi^{(n)}}\mathbf{u}^a, \qquad \hat{\mathbf{t}}^{(n)} = \sum_{a=1}^{M} \frac{d^{(n)}N_a(\hat{\xi})}{d\xi^{(n)}}\mathbf{t}^a \tag{5.12}$$

We are now in a position where the expressions for displacements and tractions given by Eqns (5.7b) and (5.7c) respectively can be reformulated by substituting in Eq. (5.10) for $\xi - \hat{\xi}$ and using the interpolations given by Eqns (5.11) and (5.12). In this example, we use the continuous quadratic shape functions given by (3.62) and let $\hat{\xi} = -1$ which gives the following expression for displacement interpolation

$$\mathbf{u} = \mathbf{u_1} + (-3\mathbf{u_1} + 4\mathbf{u}_2 - \mathbf{u_3})\left(\frac{\rho}{l}\right) + (2\mathbf{u_1} - 4\mathbf{u_2} + 2\mathbf{u_3})\left(\frac{\rho}{l}\right)^2 \tag{5.13}$$

$$= \mathbf{c_0} + \mathbf{c_1}\left(\frac{\rho}{l}\right) + \mathbf{c_2}(\frac{\rho}{l})^2 \tag{5.14}$$

From inspection this expression cannot correctly capture the required variation in crack tip displacements which we know from analytical solutions are of $\mathcal{O}(\rho^{1/2})$. However, by simply replacing ρ/l with $(\rho/l)^{1/2}$ in Eq. (5.13) the correct variation is achieved. Then, by using relation (5.10) and grouping all terms relating to $\mathbf{u_1}$, $\mathbf{u_2}$

and $\mathbf{u_3}$, it is possible to write the following shape functions, obtained by Yamada et al. [80], which can be used for crack tip displacement interpolation

$$N_1(\xi) = 1 - \frac{3}{\sqrt{2}}\sqrt{\xi + 1} + (\xi + 1) \tag{5.15a}$$

$$N_2(\xi) = 2\sqrt{2}\sqrt{\xi + 1} - 2(\xi + 1) \tag{5.15b}$$

$$N_3(\xi) = \frac{-1}{\sqrt{2}}\sqrt{\xi + 1} + (\xi + 1) \tag{5.15c}$$

A more general procedure was proposed by Akin [81] who derived singular displacement shape functions by considering a new function given by

$$F(\xi) = 1 - N_1(\xi) \tag{5.16}$$

where it is assumed that the crack tip lies at node 1. The shape functions can then be derived by using the following relations

$$N_1 = 1 - \sqrt{F(\xi)} \tag{5.17a}$$

$$N_\alpha = \frac{N_\alpha(\xi)}{\sqrt{F(\xi)}}, \qquad \alpha = 2, M \tag{5.17b}$$

which, for a quadratic 2D elements gives the following shape functions

$$N_1 = 1 - \sqrt{1 - \frac{\xi}{2}(\xi - 1)} \tag{5.18a}$$

$$N_2 = \frac{1 - \xi^2}{\sqrt{1 - \frac{\xi}{2}(\xi - 1)}} \tag{5.18b}$$

$$N_3 = \frac{\xi(1 + \xi)}{2\sqrt{1 - \frac{\xi}{2}(\xi - 1)}} \tag{5.18c}$$

Since tractions are represented independently of displacements in the BEM formulation, the application of the method to fracture problems also presents singular tractions on elements adjacent to the crack tip. Therefore, to achieve acceptable accuracies, it is also important to interpolate these singular tractions correctly. Tanaka and Itoh [82] presented special shape functions for interpolating tractions which are derived using a similar procedure to that given above and, for a continuous quadratic boundary element where $\hat{\xi} = 1$, they can be written as

$$N_1^{trac} = \frac{\xi(\xi - 1)}{2\sqrt{\xi + 1}} \tag{5.19a}$$

$$N_2^{trac} = \frac{(1 - \xi)^2}{\sqrt{\xi + 1}} \tag{5.19b}$$

$$N_3^{trac} = \frac{\xi(\xi + 1)}{\sqrt{2(\xi + 1)}} \tag{5.19c}$$

The use of singular crack tip shape functions such as these is subject to certain restrictions similar to those outlined in the previous section for quarter-point elements. For example, the expressions given here are only valid for elements adjacent to the crack tip while in reality, the singular zone may extend beyond this. Furthermore, the functions can only be applied to flat elements which restricts the type of fracture problem that can be modelled. However, as is true with QP elements, they present a simple and easy to implement procedure to improve the approximation of conventional quadratic elements when modelling cracks.

5.2 Singular boundary element methods

The previous section illustrated special crack tip elements and shape functions that could be applied to both the FEM and BEM, but now focus is given to the discussion of methods specific to the BEM which account for the crack tip singularity. Perhaps the most popular boundary element technique is that of the DBEM (which was outlined in Sec. 3.2.4), but the method does not explicitly account for the singular field experienced around the crack. Rather, the main feature of the method is the use of an independent BIE to overcome the problem of coincident crack surfaces. Two boundary element methods which explicitly account for the singular crack tip field are outlined presently: the singularity subtraction technique and the use of singular Hermitian elements.

5.2.1 Singularity subtraction technique

The singularity subtraction technique (SST) was first introduced by Symm [83] and later by Papamichel and Symm [84], but the first application of the method to fracture problems was by Aliabadi et al. [85] with later modifications of the method to incorporate the DBEM formulation [86]. The technique represents the displacements and tractions as the sum of a “regular” and “singular” field and, by performing a BEM analysis using the regular field (where the difficulties created by the singularity have been removed), crack problems can be solved with great accuracy. In addition, since the SIFs become unknowns in the formulation, they can be output directly, with no post-processing required. A brief outline of the method is given here along with a description of how the BEM matrices are constructed using the regularised displacement and traction fields.

If the state (u^R, t^R) represents the regular field which has the singularity removed and (u^s, t^s) represents the singular field of a crack tip, then, using the SST, displacements and tractions can be written as

$$u_i = (u_i - u^s) + u^s \qquad\qquad t_i = (t_i - t^s) + t^s \tag{5.20}$$

$$= u^R + u^s \qquad\qquad = t^R + t^s \tag{5.21}$$

Secs 2.2 and 2.3 demonstrated that the form of the singular field around a crack tip is already known, which allows, (assuming the body contains a single edge crack) u^s and t^s to be expressed in terms of the known functions and SIFs given by (2.36) and (2.37). But, by regularising the field in this way, the boundary conditions of the problem must also be modified in a similar fashion if the singular field is to be removed. Denoting the applied boundary conditions as $(\bar{u}_i, \bar{t}_i)$ and the values of the singular displacements and tractions on the boundary as $(\bar{u}_i^s, \bar{t}_i^s)$[1], the boundary conditions for the regular problem become

$$u_i^R = \bar{u}_i - \bar{u}_i^s \qquad\qquad t_i^R = \bar{t}_i - \bar{t}_i^s \tag{5.22}$$

Now, the regular field is used to construct the matrices which are used to perform a conventional BEM analysis (3.77) giving

$$[\mathbf{A}]\{\mathbf{x}^R\} = [\mathbf{B}]\{\mathbf{y}^R\} \tag{5.23}$$

Since $\mathbf{y}^R$ is a vector containing the regular field boundary conditions given by

---

[1] These will contain the SIFs as unknowns

Eqns (5.22), the above system of equations can be written as

$$[\mathbf{A}]\{\mathbf{x}^R\} = [\mathbf{B}]\Big(\{\mathbf{y}\} - [\mathbf{E}]\{\mathbf{z}\}\Big) \tag{5.24}$$

$$= \{\mathbf{f}\} - [\mathbf{C}]\{\mathbf{z}\} \tag{5.25}$$

where $\mathbf{y}$ is a vector of the real applied boundary conditions $(\bar{u}_i, \bar{t}_i)$, $\mathbf{E}$ is a matrix containing the singular field components evaluated at the boundary and $\mathbf{z}$ is a vector of the unknown SIFs. By taking all unknowns to the left hand side, the partitioned form the matrix equation can be expressed as

$$\begin{bmatrix} \mathbf{A} & \vdots & \mathbf{C} \end{bmatrix} \left\{ \begin{array}{c} \mathbf{x}^R \\ \cdots \\ \mathbf{z} \end{array} \right\} = \{\mathbf{f}\} \tag{5.26}$$

which is underdetermined and cannot be solved by conventional means. To provide additional relations, Portela et al. proposed a condition that forces the traction of the regular field at the crack tip to equal zero (ie. $t^R = 0$). Then, by considering an internal point p lying on the crack plane and approaching the crack tip, it is possible to use the TBIE (3.82) to formulate an independent equation that can be used to solve the additional unknowns. Denoting the traction at the point p as $\mathbf{t}_p^R$, this can be written in matrix form as

$$\mathbf{t}_p^R + [\mathbf{A}_p]\{\mathbf{x}^R\} = [\mathbf{B}_p]\Big(\{\mathbf{y}\} - [\mathbf{E}]\{\mathbf{z}\}\Big) \tag{5.27}$$

$$= \{\mathbf{f}_p\} - [\mathbf{C}_p]\{\mathbf{z}\} \tag{5.28}$$

The internal point can not lie directly on the crack tip due to unbounded terms, so instead a series of internal points which are then extrapolated to the crack tip are used. By introducing the above equation to (5.26), the partitioned system of equations becomes

$$\begin{bmatrix} \mathbf{A} & \vdots & \mathbf{C} \\ \cdots & & \cdots \\ \mathbf{A}_p & \vdots & \mathbf{C}_p \end{bmatrix} \left\{ \begin{array}{c} \mathbf{x}^R \\ \cdots \\ \mathbf{z} \end{array} \right\} = \left\{ \begin{array}{c} \mathbf{f} \\ \cdots \\ \mathbf{f}_p \end{array} \right\} \tag{5.29}$$

which is square and can now be solved.

One shortcoming of the method which was pointed out in [86] is the use of the first-order terms of the Williams expansion to represent the singular field which are only valid in a local region surrounding the crack tip. They cannot be used for regularisation over the global domain but instead, partitioning of the domain into near-tip fields and far-tip fields (see Fig. 5.6), is required. This introduces an additional computational burden due to the creation of a shared boundary and an increased implementation complexity with the need for equilibrium and compatibility equations in a multi-region analysis. The method does, however, demonstrate very high accuracies for SIF determination with few degrees of freedom and has the added advantage of requiring no post-processing to determine SIFs.

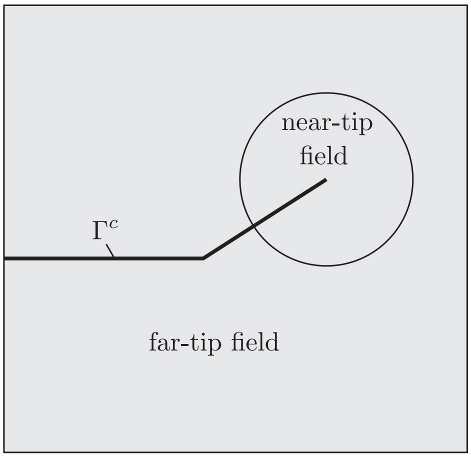

Figure 5.6: Domain partitioning for application of SST technique

5.2.2 Singular Hermitian elements with additional BIEs

Another boundary element technique which explicitly includes the singular crack tip field with Hermitian elements is that originally proposed by Watson [25] and then later extended to 3D problems [87]. Use is made of cubic Hermitian elements which not only demonstrate C_1 continuity, but, due to the requirement of fewer elements for a given accuracy, offer computational advantages over other element types. Fig. 5.7 illustrates a cubic Hermitian element which allows interpolation of geometry in the following manner:

$$x_i = \sum_{a=1}^{2} \left[M_a(\xi) x_i^a + N_a(\xi) m_i^a \right] \tag{5.30}$$

where x_i^a is a nodal coordinate and m_i^a is a tangential vector component at node a. The shape function expressions $M_a(\xi)$ and $N_a(\xi)$ are given by

$$M_1(\xi) = \frac{1}{4}(1+\xi)^2(2-\xi) \qquad N_1(\xi) = -\frac{1}{4}(1+\xi)^2(1-\xi) \tag{5.31}$$

$$M_2(\xi) = \frac{1}{4}(1-\xi)^2(2+\xi) \qquad N_2(\xi) = \frac{1}{4}(1-\xi)^2(1+\xi) \tag{5.32}$$

For the formulation of singular crack tip elements, the interpolation of displacements and tractions is modified to include the singular field by using the following expressions

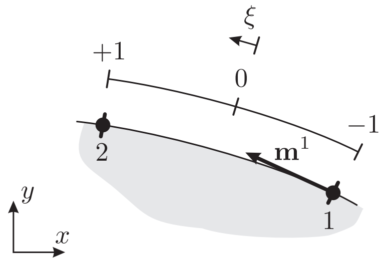

Figure 5.7: Cubic Hermitian boundary element

$$u_i(\xi) = \sum_{a=1}^{2}\left[M_a(\xi)u_i^a + N_a(\xi)w_i^a + \sum_{k=1}^{4}\Psi_{aik}^u\phi_k\right] \tag{5.33}$$

$$t_i(\xi) = \sum_{a=1}^{2}\left[M_a(\xi)t_i^a + N_a(\xi)s_i^a + \sum_{k=1}^{4}\Psi_{aik}^t\phi_k\right] \tag{5.34}$$

where w_i^a and s_i^a are nodal derivative components of displacement and tractions respectively, ϕ_k are the first and second order coefficients of the Williams expansion and the functions Ψ_{aik}^u and Ψ_{aik}^t are constructed in such a way that they exhibit the desired crack tip behaviour but allow inter-element continuity. For example, if ψ_{ik}^u corresponds to the kth term of the Williams expansion for displacements (Eqns (2.26)) and the crack is assumed to lie at the position $\xi = -1$ on the element, then the function Ψ_{aik}^u is given by

$$\Psi_{aik}^u = \psi_{aik}^u(\xi) - \left\{M_2(\xi)\psi_{2ik}^u + N_2(\xi)\frac{\mathrm{d}\psi_{2ik}^u}{\mathrm{d}\xi}\right\} \tag{5.35}$$

By expressing the displacement and tractions using Eqns (5.33) and (5.34), it can be seen that on singular elements there will be eight unknowns whereas the straightforward application of the DBIE (Eq. (3.52)) only provides two independent relations. As a solution to this, Watson derived three additional BIEs by differentiating with respect to the source point and multiplying the kernels by source point normals and tangents (similar to the formulation of the TBIE). The singular integrals seen in each of these can not be evaluated in a CPV or Hadamard finite part sense and therefore the use of several trial displacement fields, similar to the rigid-body motion technique described previously, is needed. Unfortunately, the implementation of the method becomes very complex, and it is even noted in [25] that one of the additional BIEs would be very complicated to calculate analytically but instead is obtained through numerical differentiation. The application of the method to 3D problems introduces an even greater number of unknowns and in this case, rather than deriving additional BIEs, additional collocation points are used to provide the extra relations. This is an important feature since a similar technique is used in the present work to solve for the additional unknowns created enrichment.

5.3 Singular finite elements

5.3.1 Fractal elements

The fractal finite element method (FFEM), pioneered by Leung and Su [88], is a method that technically does not fall under the category of either singular or enriched elements since it relies on the use of multiple "self-similar" elements that decrease in size towards the crack tip. By incorporating several layers of these self-similar elements and relating the degrees of freedom of each to a much smaller number of global degrees of freedom, the resulting system of equations is reduced significantly. Fig. 5.8a illustrates the use of fractal elements to model an edge crack (the crack surface is denoted by Γ_c) where the domain is separated into a "regular" and "singular" region. A detailed view of the singular region is shown in Fig. 5.8b. The formulation is based on the fact that displacements around a crack tip are known to vary according to the Williams expansions of (2.26a) and (2.26b) where the unknowns a_n are dependent on the problem being solved. By expressing the displacements in the singular region as

$$\{\mathbf{d}\} = [T]\{\mathbf{a}\} \tag{5.36}$$

where **d** and **a** are vectors containing the singular region displacements and Williams expansion coefficients respectively and $[T]$ is a rectangular transformation matrix, a large number of DOF can be reduced to a much smaller number. Then, by using the transformation given by (5.36) along with a geometric series representing the number of self-similar layers, the global stiffness matrix can be formed with a significant reduction in size.

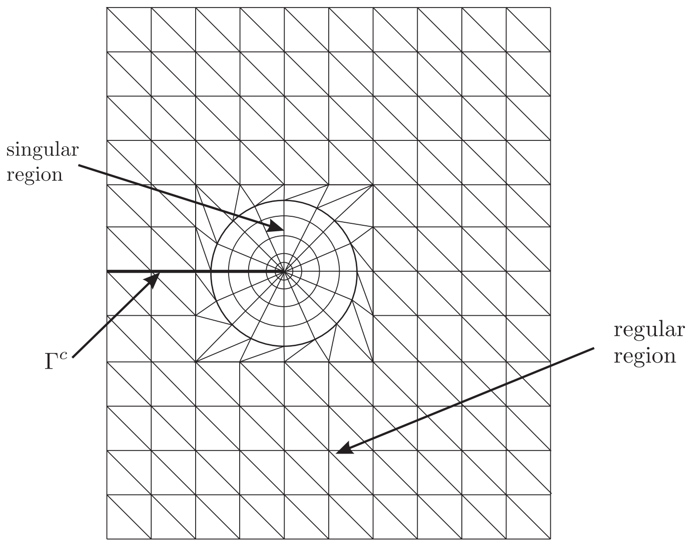

(a) Fractal finite element mesh for edge crack

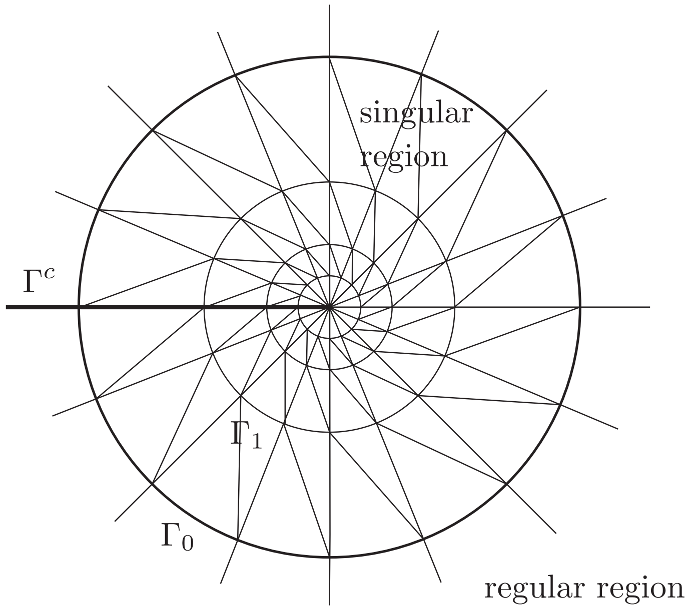

(b) Singular region surrounding crack tip

Figure 5.8: Fractal finite element meshes

5.3.2 Hybrid elements

Another successful technique that has been applied in the FEM is the use of "hybrid" elements that incorporate the crack-tip singular behaviour through a variational formulation. A FEM mesh is constructed by using a hybrid element at the crack tip while elements using conventional interpolation are used elsewhere (see Fig. 5.9). The work can be originally attributed to Tong et al. [89] and has been more recently been extended by Karihaloo and Xiao to incorporate higher order terms of the Williams expansion [16] and also to formulate a coupled method with XFEM [90]. The method is based on the Modified Hellinger-Reissner principle (see [91] for an excellent overview of variational methods applied to mechanics) which, after suitable manipulation, allows the element variational functional to be expressed as

$$\Pi_m^e = \int_{S_\sigma^e} \left(\frac{1}{2} t_i - \bar{t}_i \right) u_i ds - \int_{\partial \tilde{A}^e} t_i \left(\frac{1}{2} u_i - \bar{u}_i \right) ds \tag{5.37}$$

where u_i and t_i represent unknown displacements and tractions while $\bar{u}_i$ and $\bar{t}_i$ represent known displacements and tractions over parts of the boundary S_σ^e and $\partial \tilde{A}^e$ respectively. Using truncated expressions of (2.26) and (2.25) to substitute for u_i and t_i (while noting $t_i = \sigma_{ij} n_j$), the unknowns then become the coefficients of the Williams expansion (a_n, b_n). The element stiffness matrix and nodal force vector are determined by setting (5.37) equal to zero (since this is the stationary condition). Interestingly, in the calculation of the element stiffness matrix and the nodal force vector, it is found that all numerical integrations are taken along the boundary with no domain integration required. In fact, as noted by Fawkes et al. [92], it is found that the hybrid element formulation is a type of boundary integral equation identical to that derived by Brebbia [93] using a Galerkin procedure and goes on to comment that an improvement in the method would be to cast the problem entirely as a boundary element method.

5.3.3 Benzley singular elements

The idea of enriching elements surrounding the crack tip has been studied extensively where various approaches have been taken. Benzley [94] took the approach of expressing displacements within enriched elements in the following manner

$$u_j = \sum_{a=1}^{M} N_a u_j^a + K_{\mathrm{I}} \left(Q_{\mathrm{I}j} - \sum_{a=1}^{M} N_a \bar{Q}_{\mathrm{I}ja} \right) + K_{\mathrm{II}} \left(Q_{\mathrm{II}j} - \sum_{a=1}^{M} N_a \bar{Q}_{\mathrm{II}ja} \right) \tag{5.38}$$

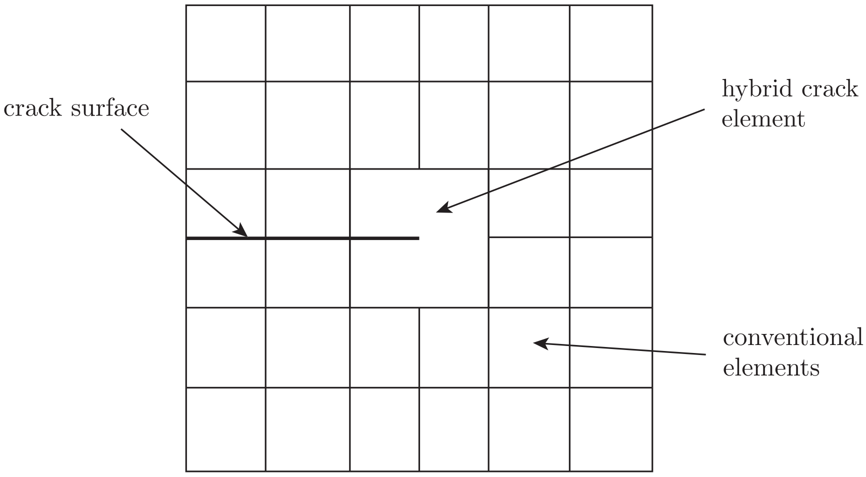

Figure 5.9: Finite element mesh for an edge crack modelled with a "hybrid" element

where the functions Q_{lj} are given by the near-field terms of the Williams expansion

$$Q_{\mathrm{I}1} = \frac{1}{2\mu}\sqrt{\frac{\rho}{2\pi}}\cos(\theta/2)\left[\kappa - 1 + 2\sin^2(\theta/2)\right] \tag{5.39a}$$

$$Q_{\mathrm{II}1} = \frac{1}{2\mu}\sqrt{\frac{\rho}{2\pi}}\sin(\theta/2)\left[\kappa + 1 + 2\cos^2(\theta/2)\right] \tag{5.39b}$$

$$Q_{\mathrm{I}2} = \frac{1}{2\mu}\sqrt{\frac{\rho}{2\pi}}\sin(\theta/2)\left[\kappa + 1 - 2\cos^2(\theta/2)\right] \tag{5.39c}$$

$$Q_{\mathrm{II}2} = -\frac{1}{2\mu}\sqrt{\frac{\rho}{2\pi}}\cos(\theta/2)\left[\kappa - 1 - 2\sin^2(\theta/2)\right] \tag{5.39d}$$

and the term $\bar{Q}_{lja}$ is the value of Q_{lj} evaluated at node a. By formulating the elements in this way the term u_j^a represents real displacements while the SIFs are direct outputs of the system. In the implementation of the method, only elements adjacent to the crack tip were enriched while those that bordered the enriched elements and conventional elements were formulated to include a bilinear smoothing function. This ensured displacement compatibility between adjoining element nodes. This is written as

$$u_j = \sum_{a=1}^{M} N_a u_j^a + R(\xi,\eta)\left\{K_{\mathrm{I}}\left(Q_{\mathrm{I}j} - \sum_{a=1}^{M} N_a \bar{Q}_{\mathrm{I}ja}\right) + K_{\mathrm{II}}\left(Q_{\mathrm{II}j} - \sum_{a=1}^{M} N_a \bar{Q}_{\mathrm{II}ja}\right)\right\} \tag{5.40}$$

where the function $R(\xi,\eta)$ is such that it equals 1 on boundaries with enriched elements and 0 on boundaries of unenriched elements.

5.4 Enrichment through the partition of unity method

The concept of Partition of Unity can be attributed to work by Babuška and Melenk [95] with the original idea now implemented in several successful numerical methods such as the Generalised Finite Element Method [96], [97] and the eXtended Finite Element Method [98]. Without delving into the mathematical details of the derivation, the method can be explained simply by considering a function that forms a partition of unity. That is, if a set of functions $f_a(\mathbf{x})$ are defined on a domain Ω^{PU} and the functions satisfy the following relation

$$\sum_a f_a(\mathbf{x}) = 1, \quad \forall \mathbf{x} \in \Omega^{PU} \tag{5.41}$$

then they are said to form a partition of unity. This means that at any point within the domain the sum of the functions will always equal one. Using this relation, the following can also be written

$$\sum_a f_a(\mathbf{x})\psi(\mathbf{x}) = \psi(\mathbf{x}) \tag{5.42}$$

where $\psi(\mathbf{x})$ is an arbitrary function. This is an extremely powerful relation and it's importance cannot be overemphasized in the present work. It states that if we know a function that forms a partition of unity $f_a(\mathbf{x})$ and another function $\psi(\mathbf{x})$ which we know from *a priori* knowledge captures the field we are trying to recover, then we are able to include the function $\psi(\mathbf{x})$ within the approximation and more accurate results are expected. In many cases the field that is being approximated does not present difficulties for conventional interpolation functions, but in the case of problems containing singularities (such as a crack or inclusion), the approximation performs poorly. For example, the interpolation that is most often used in the FEM and BEM for displacements takes the form

$$u_j(\mathbf{x}) = \sum_{a \in S} N_a(\mathbf{x}) u_j^a \tag{5.43}$$

where S is the set of nodes of the mesh, $N_a(\mathbf{x})$ is the global shape function associated with node a and u_j^a is a nodal displacement. The shape functions $N_a(\mathbf{x})$, which are most often represented by polynomial functions, form a partition of unity and have a large influence on the displacement approximation. For many cases the use of polynomial functions is sufficient, but in the case of a crack where a $\rho^{1/2}$ singularity in displacements is seen, the approximation is often poor. The PUM provides a solution to this by taking into account relation (5.42) and making the following *enriched* approximation

$$u_j(\mathbf{x}) = \sum_{a \in S} N_a(\mathbf{x}) u_j^a + \sum_{b \in P.U.} f_b(\mathbf{x}) \psi(\mathbf{x}) A_j^b \tag{5.44}$$

where $P.U.$ refers to the set of functions that form the partition of unity, $f_b(\mathbf{x})$ is the bth function of the partition of unity, $\psi(\mathbf{x})$ is the appropriate enrichment function and A_j^b is the coefficient (associated with the function $f_b(\mathbf{x})$) that remains unknown. If more than one enrichment function is used for enrichment then the relation becomes

$$u_j(\mathbf{x}) = \sum_{a \in S} N_a(\mathbf{x}) u_j^a + \sum_{b \in P.U.^l} f_b(\mathbf{x}) \sum_l \psi_l(\mathbf{x}) A_{jl}^b \tag{5.45}$$

In many cases the function $f_b(\mathbf{x})$ is replaced by the conventional shape functions and enrichment can now be applied over a set of enriched nodes denoted by S^{enr}. This is written as

$$u_j(\mathbf{x}) = \sum_{a \in S} N_a(\mathbf{x}) u_j^a + \sum_{b \in S^{enr}} N_b(\mathbf{x}) \sum_l \psi_l(\mathbf{x}) A_{jl}^b \tag{5.46}$$

This expression illustrates an example of *extrinsic* enrichment where additional degrees of freedom are introduced for each enrichment function at each enriched node. An additional computational cost is associated with each of these, and it soon becomes clear that as the number of enriched nodes is increased, the size of the system will increase at a faster rate than if conventional interpolation is used. However, the use of enrichment allows much fewer elements to be used and usually, a local enrichment strategy enrichment is employed where only those nodes that fall within a certain region of the singularity are enriched; any nodes that do not lie in this region are approximated in the normal way and the number of additional DOF is reduced to a minimum. This form of local enrichment has been applied successfully to the FEM to allow accurate solutions of cracked problems to be found and is commonly referred to as the eXtended Finite Element Method (XFEM).

5.4.1 The eXtended Finite Element Method (XFEM)

The original implementation of XFEM can be attributed to the work by Belytschko and Black [99] who used the PUM to enrich nodes surrounding the crack with asymptotic functions that are capable of capturing the singular field around a crack tip. In most cases (except for extremely curved cracks) remeshing was not required for incremental crack propagation steps representing a significant improvement over the standard application of the FEM to fracture problems. But perhaps the most well-known paper related to the development of XFEM is that by Moës et al. [98] which outlined a more general procedure that not only included the asymptotic crack-tip functions, but made use of the Heaviside step function to account for the strong discontinuity seen across the crack faces. In this way, both the singular strains seen at the crack-tip field and the strong discontinuity in strains across the crack faces are accounted for and represented completely independently of the mesh. There are two clear advantages of using this strategy:

- Since the crack is represented independently of the mesh then, with minimal remeshing required for each crack propagation step, significant computational savings are made.
- As mentioned at the beginning of this chapter, the rate of convergence of a problem containing a crack is governed by the strength of the singularity. Therefore, by including functions which can capture this singular field, we expect to obtain both smaller errors and higher convergence rates.

The XFEM conventionally uses an extrinsic form of enrichment where additional degrees of freedom are introduced to each enriched node. Including the two forms of enrichment - Heaviside step functions to account for the discontinuity across crack faces and asymptotic functions describing the crack tip behaviour - displacements can be represented as

$$u_j(\mathbf{x}) = \sum_{a \in S} N_a(\mathbf{x}) u_j^a + \sum_{b \in S^H} N_b(\mathbf{x}) H(\mathbf{x}) B_j^b + \sum_{d \in S^{cr}} N_d(\mathbf{x}) \sum_l \psi_l(\mathbf{x}) D_{jl}^d \tag{5.47}$$

where B_j^b and D_{jl}^d represent additional enrichment coefficients corresponding to the Heaviside and crack-tip functions respectively. S is the set of nodes of the mesh while the sets S^H and S^{cr} represent the nodes that are enriched by the Heaviside and asymptotic functions respectively. To illustrate this clearly, Fig. 5.11 shows a mesh in which a crack spans several elements and does not conform to the mesh.

Any nodes whose support (ie. those elements which are connected to that particular node) are cut by the crack but do not contain the crack are denoted by the set S^H, and it is these nodes that are enriched with the Heaviside step function (circled nodes in Fig. 5.11). Any nodes whose support contains the crack tip itself are denoted by the set S^{cr} and are enriched by the crack-tip basis given by (5.48) (square nodes in Fig. 5.11). The Heaviside function $H(\mathbf{x})$ is defined by considering a point x within the domain (see Fig. 5.10) and it's nearest point to the crack surface x^*. By using a curvilinear coordinate s to define a normal and tangent vector e_n and e_s, the Heaviside function is defined as $+1$ when the sign of the scalar product $(x - x^*).e^n$ is positive and -1 otherwise. $\psi_l(\mathbf{x})$ is the set of crack-tip basis functions obtained from the first-order terms of the Williams expansions given by

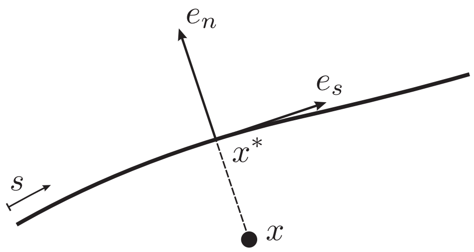

Figure 5.10: Coordinate system used for Heaviside function definition

$$\psi_l(\rho,\theta) = \left\{\sqrt{\rho}\cos\left(\frac{\theta}{2}\right), \sqrt{\rho}\sin\left(\frac{\theta}{2}\right), \sqrt{\rho}\sin\left(\frac{\theta}{2}\right)\sin(\theta), \sqrt{\rho}\cos\left(\frac{\theta}{2}\right)\sin(\theta)\right\} \tag{5.48}$$

To illustrate the effects of each type of enrichment we first consider an element whose nodes are enriched with the Heaviside function such as that in Fig. 5.12a. Then, by plotting the function $N_1 H(\mathbf{x})$ (where N_1 is the linear shape function $1/4(\xi - 1)(\eta - 1)$), the ability of the enriched approximation to model a discontinuity is evident. In a similar manner, an element containing the crack tip and whose nodes are enriched by the crack-tip basis functions is considered (see Fig. 5.13a). By taking, for example, the basis function $\sqrt{\rho}\sin\theta/2$ and the shape function N_1, the resulting product can be plotted as shown in Fig. 5.13b. In this case, the crack-tip basis function is discontinuous across the crack face allowing, in combination with the other enrichment functions in (5.48), both the strong discontinuity and the correct variation in crack-tip displacements to be captured.

One consequence of expressing the displacement approximation in this manner is the careful consideration that must be given to the integration of enriched elements. Normally Gaussian quadrature (which is capable of evaluating the integral of a polynomial function exactly) is used for element integration, but the use of asymptotic

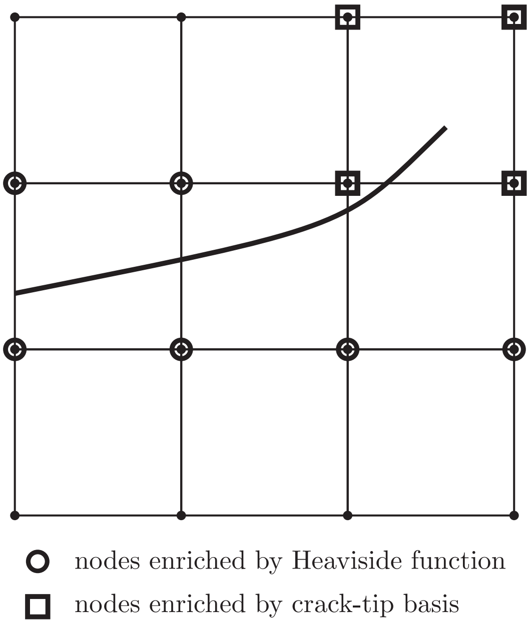

Figure 5.11: Example of XFEM mesh with enriched nodes

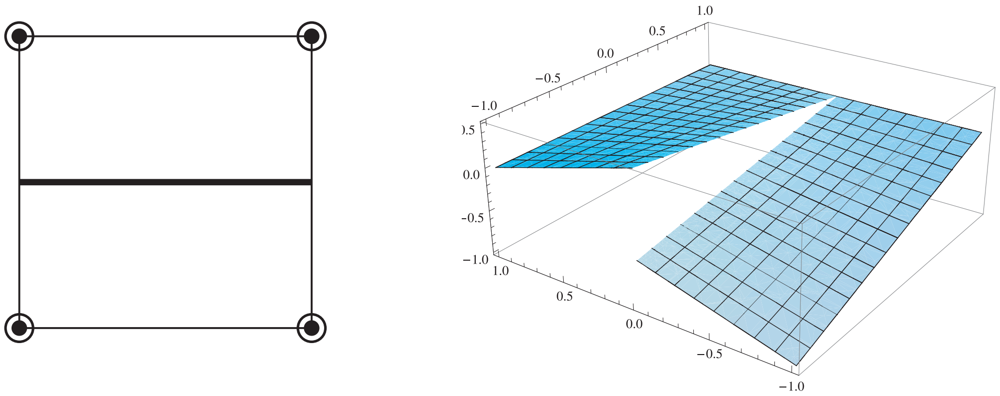

(a) Element with nodes enriched with Heaviside step function

(b) Plot of $N_1 H(\mathbf{x})$

Figure 5.12: XFEM Heaviside enrichment

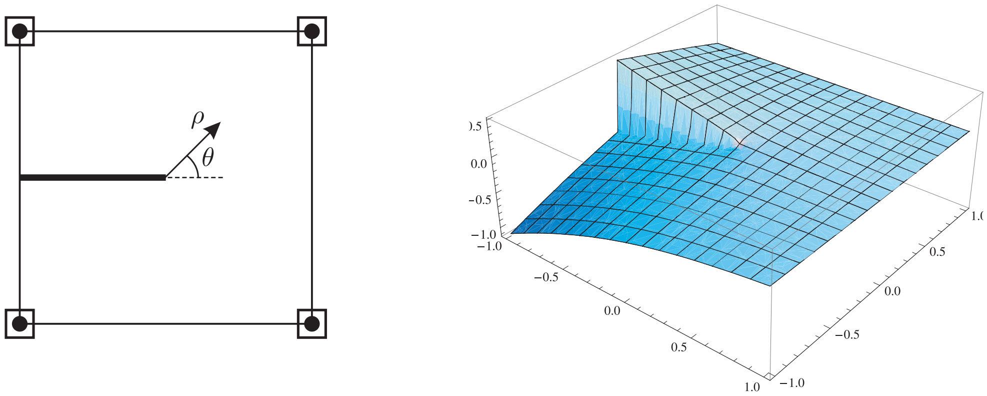

(a) Element with nodes enriched with crack-tip basis

(b) Plot of $N_1\sqrt{\rho}\sin(\theta/2)$

Figure 5.13: XFEM crack-tip enrichment

functions and the Heaviside function presents difficulties for conventional numerical integration techniques. In the case of the asymptotic crack-tip enrichment functions this problem is created by the singular gradient seen at the crack tip (due to the $\rho^{1/2}$ dependency) while in the case of the Heaviside function, the integrand becomes discontinuous and conventional numerical quadrature routines cannot be applied. For the asymptotic crack tip functions one solution, of course, is to use high-order quadrature to reduce the error in integration[2], but this is inefficient and other methods are sought. Dolbow [100] proposed two techniques to deal with the case when the crack cuts an element and is enriched with the Heaviside function (eg. Fig. 5.12). The first involves splitting the element into sub-triangles which conform to the crack while the second applies a regular grid of sub-quads, much like the integration technique outlined in Sec. 4.2.1. For the evaluation of the singular integrals seen in an element which contains a crack tip (Fig. 5.13a) element subdivision is often used, but a more efficient technique outlined by Bechet et al. [101] performs multiple transformations to arrive at a non-singular integral over a regular quad. They showed that by using this technique, higher convergence rates are to be expected.

One final feature of XFEM which should be mentioned is the region over which enrichment should be applied. Referring back to Fig. 5.11 it can be seen that the crack-tip basis enrichment is applied only to the element containing the crack tip. The flexibility of XFEM allows the crack-tip enrichment to be applied over an

---

[2] For the function $\sqrt{\xi + 1}$ evaluated over the interval $[-1, 1]$ at least 5 Gauss points must be used for 0.1% accuracy

arbitrary region where two main types, as outlined in [101], can be implemented:

- **Topological enrichment**. Only those elements which touch the crack tip are enriched (Fig. 5.14). The enrichment zone therefore depends on the mesh density.
- **Geometrical enrichment**. A fixed radius is specified within which all elements are enriched (Fig. 5.15). As the mesh is refined the number of enriched elements will increase.

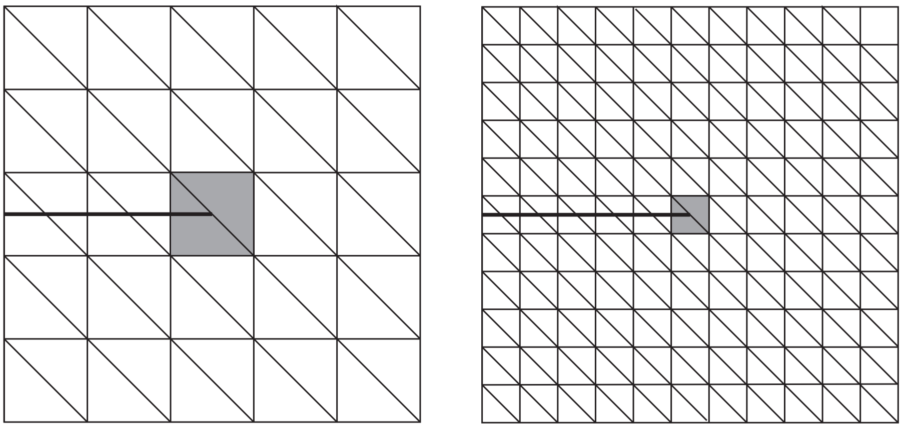
(a) Coarse mesh (b) Fine mesh

Figure 5.14: Topological enrichment strategy

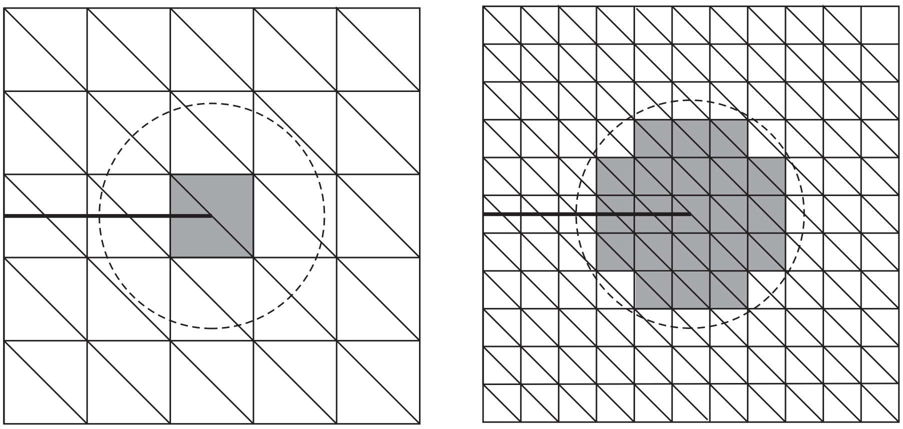
(a) Coarse mesh (b) Fine mesh

Figure 5.15: Geometrical enrichment strategy

5.4.2 Enrichment of meshless methods

Meshless methods, which offer distinct advantages for the analysis of crack problems due to absence of a mesh, can also be enriched through the PUM in a similar manner to XFEM. Without enrichment, high densities of nodes are required to capture the singular field around the crack tip (eg. Fig. 2.11) and in some cases this may lead to ill-conditioned matrices. It is therefore much more efficient to include crack-tip enrichment functions and, as shown by Fleming et al. [102], it may be *necessary* to use enrichment if large errors are to be avoided. Two techniques, termed extrinsic and intrinsic enrichment, can be used to apply the asymptotic crack-tip functions where each differs in the way shape functions are constructed.

Extrinsic enrichment can be used with an interpolation scheme similar to that of Benzley (Sec. 5.3.3) which allows the direct output of SIFs if Eq. (5.38) is used. Another form of extrinsic enrichment uses the interpolation given by (5.46) which introduces additional unknowns that do not take on any meaningful values by themselves but, when combined with the terms u_j^a, return enriched displacements. Contrary to this, intrinsic enrichment prevents the need to introduce additional unknowns but instead includes the branch functions (as given by (5.48)) within the basis that is used to construct the MLS shape functions. For example, combining a linear basis with the enrichment functions, the new basis vector can be written as

$$\mathbf{p}^{\mathrm{T}}(\mathbf{x}) = \left[1, x, y, \sqrt{\rho}\cos\left(\frac{\theta}{2}\right), \sqrt{\rho}\sin\left(\frac{\theta}{2}\right) \sqrt{\rho}\sin\left(\frac{\theta}{2}\right)\sin(\theta), \sqrt{\rho}\cos\left(\frac{\theta}{2}\right)\sin(\theta)\right] \tag{5.49}$$

which can be used to construct the shape functions given by (2.59). In some cases, the introduction of additional enrichment functions within the basis causes problems to allow the inversion of the moment matrix (denoted by $\mathbf{A}^{-1}(\mathbf{x})$ in Eq. (2.59)) where special preconditioning techniques such as that illustrated in [103] can be used to alleviate ill-conditioning.

5.5 BEM enrichment

In Sec. 5.2 two BEM techniques which allow fracture problems to be modelled accurately were described but both exhibit certain drawbacks in their implementation. The DBEM (Sec. 3.2.4) offers a much more simple and general approach, but, if the implementation of [24] is used, then no explicit account of the crack tip singularity is made. This thesis proposes a new method where enrichment through the PUM is applied to the BEM (and DBEM) in much the same manner as that for XFEM and enriched meshless methods with considerable gains in accuracy.

Chapter 6

Enriched BEM through PUM (local formulation)

This chapter is focused on the discussion of a new method which applies enrichment to the BEM (and DBEM) for accurate fracture modelling. By using functions which are known to capture the singular field around a crack tip and incorporating these within the formulation through the PUM, enrichment is applied in a manner very similar to that of the XFEM. Obviously due to the differences between a domain and a boundary discretisation method the implementation shown here differs, but the underlying principle is the same. The discussion is split into three sections: first, the formulation of the method is given with the enriched boundary integral equations outlined; next, the implementation of the method is described and finally, verification and testing of the method is made by comparing against results of standard fracture specimens.

6.1 Formulation

The objective of any enrichment strategy is to include, via the approximation, functions that capture the required variation that would present difficulties for conventional polynomial interpolation functions. Various enrichment techniques were outlined in chapter 5, but the technique which presents particularly attractive features is that of the PUM since it allows arbitrary functions to be included within the approximation in a simple manner. In the case of a crack, the most sensible choice of functions correspond to the first-order terms of the exact crack tip solution which is the methodology used in XFEM. The same functions are used here to give an identical expression for enriched displacements, and these are then applied to the

DBIE and TBIE to arrive at an enriched BEM/DBEM through the PUM.

6.1.1 Enriched displacement approximation

The PUM states that if we have a set of functions that form a partition of unity over a domain, then it is possible to include another function, which we know from *a priori* knowledge captures the field we are trying to recover, within the approximation. The advantage of the method, is that whereas conventional polynomial functions will encounter difficulties trying to approximate a singular field (for example), the PUM can capture the field with much higher accuracy for fewer degrees of freedom. In the conventional BEM formulation, displacements are approximated by Eq. (3.64a) where the shape functions usually take the form of quadratic polynomial functions. We note that these functions form a partition of unity over the local sub-domain of a boundary element and therefore, it is possible to express enriched displacements over an element n as

$$u_j^n(\xi) = \sum_{a=1}^{M} N_a(\xi) u_j^{na} + \sum_{a=1}^{M} \sum_{l=1}^{L} N_a(\xi) \psi_l^u(\xi) A_{jl}^{na} \tag{6.1}$$

where M is the number of nodes on the element ($M = 3$ for quadratic elements), $\psi_l^u(\xi)$ is the set of L basis functions derived from the first-order terms of the Williams expansion and given by (5.48) and A_{jl}^{na} represents an enrichment coefficient. It should be noted that u_j^{na} no longer represents a nodal displacement but is instead a nodal coefficient that, when combined with the second term of (6.1), returns real displacements. The power of this expression is the ability to capture the crack-tip singular field using relatively coarse meshes that would otherwise incur large errors with the use of conventional polynomial shape functions. As with any numerical method, any gain in accuracy is accompanied by a corresponding computational cost, and in this case the compromise is made with the requirement to compute additional unknown terms represented by A_{jl}^{na}. However, as will be shown shortly, by employing an enrichment strategy where only those elements affected by the singularity are enriched, the number of additional DOF required is kept to a minimum and is very small compared with the total DOF.

It is now instructive to consider two crack examples that may be encountered in a BEM fracture analysis: that of a flat crack and a curved crack. Using discontinuous quadratic boundary elements, a flat crack can be represented by Fig. 6.1a while similarly, a curved crack can be represented by Fig. 6.1b. In the case of a flat crack

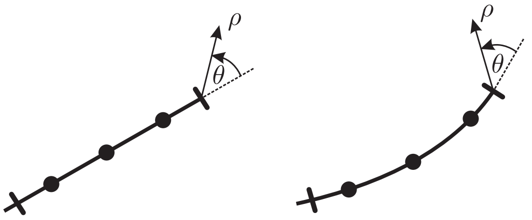

(a) Flat crack (b) Curved crack

Figure 6.1: Local crack tip coordinate system for different crack geometries

the polar crack angle θ remains constant on both the upper and lower crack surfaces ($\theta = \pm\pi$) and only the polar distance ρ varies as we move along the element. The consequence of this is that, referring back to the crack tip basis functions given by Eq. (5.48), three of the terms equate to zero and the enrichment basis reduces to

$$\psi_l^u(\xi) = \{\sqrt{\rho}\} \tag{6.2}$$

where $L = 1$. With this reduced enrichment basis each enriched node only introduces two additional DOF (one for each direction). Contrary to this, the curved crack shows a variation in the crack angle θ over the element allowing us to use all four enrichment functions ($L = 4$) and eight additional DOF for each enriched node. Therefore, since an additional equation is required for each introduced DOF, it is important to note this dependency on geometry to allow a square, solvable system to be formed.

All the work in this thesis assumes traction free cracks and, since the DBEM is used to model fracture problems, singular tractions are not seen on any boundary elements. As a result, it is not necessary to provide enrichment of tractions, but it would be entirely possible to formulate an expression similar to (6.1) using a set of basis functions derived from the stresses given by the Williams expansion and the relation $t_i = \sigma_{ij} n_j$.

6.1.2 Enriched DBIE and TBIE

Now that the enriched approximation for displacements has been described, the process of including this relation within both the DBIE and TBIE to allow the formation of an enriched BEM is outlined. Dealing with the case of the DBIE first, Eq. (6.1) is substituted into the discretised form of the boundary integral equation

(3.68) to give

$$C_{ij}(\mathbf{x}')\left(\sum_{a=1}^{M} N_a(\xi')u_j^{\bar{n}a} + \sum_{a=1}^{M}\sum_{l=1}^{L} N_a(\xi')\psi_l^u(\xi')A_{jl}^{\bar{n}a}\right)$$
$$+\sum_{n=1}^{N_e}\sum_{a=1}^{M} P_{ij}^{na}u_j^{na} + \sum_{n=1}^{N_e}\sum_{a=1}^{M}\sum_{l=1}^{L} \tilde{P}_{ijl}^{na}A_{jl}^{na} = \sum_{n=1}^{N_e}\sum_{a=1}^{M} Q_{ij}^{na}t_j^{na} \tag{6.3}$$

ξ' is the local coordinate of the source point located on element $\bar{n}$, the components P_{ij}^{na} and Q_{ij}^{na} are still given by Eqns (3.69) and the new enrichment term $\tilde{P}_{ijl}^{na}$ is given by

$$\tilde{P}_{ijl}^{na} = \int_{-1}^{1} T_{ij}(\mathbf{x}', \mathbf{x}(\xi))N_a(\xi)\psi_l^u(\xi)J^n(\xi)\,\mathrm{d}\xi \tag{6.4}$$

This is evaluated only for enriched elements; for all other unenriched elements this term is neglected.

Before we proceed to enrichment of the TBIE, a few important points need to be made about this equation. In the conventional application of the BEM, collocation takes place at nodal points giving jump terms that only apply to the source point node. Equation (6.3) is more general than this since it allows collocation points to lie at *any* local coordinate ξ' (not necessarily at nodal points) and does so by distributing the jump term using the shape functions N_a and the basis functions ψ_l^u. To illustrate this difference we first consider a discontinuous element (Fig. 3.11) where the source point is located at the first node ($\xi' = -2/3$). In this case the only shape function which is non-zero is N_1 and therefore the jump term only contributes to that node. If the collocation point is on a flat surface then the jump terms for the singular element are given by the bold values in Table 6.1 which clearly shows that only the first node is affected. If collocation now takes places at a non-nodal location - the coordinate $\xi' = -0.8$ is chosen arbitrarily here - and the enriched displacement interpolation is used, then the jump term must be distributed across all the nodes of the element. Inspecting Fig. 3.11 shows that at the point $\xi = -0.8$ all the shape functions are non-zero and the corresponding jump terms for $u_j^{\bar{n}a}$ are given by the second column in Table 6.2. Next, by letting $\psi^u = \rho^{1/2}$ and multiplying this enrichment function by each of the shape functions (see Fig. 6.2), the value of each can be determined at $\xi = -0.8$ and used to distribute the jump term giving the values shown in the fourth column of Table 6.2. The same technique has been applied successfully to wave problems by Perrey-Debain et al. [104] but it is believed that this is the first application of the method to allow enrichment of elastostatic problems.

Table 6.1: Jump term for nodal collocation with conventional displacement interpolation ($\xi' = -2/3$)

a	$N_a(\xi')$[c]	$C_{ij}N_a(\xi')$[d]
1	1.0	**0.5**
2	0.0	**0.0**
3	0.0	**0.0**

---

[c] Using Eqns (3.63)
[d] Assuming $C_{ij} = 0.5$

Table 6.2: Jump term for general collocation with enriched displacement interpolation ($\xi' = -0.8, \psi^u = \rho^{1/2}$)

a	$N_a(\xi')$	$C_{ij}N_a(\xi')$	$N_a(\xi')\psi^u(\xi')$	$C_{ij}N_a(\xi')\psi^u(\xi')$
1	1.32	**0.66**	1.77	**0.89**
2	-0.44	**-0.22**	-0.59	**-0.30**
3	0.12	**0.06**	0.16	**0.08**

The reader may wonder why such effort has been made to allow for collocation at any general point on an element when the formulation becomes much simpler when nodal collocation is used. To explain this, we refer back to Eq. (6.1) which shows that by including enrichment additional coefficients A_{jl}^{na} are introduced. The strategy which is used to solve for these additional unknowns, which is the same as that used in [104], is to collocate at additional points between nodes on the boundary. This should be a satisfactory explanation for now, with further details on the application of the technique given in the implementation section.

The previous discussion has focused on the enrichment of the DBIE, but to allow the use of the DBEM to allow general fracture problems to be modelled, enrichment must also be applied to the TBIE. This is achieved in exactly the same manner by substituting Eq. (6.1) into the discretised form of the BIE (3.83)

$$\frac{1}{2}\left(\sum_{a=1}^{M} N_a(\xi')t_j^{\bar{n}a}\right) + n_i(\mathbf{x}')\sum_{n=1}^{N_e}\sum_{a=1}^{M} E_{kij}^{na}u_k^{na}$$
$$+ n_i(\mathbf{x}')\sum_{n=1}^{N_e}\sum_{a=1}^{M}\sum_{l=1}^{4}\tilde{E}_{kijl}^{na}A_{kl}^{na} = n_i(\mathbf{x}')\sum_{n=1}^{N_e}\sum_{a=1}^{M} F_{kij}^{na}t_k^{na} \qquad (6.5)$$

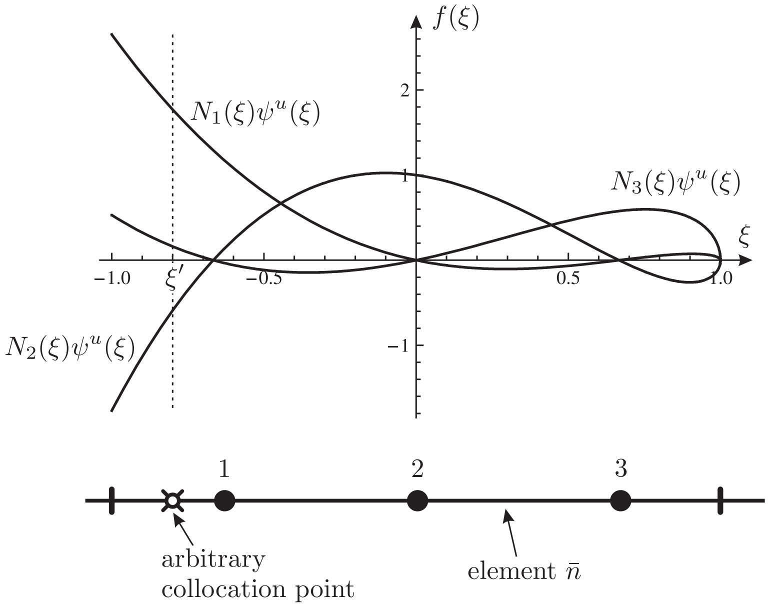

Figure 6.2: Enriched interpolation functions evaluated at arbitrary collocation point

where, as before, E_{kij}^{na} and F_{kij}^{na} are given by (3.84a) and (3.84b) respectively and the integral term $\tilde{E}_{kijl}^{na}$ containing the enrichment functions is given by

$$\tilde{E}_{kijl}^{na} = \int\!\!\!\!\!\!=_{-1}^{1} S_{kij}(\mathbf{x}', \mathbf{x}(\xi)) N_a(\xi) \psi_l^u(\xi) J^n(\xi)\, \mathrm{d}\xi \tag{6.6}$$

which is only included for enriched elements. To allow the collocation point to lie at any general position on an element the jump term (given by the first term in (6.5)) is distributed using the shape functions in exactly the same manner as before. In this case though, because it is assumed that the cracks are traction free and the integral equation of (6.5) is only used for collocation on a crack surface (see Sec. 3.2.4), this term simply equals zero.

The enriched BIEs given by Eqns (6.3) and (6.5) are not quite in their final form since they do not provide a system of equations that will allow all unknown boundary parameters to be solved for. Therefore, in the same manner as Sec. 3.1.7, the source point is chosen to lie at a series of collocation points, where each point provides a unique relation between the boundary parameters. Replacing the source point $\mathbf{x}'$ with $\mathbf{x^c}$ and noting that the DBIE is used for the boundary $\Gamma^R \cup \Gamma^{c+}$ while the TBIE is used for the boundary Γ^{c-} (see Figs 3.16 and 3.17), the enriched BIEs can then be written as

$$C_{ij}(\mathbf{x^c})\left(\sum_{a=1}^{M}N_a(\xi^c)u_j^{\bar{n}a}+\sum_{a=1}^{M}\sum_{l=1}^{L}N_a(\xi^c)\psi_l^u(\xi^c)A_{jl}^{\bar{n}a}\right)$$
$$+\sum_{n=1}^{N_e}\sum_{a=1}^{M}P_{ij}^{na}(\mathbf{x^c})u_j^{na}$$
$$+\sum_{n=1}^{N_e}\sum_{a=1}^{M}\sum_{l=1}^{L}\tilde{P}_{ijl}^{na}(\mathbf{x^c})A_{jl}^{na}=\sum_{n=1}^{N_e}\sum_{a=1}^{M}Q_{ij}^{na}(\mathbf{x^c})t_j^{na}\quad \mathbf{x^c}\in\Gamma^R\cup\Gamma^{c+} \tag{6.7}$$

and

$$\frac{1}{2}\left(\sum_{a=1}^{M}N_a(\xi^c)t_j^{\bar{n}a}\right)+n_i(\mathbf{x^c})\sum_{n=1}^{N_e}\sum_{a=1}^{M}E_{kij}^{na}(\mathbf{x^c})u_k^{na}$$
$$+n_i(\mathbf{x^c})\sum_{n=1}^{N_e}\sum_{a=1}^{M}\sum_{l=1}^{4}\tilde{E}_{kijl}^{na}(\mathbf{x^c})A_{kl}^{na}=n_i(\mathbf{x^c})\sum_{n=1}^{N_e}\sum_{a=1}^{M}F_{kij}^{na}(\mathbf{x^c})t_k^{na}\quad \mathbf{x^c}\in\Gamma^{c-} \tag{6.8}$$

where ξ^c is the local coordinate of the collocation point on element $\bar{n}$. It is now possible to use these equations to form an implementation strategy for the modelling of crack problems:

- The enriched DBIE (Eq. (6.7)) is used for collocation on one side of each crack face and for all non-cracked surfaces. For any elements which are enriched, the integral given by (6.4) must be evaluated, otherwise $\tilde{P}_{ijl}^{na}=0$.
- The enriched TBIE (Eq. (6.8) is used for collocation on the opposite crack faces to which the DBIE is applied. Any enriched elements require the evaluation of (6.6), but otherwise $\tilde{E}_{kijl}^{na}=0$.
- The same degree of displacement continuity required for the DBEM is also needed for the enriched TBIE, therefore discontinuous elements are used on all crack surfaces.

However, before this strategy is applied, there are a few key issues that must be dealt with before the method can be fully implemented. Primarily, these are:

1. By applying enrichment additional DOF are introduced to the system. The use of additional collocation points was discussed briefly here as a solution, but more thought needs to be given to the implementation of this technique.

2. As was shown in Sec. 4.4.3, the integration of the strongly singular and hypersingular integrals seen in the unenriched DBIE and TBIE can be evaluated using simple analytical expressions, but with the introduction of the enrichment functions ψ_l^u, these can no longer be used. Alternative integration techniques must therefore be employed.

3. An enrichment strategy which details the number of elements which should be enriched needs to be employed. Enriching all elements is not a feasible option since the large increase in DOF would be costly.

The next section aims to address each of these items.

6.2 Implementation

Constructing the enriched DBIE and TBIE is relatively straightforward since, as was shown in Sec. 6.1.1, it is merely a case of substituting the enriched displacement relation into the relevant BIEs. However, the task of *applying* the method requires some further thought and it is the goal of this section to outline the procedures that are required to apply the enriched BEM for numerical computation.

6.2.1 Additional collocation points

The present work draws many parallels with XFEM since the same expression for displacement enrichment is used (excluding the Heaviside enrichment functions), but the manner in which the additional unknowns are solved for differs and is it here that we find the methods diverge. In the XFEM, by interpolating displacements using Eq. (5.47), those elements which are chosen to be enriched have extra terms in their element stiffness matrices and body force vectors which are created by the additional enrichment functions. For example, the elements stiffness matrix $[\mathbf{K^e}]$ is made up of components given by

$$[\mathbf{K^e}]_{ij} = \begin{bmatrix} \mathbf{K}_{ij}^{uu} & \mathbf{K}_{ij}^{ua} & \mathbf{K}_{ij}^{ub} \\ \mathbf{K}_{ij}^{au} & \mathbf{K}_{ij}^{aa} & \mathbf{K}_{ij}^{ab} \\ \mathbf{K}_{ij}^{bu} & \mathbf{K}_{ij}^{ba} & \mathbf{K}_{ij}^{bb} \end{bmatrix} \qquad i,j = 1, M \tag{6.9}$$

where M is the number of nodes on each element and the symbols u, a and b refer to conventional displacement interpolation, Heaviside functions and crack tip enrichment functions. The element force vector also increases in size in a similar fashion where further details can be found, for example, in [105]. What is important is that in this formulation the additional DOF introduced by enrichment are accounted for implicitly within the method; in contrast, introducing enrichment to the BEM and DBEM does not account for the extra DOF and so it is necessary to *explicitly* introduce additional equations. In the present method this is achieved by the use of extra[1] collocation points.

The idea of using additional collocation points to solve for additional unknowns introduced by enrichment is not new and has been applied successfully to apply enrichment of the BEM for wave applications by Perrey-Debain et al. [104]. In this work a plane wave basis is introduced through the PUM that demonstrates a substantial increase in accuracy but at the cost of calculating additional DOF corresponding to each plane wave at an enriched node. However, by collocating at points positioned between nodes, it is possible to obtain a sufficient number of extra equations that relate all the boundary parameters and a square system can then be formed.

Exactly the same technique is applied in the present work to solve for the enrichment coefficients A^{na}_{jl} (Eq. (6.1)) and it should become clear now why such effort was made in the formulation of the enriched BIEs to allow collocation at any general position on an element. All that is necessary now is to determine the number and position of these collocation points that will allow the additional coefficients to be solved for. For this purpose, we consider two scenarios: enrichment of a flat crack and enrichment of a curved crack.

As explained in Sec. 6.1.1, in the case of a flat crack the enrichment functions reduce to the simple basis given by (6.2). Bearing in mind that for each enriched node an additional coefficient will be introduced for each basis function in each direction, the use of discontinuous quadratic elements will result in six additional DOF for each enriched element. Therefore, since collocation produces two equations (one in each global direction), three additional collocation points are required for enrichment of a flat element. This is illustrated in Fig. 6.3 which shows the additional points spaced arbitrarily between nodes for two enriched elements. In fact, since the crack is made up of two coincident surfaces (it may be helpful to refer back to Fig. 3.17), there are four enriched elements with three additional collocation points on each - they are just drawn as coincident in Fig. 6.3.

Considering now the case of a curved crack, where, due to the variation in the

---

[1] that is, in addition to collocation at nodal points

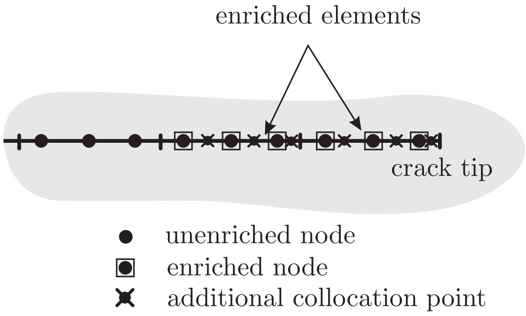

Figure 6.3: Additional collocation points for enrichment of flat crack elements

crack angle θ along each of the crack surfaces, it is possible to use all four crack tip enrichment functions. Using the example of a discontinuous quadratic element once again, application of enrichment to a curved element will produce a total of twenty-four additional DOF requiring the use of twelve additional collocation points[2]. Fig. 6.4 illustrates two coincident curved crack elements with enrichment applied and containing twelve additional collocation points .

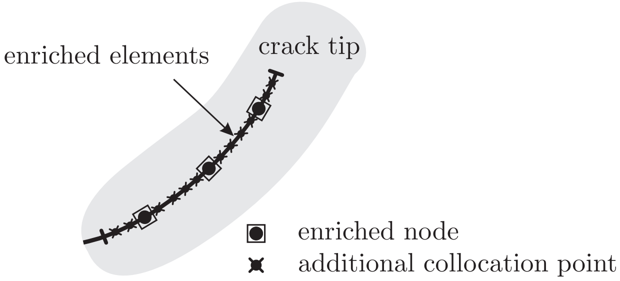

Figure 6.4: Additional collocation points for enrichment of curved crack elements

In Figs 6.3 and 6.4 which illustrate enriched elements, the additional collocation points are positioned between nodes and spaced evenly throughout the element. Using this strategy, an assumption has been made that the additional collocation points are to be placed on the boundary of the problem (rather than the interior or exterior of the domain) and that they should be placed on enriched elements (rather than other, unenriched elements). What was found after trying other strategies was the creation of a singular system such that, even with a special numerical solver[3], a sensible solution could not be retrieved. The technique outlined in [104] of spacing the extra points evenly throughout enriched elements was also used but, as will be

---

[2] where each point produces two equations - one for each direction

[3] a singular value decomposition (SVD) technique was used

shown in Sec. 6.3.3, as long as these points do not lie too close to one another or to existing nodes (since this will create identical rows in the system of equations), a valid solution is obtained.

6.2.2 Singular integration for general collocation points

An important feature of any BEM implementation is the evaluation of the singular integrals encountered when the source and field points coincide. For the enriched BEM, the way in which the integrals are evaluated was touched on briefly in Sec. 4.4.4, but a more thorough explanation and justification of the technique is given presently.

The most desirable method of evaluating singular integrals is to use analytical expressions such as those given by Eqns (4.11) and (4.16), but when the enriched integrals of (6.4) and (6.6) are considered, the task of obtaining analytical expressions becomes more complex. Even for the simplest case of a flat crack with an enriched element adjacent to the crack tip, the integral expressions are given by lengthy functions (see Appendix C.7). In addition, it is found that for the case of curved enriched elements, analytical expressions cannot be found and other methods must be adopted. It is for these reasons that a numerical integration routine, based on the subtraction of singularity method, is used for the evaluation of all singular enriched integrals.

Recalling Eqn. (4.31) which allows the evaluation of hypersingular and strongly singular integrals through the subtraction of singularity method, the expression can be seen to rely on the determination of the functions $F_{-2}(\xi')$ and $F_{-1}(\xi')$. These non-singular functions can be determined by using appropriate Taylor series expansions around the source point ξ' which, in the case of the enriched hypersingular integral given by Eq. 6.6, are given by

$$F_{-2}(\xi') = DS_{-2}(\xi_p)N_a(\xi')\psi_l^u(\xi') \tag{6.10a}$$

$$\begin{aligned} F_{-1}(\xi') = D\bigg[& S_{-2}(\xi')\bigg(N_a(\xi')h(\xi')\frac{d\psi_l^u(\xi')}{d\xi} \\ & + \psi_l^u(\xi')\left(h(\xi')\frac{dN_a(\xi')}{d\xi} + N_a(\xi')g(\xi')\right)\bigg) \\ & + S_{-1}(\xi')N_a(\xi')h(\xi')\psi_l^u(\xi')\bigg] \end{aligned} \tag{6.10b}$$

where D is a constant and the functions $S_{-1}(\xi')$, $S_{-2}(\xi')$, $h(\xi')$ and $g(\xi')$ are algebraic expressions involving the components $r_{,i}$, $n_{,i}$ and the Jacobian of transformation $J^n(\xi')$. A full definition of these terms is given in Appendix C.6.2. Exactly the same technique can be used for the evaluation of the strongly singular enriched integrals given by Eq. 6.4 where it is found, due to the lower order of singularity, that the term $F_{-2}(\xi') = 0$. Since these enriched integrals ($\tilde{P}^{na}_{ijl}$ and $\tilde{E}^{na}_{kijl}$) are the only new terms added to the conventional BEM and DBEM formulation, it is now possible to evaluate all integrals for the implementation of the enriched method.

6.2.3 Enrichment strategy

The technique by which crack tip enrichment functions are included has been described, but no mention has been made of the *number* of elements that should be enriched to achieve an accurate but also efficient solution. This subject draws many parallels with XFEM where - as was described in Sec. 5.4.1 - there are two forms of enrichment: topological and geometrical. Out of these two choices geometrical enrichment is preferred, since there is no dependence on the mesh density and, as is generally accepted in LEFM, the singularity dominates a finite region surrounding the crack tip (see Sec. 2.4). However, as described by Bechet et al. [101] and Laborde et al. [106] the enrichment of multiple elements may lead to ill-conditioned matrices. As will be shown shortly, the same is found to be true in the present work and it is necessary in the current formulation, without undue loss of accuracy, to apply topological enrichment for the enriched BEM (see Fig. 6.5).

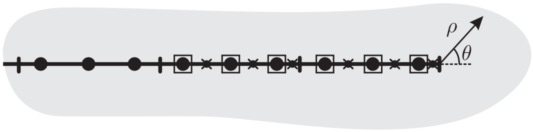

(a) Coarse mesh

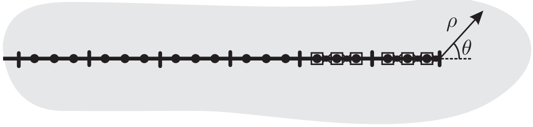

(b) Fine mesh

Figure 6.5: Topological enrichment for enriched BEM

6.2.4 Matrix construction

Before results are given for the application of the method, it is also useful to make some comments on how the system of equations is formed and in particular, how the submatrices which are used to construct the matrices **H** and **G** (Eq. (3.76)) are determined. So far indicial notation has been used primarily throughout the formulation of the method, therefore this section may be of particular use for readers more familiar with matrix notation.

The easiest way to demonstrate the formation of the matrices is through an example which, in this case, is chosen to be the problem of straight edge crack in a finite plate. By discretising the boundary with quadratic discontinuous boundary elements and applying enrichment solely to crack tip elements, the problem can be represented by Fig. 6.6. Since the crack is flat, it is necessary to include three additional collocation points on each enriched element which in the present example are positioned at coincident points on the upper and lower crack surfaces.

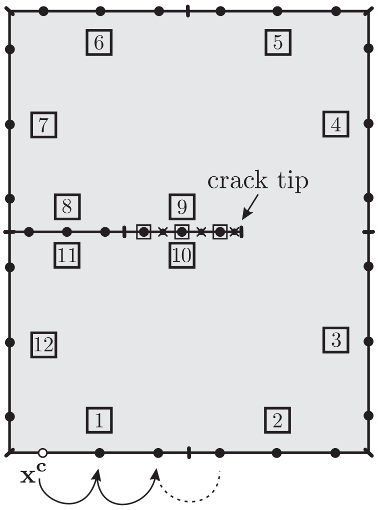

Figure 6.6: Edge crack problem with enrichment applied to crack tip elements

The first step in forming the matrices is to collocate at each of the nodal points and additional collocation points around the boundary. If the point lies on any non-crack surface or on the upper crack surface the enriched DBIE of (6.3) is used, but in the case the collocation point lies on the lower crack surface, the enriched TBIE of (6.5) is used instead. It may be useful to refer back to Fig. (3.17) which illustrates this collocation strategy. Each collocation point forms two rows in the matrices **H** and **G** (one for each source point direction x, y) where the columns within these rows are formed by integrating over each of the elements around the boundary.

To facilitate the construction of these matrices, the integral terms corresponding to a particular element and collocation point are most often placed in submatrices which can then be manipulated easily to form each row of the matrices **H** and **G**. To illustrate this process more clearly and to show the formation of a submatrix for an enriched element, we take the example of collocation at an additional point on an element enriched using (6.2). Assuming the collocation point lies on the enriched element on the upper crack surface (element nine) and using an unenriched element for comparison, the submatrices are constructed in the manner shown in Fig. 6.7. The notation $\mathbf{H}_c^n$ and $\mathbf{G}_c^n$ is used to denote the submatrices corresponding to collocation point c and field element n

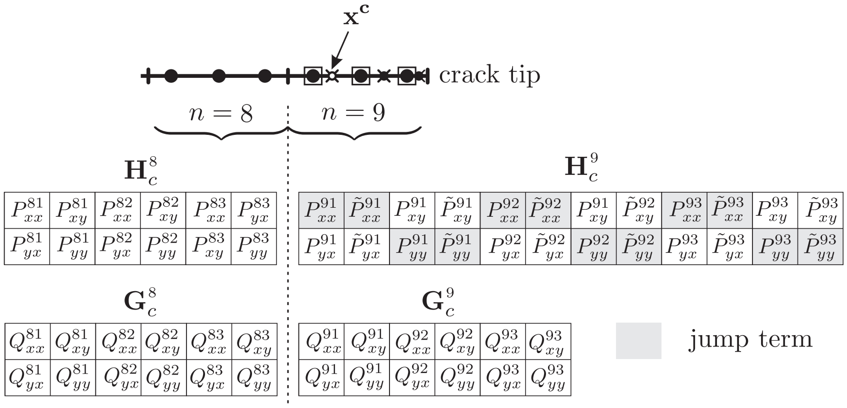

Figure 6.7: DBIE submatrices for general collocation point on enriched element

Comparing first the **G** submatrices for each element, each is of dimension 2 × 6 because, as explained previously, the assumption of traction free cracks precludes the need for traction enrichment. The use of displacement enrichment however, increases the size of the **H** submatrix for element nine to 2 × 12. In addition, since the collocation point has been deliberately placed at non-nodal point on this element, the jump term must be distributed amongst all the nodes as shown by the shaded terms.

One the submatrices haven been determined, they are placed within the matrices **H** and **G** according to the collocation number c and the element number n. Fig. 6.8 demonstrates this process and shows explicitly the creation of rows by collocation and the formation of columns by integrating over elements. The vector $\mathbf{u}$ now contains the enrichment coefficients A_{jl}^{na} (in addition to the conventional displacement terms u_j^{na}) whereas the the vector $\mathbf{t}$ remains unchanged. Once each of these matrices are fully populated, it is a simple task of swapping columns to place all unknown parameters on the LHS and multiplying the known terms on the RHS to arrive at the familiar relation $\mathbf{Ax} = \mathbf{b}$ which can then be solved.

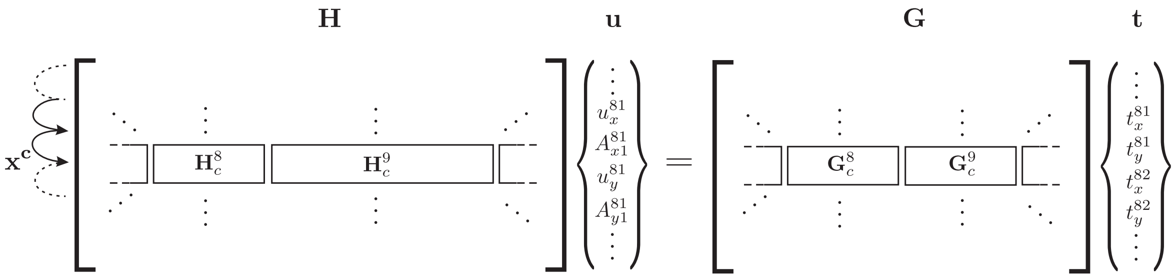

Figure 6.8: Construction of **H** and **G** matrices from submatrix terms

6.3 Verification and testing

Now that the various issues required for implementation of the enriched BEM have been discussed, attention is now focussed towards numerical results to verify the ability of the method to accurately analyse crack problems. To achieve this, the section is split into four parts: first, the ability of the method to capture the singular crack tip field is verified; next, a comparison is made between methods for determining SIFs; the effect of the position of additional collocation points is shown and finally, the effect of increasing the number of enrichment elements is quantified. At present, more focus is given to the implementation of the method - application of the method to a variety of crack geometries is left until Chapter 8 since this will allow for comparison with the enrichment method presented in the next chapter.

6.3.1 Enriched BIE verification

Before the enriched BEM can be applied to crack problems to evaluate the accuracy of the method, it is first necessary to ensure that the enriched BIEs are capable of capturing the displacement and traction field encountered around a crack. To do this, the problem of a centre crack within an infinite plate is used where a certain region surrounding one of the crack tips (see Fig. 6.9a) is used to create a boundary mesh (eg. Fig. 6.9b). Using Eqns (2.36) and (2.37) and setting $K_{\mathrm{I}} = 1.0$ (arbitrarily) and $K_{\mathrm{II}} = 0$, the exact displacements and stresses can be found around the entire boundary for the problem. In addition, by noting that the crack tip displacement in this problem is equal to zero ($u_j^{na} = 0$), the values of each of the enrichment coefficients A_{jl}^{na} in Eq. (6.1) can be found exactly by comparing the appropriate enrichment functions of (5.48) with expressions (2.37). Enriching every element around the boundary and substituting in the exact values for A_{jl}^{na} and t_j^{na}, the LHS and RHS of Eq. (6.3) can be evaluated at each of the collocation points and compared. If the boundary integrals are evaluated to sufficient accuracy, then the difference between LHS and RHS should approximately equal zero (to machine precision), and if this is not the case, then any integration inaccuracies will be highlighted. Implementing the above strategy shows that for all collocation points around the boundary, including additional collocation points, the enriched BIEs are capable of capturing the singular field with differences between the LHS and RHS in the order of $5 \times 10^{-5}\%$. We can therefore be confident that the enriched BEM is capable of capturing the singular field around a crack tip. In order to assess the accuracy of the method however, it is necessary to formulate the problem in such a way that certain variable over part of the boundary remain unknown, and this is what the discussion focusses on next.

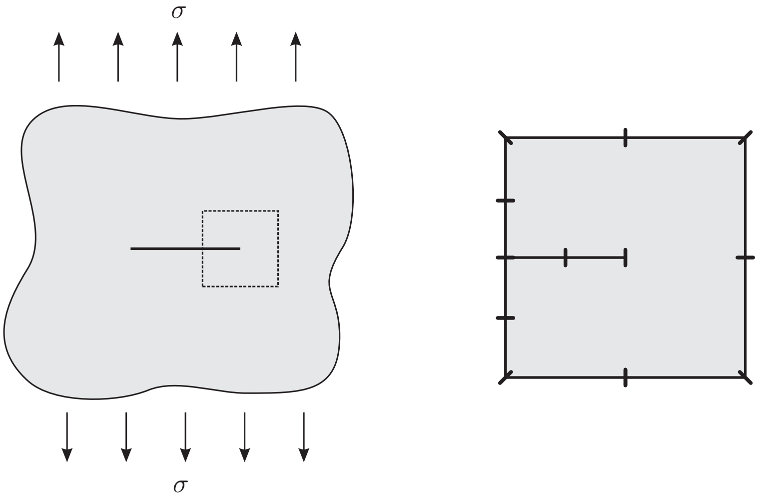

(a) Selected region surrounding crack tip in infinite plate

(b) Example boundary mesh of selected region

Figure 6.9: Discretisation of uniaxially loaded infinite plate problem

If the exact displacements for the infinite plate problem are prescribed on all non-crack boundaries and zero tractions are specified on the crack itself, then the crack displacements become unknowns. It is then possible, by comparing the results of both the unenriched and enriched formulations to the known solution, to investigate the effects of including enrichment and quantify the improvements seen in accuracy. The mesh used for the analysis is shown in Fig. 6.10a where four elements per line were used and only the elements adjacent to the crack were enriched. Exactly the same mesh was used in the unenriched case, with no crack elements enriched. By plotting the displacements of the nodes nearest to the crack tip (since these are most affected by the singularity) it is possible to see the effects of including enrichment. Fig. 6.11 shows that the enriched displacements match the exact values closely whereas the unenriched values, as the crack tip is approached, diverge from the exact solution. However, even although it is apparent from this figure that enrichment is capturing the singular field of the crack tip, it is still necessary to assess the accuracy of the method in determining SIFs, since accurate evaluation of these parameters is crucial in fracture mechanics. Therefore, using the same problem, attention is now drawn to the evaluation of SIFs using different techniques.

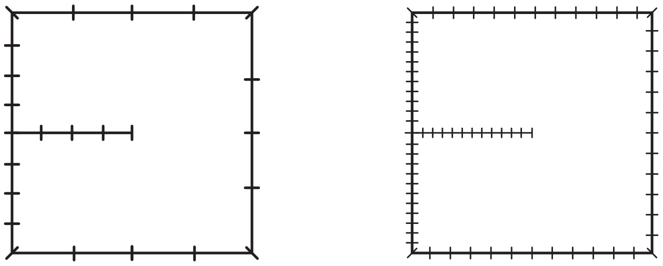

(a) Four elements per line (coarse mesh)

(b) Twelve elements per line (fine mesh)

Figure 6.10: Boundary meshes used for infinite plate problem

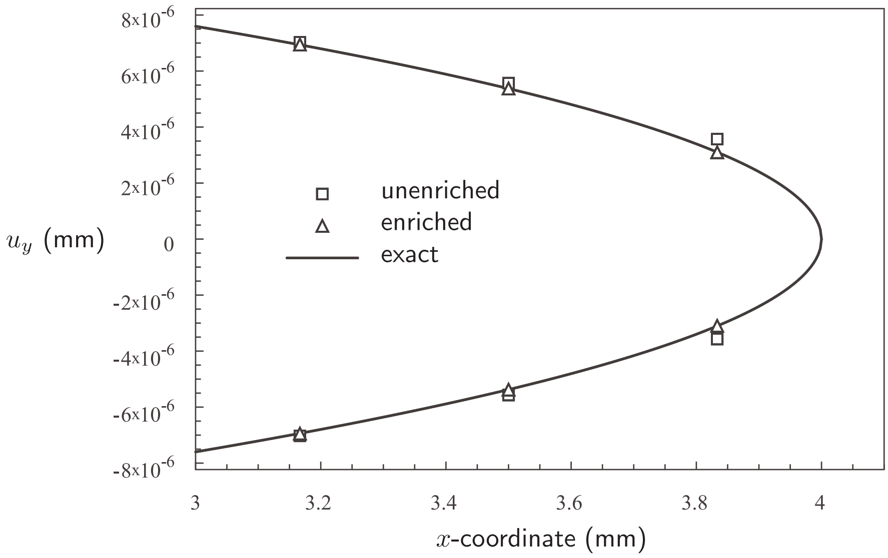

Figure 6.11: Crack tip displacement comparison for infinite plate problem

6.3.2 SIF determination

In Sec. 2.6.1 the technique of using displacements along the crack to determine SIFs was outlined, but it was also noted that the method often presents difficulties in obtaining a single value for the SIF. Nevertheless, the method is still useful in providing an assessment of SIF accuracy for both the unenriched and enriched formulations and it is used presently for this purpose. The same infinite plate problem as implemented in Sec. 6.3.1 (where exact displacement boundary conditions are specified on all non-cracked boundaries) was used to carry out four simulations: two unenriched analyses where a coarse and fine mesh were used with four and twelve elements on each line respectively, two enriched analyses with a coarse and fine mesh (using the same number of elements as before) and enriching only the crack tip elements. Substituting the nodal displacements Eq. (2.62a), the mode I SIF can be determined for each of the nodes along the crack. Fig. 6.12 illustrates the results of each of the simulations. Two important comments can be made about this figure:

- A clear improvement in accuracy is seen once enrichment is introduced - the unenriched SIFs diverge from the exact solution as the crack tip is approached while the enriched SIFs remain consistently accurate
- Comparing the fine and coarse mesh results for the enriched implementation the results are accurate for *both* meshes. The enrichment is therefore achieving the desired result of obtaining **higher accuracies for fewer degrees of freedom**

A much more robust method of calculating SIFs, and one which is used widely in numerical fracture mechanics, is that of the J-integral as described in Sec. 2.6.2. Defining a set of circular integration paths centred at the crack and numbered as shown in Fig. 6.13, it is possible to evaluate the J-integral for each and determine the mode I SIF using expression (2.68) (noting that for this problem, $K_{\mathrm{II}} = 0$). The reason for evaluating the integral multiple times over different paths is to verify the path-independence of the method and to give confidence in the determined SIF value. Fig. 6.13 also illustrates the placement of integration points around each of the circular paths which allows, using an appropriate integration rule (eg. trapezoidal rule, Gaussian quadrature), the J-integral to be evaluated. The implementation of this procedure outlined in [24] which evaluates SIFs using the DBEM (with no enrichment) uses a total of twelve integration points using the trapezoidal rule but, as will be shown shortly, this does not represent the converged value of the J-integral

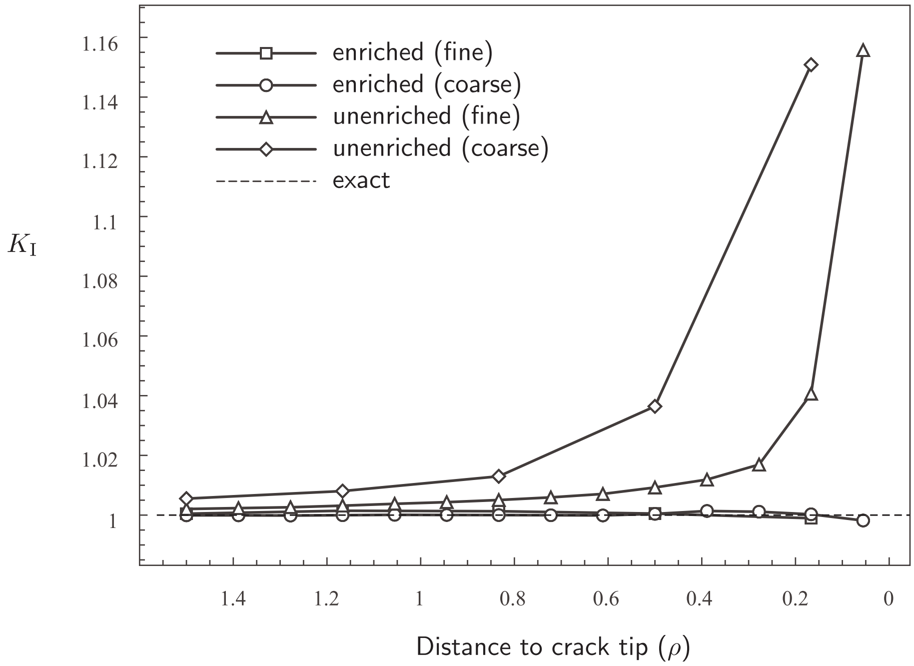

Figure 6.12: Comparison of enriched and unenriched mode I SIF using nodal displacements

and more integration points (or a higher-order quadrature routine) are required. Taking the case of the unenriched DBEM first, a coarse mesh of four elements per line was used while the J-integral was evaluated using an increasing number of integration points varying from ten to fifty. The results for each of the integration paths are shown in Fig. 6.14 which, after inspection, allow a few points to be made on the J-integral convergence. Firstly, there is a notable difference between paths two and three compared to all others which is attributed to errors in integration as the points are positioned very close to the boundary; Sec. (7.3.1) gives a much more comprehensive investigation into this. Paths four to eight are consistent with one another and convergence is achieved at approximately thirty points. If the same analysis is applied to the enriched DBEM, the results shown in Fig. 6.15 are obtained where, once again, a clear difference between paths two and three and the others is seen. At first glance it appears that there is a much larger variation between the results of paths four to eight (compared to the unenriched analysis), but after comparing the y-axis scales of Figs 6.14 and 6.15, it can be seen that in fact, the results of the enriched analysis show much *less* variation. The results converge at approximately thirty integration points except for paths two and four: in the case of path two the integration path is so small that as the number of points increases, eventually they lie at locations close to the boundary resulting in nearly-singular integrals (see Sec. 4.2) which affect the accuracy; path four converges at approximately fifty points but, comparing this value with that obtained at thirty points for example, the change in value can be seen to be minimal. The following recommendations can therefore be made for the implementation of the J-integral in the DBEM: if circular integration paths centred at the crack tip are used then those paths which do not start/finish on the crack tip elements will yield the most accurate results; if the trapezoidal rule is used, then it is recommended to use more than thirty integration points.

The J-integral was applied, in the same manner as before, using four tests to assess the effect on the SIF after introducing enrichment: a coarse and fine mesh using no enrichment and a coarse and fine mesh with enrichment only applied to elements adjacent to the crack tip. Exactly the same meshes as used for displacement extrapolation were applied. Fig. 6.16 demonstrates the results obtained for each of the analyses and after inspection, some conclusions can be drawn:

- As expected, all four meshes show slightly less accurate results for paths two and three while for paths four to eight, the path independence of the integral is demonstrated clearly .
- A large improvement in accuracy is seen once enrichment is introduced for both the coarse and fine meshes.
- Accurate results are seen for both the fine *and* coarse meshes in the enriched analyses.

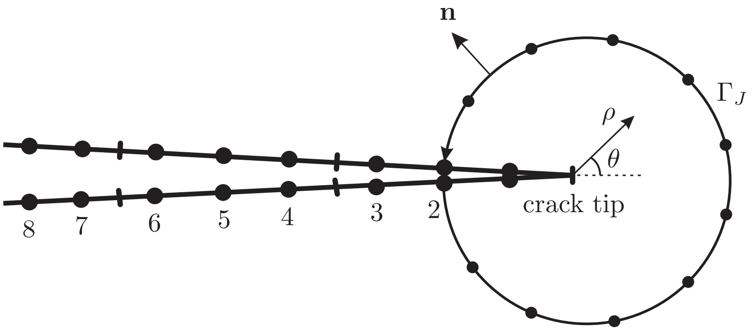

Figure 6.13: Definition of J-integral paths for SIF determination

6.3.3 Placement of additional collocation points

Sec. 6.2.1 explained the technique of using additional collocation points to solve for the additional unknowns introduced through enrichment where it was proposed that

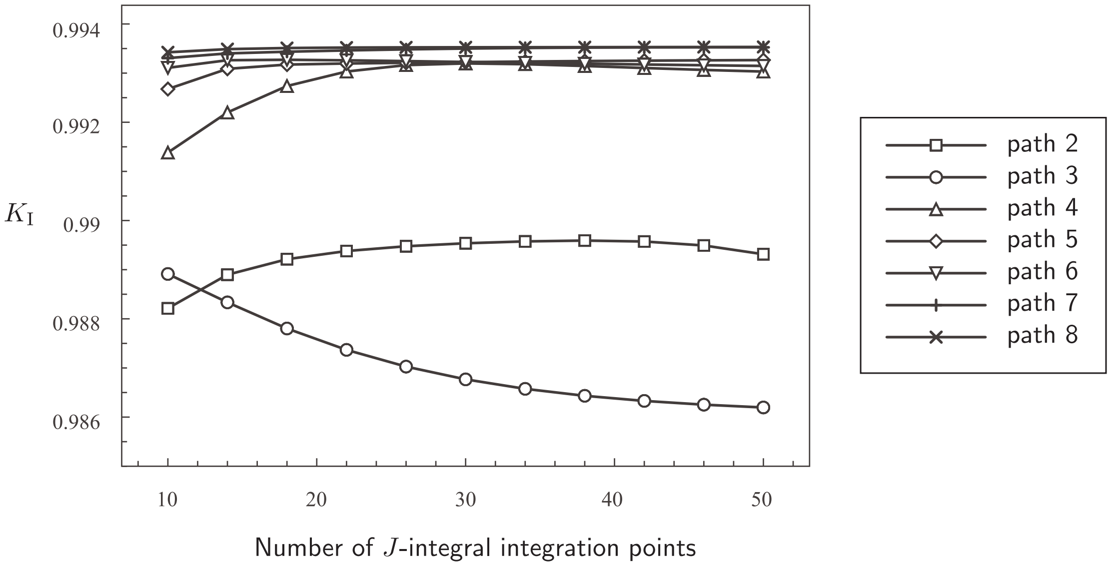

Figure 6.14: Convergence of J-integral for various integration paths using unenriched DBEM

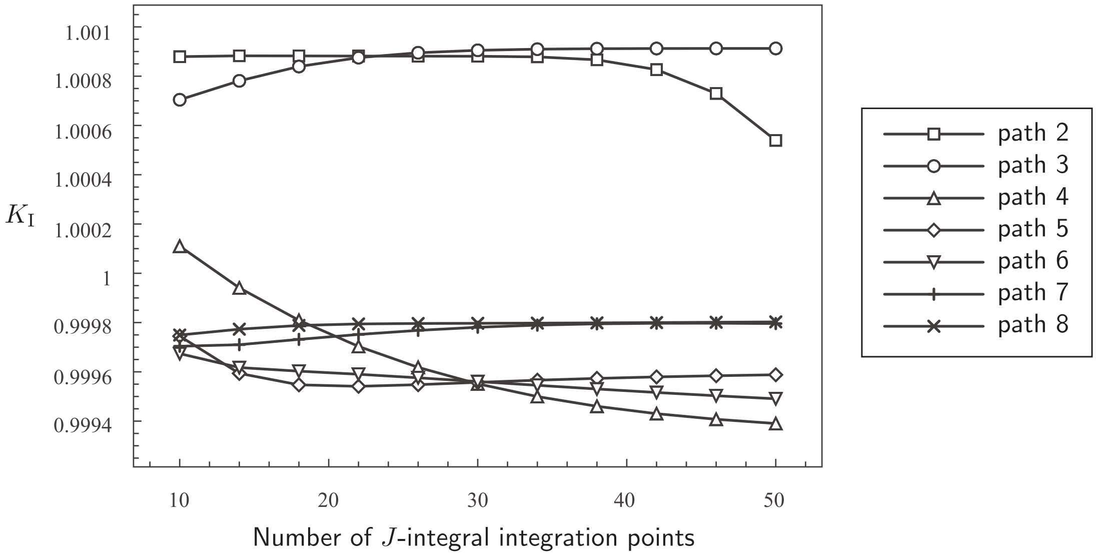

Figure 6.15: Convergence of J-integral for various integration paths using enriched DBEM

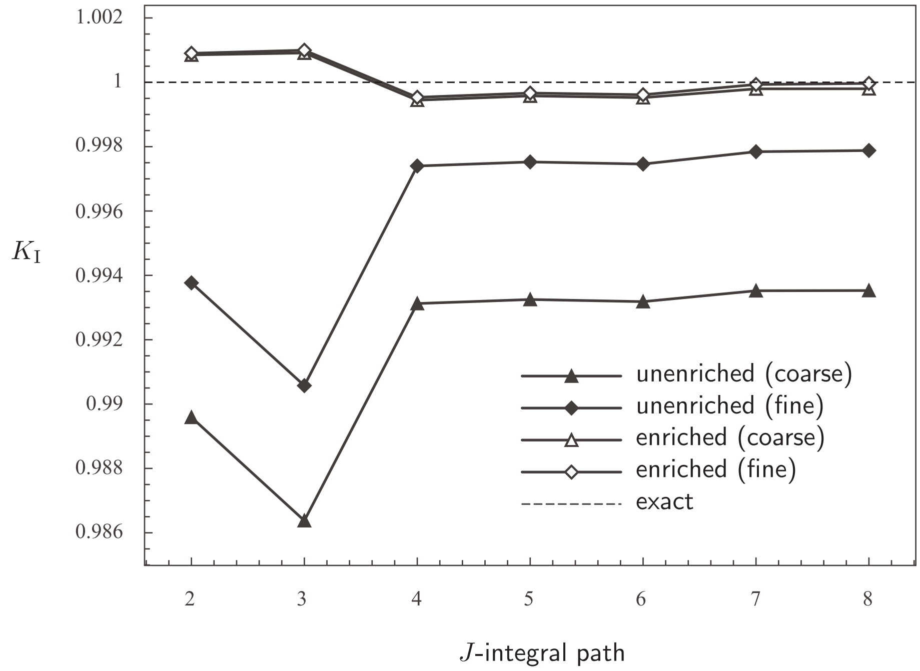

Figure 6.16: Comparison of unenriched and enriched K_I values evaluated using J-integral

these should be placed on enriched elements and spaced evenly between nodes. The reasoning behind this placement strategy can be explained twofold: intuitively, the points should be positioned near the nodes that are enriched rather than far away where the singularity has little effect; secondly, placing the points on or near existing nodes will create a singular system and should be avoided. The objective of this section is to demonstrate that this strategy is the most appropriate for collocation point placement with the aid of numerical results.

To demonstrate the effect of additional collocation point placement, the infinite plate problem with Dirichlet boundary conditions imposed on all non-crack boundaries was used. The plate was modelled with a coarse mesh of four elements per line (Fig. 6.10a) with enrichment only applied to the elements adjacent to the crack tip. First, the additional collocation points were placed on the elements next to the enriched elements (which are themselves unenriched) and placed at positions as indicated in Fig. 6.17a to investigate the effect of moving the additional points further away from the enrichment. What is immediately apparent is the significant effect on the conditioning of the system where, even for this example where the additional points are relatively close to the enriched elements, condition numbers in the order of 10^{21} are seen. Tests were also carried out with additional points placed outside the problem domain (a technique which has been implemented by Berger et al. [107]) but these too showed similar detrimental effects on the conditioning of the system. In contrast, placement of additional points within enriched elements had a much smaller influence on the conditioning where, using the same example as before but placing the points as in Fig. 6.17b, a much smaller condition number of order 10^{10} was experienced. It was therefore decided that all future analyses should include additional collocation points within enriched elements.

(a) Outside enriched elements

(b) Inside enriched elements

Figure 6.17: Effect of global position of additional collocation points

The second series of tests investigated the effect of the collocation point placement within enriched elements by changing the local coordinates of the additional points. Since only the elements adjacent to the crack tip were enriched, only six additional points (three for each element) were required and these were placed at coincident points on the upper and lower crack surfaces. A variety of collocation point positions were tested while the mode I SIF was determined for each (using the J-integral with path four) to illustrate the effect on accuracy. The results are shown in Table 6.3. The first four tests show that the position of the points has little effect on the accuracy, even when they are positioned close together or close to nodal points. In addition, the condition number of the system remains largely unchanged. The last four tests investigate the effect as one of the additional points approaches a nodal point and, as expected, the conditioning of the system is affected. A Gaussian elimination solver can be used in the first of these tests, but as the point is moved closer to the nodal position, the SVD solver needs to be employed (as signified by the dashed line). Even so, sensible results are still obtained and it is only when machine precision is approached that the accuracy begins to deteriorate. There is therefore a large degree of flexibility on the placement of the collocation points within the enriched elements and there can be confidence in the strategy of placing the points evenly spaced between nodes.

6.3.4 Effect of enrichment zone size

One of the features of enriching the approximation through the PUM is the ability to extend the zone of enrichment and therefore capture the crack tip singularity

Table 6.3: Effect of collocation point placement (local coordinates)

Collocation positions	ξ	K_{I}	% error	Condition Number[a]
	-0.8,-0.3,0.8	0.999444	0.0556	6.80×10^{10}
	-0.6,-0.5,-0.4	0.999397	0.0603	4.73×10^{12}
	-0.6,-0.5,0.65	0.999445	0.0555	3.65×10^{11}
	-0.67,-0.1,0.65	0.999511	0.0489	1.18×10^{12}
	-0.8,1e-3,0.8	0.999520	0.0480	8.03×10^{12}
	-0.8,1e-6,0.8	0.999520	0.0480	8.04×10^{15}
	-0.8,1e-9,0.8	0.998912	0.1088	1.06×10^{19}
	-0.8,1e-12,0.8	0.998912	0.1088	1.71×10^{21}

---

[a] dashed line signifies point after which SVD solver must be used

with greater accuracy. What is expected is that as the number of enriched elements increases, the error in SIF should decrease but, of course, with an associated cost of computing additional enrichment coefficients. To determine the effect of increasing enrichment five meshes ranging from four elements to twelve elements per line were used to model a flat crack within an infinite plate. For each mesh the number of enriched elements was increased from zero (unenriched) to the case where all elements on the crack faces were enriched. To allow comparison between different mesh densities the following expression is used to normalise the number of enriched elements

$$\bar{N}_{enr} = \frac{\text{number of enriched elements}}{\text{number elements on crack faces}} \tag{6.11}$$

where, using the coarse mesh of four elements per line as an example, $\bar{N}_{enr} = 0.25$ for enriching the crack tip elements (Fig. 6.18a) and $\bar{N}_{enr} = 1$ for all elements on the crack faces enriched (Fig. 6.18b). The J-integral with path four (Fig. 6.13) was used to determine the SIF with the results for each mesh shown in Fig. 6.19. Inspection of the results shows that initially the error in SIF is reduced as enrichment increases for each mesh, but as enrichment is applied to greater numbers of elements this is not necessarily true. For low mesh densities with large numbers of enriched elements no problems are encountered, but for high mesh densities with many enriched elements the accuracy deteriorates. In fact, the results for the mesh with twelve elements per line diverge so much from the solution that they are not plotted here. To

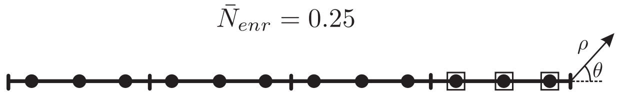

(a) Crack tip elements enriched

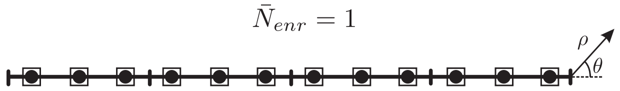

(b) Full enrichment of crack faces

Figure 6.18: Varying enrichment over crack faces

understand what is happening in these simulations it is beneficial to calculate the condition number as the number of enriched element increases. Fig. 6.20 illustrates the results for the coarse and fine meshes with four and twelve elements per line respectively and it is immediately apparent that the conditioning of the system is affected significantly by enrichment (the y axis is plotted with a log scale). Close inspection shows that by comparing the condition numbers between the coarse and fine meshes with no enrichment applied a difference of approximately an order of magnitude is seen. Noting that each point as we move from left to right along each of the plots in Fig. 6.19 signifies two additional enriched elements (one on each crack surface), it can be seen this this order of magnitude difference is maintained between equal numbers of enriched elements. Therefore, it can be deduced that the main contribution to the adverse conditioning of the system is the number of enriched elements while, in comparison, the effect of increasing the mesh density is negligible.

Referring back to the enrichment strategies known as geometrical and topological enrichment (Sec. 5.4.1) it becomes clear that, with the knowledge that there is a detrimental effect on the conditioning of the system as the number of enriched elements is increased, topological enrichment is preferred in the current implementation. If geometrical enrichment is employed, then as the mesh density increases the number of enriched elements also increases and may reach a critical number at which the accuracy of the solution degrades. Topological enrichment, however, gives control over the number of enriched elements (and therefore the conditioning of the system) lending more confidence to the results. For this reason, all future applications of the method apply enrichment using the topological strategy

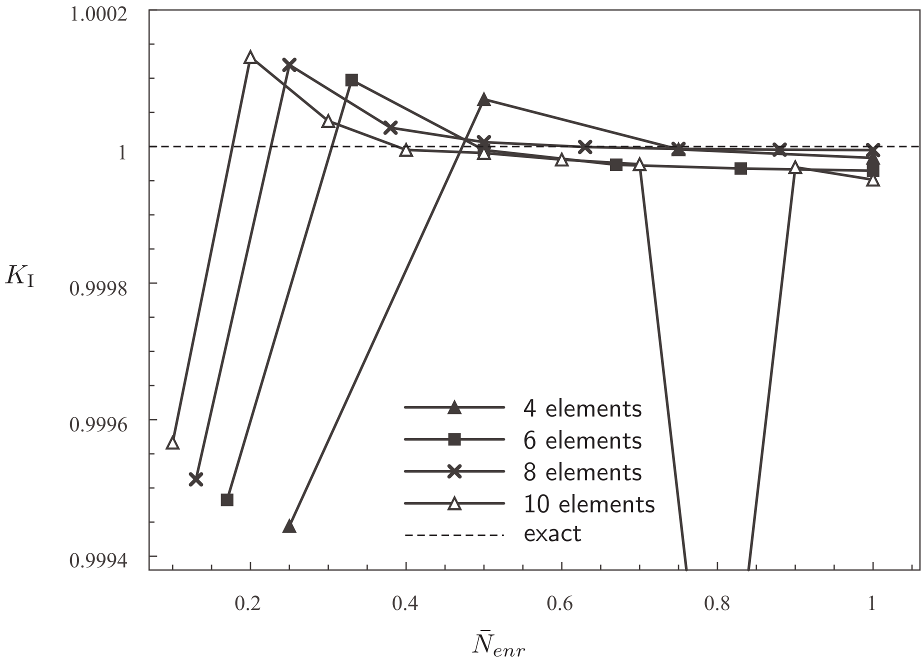

Figure 6.19: SIF accuracy for increasing enrichment

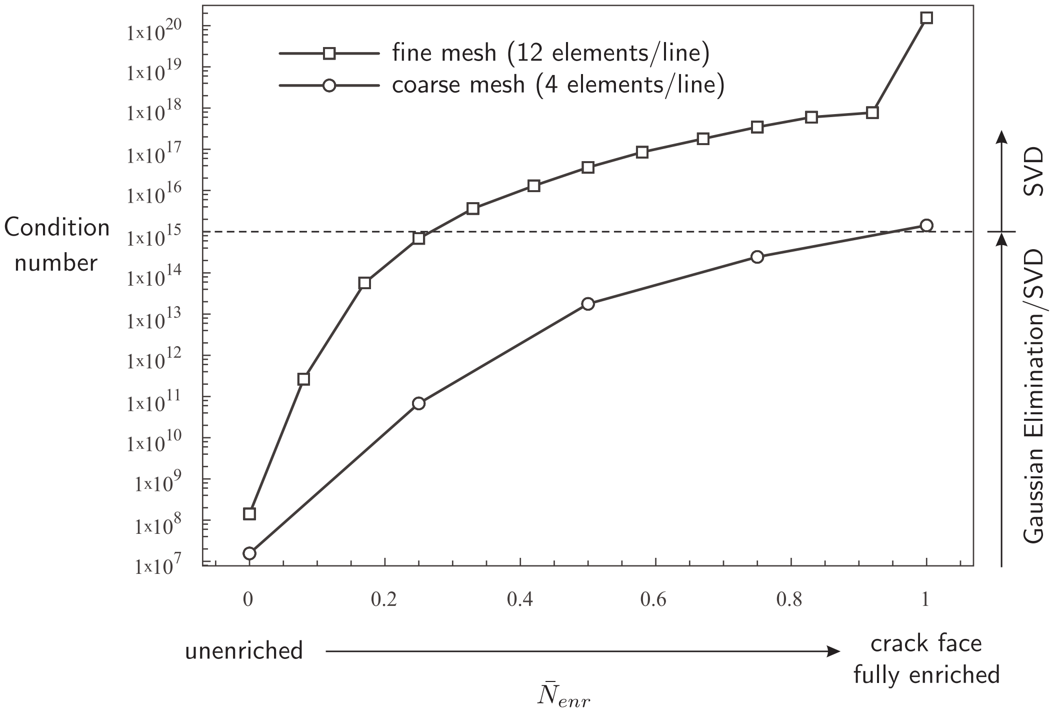

Figure 6.20: Effect of increasing enrichment on condition number

6.3.5 Curved crack

Finally, since all of the previous analyses have been concerned with a flat crack that (as explained in Sec. 6.2.1) reduce the enrichment basis to a single simple function, it is useful to consider the case of a curved crack that will make use of the complete enrichment basis. Before any assessment of accuracy was made by comparing with analytical solutions, the ability of the method to incorporate the multiple basis functions was first tested. To do this, a finite plate containing a circular crack (Fig. 6.21a) was modelled with a coarse mesh of four elements per line (Fig. 6.21b) and enrichment was applied only to the elements adjacent to the crack tip. Since the full basis of enrichment functions may be used, a total of twenty-four additional collocation points (twelve for each enriched element) were placed on the enriched elements and spaced evenly as in Fig. 6.4. The [exaggerated] displacements along each of the crack faces for unenriched and local PUM enriched analyses are shown in Fig. 6.22 where it can be seen that the unenriched displacements display the expected profile while in contrast, the enriched implementation is showing erroneous results. Since Sec. 6.3.4 demonstrated that enrichment can have a detrimental effect on the conditioning of the system, the condition numbers of the unenriched and enriched implementations are compared (Table. 6.4) and, as can be clearly seen, there is a very significant effect after introducing enrichment. For such an ill-conditioned system, even the use of a SVD solver is unable to produce sensible results.

Table 6.4: Condition numbers for unenriched and enriched implementations of curved crack problem

Method	Condition Number
unenriched	4.52×10^{6}
enriched	2.40×10^{22}

6.4 Remarks

The implementations have shown that great improvements in accuracy are obtained when enrichment through the PUM is applied to the BEM, but a recurring theme which occurs throughout all the results is the effect enrichment has on the conditioning of the system. The effect becomes so detrimental in the case of a curved crack that no sensible results can be obtained. Therefore, the impetus to arrive at

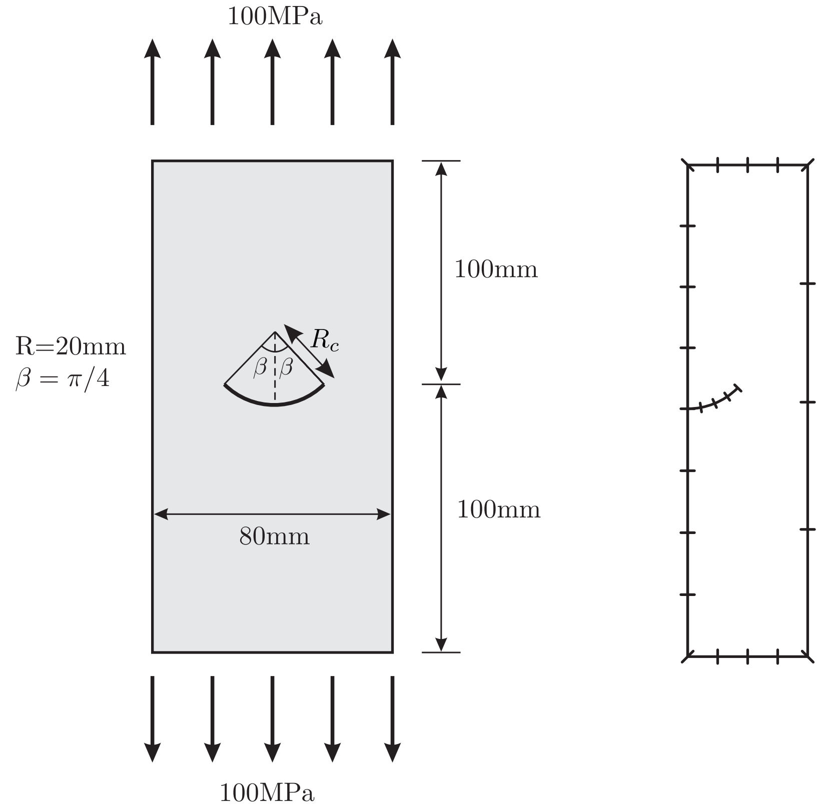

(a) Problem dimensions and loading (b) Boundary element mesh

Figure 6.21: Curved crack in a finite plate

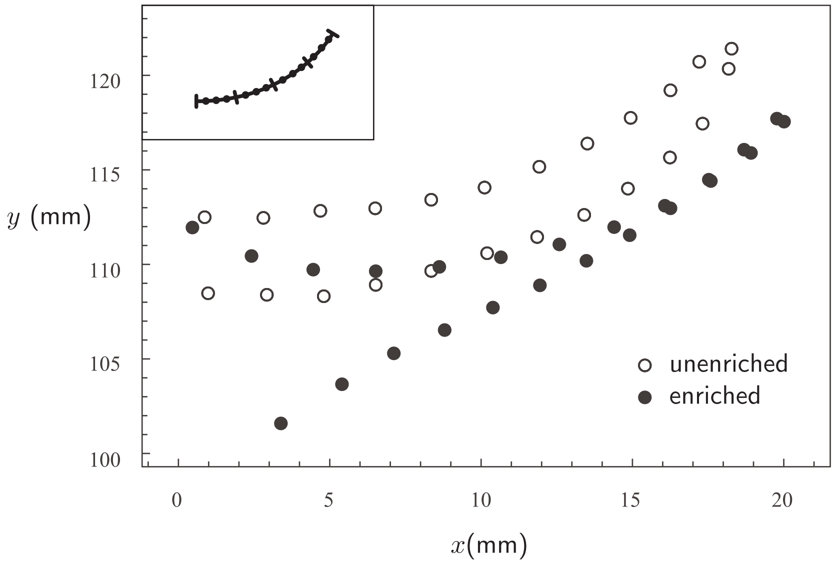

Figure 6.22: Exaggerated displacements along crack faces for enriched and unenriched analyses of curved crack problem

an alternative form of enrichment which does not affect the singularity of the system is great, and it is for this reason that a new implementation, which precludes the need for additional collocation points, is now presented.

Chapter 7

Enriched BEM with combined basis (global formulation)

As demonstrated in Chapter 6, the application of enrichment through the PUM to the BEM/DBEM brought large increases accuracy for a small number of introduced degrees of freedom, thus demonstrating a significant improvement over the conventional BEM/DBEM implementation. However, the use of a large number of enriched elements or the implementation of a curved crack had a detrimental effect on the conditioning of the system which, in many cases, led to a solution of poor quality. To provide a solution to these problems, this chapter introduces an alternative form of enrichment which has little effect on the conditioning of the system and includes only two additional degrees of freedom. In addition, the implementation of the method is simplified, since it precludes the need for additional collocation points. Instead, it significantly reduces the number of introduced unknowns and formulates additional boundary integral equations from the crack tip solution; this leads to a restriction that only a single crack tip can be modelled using the method. In much the same manner as before, a detailed outline of the formulation is given first and then, by using an exact reference solution, the ability of the method to capture the singularity of a crack tip is verified and compared against the unenriched formulation. In addition, the much more favourable conditioning of the system is illustrated which allows (in contrast to the previous method of enrichment) application of the technique to a curved crack problem.

7.1 Formulation

The previous enrichment formulation described in Sec. 6.1.1 included the required singular crack tip field through the use of appropriate basis functions and the Partition of Unity Method. Instead, it is also possible to include enrichment with a combined form of the basis functions seen in Eqn. (5.48) in a fashion very similar to that implemented by Benzley (Sec. 5.3.3). In this way, only two additional degrees of freedom - which correspond to mode I and mode II fracture - are introduced and these take the form of enrichment coefficients. Furthermore, it is also possible, by subtracting off the nodal values of the shape functions, to return nodal displacements and SIFs *directly* which eliminates the need to carry out a post-processing routine. This section describes both forms of interpolation and, once these have been included in the DBIE and TBIE, the procedure by which two additional BIEs, derived from the first-order terms of Williams crack tip solution (Eqns (2.25) and (2.26)), is described.

7.1.1 Enriched displacement interpolation

To arrive at the expression for enriched displacements, it is necessary to use the first-order terms of Eqn. (2.26) to express crack tip displacements as

$$u_j = K_{\mathrm{I}}\psi^u_{\mathrm{I}j}(\rho,\theta) + K_{\mathrm{II}}\psi^u_{\mathrm{II}j}(\rho,\theta) \tag{7.1}$$

where the the usual mode I and II SIFs are present and the combined enrichment functions $\psi^u_{\mathrm{I}j}$ and $\psi^u_{\mathrm{II}j}$ are given by

$$\psi^u_{\mathrm{I}x} = \frac{1}{2\mu}\sqrt{\frac{\rho}{2\pi}}\cos(\theta/2)[\kappa - 1 + 2\sin^2(\theta/2)] \tag{7.2a}$$

$$\psi^u_{\mathrm{II}x} = \frac{1}{2\mu}\sqrt{\frac{\rho}{2\pi}}\sin(\theta/2)[\kappa + 1 + 2\cos^2(\theta/2)] \tag{7.2b}$$

$$\psi^u_{\mathrm{I}y} = \frac{1}{2\mu}\sqrt{\frac{\rho}{2\pi}}\sin(\theta/2)[\kappa + 1 - 2\cos^2(\theta/2)] \tag{7.2c}$$

$$\psi^u_{\mathrm{II}y} = -\frac{1}{2\mu}\sqrt{\frac{\rho}{2\pi}}\cos(\theta/2)[\kappa - 1 - 2\sin^2(\theta/2)] \tag{7.2d}$$

Expression (7.1) on its own gives the required crack tip displacement field, but to allow any arbitrary displacement field to be approximated (which may contain rigid body motion), it is necessary to reformulate this as

$$u_j = \sum_{a=1}^{M} N_a u_j^a + \tilde{K}_{\mathrm{I}} \psi_{\mathrm{I}j}^u + \tilde{K}_{\mathrm{II}} \psi_{\mathrm{II}j}^u \tag{7.3}$$

which is very similar to that given by Eqn. (5.38). By including the nodal terms u_j^a in this fashion, the terms $\tilde{K}_{\mathrm{I}}$ and $\tilde{K}_{\mathrm{II}}$ do not correspond to SIFs but rather, they represent enrichment coefficients for each fracture mode. Therefore, to return real displacements, these coefficients must be multiplied by the relevant enrichment functions (Eqns 7.2) and then combined with the terms u_j^a, which can be interpreted as displacements representing rigid-body motion of the crack tip. Since the correct crack tip displacement behaviour is included in this formulation, it is expected, in much the same manner as the PUM formulation, that more accurate results will be obtained for crack problems once this expression is substituted into the DBIE and TBIE for the crack tip displacement approximation.

7.1.2 Alternative enriched interpolation - direct SIF output

The interpolation procedure outlined in the previous section showed that the nodal values u_j^a did not represent real displacements and an additional calculation was required to obtain the correct result. Instead, an alternative form of interpolation, and one that was successfully implemented by Benzley (Eqn. (5.38)), is to subtract off the nodal values of the enrichment functions, thereby returning real displacements and, more importantly, stress intensity factors. Using the same notation as in the previous section, this is achieved by interpolating displacements in the following way

$$u_j = \sum_{a=1}^{M} N_a u_j^a + K_{\mathrm{I}} \sum_{a=1}^{M} N_a \left(\psi_{\mathrm{I}j}^u - \bar{\psi}_{\mathrm{I}ja}^u \right) + K_{\mathrm{II}} \sum_{a=1}^{M} N_a \left(\psi_{\mathrm{II}j}^u - \bar{\psi}_{\mathrm{II}ja}^u \right) \tag{7.4}$$

where the function $\bar{\psi}_{lja}^u$ denotes the value of the enrichment function ψ_{lj}^u at node a. The ability of this interpolation to return real displacements is obtained by the use of the functions $N_a \left(\psi_{lj}^u - \bar{\psi}_{lja}^u \right)$ ($l = \mathrm{I}, \mathrm{II}$) which not only equal zero at node a, but also equal zero at all other nodal points on the element. To illustrate this more clearly, the enrichment function $\psi_{\mathrm{I}y}^u(\xi)$, shown in Fig. 7.1a, is taken over a flat discontinuous element (lying adjacent to the crack tip) and then combined with the shape function for node $a = 1$ to arrive at the required interpolation function, illustrated in Fig. (7.1b). From this, it can be clearly seen that the enrichment function passes through zero at each of the nodal points and thus, the second and third terms of

Eqn. (7.4) will disappear at nodal points. However, even although the direct output of displacements is useful, what is even more beneficial when interpolating displacements in this manner is the ability to return K_{I} and K_{II} directly (rather than nodal enrichment coefficients) precluding the need for post-processing routines. But before post-processing routines can be discarded altogether, the accuracy of the SIFs returned directly must be assessed and compared with other methods. The details and results of such a study are outlined in Sec. 7.3.2.

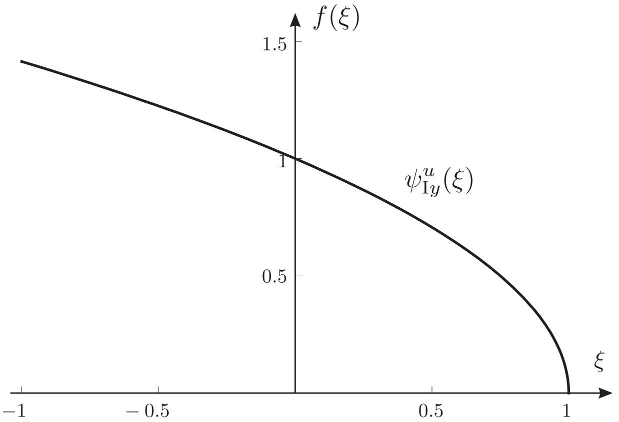

(a) Enrichment function for flat crack, $\theta = \pi$

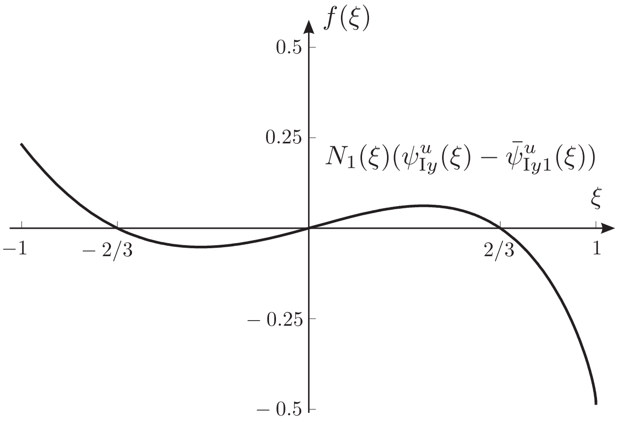

(b) Enrichment interpolation function for node 1

Figure 7.1: Enrichment interpolation for direct direct SIF output

7.1.3 Enriched DBIE and TBIE

The previous two sections outlined enriched displacement approximations that can be used to capture the singular field experienced around a crack tip, but to arrive at an enriched BEM/DBEM formulation, it is necessary to substitute these expressions into the displacement BIE and traction BIE given by Eqns (3.68) and (3.83) respectively. This is exactly the same procedure as carried out for the PUM enrichment, but with some fundamental differences. Before, to solve for the additional DOF created by enrichment, the PUM enrichment method made use of additional collocation points that provide extra relations between the boundary parameters. Because of this, it was necessary to formulate the BIEs in such a way that collocation could take place at any arbitrary point on the boundary (not necessarily at nodal points). In contrast, the present method makes no such demand since, as will be shown in Sec. 7.2.1, the enrichment coefficients are combined into just two terms and these can be solved for by two appropriately formed BIEs.

With the assumption that collocation only occurs at nodal points, the enriched DBIE can be formed by substituting either the displacement approximation given by Eq. (7.3) or (7.4) (in the case of direct SIF output) into Eq. (3.68). For illustration, only the approximation given by (7.3) will be applied here since the task of applying the second displacement approximation is almost identical. Following the same procedure as for the PUM enrichment, the enriched DBIE is given by

$$C_{ij}(\mathbf{x}')\left(u_j(\mathbf{x}') + \tilde{K}_l\psi^u_{lj}(\mathbf{x}')\right) + \sum_{n=1}^{N_e}\sum_{a=1}^{M} P^{na}_{ij}u^{na}_j + \sum_{n=1}^{N_e}\sum_{a=1}^{M} \tilde{P}^{na}_{ijl}\tilde{K}_l = \sum_{n=1}^{N_e}\sum_{a=1}^{M} Q^{na}_{ij}t^{na}_j, \qquad l = \text{I,II}. \tag{7.5}$$

The terms P^{na}_{ij} and Q^{na}_{ij} are the same as Eqns (3.69a) and (3.69b) while $\tilde{P}^{na}_{ijl}$ is given by

$$\tilde{P}^{na}_{ijl} = \int_{-1}^{1} N_a(\xi)T_{ij}[\mathbf{x}', \mathbf{x}(\xi)]\psi^u_{lj}(\xi)J^n(\xi)d\xi \tag{7.6}$$

if element n is enriched or $\tilde{P}^{na}_{ijl} = 0$ otherwise. Unlike Eq. (6.3) where shape functions were used to distribute the jump term C_{ij}, allowing collocation at any general point on the boundary, no shape functions are present in the first term of (7.5) since additional collocation points are not required. Meanwhile, for the implementation of the DBEM, the TBIE is enriched in exactly the same manner by substituting expression (7.3) into the discretised TBIE given by (3.83). This can then be written as

$$\frac{1}{2}t_j(\mathbf{x}') + n_i(\mathbf{x}')\sum_{n=1}^{N_e}\sum_{a=1}^{M} E^{na}_{kij}u^{na}_k + n_i(\mathbf{x}')\sum_{n=1}^{N_e}\sum_{a=1}^{M} \tilde{E}^{na}_{kijl}\tilde{K}_l = n_i(\mathbf{x}')\sum_{n=1}^{N_e}\sum_{a=1}^{M} F^{na}_{kij}t^{na}_k \tag{7.7}$$

where

$$\tilde{E}^{na}_{kijl} = \int_{-1}^{1} N_a(\xi) S_{kij}[\mathbf{x}', \mathbf{x}(\xi)] \psi^u_{lk}(\xi) J^n(\xi) d\xi \tag{7.8}$$

if element n is enriched or $\tilde{E}^{na}_{kijl} = 0$ otherwise.

Now that the enriched BIEs have been described, the system of equations can be formed - in exactly the same manner as described in Sec. 6.1.2 - by collocating around the boundary but taking care to use different BIEs on each side of the crack surface. Replacing $\mathbf{x}'$ with $\mathbf{x}^\mathbf{c}$ in Eqns (7.5) and (7.7), and arbitrarily choosing the enriched DBIE for the upper crack surface Γ^{c+} while the enriched TBIE is used on the lower crack surface Γ^{c-} (it may be useful to refer back to Figs 3.16 and 3.17), the system of equations can be written as

$$\begin{aligned} C_{ij}(\mathbf{x}^\mathbf{c})\big(u_j(\mathbf{x}^\mathbf{c}) + \tilde{K}_l \psi^u_{lj}(\mathbf{x}^\mathbf{c})\big) &+ \sum_{n=1}^{N_e}\sum_{a=1}^{M} P^{na}_{ij}(\mathbf{x}^\mathbf{c}) u^{na}_j \\ &+ \sum_{n=1}^{N_e}\sum_{a=1}^{M} \tilde{P}^{na}_{ijl}(\mathbf{x}^\mathbf{c}) \tilde{K}_l = \sum_{n=1}^{N_e}\sum_{a=1}^{M} Q^{na}_{ij}(\mathbf{x}^\mathbf{c}) t^{na}_j \quad \mathbf{x}^\mathbf{c} \in \Gamma^R \cup \Gamma^{c+} \end{aligned} \tag{7.9}$$

and

$$\begin{aligned} \frac{1}{2} t_j(\mathbf{x}') &+ n_i(\mathbf{x}') \sum_{n=1}^{N_e}\sum_{a=1}^{M} E^{na}_{kij}(\mathbf{x}^\mathbf{c}) u^{na}_k \\ &+ n_i(\mathbf{x}') \sum_{n=1}^{N_e}\sum_{a=1}^{M} \tilde{E}^{na}_{kijl}(\mathbf{x}^\mathbf{c}) \tilde{K}_l = n_i(\mathbf{x}') \sum_{n=1}^{N_e}\sum_{a=1}^{M} F^{na}_{kij}(\mathbf{x}^\mathbf{c}) t^{na}_k \quad \mathbf{x}^\mathbf{c} \in \Gamma^{c-} \end{aligned} \tag{7.10}$$

This marks the end of the enrichment formulation, but before we move on, it is useful to make some key points relating the present procedure to the previous form of enrichment and the tasks that are required to fully implement the method:

- The introduction of enrichment functions to singular and hypersingular integrals ($\tilde{P}^{na}_{ijl}$ and $\tilde{E}^{na}_{kijl}$) requires the use of a special numerical integration routine. Although analytical expressions can be derived, they are limited in their application and cannot be used for curved elements. An integration procedure capable of evaluating general singular and hypersingular integral was presented in Sec. 6.2.2 and exactly the same routine is used in the present work.

- Eqns (7.9) and (7.10) allow a system of equations to be formed, but these do not provide a sufficient number of relations to solve for the additional unknowns $\tilde{K}_\mathrm{I}$ and $\tilde{K}_\mathrm{II}$. It has been mentioned briefly before that additional

BIEs, formed from the crack tip solution, are used to provide the extra relations, but a description of how they are formed and the process by which they are implemented is now required.

7.2 Implementation

With the introduction of only two additional degrees of freedom, the current enrichment formulation demonstrates a simplification over the previous method of enrichment since no additional collocation points are required and, correspondingly, the system of equations is reduced in size. What will be shown here is the construction of two additional BIEs formed from the crack solution which, when used in conjunction with the enriched BIEs given in the previous section, creates a simple procedure that can be easily implemented.

7.2.1 Additional crack tip BIEs

To explain the use of the crack-tip displacements and stresses as fundamental solutions, Betti's reciprocal theorem, which can be used to derive the BEM, is recalled. Denoting two separate states as (u_i, t_i) and (u_i^*, t_i^*) and ignoring body forces, Betti's reciprocal theorem can be written as

$$\int_\Gamma t_j^* u_j d\Gamma = \int_\Gamma u_j^* t_j d\Gamma \tag{7.11}$$

where both integrals are taken along the boundary of the domain. Conventionally, the state (u_i^*, t_i^*) is chosen to correspond to Kelvin's point force solution in an infinite domain where certain assumptions are made about the behaviour of the material (i.e. linear elasticity). Instead, the crack-tip solution for displacements and tractions can be used where u_j^* is given by Eq. (7.1) and t_j^* can be expressed as

$$t_j^* = K_{\mathrm{I}} \psi_{\mathrm{I}j}^t(\rho, \theta) + K_{\mathrm{II}} \psi_{\mathrm{II}j}^t(\rho, \theta) \tag{7.12}$$

where the functions $\psi_{\mathrm{I}j}^t$ and $\psi_{\mathrm{II}j}^t$ are determined from the stresses given by Eqns (2.36) and the relation $t_i = \sigma_{ij} n_j$ (see Appendix D.1). Then, by arbitrarily choosing $K_{\mathrm{I}} = 1$ and $K_{\mathrm{II}} = 0$, an addition BIE is formulated

$$\int_\Gamma \psi_{\mathrm{I}j}^t(\rho, \theta) u_j d\Gamma = \int_\Gamma \psi_{\mathrm{I}j}^u(\rho, \theta) t_j d\Gamma \tag{7.13}$$

This can be discretised using shape functions and summing over all elements to give

$$\sum_{n=1}^{N_e}\sum_{a=1}^{M} V_{\mathrm{I}j}^{na} u_j^{na} = \sum_{n=1}^{N_e}\sum_{a=1}^{M} W_{\mathrm{I}j}^{na} t_j^{na} \tag{7.14}$$

where

$$V_{\mathrm{I}j}^{na} = \int_{-1}^{1} N_a(\xi)\psi_{\mathrm{I}j}^{t}(\xi)J^n(\xi)d\xi \tag{7.15a}$$

$$W_{\mathrm{I}j}^{na} = \int_{-1}^{1} N_a(\xi)\psi_{\mathrm{I}j}^{u}(\xi)J^n(\xi)d\xi \tag{7.15b}$$

The second additional BIE is derived in exactly the same manner but instead using the values $K_{\mathrm{I}} = 0$ and $K_{\mathrm{II}} = 1$. However, before Eq. (7.14) can be applied to the enriched formulation, expression (7.3) must be substituted for u_j. This can be written as

$$\sum_{n=1}^{N_e}\sum_{a=1}^{M} V_{\mathrm{I}j}^{na} u_j^{na} + \sum_{n=1}^{N_e}\sum_{a=1}^{M} \tilde{V}_{\mathrm{I}jl}^{na}\tilde{K}_l = \sum_{n=1}^{N_e}\sum_{a=1}^{M} W_{\mathrm{I}j}^{na} t_j^{na} \tag{7.16}$$

where the additional term $\tilde{V}_{\mathrm{I}jl}^{na}$ is expressed as

$$\tilde{V}_{\mathrm{I}jl}^{na} = \int_{-1}^{1} N_a(\xi)\psi_{\mathrm{I}j}^{t}(\xi)\psi_{lj}^{u}(\xi)J^n(\xi)d\xi \tag{7.17}$$

except for unenriched elements where $\tilde{V}_{\mathrm{I}jl}^{na} = 0$.

In this way two additional BIEs are formed allowing the solution of the extra DOF $\tilde{K}_{\mathrm{I}}$ and $\tilde{K}_{\mathrm{II}}$.

7.2.2 Matrix construction

Now that each BIE has been described, it is useful to explain how the matrices **H** and **G** are constructed from submatrix terms in exactly the same manner as described in Sec. 6.2.4 for PUM enrichment. The fundamental difference however, is the combination of all enrichment coefficients into two additional unknowns $\tilde{K}_{\mathrm{I}}$ and $\tilde{K}_{\mathrm{II}}$ (or K_{I} and K_{I} in the case of direct SIF output) requiring no additional collocation points. Construction of the matrices can be described using the same example of a plate with a flat edge crack (Fig. 3.14) in which enrichment is applied to elements adjacent to the crack tip. The collocation point $\mathbf{x}^{\mathbf{c}}$ is taken to lie at each nodal point in turn where, if the point lies on any non-crack surface or the upper crack surface, the enriched DBIE of (7.5) is used. If the point lies on the lower crack surface, then the enriched TBIE (7.7) is used. Taking elements eight and nine as an example where the collocation point is chosen to lie on the first node of element nine, the submatrices for the enriched DBIE can be constructed as shown in Fig. 7.2a. The submatrices $\mathbf{H}_c^n$ and $\mathbf{G}_c^n$ are formed in exactly the same manner as in the unenriched DBEM while the enrichment terms are grouped together in the submatrix $\tilde{\mathbf{H}}_c^n$. Inspection of the terms A,B,C and D reveals that, due to the summation of the integral terms for each local node, it is not necessary to perform the integral of (7.6) for each local node - instead, the integration could be simplified by omitting the shape function and performing only one integral. However, implementing this into an existing DBEM computer routine may prove to be more costly than simply evaluating each nodal term and performing a summation.

In a very similar fashion, the additional BIEs (7.16) can be included by constructing a series of submatrices $\mathbf{V}^n$, $\mathbf{W}^n$ and combining all enrichment terms into a submatrix $\tilde{\mathbf{V}}^n$ (Fig. 7.2b). But, in contrast to the previous submatrix terms, since the additional BIEs do not correspond to a particular collocation point, these are only evaluated once for each element. Fig. 7.3 illustrates how the matrices $\mathbf{H}$ and $\mathbf{G}$ can then be constructed by substituting in the submatrix terms $\mathbf{H}_c^n$, $\mathbf{G}_c^n$ and $\tilde{\mathbf{H}}_c^n$ for each collocation point $\mathbf{x^c}$ (thus forming multiple rows) while the matrices $\mathbf{V}^n$, $\mathbf{W}^n$ and $\tilde{\mathbf{V}}^n$ are placed at the bottom of the matrix (arbitrarily). The symbol $+=$ denotes that a submatrix is added to any existing values in the matrix and therefore, for any particular row in the matrix $\mathbf{H}$, all the enrichment terms corresponding to that collocation point (or additional BIE) will be accumulated in the last two columns. For example, the present model applies enrichment to elements nine and ten and therefore, the last two columns in the matrix $\mathbf{H}$ will be made up of $\tilde{\mathbf{H}}_c^9+\tilde{\mathbf{H}}_c^{10}$ (or $\tilde{\mathbf{V}}^9+\tilde{\mathbf{V}}^{10}$). Finally, once the matrices are fully populated after collocating at each nodal point in turn, all unknowns are taken to the LHS while all known parameters are taken to the RHS thus forming the familiar system of equations $\mathbf{Ax} = \mathbf{b}$ which can then be solved.

7.3 Verification and testing

With the details of implementation now covered, it is necessary, using exactly the same procedure as for the previous method of enrichment (6.3.1), to verify that the method is capable of capturing the exact crack tip solution. Therefore, a portion of an infinite plate containing a straight centre crack and subject to a uniaxial stress (Fig. 6.9a) is modelled using a boundary element mesh where exact displacements

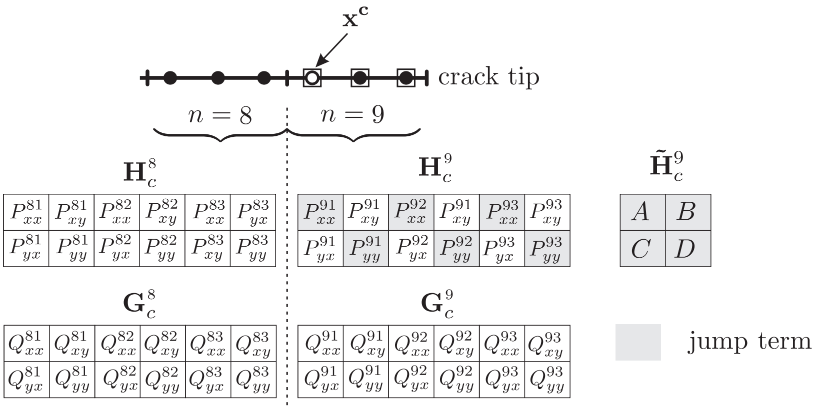

$$\mathbf{H}_c^8: \begin{array}{|c|c|c|c|c|c|}\hline P_{xx}^{81} & P_{xy}^{81} & P_{xx}^{82} & P_{xy}^{82} & P_{xx}^{83} & P_{yx}^{83} \\ \hline P_{yx}^{81} & P_{yy}^{81} & P_{yx}^{82} & P_{yy}^{82} & P_{xy}^{83} & P_{yy}^{83} \\ \hline \end{array} \qquad \mathbf{H}_c^9: \begin{array}{|c|c|c|c|c|c|}\hline P_{xx}^{91} & P_{xy}^{91} & P_{xx}^{92} & P_{xy}^{91} & P_{xx}^{93} & P_{xy}^{93} \\ \hline P_{yx}^{91} & P_{yy}^{91} & P_{yx}^{92} & P_{yy}^{92} & P_{yx}^{93} & P_{yy}^{93} \\ \hline \end{array} \qquad \tilde{\mathbf{H}}_c^9: \begin{array}{|c|c|}\hline A & B \\ \hline C & D \\ \hline \end{array}$$

$$\mathbf{G}_c^8: \begin{array}{|c|c|c|c|c|c|}\hline Q_{xx}^{81} & Q_{xy}^{81} & Q_{xx}^{82} & Q_{xy}^{82} & Q_{xx}^{83} & Q_{xy}^{83} \\ \hline Q_{yx}^{81} & Q_{yy}^{81} & Q_{yx}^{82} & Q_{yy}^{82} & Q_{yx}^{83} & Q_{yy}^{83} \\ \hline \end{array} \qquad \mathbf{G}_c^9: \begin{array}{|c|c|c|c|c|c|}\hline Q_{xx}^{91} & Q_{xy}^{91} & Q_{xx}^{92} & Q_{xy}^{92} & Q_{xx}^{93} & Q_{xy}^{93} \\ \hline Q_{yx}^{91} & Q_{yy}^{91} & Q_{yx}^{92} & Q_{yy}^{92} & Q_{yx}^{93} & Q_{yy}^{93} \\ \hline \end{array}$$

$$\begin{aligned}
A &= \tilde{P}_{xx\mathrm{I}}^{91} + \tilde{P}_{xy\mathrm{I}}^{91} + \tilde{P}_{xx\mathrm{I}}^{92} + \tilde{P}_{xy\mathrm{I}}^{92} + \tilde{P}_{xx\mathrm{I}}^{93} + \tilde{P}_{xy\mathrm{I}}^{93} \\
B &= \tilde{P}_{xx\mathrm{II}}^{91} + \tilde{P}_{xy\mathrm{II}}^{91} + \tilde{P}_{xx\mathrm{II}}^{92} + \tilde{P}_{xy\mathrm{II}}^{92} + \tilde{P}_{xx\mathrm{II}}^{93} + \tilde{P}_{xy\mathrm{II}}^{93} \\
C &= \tilde{P}_{yx\mathrm{I}}^{91} + \tilde{P}_{yy\mathrm{I}}^{91} + \tilde{P}_{yx\mathrm{I}}^{92} + \tilde{P}_{yy\mathrm{I}}^{92} + \tilde{P}_{yx\mathrm{I}}^{93} + \tilde{P}_{yy\mathrm{I}}^{93} \\
D &= \tilde{P}_{yx\mathrm{II}}^{91} + \tilde{P}_{yy\mathrm{II}}^{91} + \tilde{P}_{yx\mathrm{II}}^{92} + \tilde{P}_{yy\mathrm{II}}^{92} + \tilde{P}_{yx\mathrm{II}}^{93} + \tilde{P}_{yy\mathrm{II}}^{93}
\end{aligned}$$

(a) **H** and **G** submatrices formed by collocation

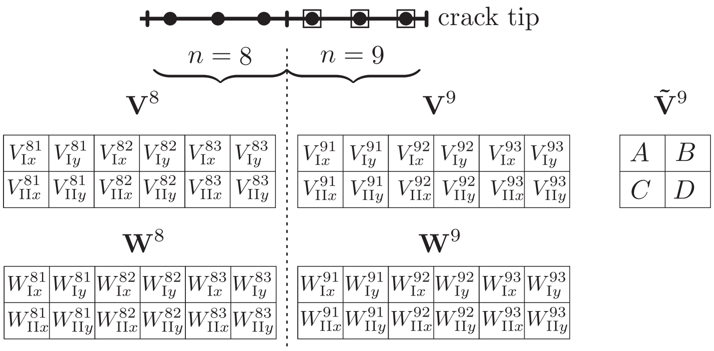

$$\mathbf{V}^8: \begin{array}{|c|c|c|c|c|c|}\hline V_{\mathrm{I}x}^{81} & V_{\mathrm{I}y}^{81} & V_{\mathrm{I}x}^{82} & V_{\mathrm{I}y}^{82} & V_{\mathrm{I}x}^{83} & V_{\mathrm{I}y}^{83} \\ \hline V_{\mathrm{II}x}^{81} & V_{\mathrm{II}y}^{81} & V_{\mathrm{II}x}^{82} & V_{\mathrm{II}y}^{82} & V_{\mathrm{II}x}^{83} & V_{\mathrm{II}y}^{83} \\ \hline \end{array} \qquad \mathbf{V}^9: \begin{array}{|c|c|c|c|c|c|}\hline V_{\mathrm{I}x}^{91} & V_{\mathrm{I}y}^{91} & V_{\mathrm{I}x}^{92} & V_{\mathrm{I}y}^{92} & V_{\mathrm{I}x}^{93} & V_{\mathrm{I}y}^{93} \\ \hline V_{\mathrm{II}x}^{91} & V_{\mathrm{II}y}^{91} & V_{\mathrm{II}x}^{92} & V_{\mathrm{II}y}^{92} & V_{\mathrm{II}x}^{93} & V_{\mathrm{II}y}^{93} \\ \hline \end{array} \qquad \tilde{\mathbf{V}}^9: \begin{array}{|c|c|}\hline A & B \\ \hline C & D \\ \hline \end{array}$$

$$\mathbf{W}^8: \begin{array}{|c|c|c|c|c|c|}\hline W_{\mathrm{I}x}^{81} & W_{\mathrm{I}y}^{81} & W_{\mathrm{I}x}^{82} & W_{\mathrm{I}y}^{82} & W_{\mathrm{I}x}^{83} & W_{\mathrm{I}y}^{83} \\ \hline W_{\mathrm{II}x}^{81} & W_{\mathrm{II}y}^{81} & W_{\mathrm{II}x}^{82} & W_{\mathrm{II}y}^{82} & W_{\mathrm{II}x}^{83} & W_{\mathrm{II}y}^{83} \\ \hline \end{array} \qquad \mathbf{W}^9: \begin{array}{|c|c|c|c|c|c|}\hline W_{\mathrm{I}x}^{91} & W_{\mathrm{I}y}^{91} & W_{\mathrm{I}x}^{92} & W_{\mathrm{I}y}^{92} & W_{\mathrm{I}x}^{93} & W_{\mathrm{I}y}^{93} \\ \hline W_{\mathrm{II}x}^{91} & W_{\mathrm{II}y}^{91} & W_{\mathrm{II}x}^{92} & W_{\mathrm{II}y}^{92} & W_{\mathrm{II}x}^{93} & W_{\mathrm{II}y}^{93} \\ \hline \end{array}$$

$$\begin{aligned}
A &= \tilde{V}_{\mathrm{I}x\mathrm{I}}^{91} + \tilde{V}_{\mathrm{I}y\mathrm{I}}^{91} + \tilde{V}_{\mathrm{I}x\mathrm{I}}^{92} + \tilde{V}_{\mathrm{I}y\mathrm{I}}^{92} + \tilde{V}_{\mathrm{I}x\mathrm{I}}^{93} + \tilde{V}_{\mathrm{I}y\mathrm{I}}^{93} \\
B &= \tilde{V}_{\mathrm{I}x\mathrm{II}}^{91} + \tilde{V}_{\mathrm{I}y\mathrm{II}}^{91} + \tilde{V}_{\mathrm{I}x\mathrm{II}}^{92} + \tilde{V}_{\mathrm{I}y\mathrm{II}}^{92} + \tilde{V}_{\mathrm{I}x\mathrm{II}}^{93} + \tilde{V}_{\mathrm{I}y\mathrm{II}}^{93} \\
C &= \tilde{V}_{\mathrm{II}x\mathrm{I}}^{91} + \tilde{V}_{\mathrm{II}y\mathrm{I}}^{91} + \tilde{V}_{\mathrm{II}x\mathrm{I}}^{92} + \tilde{V}_{\mathrm{II}y\mathrm{I}}^{92} + \tilde{V}_{\mathrm{II}x\mathrm{I}}^{93} + \tilde{V}_{\mathrm{II}y\mathrm{I}}^{93} \\
D &= \tilde{V}_{\mathrm{II}x\mathrm{II}}^{91} + \tilde{V}_{\mathrm{II}y\mathrm{II}}^{91} + \tilde{V}_{\mathrm{II}x\mathrm{II}}^{92} + \tilde{V}_{\mathrm{II}y\mathrm{II}}^{92} + \tilde{V}_{\mathrm{II}x\mathrm{II}}^{93} + \tilde{V}_{\mathrm{II}y\mathrm{II}}^{93}
\end{aligned}$$

(b) Submatrices for additional BIEs

Figure 7.2: Construction of submatrices for combined enrichment method

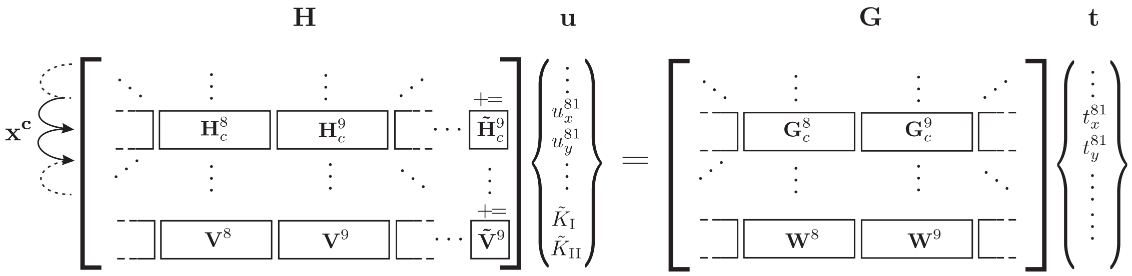

Figure 7.3: Construction of **H** and **G** matrices from submatrix terms for combined enrichment method

and tractions can be prescribed on all boundaries. If all elements around the boundary are enriched, then the displacement at each node is given by Eq. (7.3) where the terms u_j^a, $\tilde{K}_{\mathrm{I}}$ and $\tilde{K}_{\mathrm{II}}$ can be found from the exact crack solution. In fact, since the terms u_j^a represent rigid body motion of the crack tip, they equal zero for the infinite plate problem and the coefficients $\tilde{K}_{\mathrm{I}}$ and $\tilde{K}_{\mathrm{II}}$ are equal to the real SIFs (set arbitrarily to $K_{\mathrm{I}} = 1.0$ and $K_{\mathrm{II}} = 0$). Imposing these boundary conditions and comparing the LHS and RHS for each of the collocation points, it is found, as before, that both sides are equal (to machine precision) with differences in the order of 10^{-5}%. We can therefore be confident that, assuming no conditioning problems are encountered in solving the system of equations, the method will be able to capture the singularity experienced at a crack tip.

The next step is to assess the ability of the method to solve a more realistic scenario where parameters on part of the boundary remain unknown and need to be solved for. Like before, the problem of an infinite plate[1] can be formulated in this way by imposing the exact displacement boundary conditions on all non-crack boundaries (using Eqns (2.37) and letting $K_{\mathrm{I}} = 1.0$ and $K_{\mathrm{II}} = 0$) and zero tractions on crack faces. Using exactly the same mesh as for the previous form of enrichment where four elements are used on all lines and spaced equally throughout (Fig. 6.10a), an initial qualitative assessment of the ability of the method to capture the crack tip singularity can be made by comparing displacements along the crack faces. Fig. 7.4 illustrates the results of an unenriched DBEM analysis (using the same mesh) and the results from the present enrichment strategy where only the crack tip elements are enriched. The inclusion of enrichment is clearly improving accuracy, particularly as the crack tip is approached, and exhibits results very similar to the previous form of enrichment (see Fig. 6.11). This confirms that enrichment is achieving its goal of

---

[1] This problem continues to be used to allow comparison with *exact* solutions

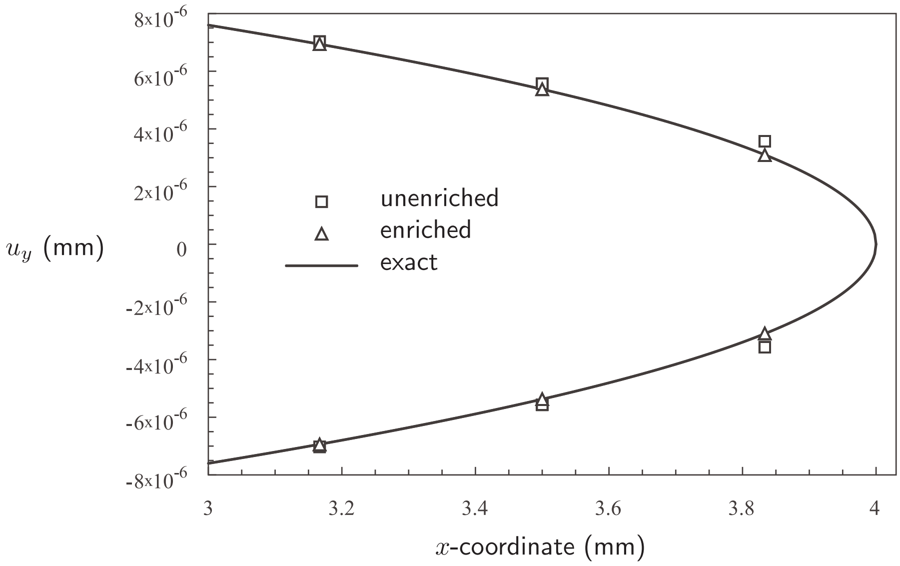

Figure 7.4: Crack tip displacement comparison for combined enrichment and unenriched DBEM

higher accuracies for a small number of introduced DOF, but by themselves these results are not especially useful since it is the value of the SIFs - whose accuracy is paramount in fracture design - that we are most concerned with. For this reason, the discussion now focusses on the accurate evaluation of these parameters.

7.3.1 J-integral SIF determination

The simplest technique of obtaining SIFs is through displacement extrapolation where a rearranged form of the crack tip displacements given by Eqns (2.37) can be used. However, as shown by Fig. 6.12, it is often not clear what value represents the best approximation and in some cases it is difficult to make *any* sensible approximation (particularly in the case of quadratic approximations). Therefore this method is not used here but instead, the much more robust J-integral method, which has been applied successfully to the previous form of enrichment, is employed.

Using a set of circular integration paths centred at the crack tip and starting and finishing at nodal points (Fig. 6.13), the mode I SIFs can be determined using Eq. (2.68) (since $K_{\text{II}} = 0$). Two meshes were used for comparison: a coarse mesh of four elements per line and a fine mesh with twelve elements per line (Figs 6.10a and 6.10b) where only the crack tip elements were enriched in each case. Fig. 7.5 illustrates the results for both the unenriched and enriched analyses where a large improvement is seen once enrichment is applied. The difference between the coarse and fine meshes for the enriched analyses is minimal, but this is only because both results [for paths four to eight] are so accurate. For example, path four of the coarse mesh gives $K_{\mathrm{II}} = 0.999969064$ while the fine mesh, using the same integral path, gives a slightly more accurate value of $K_{\mathrm{II}} = 0.9999726713$; it is only because there is such a large improvement in accuracy that these values appear coincident. However, one feature of the plot which requires further thought, and which was actually demonstrated in the previous form of enrichment (Fig. 6.16), is the discrepancy between the results obtained from the first two paths (two and three) and each of the others. To explain the reason behind this, it is necessary to investigate in more detail the J-integral values obtained from these paths.

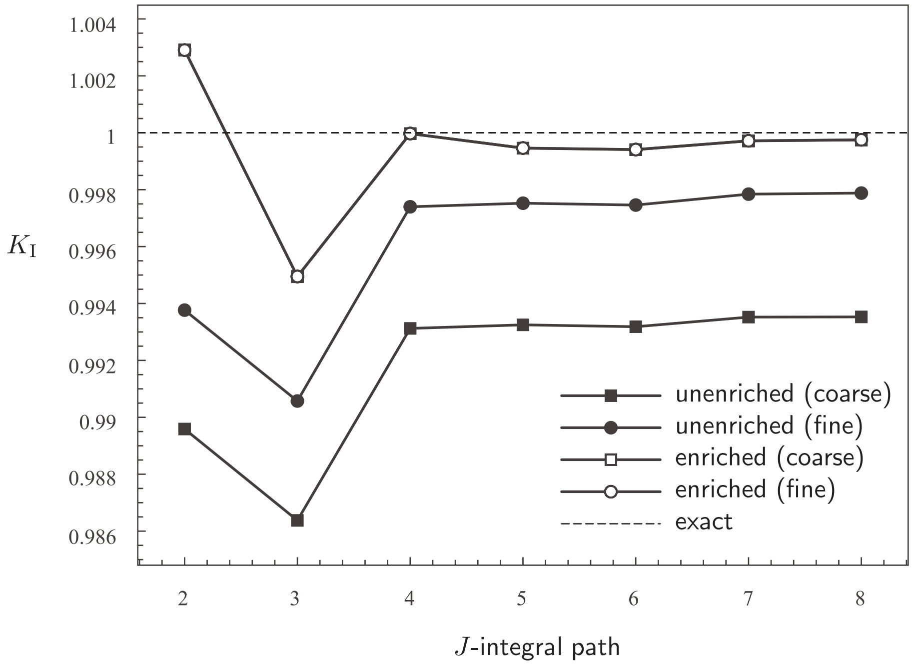

Figure 7.5: SIF comparison of unenriched and combined basis enrichment using the J-integral

In the present implementation, each of the J-integral paths consists of a series of points at which the integrand of $Wn_x - t_i u_{i,x}$ is evaluated and then integrated over the entire path using an appropriate integration technique. The number of points can be varied, and it is expected that as this number increases, the resulting SIF should approximate the correct value more closely. However, Fig. 7.6, which illustrates the SIFs for the enriched coarse mesh with varying numbers of J-integral points, shows that this is not necessarily always the case. Path four shows the expected result where the error in the SIF decreases as the number of points increases, although at a large number of points the error increases. Path three shows an altogether completely different trend where the error in the SIF actually increases as the number of points increases. To explain these features, we examine the values of the integrand as we move around each of the integral paths Γ_J.

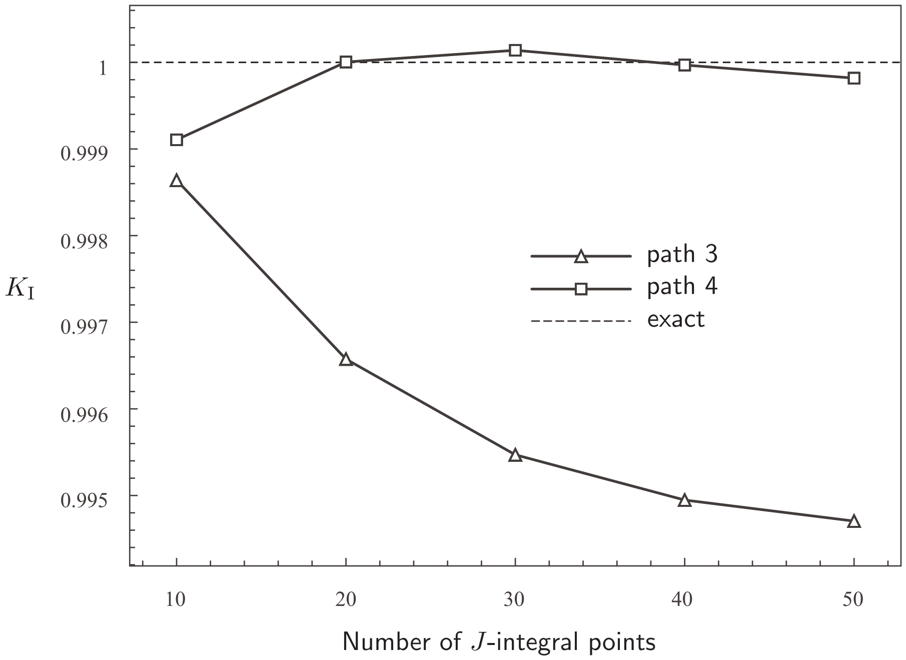

Figure 7.6: SIF dependence on number of J-integral points - combined enrichment

Taking the case of path four first (which we know demonstrates more accurate results), the computed values of the integrand can be plotted along Γ_J and compared to the known exact solution which is found using Eqns (2.36), (2.37) and (3.14) while noting that the outward pointing normals around a circle are given by simple trigonometric functions. The computed values for ten and fifty points are shown in Figs 7.7a and 7.7b where it can be seen that both sets of results compare favourably with the exact solution and explain the high accuracy of SIFs for this path. The results for path three are illustrated in Figs 7.8a and 7.8b where close inspection reveals the reason for the decrease in accuracy at higher number of J-integral points. For the case of ten points, all the computed values lies close to the exact profile, but in the case of fifty points, the values diverge from those expected at the beginning and end of the integral path. This is due to the combination of two effects:

- As the integration path decreases in size the internal points along the path move close to the boundary
- As the number of J-integral points is increased along the path, the proximity to the boundary is increased further

Therefore, since the kernels which are used to evaluate σ_{ij} and ε_{ij} are of $\mathcal{O}(1/r^2)$, the closer the internal points move to the boundary the larger the inaccuracies introduced by nearly-singular integrals (Sec. 4.2). The values obtained in Figs 7.7 and 7.8 were obtained using high-order Gauss-Legendre quadrature which can be seen to be insufficient for the smaller integral paths and it is therefore necessary, either through the use of sub-elements or another technique such as the subtraction of singularity technique illustrated in [108] or a transformation [58], to accurately evaluate the nearly-singular integrals.

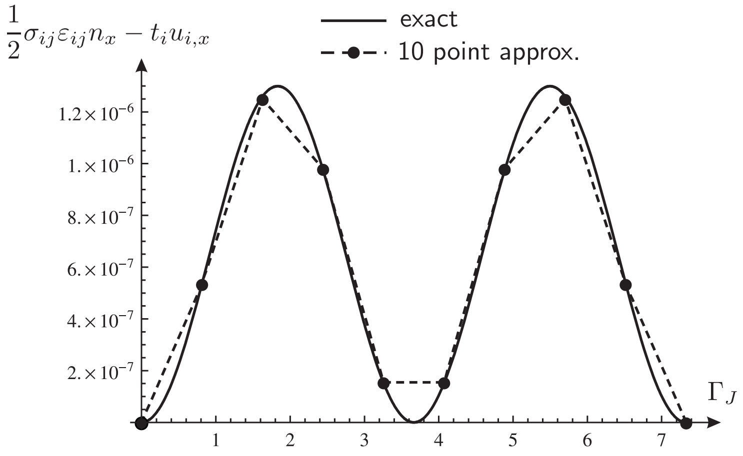

(a) 10 J-integral points

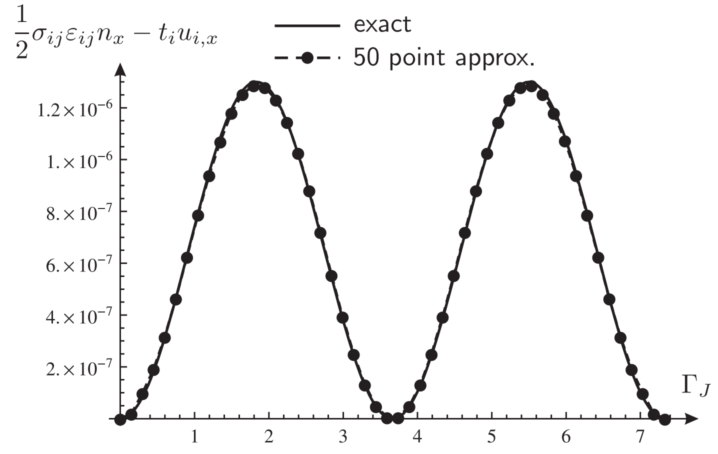

(b) 50 J-integral points

Figure 7.7: Comparison of computed and exact values for J-integral - path four

Lastly, since all the previous plots of the J-integral have used data from enriched analyses, it is useful to compare these with that obtained with an unenriched implementation. Fig. 7.9 illustrates the values obtained for an unenriched analysis using the coarse mesh of four elements per line and path four of the J-integral using fifty internal points. A direct comparison can therefore be made with the enriched

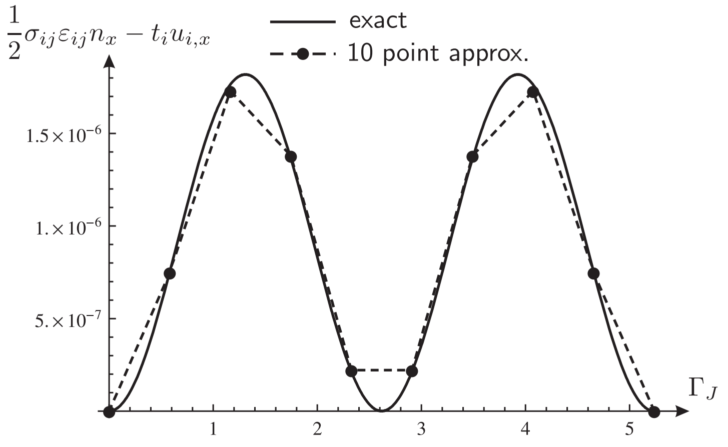

(a) 10 J-integral points

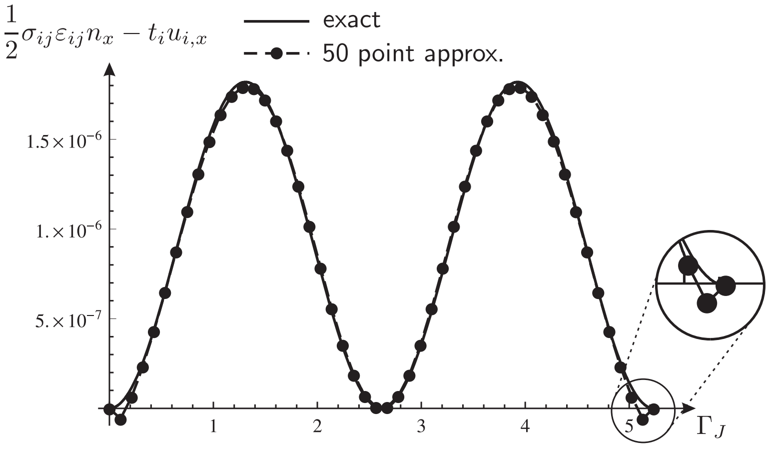

(b) 50 J-integral points

Figure 7.8: Comparison of computed and exact values for J-integral - path three

analysis shown in Fig. 7.7b. Fig. 7.9 can be imagined as split into four parts corresponding to the quadrants of the circular integration path: the second and third parts show a close correspondence with the exact result while the first and fourth demonstrate a sizeable difference. The reason for this can be explained once again by noting that the kernels used for stress and strain evaluation at internal points contain singularities that become more pronounced as the boundary is approached. The difference is not, however, created by a failure to integrate nearly-singular integrals with sufficient accuracy, but is instead created by the inaccurate displacements along the crack faces which, when multiplied by the S_{kij} kernel in (3.59), magnifies the error. A sensible question may be to ask why all four sections of the plot are not affected by this inaccuracy, but this can be answered simply by realising that the first and fourth quadrants of the integration path are closest to the crack boundary (which is where the errors arise) while the second and third are further away and less affected.

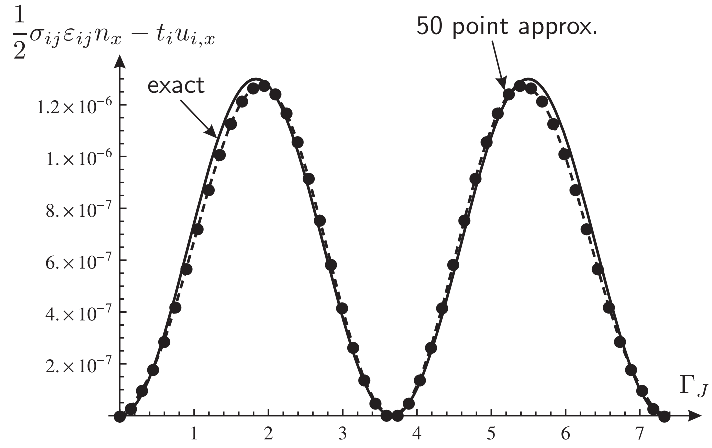

Figure 7.9: Comparison of computed and exact values for J-integral with no enrichment - path four

7.3.2 Direct SIF output

As an alternative to the J-integral technique, the present method is also capable of producing SIFs directly if the interpolation scheme outlined in Sec. 7.1.2 is used. This has an obvious advantage over the J-integral since no post-processing is required - the values can simply be obtained from the solution vector $\mathbf{x}$ - but to assess the accuracy of this technique, a direct comparison needs to be made with the results obtained with the J-integral. The infinite plate example was used with initially four elements per line which was increased in steps of two up to a total of twelve elements per line. In both methods enrichment was applied to the crack tip elements. The results are shown in Fig. 7.10 where only the J-integral results of path four are shown to allow for a clear comparison. What can be concluded from this plot is that, even though the direct output is capable of evaluating the SIF with an approximate error of 2.5%, the results obtained through the J-integral are far superior. Of course, the cost of obtaining these highly accurate results is the use of a post-processing routine that requires additional computation due to evaluation of stresses and strains at internal points, but the importance of SIF accuracy makes this procedure worthwhile. To give an idea of the proportion of the total computational time which is taken up by the J-integral evaluation, Tbl. 7.1 quantifies the runtimes for the BEM analysis and J-integral routine for both the coarse and fine meshes. It should be noted that each of the analyses used a fixed number of Gauss points and therefore considerable computational savings could be made if an adaptive integration procedure was implemented. All results were obtained on a dual core 2.20 GHz processor. The results show that the J-integral post-processing routine is comparable to BEM analysis time and, as expected, there is a linear relationship between the J-integral runtime and the number of internal points. But what is most important is that the extra runtime required to achieve highly accurate results through the J-integral is not unreasonable and, in the author's opinion, entirely justifiable.

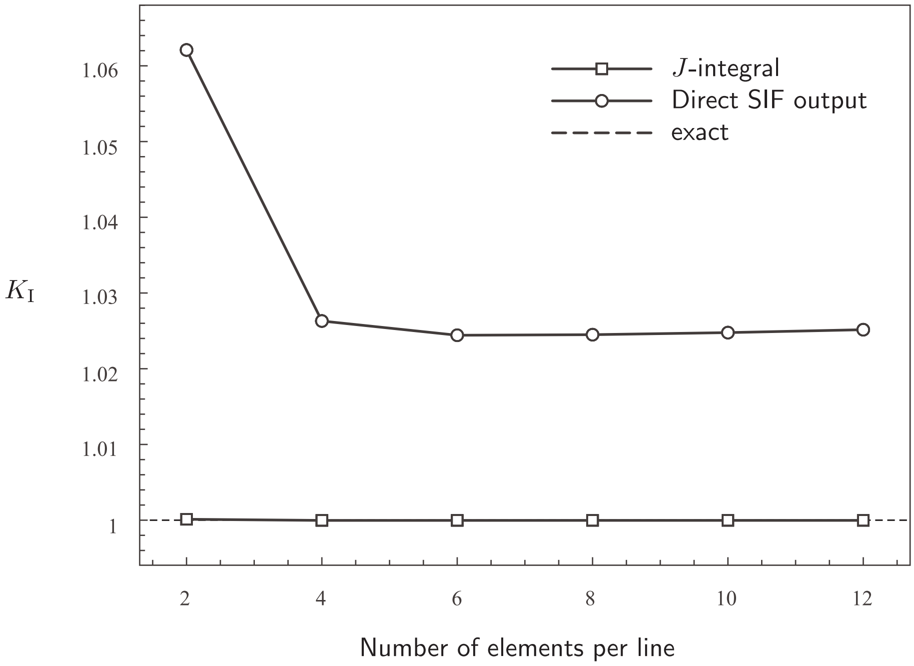

Figure 7.10: Comparison of J-integral and direct SIF output

Table 7.1: Comparison of runtimes for coarse and fine meshes and J-integral post-processing routine

		J-integral analysis(s)				
Mesh	Enriched BEM analysis(s)[b]	10pts	20pts	30pts	40pts	50pts
Coarse	2.50	0.89	1.66	2.53	3.06	3.78
Fine	23.06	2.24	4.84	7.44	9.19	12.00

---

[b] Meshing and solution of system of equations (excludes J-integral)

7.3.3 Effect of enrichment zone size

Just like the previous form of enrichment, the present method allows the zone of enrichment to be extended over multiple elements and therefore, as the zone of enrichment is increased, accuracy should improve. In this case, the cost of enriching additional elements is to compute extra integral terms that contribute to the last two columns of the **A** matrix, but it is found during implementation that for most cases the additional effort required to compute the enriched integrals once the unenriched integrals have already been determined is negligible, and enrichment can be extended easily. The same tests used to determine the effect of increasing enrichment on the PUM enrichment were used where the infinite plate example was modelled using a boundary mesh varying from four to twelve elements per line. Using Eqn. (6.11), the number of enriched elements was varied from $\bar{N}_{enr} = 0$ (no enrichment) to $\bar{N}_{enr} = 1$ (crack faces fully enriched) and, as before, path four of the J-integral was used to determine K_{I}. Fig. 7.11, which shows the results from each of the analyses, illustrates a few key features. The first point note is that the results appear to converge to a value that is incorrect - in fact, the converged value is approximately 0.99997 and the difference is only created due to the high accuracy of all the plotted results. But what is common amongst each of the meshes is the convergence achieved as the number of enriched elements is increased and this, in contrast to the PUM enrichment, is seen for *all* mesh densities. As described in Sec. 6.3.4, as the number of enriched elements increases in the PUM enrichment, there is a direct effect on the conditioning of the system which becomes so severe that at high values of $\bar{N}_{enr}$ and high mesh densities, no sensible solution can be found. In contrast, the current method of enrichment has a negligible effect on the conditioning of the system. This can be shown by plotting the condition numbers for the coarse and fine meshes as $\bar{N}_{enr}$ increases (Fig. 7.12). This shows a rise in the condition number from no enrichment to enrichment of the crack tip elements, but as $\bar{N}_{enr}$ increases further, no further rises are seen. Importantly, the values for

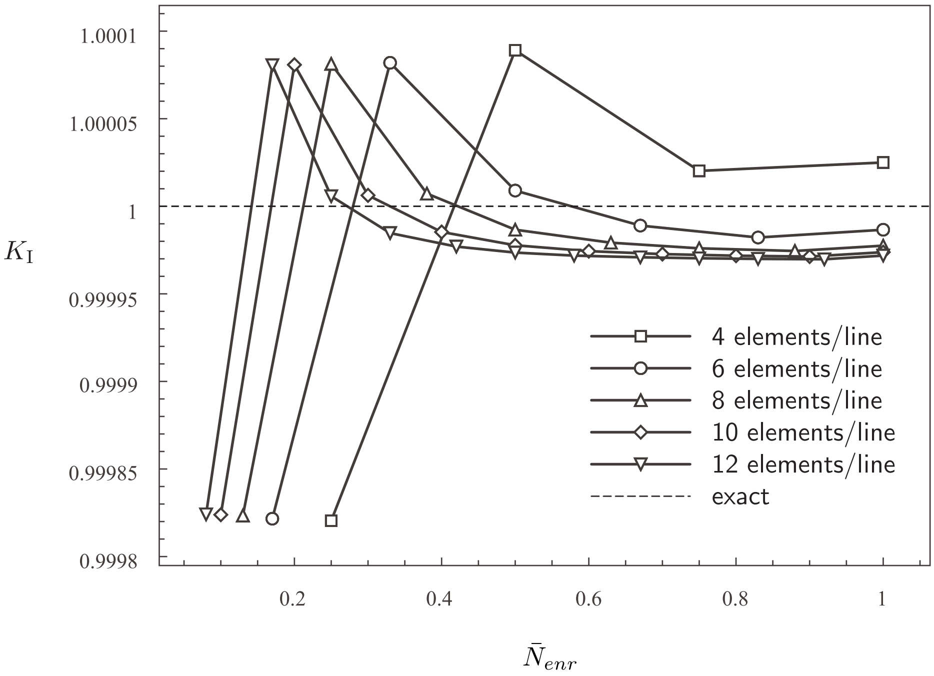

Figure 7.11: Effect on SIF for increasing enrichment - combined basis method

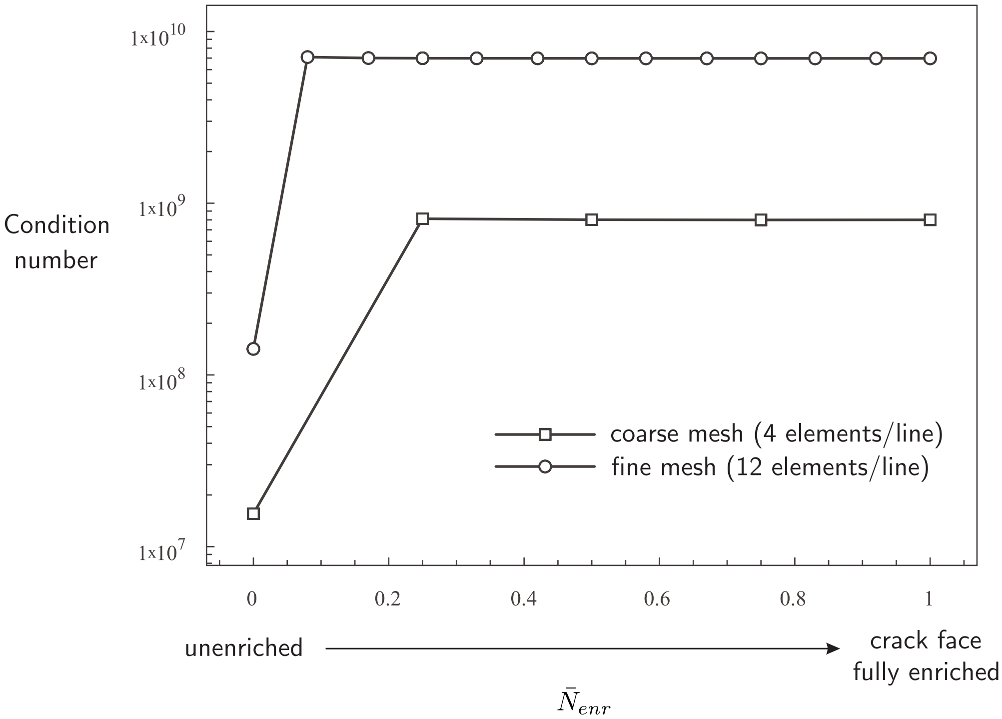

Figure 7.12: Condition numbers for combined basis enrichment with coarse and fine meshes

both meshes are relatively low which prevents the need for a special numerical solver routine - a conventional Gaussian elimination solver can be used for all cases - and this represents a significant advantage over the previous form of enrichment.

7.3.4 Curved crack analysis

As discovered in Sec. 6.3.5, the previous form of enrichment encountered difficulties when modelling curved cracks due to the large condition numbers experienced once enrichment was introduced. The present strategy has been shown to have a much smaller effect on the conditioning of the system and it is therefore expected that the same problems will not be encountered when the method is applied to a curved crack problem. As a first step in the verification of the method, the problem of a curved crack within a finite plate can be modelled (Fig. 6.21) where inspection of displacements along the crack face will reveal any irregularities. Applying a coarse mesh of four elements per line (Fig. 6.21b) and applying enrichment only to the crack tip elements, the crack face displacements are shown in Fig. 7.13 where the displacements obtained from an unenriched analysis using the same mesh are also plotted for comparison. By comparing this displacement plot with that obtained using the PUM enrichment strategy (Fig. 6.22) it is clear that the current enrichment strategy is producing a much more sensible displacement profile. However, even though the enriched implementation demonstrates the expected displacement profile, it is not possible to assess the accuracy of the method since no exact solution is given for displacements around a curved crack. Instead, by employing the analytical solution given by Muskhelishvili [13] for a curved crack in an infinite domain which states exact values for stress intensity factors, it is possible to quantify the improvements seen once enrichment is introduced.

Fig. 7.14 illustrates the problem of a curved crack within an infinite domain subject to a biaxial load which, if the loading, geometry and material properties are as described, is found to have exact values for J_1=0.06592 and J_2=-0.04661 (where J_1 and J_2 are defined by Eq. (2.76)). These values can also be represented in terms of SIFs (using relations 2.68 and 2.77), but for the purposes of this study there is little need to do so - we are simply interested in accuracy of the method which can be readily found using the computed values of J_1 and J_2. However, in contrast to all previous implementations of the J-integral where only the value of J_1 (J) was determined, the presence of a curved crack necessitates the use of the procedure described in Sec. 2.6.3 due to the presence of a non-zero integral term

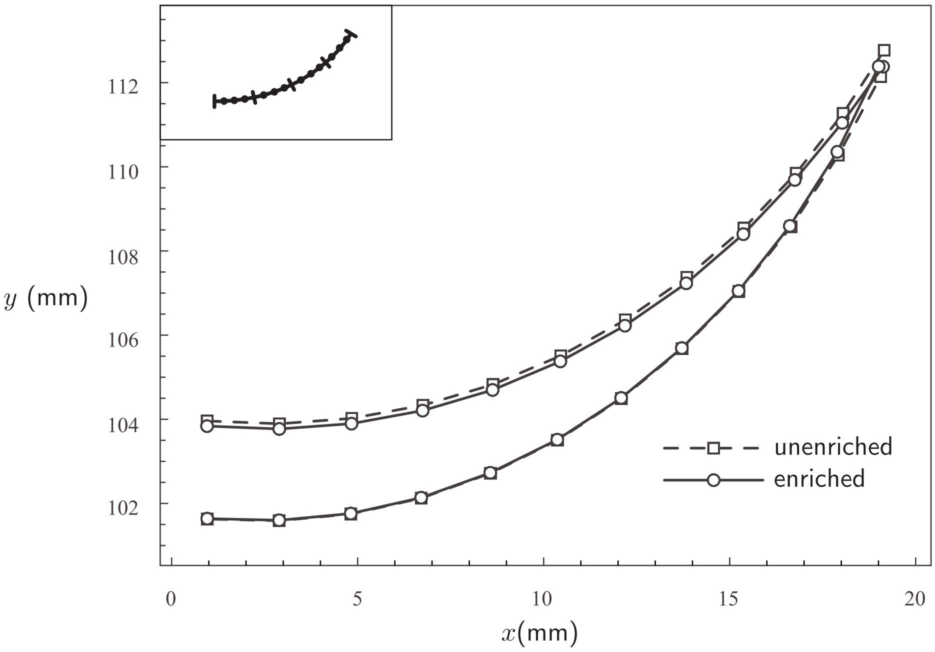

Figure 7.13: Exaggerated displacements for curved crack for unenriched and enriched analysis

found along the crack faces. Recalling Eqn. (2.80) which is the expression used to numerically determine both J_1 and J_2, the first integral term was evaluated by taking a circular integration path (centred at the crack tip) which started and finished at nodal points on the crack surface (Fig. 7.15). In addition, the integral is taken over the crack surfaces (as shown in Fig. 2.18) requiring the definition of a cutoff radius R which must take multiple values to allow Λ to be evaluated by a least-squares routine. In the present implementation five values were chosen as R=0.01l, 0.015l, 0.02l, 0.025l, 0.03l which are of the recommended order as described in [37]. To approximate an infinite plate, a boundary mesh with dimensions L=40mm and $w/2$=20mm was used where an equal number of elements was applied to each line (Fig. 7.16a shows an example boundary mesh of six elements per line) while in the case of the enriched analysis, the elements adjacent to the crack tip were enriched (Fig. 7.16b). A convergence study was performed in which the number of elements on each line was increased from four to sixteen with the results obtained for J_1 and J_2 using path four illustrated in Figs 7.17 and 7.18 respectively. In addition, to illustrate the difference between different integral paths, Figs 7.19 and 7.20 show the results for integral paths two to eight for the enriched analyses (the results for the unenriched analyses are shown in Appendix E.1).

Clearly, the introduction of enrichment brings an increase in accuracy which

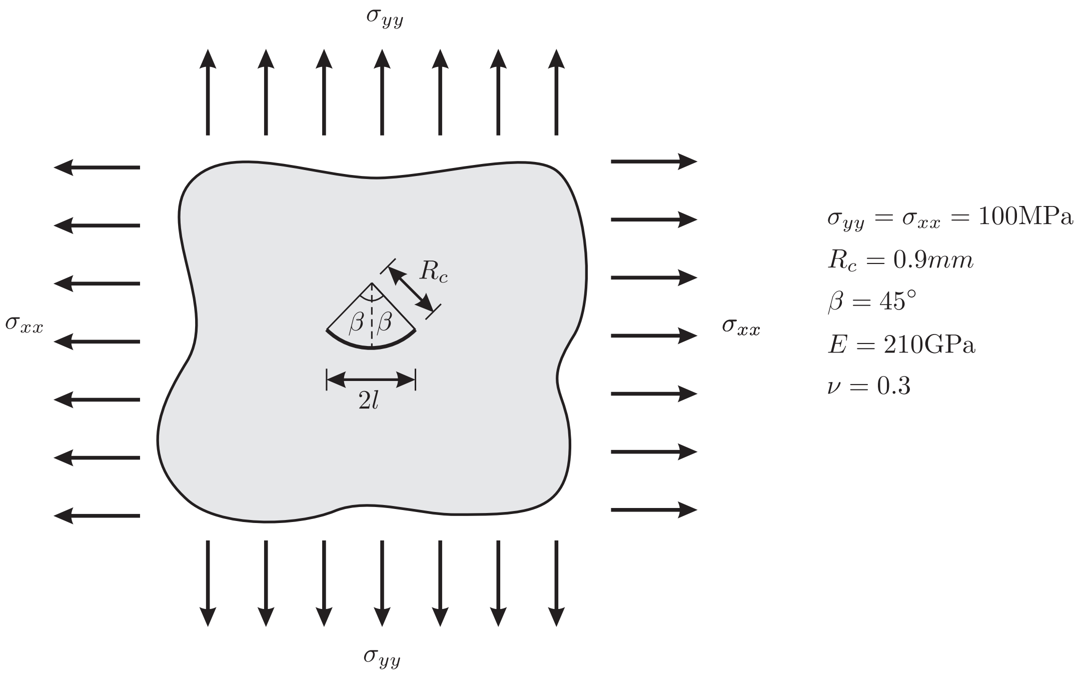

Figure 7.14: Curved crack within an infinite domain subject to a biaxial load - problem definition

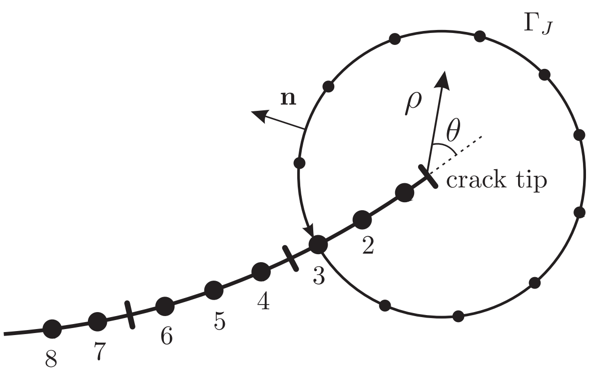

Figure 7.15: Definition of J-integral paths for curved crack (path three shown)

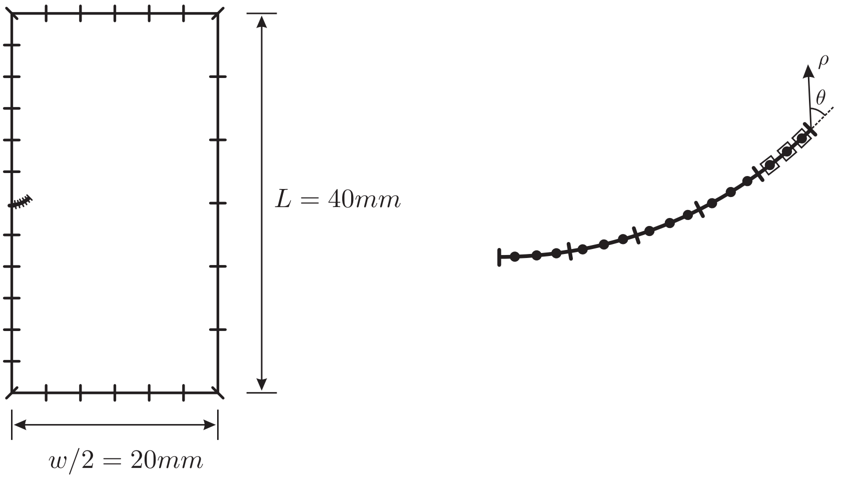

(a) Boundary element mesh - six elements per line

(b) Crack surface mesh with enriched elements

Figure 7.16: Boundary element mesh for curved crack problem

is evident in both J_1 and J_2, although it appears that at convergence an error is obtained in both values - an explanation for this will be given shortly. Turning now to the results for differing integral paths, path independence is demonstrated for paths four to eight (for both J_1 and J_2) while paths two and three demonstrate results which differ from the other paths. The reason for this is exactly the same as that given for flat cracks in Sec. 7.3.1 - the close proximity of internal integration points to the boundary results in errors that are accumulated in the J_k-integral. But the most important point which is realised from these results is the obvious benefit of using enrichment where, for only two additional degrees of freedom, a significant increase in accuracy is obtained.

It was mentioned previously that, even although the results obtained through the enriched implementation show higher accuracies than the unenriched implementation, the values for J_1 and J_2 did not converge to the exact values. It is useful to investigate the source of this error, and to do this, it is necessary to recall the crack tip functions which are used as weighting functions to solve for the extra unknowns (Eqns (7.2) and (D.1.1)). The expressions, in fact, are taken from the solution of a *flat* crack and it soon becomes clear that the application of these functions to a curved crack will introduce a certain error. However, with the increase in accuracy illustrated in the previous results this error must be small, and it is possible to show that this is the case by performing a study on the additional boundary integrals, using a variety of curved crack geometries.

In Sec. 7.2.1, it was explained that two additional boundary integral equations could be obtained by substituting the exact solution for displacements and tractions

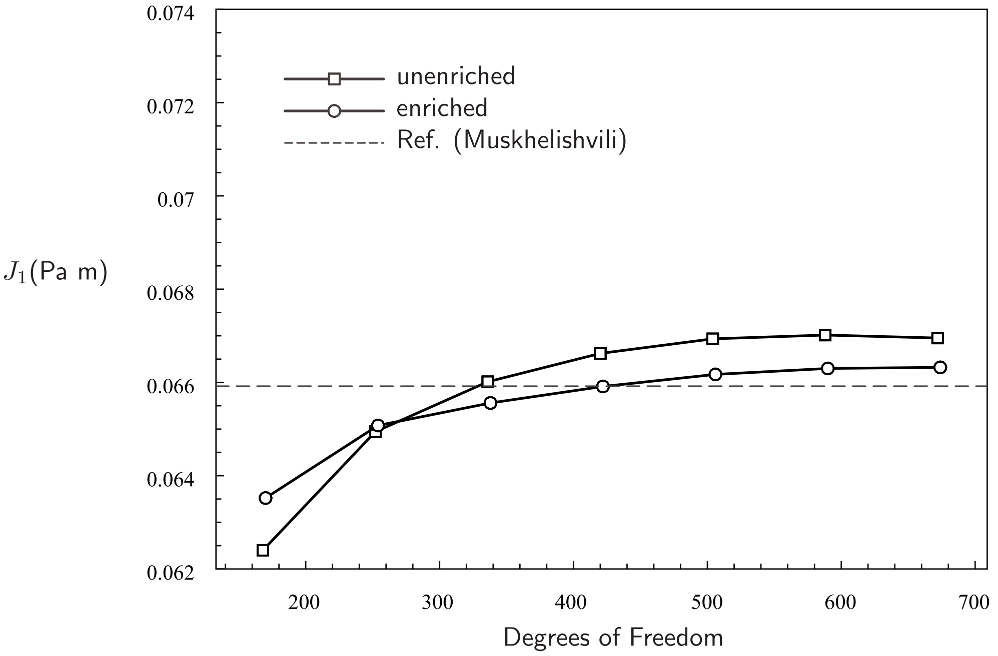

Figure 7.17: Comparison of unenriched and enriched J_1 values for increasing mesh density

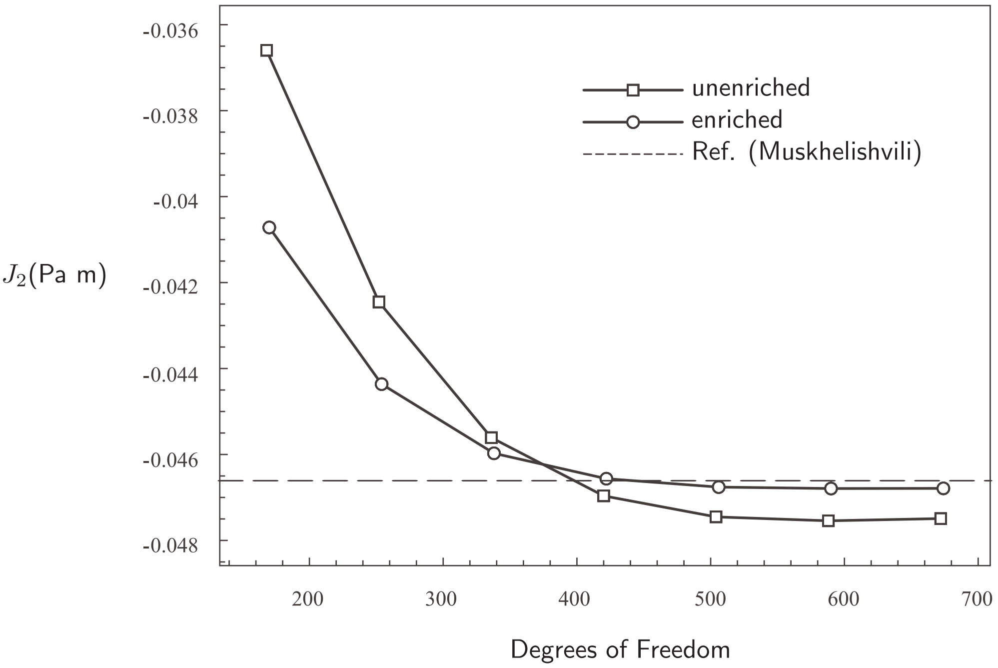

Figure 7.18: Comparison of unenriched and enriched J_2 values for increasing mesh density

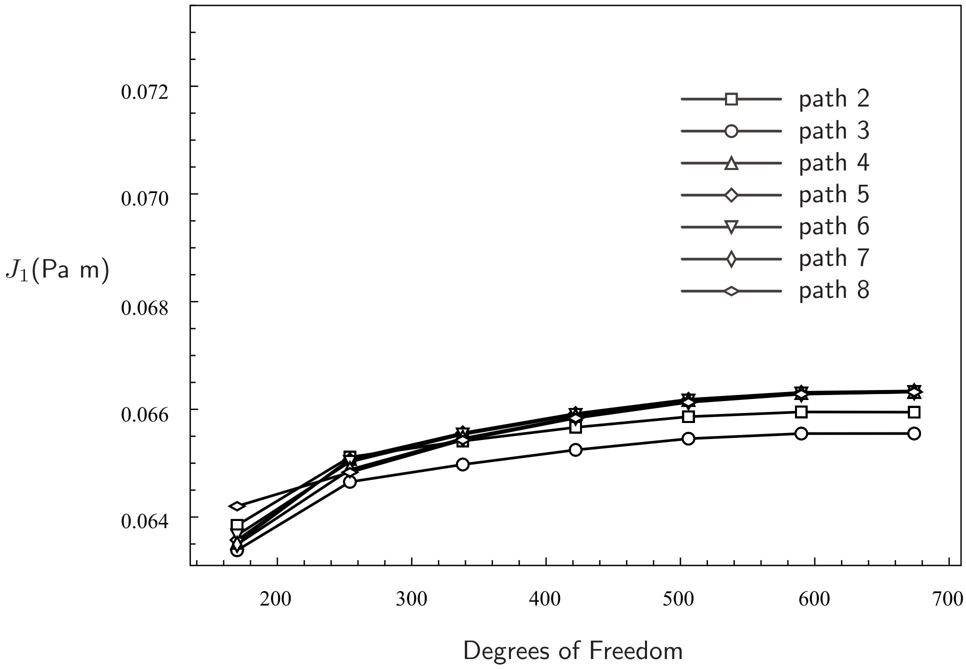

Figure 7.19: J_1 path independence for enriched curved crack analysis

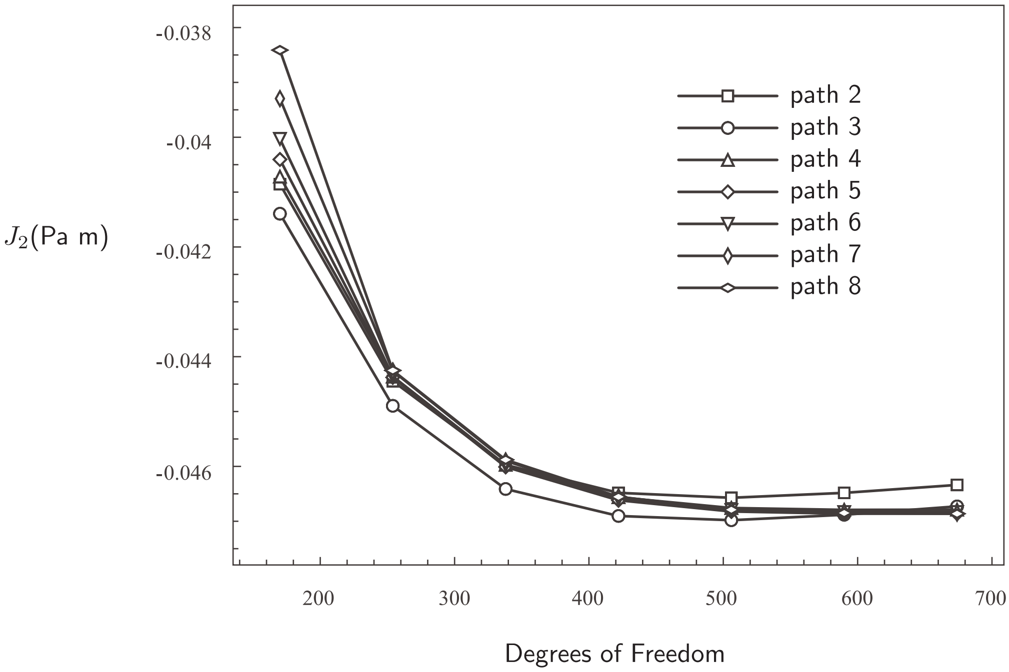

Figure 7.20: J_2 path independence for enriched curved crack analysis

(a) R_c=20mm (b) R_c=50mm

Figure 7.21: Curved crack geometries for error study

around a flat crack for u_j^* and t_j^* in Eq. (7.11). If we presume that there exists a solution for displacements and tractions around a curved crack, and these are denoted by the functions $\hat{\psi}_{\mathrm{I}j}^u$ and $\hat{\psi}_{\mathrm{I}j}^t$ (for mode I), then an additional BIE can be written as

$$\int_\Gamma \hat{\psi}_{\mathrm{I}j}^t(\rho,\theta)u_j d\Gamma = \int_\Gamma \hat{\psi}_{\mathrm{I}j}^u(\rho,\theta)t_j d\Gamma \tag{7.18}$$

or

$$\int_\Gamma \hat{\psi}_{\mathrm{I}j}^t(\rho,\theta)u_j d\Gamma - \int_\Gamma \hat{\psi}_{\mathrm{I}j}^u(\rho,\theta)t_j d\Gamma = 0 \tag{7.19}$$

where u_j and t_j are the displacements and tractions for a curved crack problem. Since the curved crack solution does not exist, the flat crack solution is used instead which, when applied to a curved crack problem, will introduce an error e as

$$\int_\Gamma \psi_{\mathrm{I}j}^t(\rho,\theta)u_j d\Gamma - \int_\Gamma \psi_{\mathrm{I}j}^u(\rho,\theta)t_j d\Gamma = e \tag{7.20}$$

Therefore, to determine the value of e, it is a requirement to find a solution to a curved crack problem (u_j, t_j). Ideally, this should be an exact solution, but, as mentioned before, this does not exist and can only be approximated by an unenriched DBEM analysis using a fine mesh. The present study used the curved crack example illustrated in Fig. 6.21 with a mesh of sixteen elements per line. Then, to demonstrate the effect of an increasing crack radius (flatter crack), the integrals seen in Eq. (7.20) were evaluated for crack radii varying from $20mm$ to $50mm$ (Figs 7.21a and 7.21b) in steps of $5mm$ with a flat crack also evaluated to allow for comparison. The values of each integral term with the associated error are shown in Table 7.2 with the errors also plotted for each mode in Fig. 7.22 for clarity.

As expected, the error for both modes decreases as the the crack becomes flatter, with the the mode II values showing a more prominent decrease. Inspecting the values for the flat crack (R_c=∞) where it is expected that the error should approximately equal zero, it is clear (especially for mode II) that this is not the case. This is caused by inaccuracies in integration and the inability of the unenriched DBEM

Table 7.2: Comparison of additional boundary integrals and errors for application of flat crack solution to curved crack with varying crack radius

	Mode I			Mode II		
R_c (mm)	$\int_\Gamma \psi^t_{\mathrm{I}j} u_j d\Gamma$ (I^1_{I})	$\int_\Gamma \psi^u_{\mathrm{I}j} t_j d\Gamma$ (I^2_{I})	$\left\lvert\frac{e}{\max(I^1_{\mathrm{I}},I^2_{\mathrm{I}})}\right\rvert$	$\int_\Gamma \psi^t_{\mathrm{II}j} u_j d\Gamma$ (I^1_{II})	$\int_\Gamma \psi^u_{\mathrm{II}j} t_j d\Gamma$ (I^2_{II})	$\left\lvert\frac{e}{\max(I^1_{\mathrm{II}},I^2_{\mathrm{II}})}\right\rvert$
20	0.29619	0.29367	0.00851	0.69011	0.68481	0.00767
25	0.33954	0.33727	0.00668	0.66225	0.65917	0.00465
30	0.36591	0.36389	0.00551	0.63556	0.63371	0.00292
35	0.38360	0.38179	0.00472	0.61299	0.61188	0.00181
40	0.39625	0.39461	0.00414	0.59426	0.59364	0.00104
45	0.40573	0.40423	0.00370	0.57866	0.57840	0.00046
50	0.41309	0.41170	0.00337	0.56557	0.56557	0.00001
∞	0.47039	0.46984	0.00115	0.42500	0.42640	0.00328

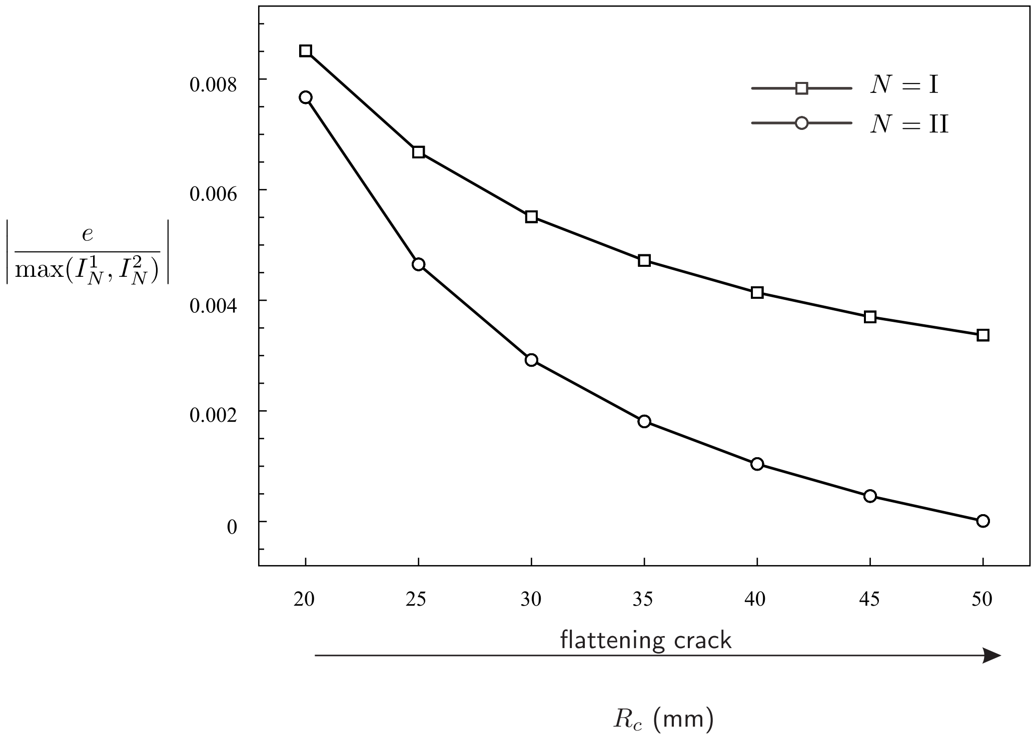

Figure 7.22: Relative error in additional boundary integral equations for increasing crack radius

analysis to capture the crack tip singularity - the most likely source of the inaccuracy - but what is most important is the relative magnitude between the integral terms and the values of e. The large difference reveals that the error introduced when using the flat crack solution in a curved crack problem is small and explains why good results are obtained when implemented. However, as is clear from Fig. 7.22, as the crack radius is decreased the introduced error increases in value.

Chapter 8

Method comparison and application

The previous two chapters outlined two methods of applying enrichment to the BEM/DBEM that allow accurate SIFs to be determined for fracture problems, but no direct comparison has been made between each technique. This first section of this chapter provides two comparisons: the first is the infinite plate problem (with an exact solution) used in Chapters 6 and 7 and the second is the edge crack problem in a finite plate. In addition, results obtained using the unenriched DBEM are also given. Leaving the details for later, it is found that the local PUM enrichment strategy in fact provides a more accurate and versatile procedure for modelling *flat* cracks. For this reason, the local PUM strategy is used to demonstrate the accuracy for a variety of mode I flat crack problems (centre crack and double edge crack) and mode II flat crack problems (slanted edge crack, slanted centre crack in a finite domain and slanted crack in an infinite domain). Of particular interest is the centre crack within an infinite domain where a comparison is made with results obtained using XFEM.

The curved crack problem is then considered again to allow comparison with published FEM results where, due to the conditioning problems experienced by the local PUM strategy for curved crack problems, the global enrichment strategy is used. Finally, since no justification has been given for the use of the J-integral over the contour integral outlined in Sec. 2.6.4, a comparison these two methods is made and conclusions drawn.

8.1 Local versus global enrichment formulations

8.1.1 Infinite plate problem - method comparison

In Secs 6.3.1 and 7.3 the problem used to demonstrate the improvement in accuracy seen once each form of enrichment was introduced was that of a crack contained in an infinite plate. Since the problem is exact, an accurate assessment can be made on the error in SIFs, and this was carried out for each type of enrichment. Each showed an improvement over the conventional DBEM implementation (which uses quadratic elements), but so far no mention has been made on the relative accuracy of the two enrichment methods. Therefore, using the same infinite plate problem and determining the mode I SIF error for each method, the relative errors can be compared. To allow for a fair comparison, only the crack tip elements were enriched in each method while in all analyses, the elements were spaced evenly (Fig. 6.10a). In each step of mesh refinement, the number of elements on each line was increased while no mesh grading was used throughout the analysis. The results for the three methods (unenriched, local PUM enrichment and global enrichment formulation) are presented in Fig. 8.1. Since the two methods of enrichment introduce additional

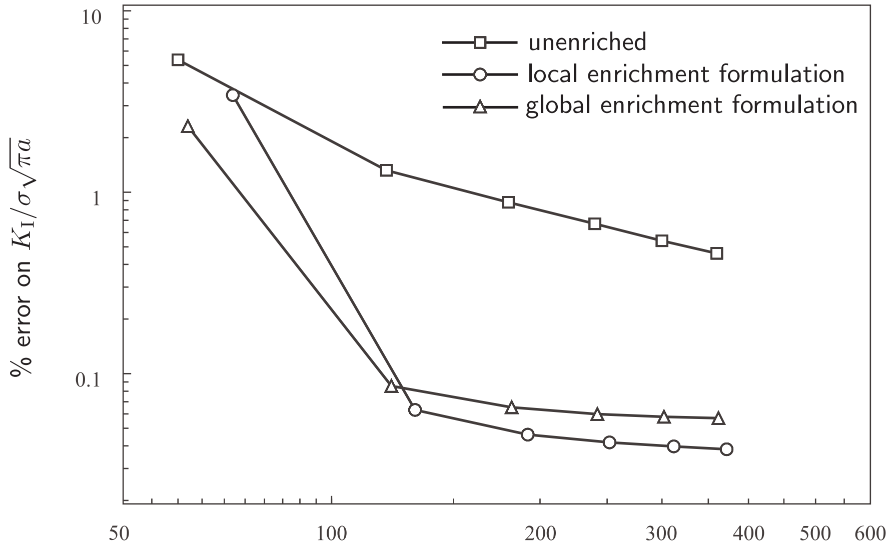

Figure 8.1: Comparison of error in stress intensity factor for methods of enrichment - infinite plate problem

DOF[1], this variable is used as a measure of mesh refinement. All three results show the expected reduction in error as the mesh is refined but with a significant difference between the unenriched and enriched analyses. For a very coarse mesh of two elements per line the results are comparable, but as the mesh is refined further, there is approximately an *order of magnitude improvement.* Of course, this comes at the price of additional DOF introduced by enrichment, but this is vastly outweighed by the improvement in accuracy. Interestingly, the results obtained with local enrichment formulation outperform the global enrichment formulation.

8.1.2 Edge crack in finite plate comparison - method comparison

The second problem which is used to provide a comparison between each enrichment formulation while also comparing against the commonly used quarter-point elements (Sec. 5.1.1) is that of an edge crack in an infinite plate (Fig. 8.2a). This problem has been analysed by Civelek and Erdogan [109] for a variety of crack lengths (a/w) with the results obtained from the study used here as a reference. The present study carried out five analyses to compare the improvement seen once enrichment is introduced. These included: unenriched DBEM, DBEM with quarter-point elements, local PUM enrichment, global enrichment with the J-integral and global enrichment with direct output. To investigate the effect of increasing the mesh density, the number of elements on each line was increased from two to twelve with no mesh grading used (the mesh for four elements per line is shown in Fig. 8.2b). All methods (except for the direct SIF output) used the J-integral with path four (Fig. 6.13) and a total of thirty integration points. In the case of enrichment being applied, only the elements adjacent to the crack tip were enriched (Fig. 8.3a) while the implementation of quarter-point elements required the use of discontinuous quarter-point elements, as shown in Fig. 8.3b.

The exaggerated displacement profile of an analysis run with four elements per line and the local PUM enrichment strategy is illustrated in Fig. 8.4 while, to allow a comparison to be made between the accuracy of each method, the normalised SIFs for each mesh are shown in Fig. 8.5. Interestingly, the use of QP elements has a marginal improvement in accuracy for low mesh densities but actually ensures the method converges to the correct value (in contrast to the unenriched DBEM).

---

[1] two for each enriched node in the PUM enrichment and two for the global system in the combined enrichment

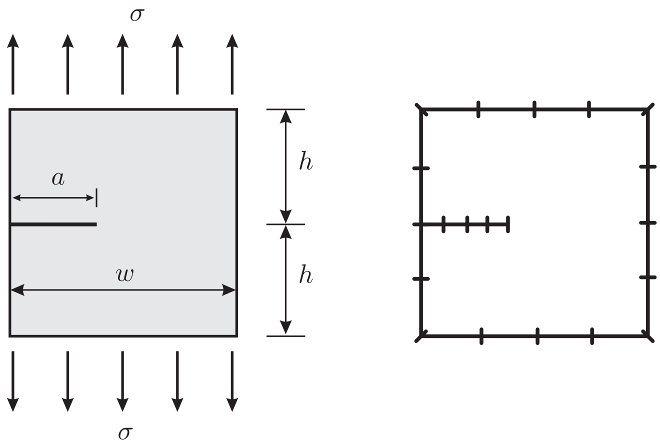

(a) Problem geometry

(b) Example boundary mesh

Figure 8.2: Edge crack under uniaxial tension

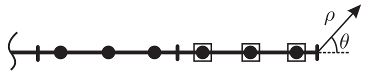

(a) Enrichment of crack tip elements

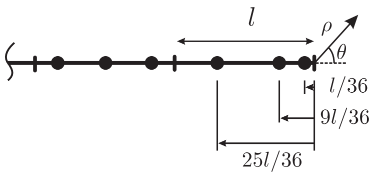

(b) Discontinuous quarter-point elements

Figure 8.3: Crack tip elements for edge crack example

Once enrichment is introduced, however, the accuracy is improved greatly and this is seen even for very coarse meshes. In the case of direct SIF output, the results obtained do not demonstrate the same high accuracy as those obtained through the J-integral (this was also shown in Sec. 7.3.2) and it is therefore recommended to use the J-integral over direct SIF output.

Lastly, to demonstrate the path independence of the J-integral after applying enrichment using the local PUM formulation, the normalised SIFs for paths two to eight are shown in Tbl. 8.1 for a variety of crack lengths. The results were obtained with a coarse mesh of four elements per line in which no grading was used. Paths four to eight are consistent with one another for all crack lengths while paths two and three, for the reasons explained in Sec. 7.3.1, show values which differ slightly.

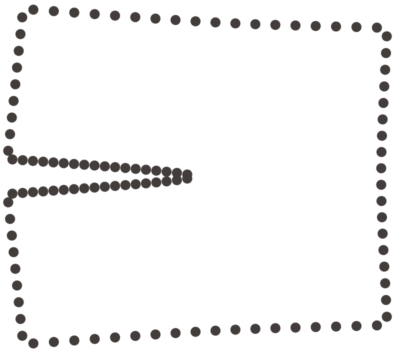

Figure 8.4: Exaggerated displacement plot for edge crack problem

Table 8.1: Mode I normalised stress intensity factors for edge crack problem (4 elements/line) - varying crack length and J-integral path using local PUM enrichment formulation

	J-integral path							
a/w	2	3	4	5	6	7	8	Ref.
0.2	1.498	1.499	1.496	1.497	1.497	1.497	1.497	1.488
0.3	1.855	1.855	1.852	1.852	1.852	1.853	1.853	1.848
0.4	2.328	2.328	2.325	2.325	2.325	2.325	2.326	2.324
0.5	3.011	3.011	3.007	3.007	3.006	3.007	3.007	3.010
0.6	4.151	4.151	4.145	4.144	4.143	4.144	4.145	4.152

The two examples illustrated in this section show quantitatively that introducing enrichment has a large improvement in SIF accuracy where, in the case of the

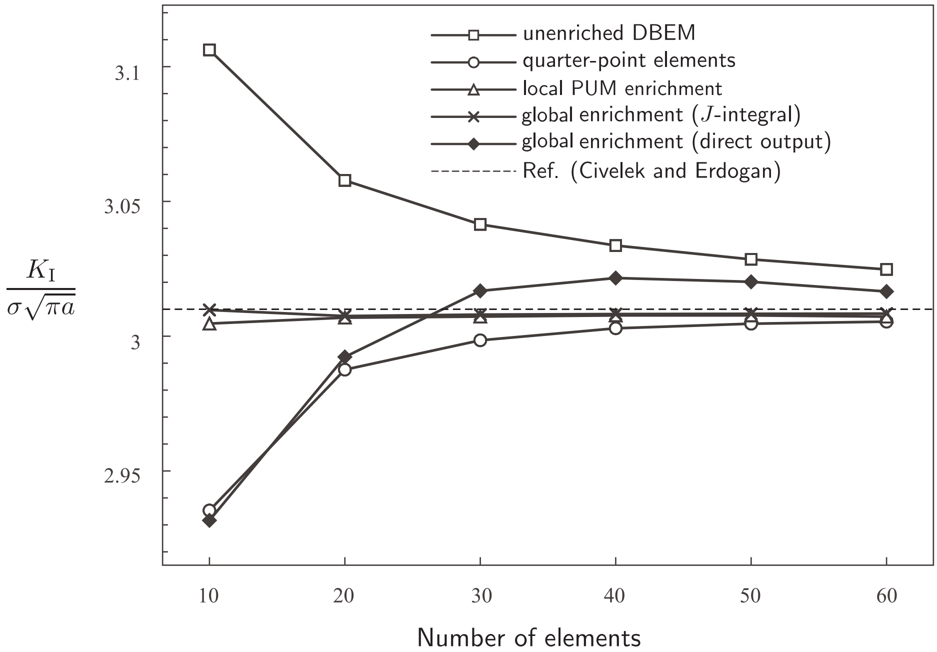

Figure 8.5: Comparison of normalised mode I SIFs for edge crack problem

infinite plate problem, this can be seen to be approximately an order of magnitude improvement. In the second example, both the enriched formulations were shown to outperform quarter-point elements with an even greater improvement over the unenriched implementation.

If a choice is to be made between the enriched local PUM formulation and global formulation it is sensible to make a decision based on the results obtained using the infinite plate example since this compares against an exact solution (in contrast to the finite plate problem). Therefore, it appears that if the problem being analysed is a *flat* crack[2], the local PUM enrichment should be preferred if accuracy is paramount. Moreover, a second, slightly more subtle difference between the two enrichment strategies also contributes to the choice of the local PUM enrichment for future flat crack examples. The global enrichment formulation relies on the use of additional BIEs which are derived from the first order terms of the Williams solution. Therefore, since only two additional BIEs can be used (corresponding to mode I and II fracture), a square system can only be formed for a single crack tip. Because the local PUM enrichment formulation does not exhibit such a limitation, multiple crack tips can be enriched and the method provides a more versatile approach; for these

---

[2] The problems encountered with curved cracks using the local PUM formulation were illustrated in Sec. 6.3.5

reasons the local PUM approach is used in the next two sections.

8.2 Mode I fracture applications (local PUM enrichment)

8.2.1 Centre crack in a semi-infinite plate

The previous problem considered a crack to lie within a finite plate, but it is also useful to analyse the problem of a centre crack within a semi-infinite plate (Fig. 8.6) since this is known to have an exact solution. Tada et al. [8] note that for a finite plate with $h/w \geq 3$, the plate can be regarded as a good approximation to the semi-infinite plate problem. To confirm this, and also to verify the accuracy of the enriched BEM against the analytical solution, a series of tests was carried out with an increasing h/w ratio while keeping a constant value of $a/w = 0.5$. The first set of tests used models varying from $h/w = 2$ to $h/w = 3$ with eight elements per line for all meshes (see Figs 8.8a and 8.8b) and all elements adjacent to crack tips enriched. However, by using a constant number of elements on side faces that increase in length, certain inaccuracies arise that are most easily explained by inspecting a plot of nodal displacements. Fig. 8.7 shows the exaggerated displacements obtained from an enriched analysis with attention given to the displacement profile on one of the side faces, adjacent to one of the crack tips. As the crack opens and creates a void, the side faces must move in creating a profile that is poorly modelled if a coarse mesh is used. Therefore, by using a fixed number of elements on these side faces, as h/w increases the length of the elements used to capture this displacement profile will also increase, leading to a detrimental effect on accuracy. An alternative strategy is required.

The second set of tests applied a graded mesh, where the sizes of the elements on the side faces were chosen to grade down to the same order of length as those on the crack faces. This ensured that the correct displacement profile was captured, regardless of the length of the side faces (see Figs 8.9a and 8.9b). The normalised mode I SIF was determined using the J-integral with the integral taken over path four, as defined in Fig. 6.13 where the results from both sets of analyses, including those using the unenriched DBEM, are shown in Fig. 8.10.

The first point to note - which is relevant to both the enriched and unenriched analyses - is the difference between the ungraded and graded meshes as the h/w ratio increases. For the ungraded meshes the normalised SIF actually increases as

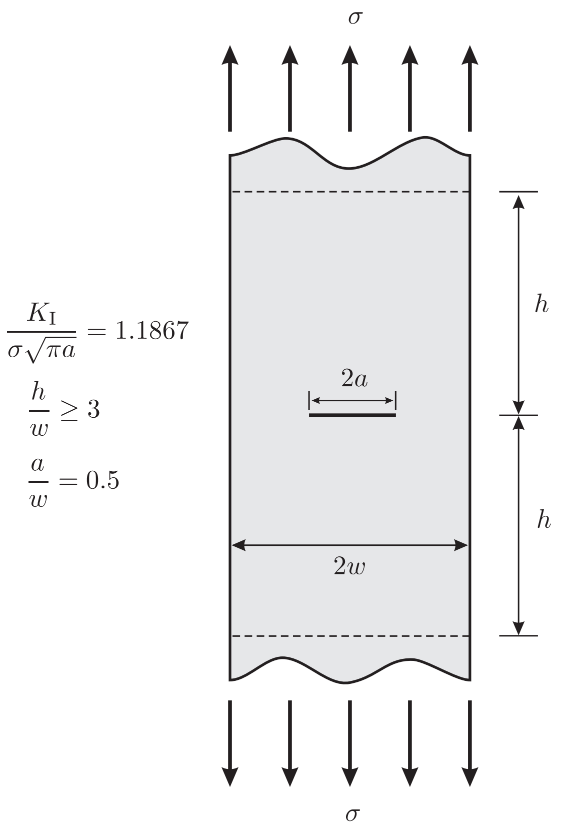

Figure 8.6: Centre crack within a semi-infinite plate

the plate increases in length (contradictory to what is expected) and this is explained by the use of large elements on the side faces near the crack tips. Using a graded mesh provides a much better convergence, and this is seen in both the unenriched and enriched analyses. The improvement once enrichment is introduced is clear, and at convergence, the enriched analysis obtains a normalised SIF of 1.1870 with an error of 0.025%.

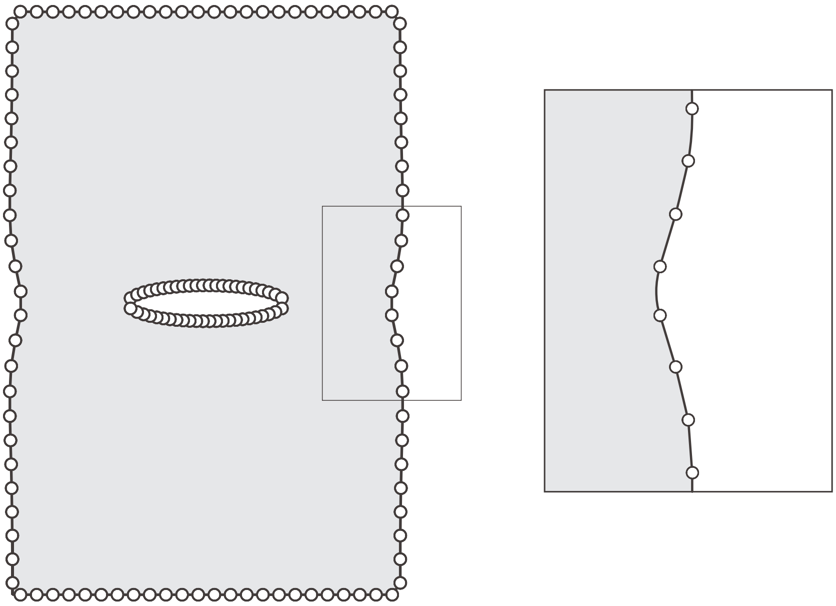

Figure 8.7: Nodal displacements for semi-infinite centre crack problem

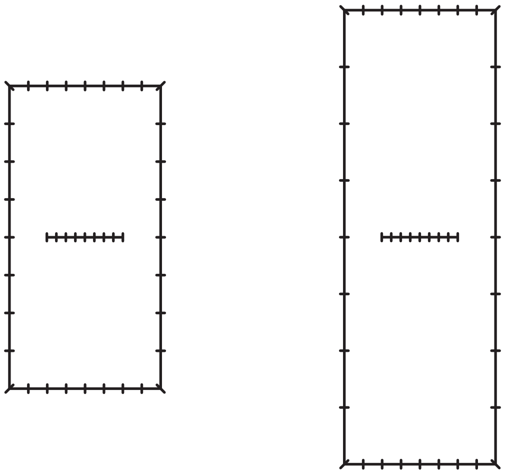

(a) $h/w = 2$ (b) $h/w = 3$

Figure 8.8: Boundary meshes for semi-infinite plate problem - no mesh grading

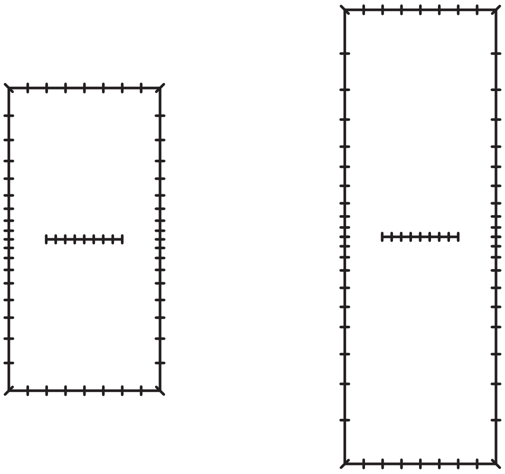

(a) $h/w = 2$ (b) $h/w = 3$

Figure 8.9: Boundary meshes for semi-infinite plate problem - graded mesh

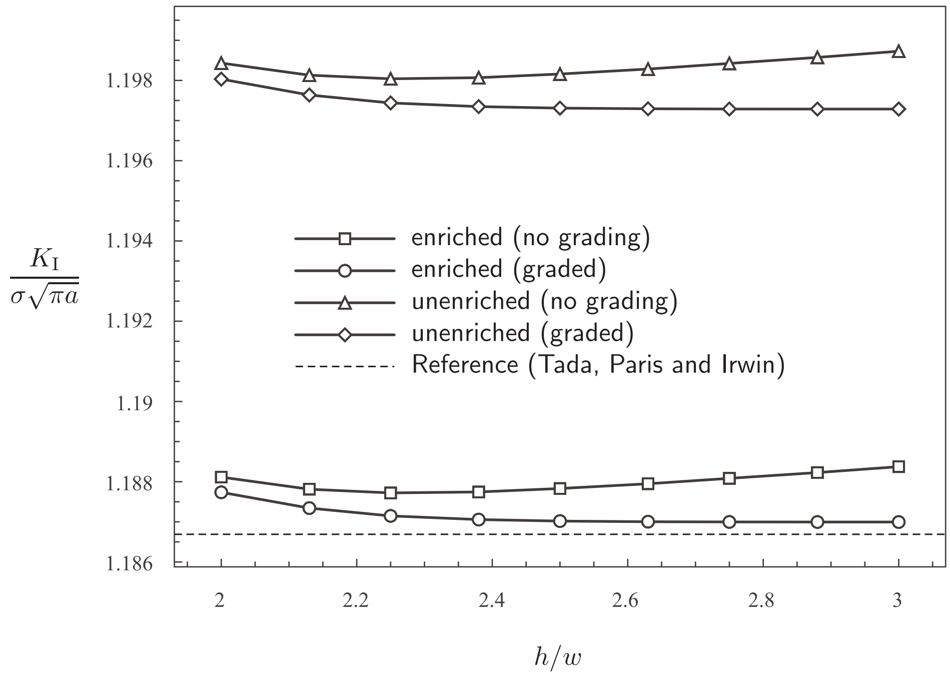

Figure 8.10: Normalised mode I SIFs for centre crack within a semi-infinite plate and increasing h/w ratio

8.2.2 Double edge crack

Another standard problem which is often used to evaluate SIF accuracy is that of the double edge crack problem (Fig. 8.11a) for which accurate results for a variety of crack lengths are given by Tada et al. [8]. This problem is useful since, in contrast to the edge crack problem seen in Sec. 8.1.2, two crack tips are present, each with an associated singular field. This presents a particular challenge since, as the cracks increase in length (increasing a/w ratio), the singular crack tip fields approach one another and it becomes increasingly difficult to capture the correct displacement and stress fields.

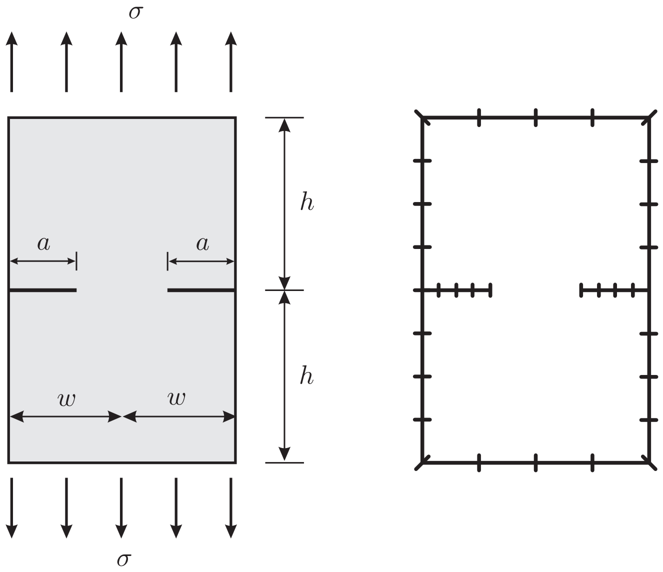

(a) Problem geometry

(b) Example boundary mesh

Figure 8.11: Double edge crack under uniaxial load

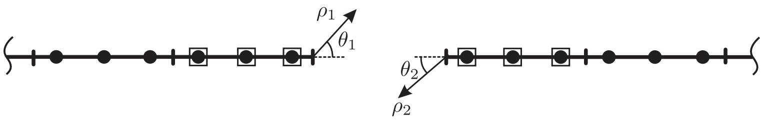

Figure 8.12: Enrichment of crack tip elements for double edge crack problem

To assess the improvement seen once enrichment is introduced, the problem was modelled with a coarse mesh of four elements per line (Fig. 8.11b) for a variety of crack lengths varying from a/w=0.2 to 0.9 (the height of the plate remained constant at h/w=2). In each, the J-integral was used to evaluate SIFs over the integral paths defined in Fig. 6.13. In the case of enriched analyses, the PUM enrichment strategy was applied with all elements adjacent to a crack tip enriched as shown in Fig. 8.12.

An example displacement profile (exaggerated for clarity) is illustrated in Fig. 8.13 while the results for both the unenriched and enriched SIFs obtained using path four[3] are shown in Fig. 8.14. From this, it can be seen that close agreement with the reference solution is seen for crack lengths a/w=0.2 to 0.5 for both the unenriched and enriched implementations. But once the crack lengths are extended beyond this, the results obtained using the unenriched DBEM start to diverge from the reference solution which is explained by the use of quadratic interpolation to model the singular fields. In contrast to this, the enriched formulation follows the reference solution for *all* crack lengths and shows that, even when the crack tips lie very close to one another, the interpolation scheme used is capable of capturing the singular field.

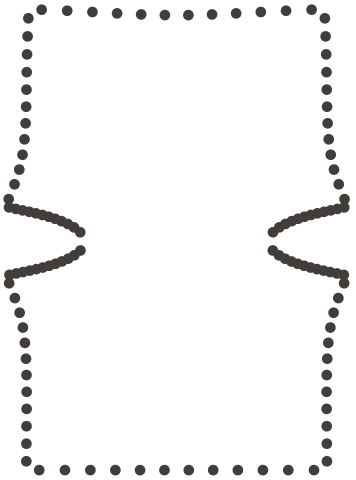

Figure 8.13: Exaggerated displacement profile for double edge crack

8.3 Mixed mode fracture applications (local PUM enrichment)

All the previous flat-crack implementations (including the method verifications in Chapters 6 and 7) have used geometries that exhibit only mode I fracture. This limits the number of crack problems that can be analysed and therefore, to illustrate that the local PUM enrichment strategy is capable of capturing the singular field for both modes I and II, the results for a number of mixed-mode fracture problems are outlined here.

---

[3] except for a/w=0.9 where, due to the close proximity of the crack tips, path three was used

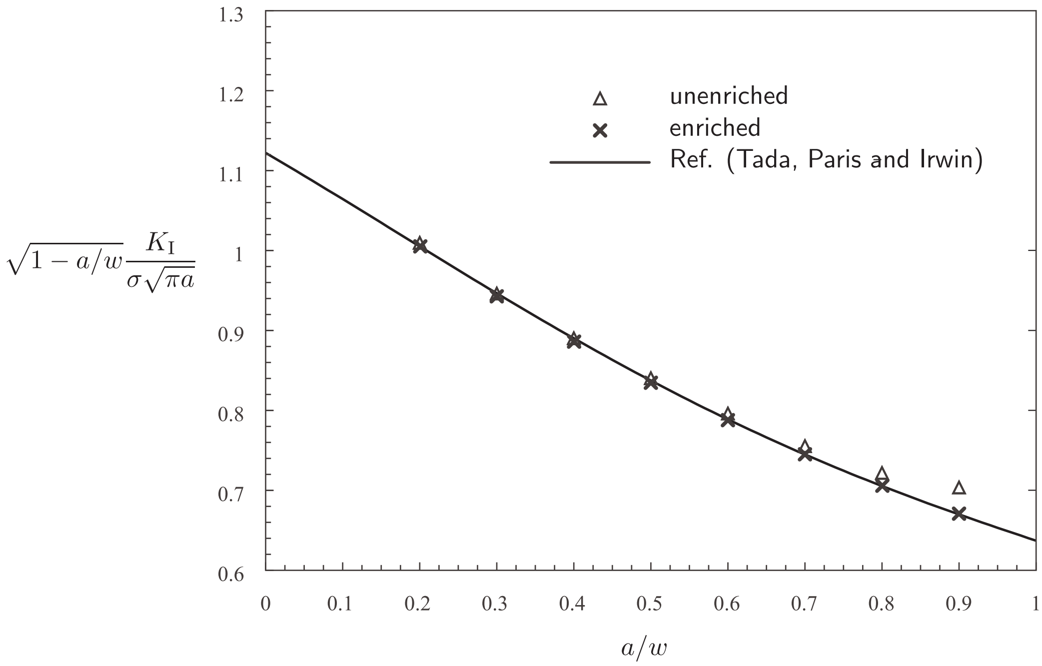

Figure 8.14: Comparison of normalised stress intensity factors for increasing crack length - double edge crack

8.3.1 Slant edge crack

The slant edge crack (Fig. 8.15a) is a commonly used specimen for fracture testing and is found in many stress intensity factor handbooks [8]. In addition, accurate results are given by Wilson [110] using the boundary collocation method (Sec. 2.5.1) to provide SIFs for both mode I and II for a variety of crack lengths a/w and angles β. Using these results as a reference, two sets of analyses were carried out: first, an unenriched DBEM analysis was carried out using a coarse mesh of four elements per line (Fig. 8.15b) for crack lengths varying from a/w=0.3 to 0.6 and $\beta = 45°$; the second carried out an enriched analysis using exactly the same geometry and mesh but with enrichment applied to the elements adjacent to the crack tip. The PUM enrichment strategy was employed throughout while SIFs were evaluated using the decomposed J-integral routine with path four (see Fig. 6.13). Normalised SIFs for each analysis are illustrated in Figs 8.16a and 8.16b with the results by Wilson plotted for comparison.

Inspection of the results shows that for each crack length (excluding $a/w = 0.3$ for K_{II}) the enriched results agree more closely with Wilson for both modes of fracture. This illustrates that the enrichment implementation is capable of producing accurate solutions for both mode I and mode II fracture which could not be verified with any

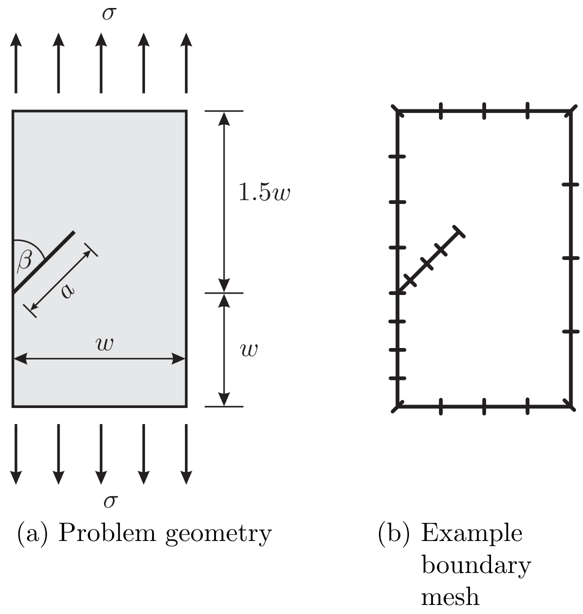

(a) Problem geometry (b) Example boundary mesh

Figure 8.15: Slanted edge crack problem

of the previous crack geometries. Finally, to verify the accuracy of the enriched implementation for different crack angles, the same analysis was carried out for $\beta = 62.5°$ with the results present in Fig. 8.17 alongside the results of Wilson. Good agreement is seen for all crack lengths and crack angles.

To provide reference values for normalised SIFs, Appendix E.2 tabulates the values for crack angles $\beta = 45°$ and $\beta = 62.5°$ for crack lengths varying from $a/w = 0.3$ to $a/w = 0.6$ for a mesh of eight elements per line (at which point convergence was achieved) with the PUM enrichment strategy applied to crack tip elements.

8.3.2 Inclined centre crack

The second mixed mode problem analysed was that of an inclined centre crack within a finite plate (Fig. 8.18a) for which accurate results have been published by Murakami [111]. In addition, the problem was analysed by Portela et al. [24] using the DBEM where no special form of interpolation or enrichment was employed to take account of the crack tip singularity. However, before comparison is made with these results, it is useful to quantify the improvement seen once enrichment is introduced to the current DBEM implementation. Three sets of tests were run: the first used no enrichment, the second used enrichment on only one of the crack tips and the third used enrichment on both crack tips. In each, no mesh grading was used while the number of elements on each line of the model was increased from

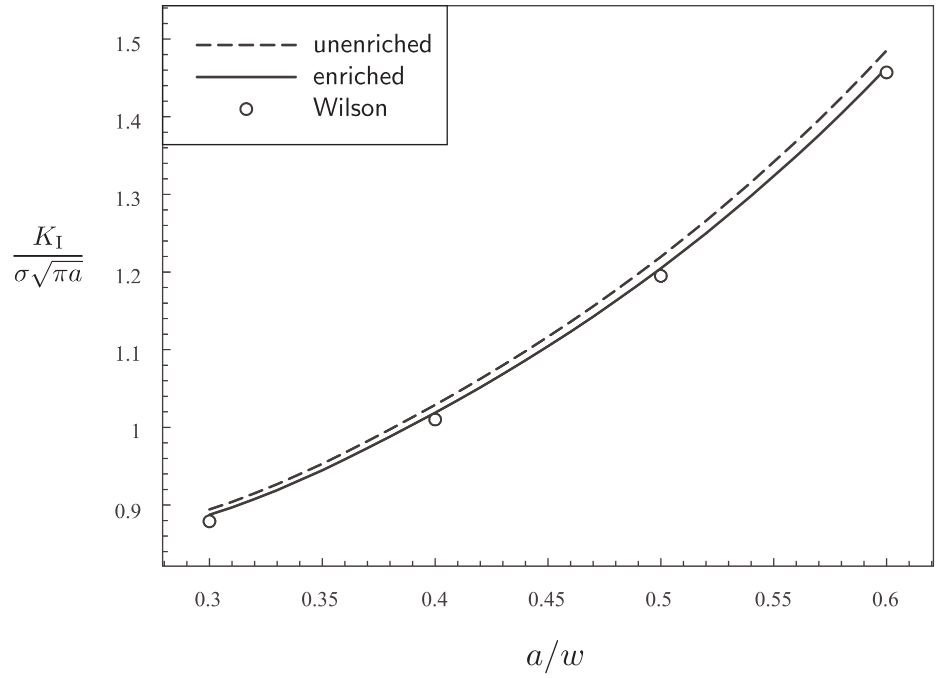

(a) Mode I SIF comparison

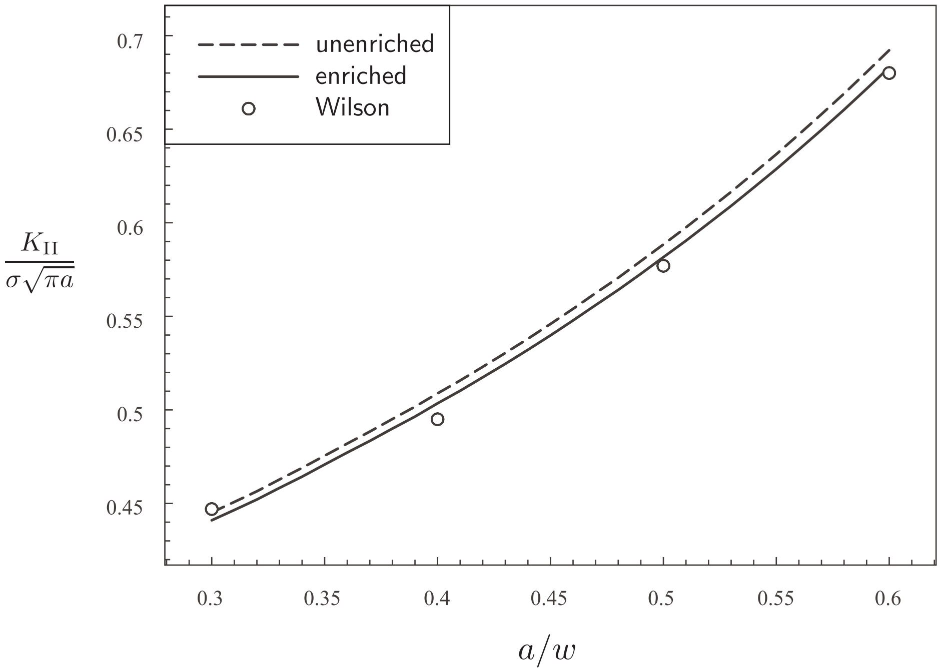

(b) Mode II SIF comparison

Figure 8.16: Comparison of unenriched and enriched SIFs for $\beta = 45°$ and varying a/w

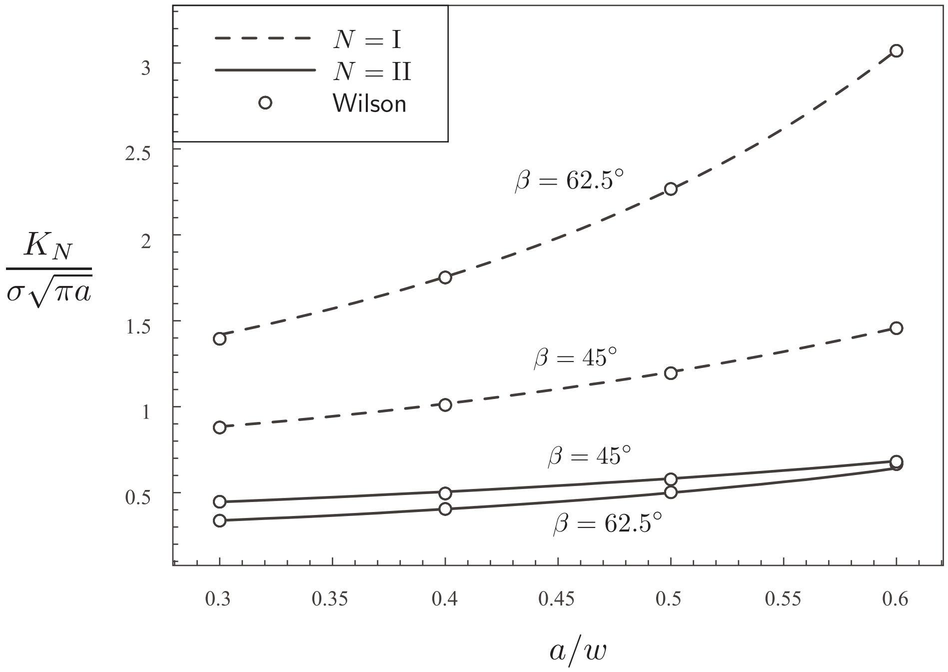

Figure 8.17: Comparison of mode I and II SIFs for slant edge crack with varying crack angle β and crack length a/w

four to twelve - Fig. 8.18b illustrates an example mesh with four elements per line. For the enriched models, enrichment was applied through the PUM (Chapter 6) while only those elements adjacent to the crack tip were chosen to be enriched. Figs 8.19a and 8.19b illustrate this enrichment strategy applied to the meshes with one and two crack tips enriched respectively. The model dimensions were chosen such that $h/w = 2$, $a/w = 0.5$ and $\beta = 45°$ and normalised SIFs were obtained using the decomposed J-integral routine (Sec. 2.6.2) using the rightmost crack tip in each case - the integral was therefore always taken over a contour surrounding an enriched crack tip.

The undeformed and deformed[4] nodal positions are shown in Fig. 8.20 for the mesh with both crack tips enriched. The J-integral results taken over path four (see Fig. 6.13) are shown in Figs 8.21 and 8.22 for mode I and II respectively. The expected improvement in accuracy after introducing enrichment is illustrated in both plots but, in contrast to previous analyses where only one crack tip has been enriched, the improvement after taking account of the singularity at both crack tips is also demonstrated. The results for mode I show that a large improvement in accuracy is seen over the single crack tip enrichment and, importantly, high accuracies

---

[4] For clarity, the displacements have been exaggerated

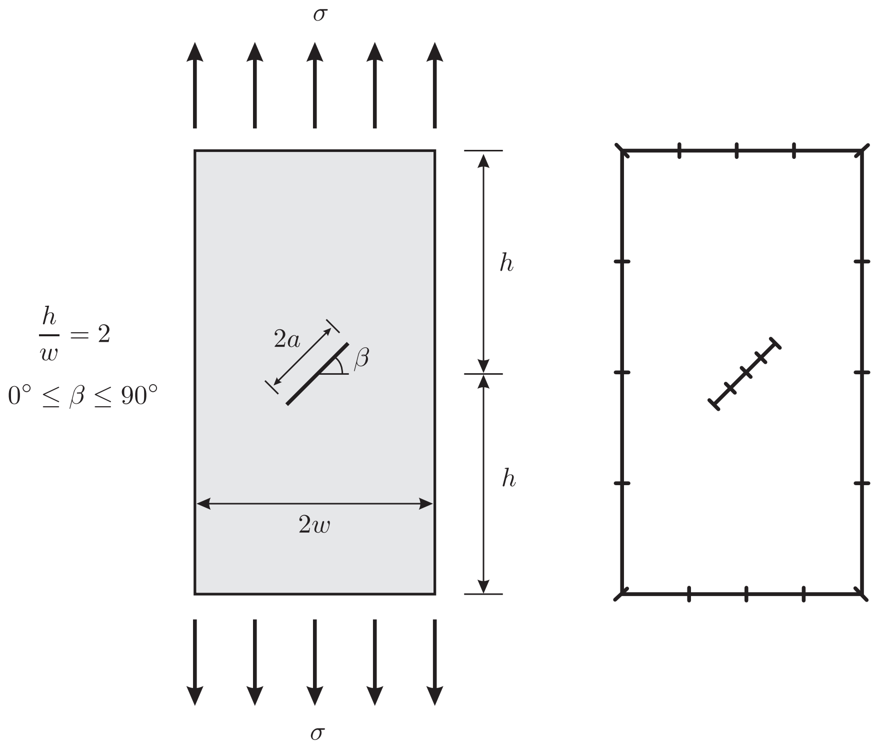

(a) Problem geometry

(b) Example boundary mesh - four elements per line

Figure 8.18: Inclined centre crack in a finite plate

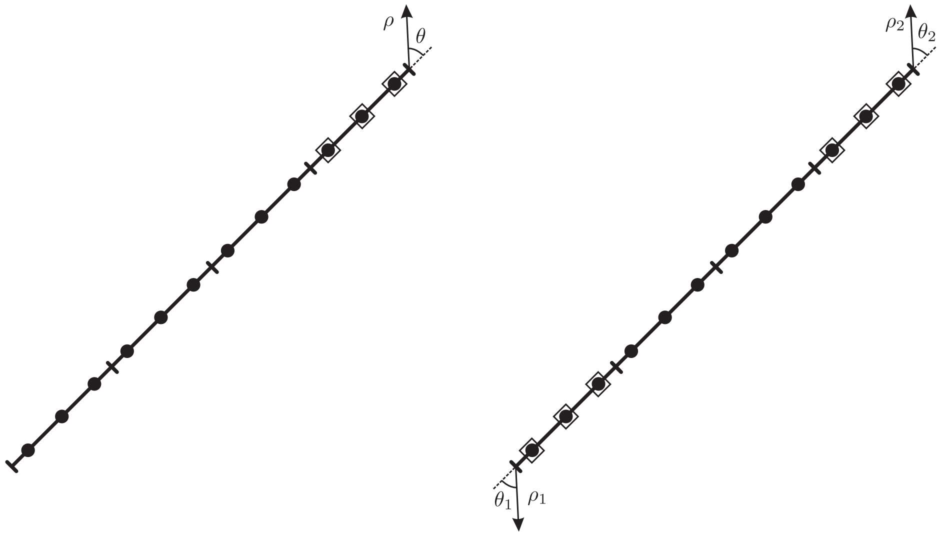

(a) One crack tip enriched

(b) Two crack tips enriched

Figure 8.19: Crack face meshes for inclined centre crack with enrichment applied

are seen for *all* meshes. The mode II results show a similar trend, although it appears that both enriched results converge to a different value (~ 0.5456) compared to the reference value (0.546). However, this is because the reference value is only prescribed to three significant figures - if a more accurate solution were available, then it is believed that the results would show a correct convergence.

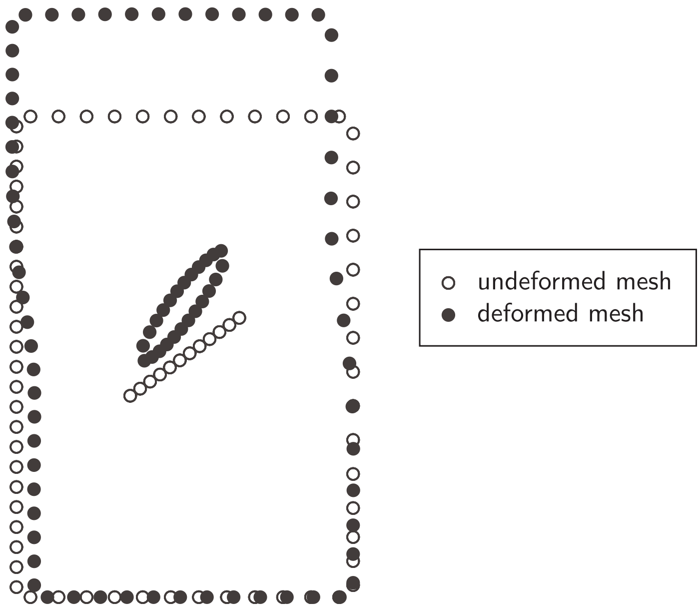

Figure 8.20: Undeformed and deformed nodal positions for inclined centre crack

It was noted previously that the same problem was analysed by Portela et al. using the DBEM with quadratic interpolation and, in addition, the same J-integral decomposition technique with circular integration paths was used to determine SIFs. Therefore, it is possible to compare both the accuracy and path-independence of the results with that of the present enriched formulation. The implementation in [24] used a total of 36 quadratic elements on the boundary with 6 used on each side of the crack face and, in contrast to the present implementation, the elements were graded towards the crack tip. Using the same example as before with $h/w = 2$, $a/w = 0.5$ and $\beta = 45°$, the results for each of the J-integral paths (both implementations use the same path definitions) are shown in Figs 8.23 and 8.24 where, to allow for comparison, meshes of four and six elements per line were used with enrichment applied to both crack tips. These show an improvement in accuracy for all integral paths, but what is most interesting is the improvement in path independence which can be seen for both modes of fracture. Finally, the method was used to determine SIFs for varying angles of β and crack length (a/w) using converged results obtained using a mesh of eight elements per line. The results for a crack length of $a/w = 0.5$

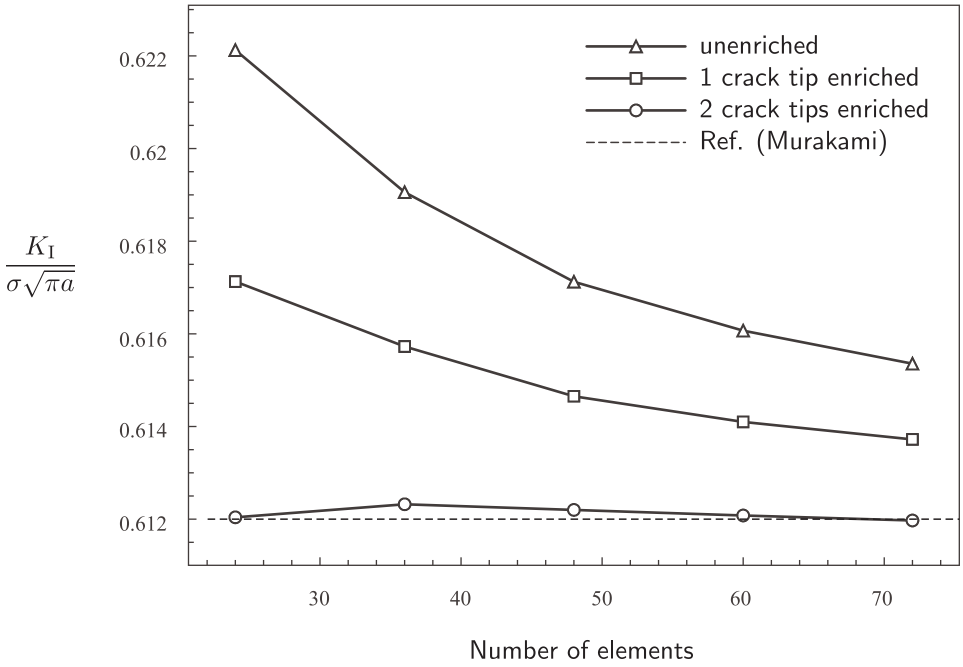

Figure 8.21: Comparison of unenriched and enriched normalised mode I SIFs for inclined centre crack

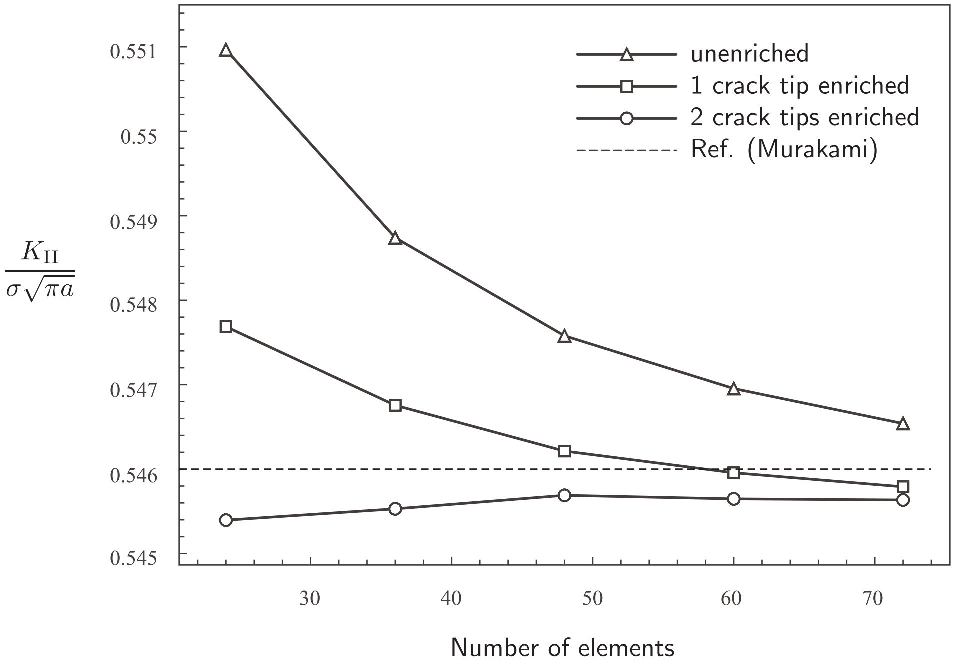

Figure 8.22: Comparison of unenriched and enriched normalised mode II SIFs for inclined centre crack

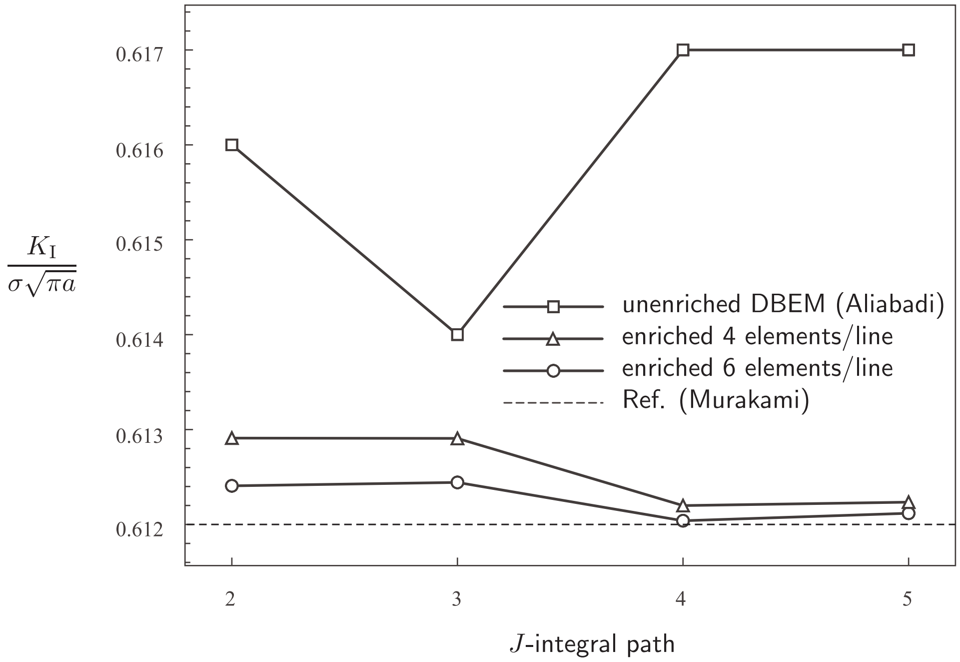

Figure 8.23: Normalised mode I SIFs for different J-integral paths - inclined centre crack

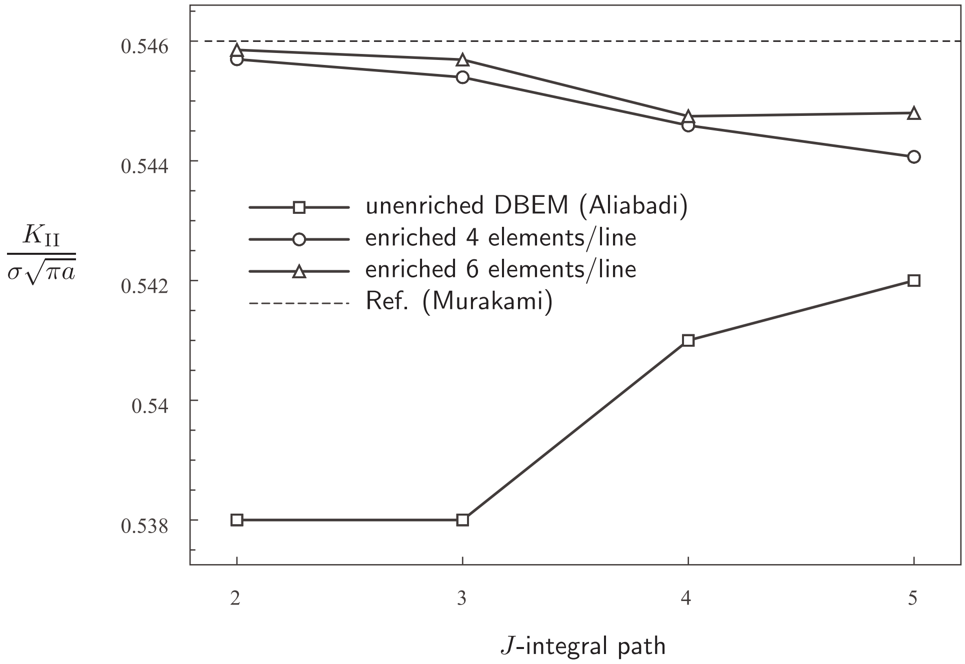

Figure 8.24: Normalised mode II SIFs for different J-integral paths - inclined centre crack

are shown in Fig. 8.25 while those for crack lengths of $a/w = 0.2, 0.3, 0.4$ and 0.6 are given in Appendix E.3.

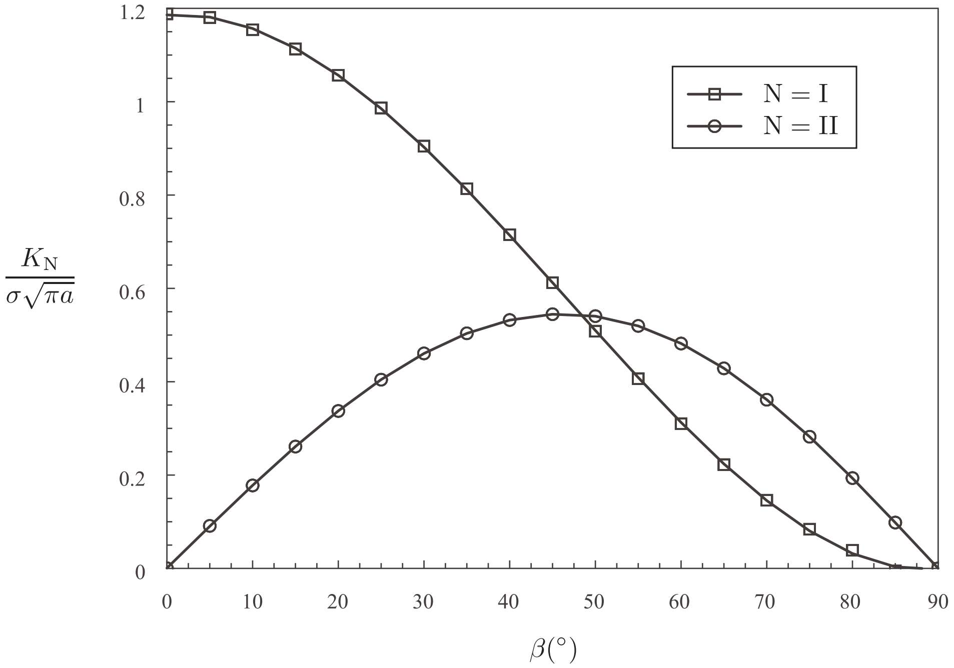

Figure 8.25: Normalised SIFs for inclined centre crack with $a/w = 0.5$ and varying crack angle

8.3.3 Inclined crack within an infinite domain

The last mixed mode problem to be considered (containing a flat crack) is that of a crack inclined at an angle β within an infinite domain under uniaxial load (Fig. 8.26a). The problem is particularly useful since an analytical solution is given for mode I and II SIFs which can be expressed as

$$K_{\mathrm{I}} = \sigma\sqrt{\pi a}\cos^2\beta \tag{8.1a}$$

$$K_{\mathrm{II}} = \sigma\sqrt{\pi a}\sin\beta\cos\beta \tag{8.1b}$$

But most importantly, the same problem has been analysed using the XFEM by Bordas et al. [112] which allows (bearing in mind the significant differences between a domain-based and boundary-based method) a comparison to be made between SIF accuracy.

In the XFEM analysis of [112] the problem was modelled with a finite plate (Fig. 8.26b) with dimensions of $2h = 2w = 10mm$ and $a = 0.5mm$ to approximate

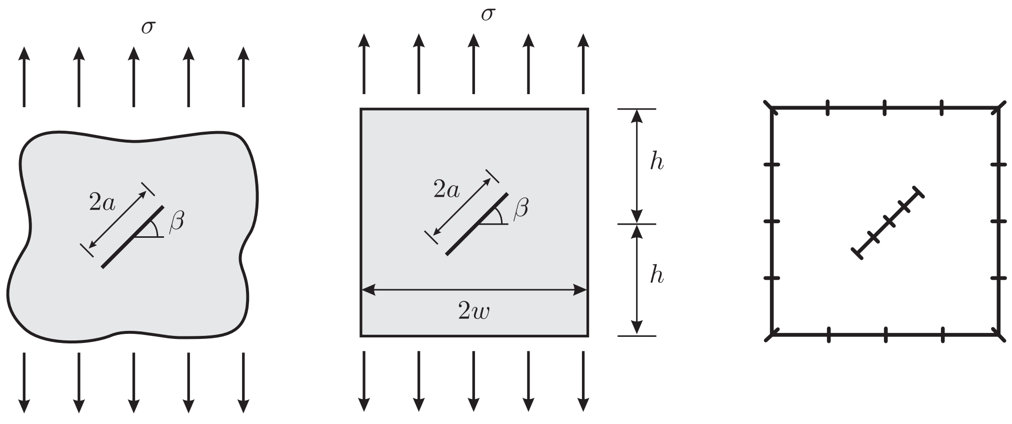

(a) infinite domain problem

(b) finite domain approximation

(c) example boundary element mesh

Figure 8.26: Inclined centre crack in an infinite domain under uniaxial load

that of the infinite plate problem. They used 1520 triangular elements throughout the domain and determined SIFs using a domain integral with varying radii. The present comparison uses the best results of the XFEM analysis which were obtained with a domain integral radius ratio of $r_d/h_{local} = 2.5$ (r_d is the domain integral radius and h_{local} is the size of the crack tip element). The enriched BEM analysis used the PUM enrichment strategy outlined in Chapter 6 with elements adjacent to crack tips enriched (Fig. 8.19b) and the decomposed J-integral to determine SIFs. The analysis was carried out with a coarse mesh of four elements per line (Fig. 8.26c) since any subsequent mesh refinement had little effect on accuracy. It should be noted that no mesh grading was used. Exactly the same plate dimensions were used as for the XFEM implementation with the results obtained using integration path four shown in Tbl 8.2 alongside the XFEM results to allow for comparison.

Table 8.2: Comparison of normalised SIFs obtained through XFEM and enriched DBEM for inclined crack in an infinite plate (% errors shown in brackets)

	XFEM		**Enr. DBEM**	
$\beta(°)$	Mode I	Mode II	Mode I	Mode II
15	0.9312 (0.19)	0.2489 (0.44)	0.9423 (1.00)	0.2501 (0.06)
30	0.7484 (0.21)	0.4413 (1.91)	0.7587 (1.16)	0.4343 (0.29)
45	0.5010 (0.20)	0.5022 (0.44)	0.5056 (1.12)	0.5011 (0.30)
60	0.2549 (1.96)	0.4366 (0.83)	0.2530 (1.20)	0.4351 (0.48)
75	0.0690 (3.00)	0.2535 (1.40)	0.0682 (1.76)	0.2512 (0.48)

Since the mesh used for the XFEM analysis is not known, it is difficult to make a fair comparison between the methods but, nonetheless, a few points can be made after inspecting the results. For the first three crack angles the XFEM outperforms the enriched DBEM for mode I SIFs, but for the latter two, the reverse is true. In the case of the mode II SIFs, the enriched DBEM outperforms the XFEM for all crack angles. Therefore, it can be stated that the results are comparable but, in the case of the enriched DBEM, these are obtained using very few DOF (24 quadratic elements).

One very useful feature of boundary element methods is the ability to increase the size of the domain without the need to use an unreasonable number of additional elements (unlike the FEM). Therefore, for infinite plate problems, it is possible to use larger domains (which more accurately represent the far-field boundary conditions) with very little additional computational cost. In fact, if the same number of elements are used around the boundary, then *no* additional computational cost will be incurred. In the analyses carried out previously on the inclined crack with an infinite plate, the far-field boundary conditions were approximated by using a square plate of length $2h$=$2w$=10mm but, to assess the effect of using a larger domain, the same analysis was also carried out on increasing side lengths up to a maximum of $2h$=$2w$=50mm. In each test exactly the same crack length of a=0.5mm was chosen and, most importantly, a mesh of four elements per line was used in each case. Using the results for $\beta = 45^\circ$, the normalised SIFs can be plotted as a function of the plate side length as shown in Fig. 8.27. This reveals that using a plate with a side length of $2h$=10mm is not providing a good approximation to the far-field boundary conditions and that even a small increase in length improves the results dramatically. Since the results converge at approximately $2h$=30mm, a second series of tests was carried out using this side length while using the same mesh of four elements per line (Fig. 8.26c). The results for each crack angle are shown in Fig. 8.28 with the XFEM results plotted for comparison. What is seen is that the enriched BEM formulation with a larger domain now outperforms XFEM for *all* crack angles for both modes I and II where no additional computational cost has been incurred.

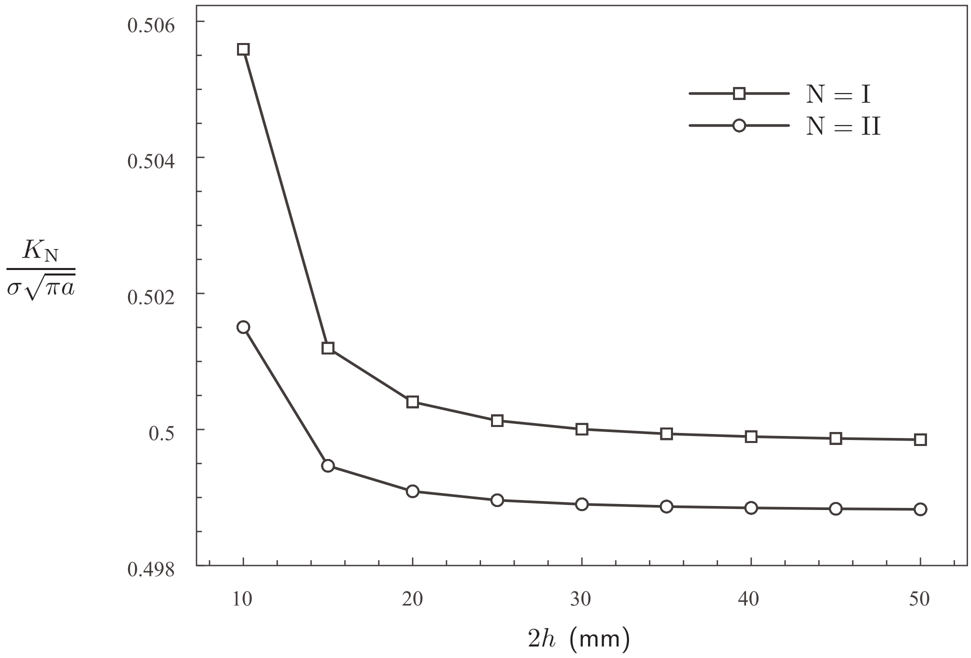

Figure 8.27: Normalised SIFs for inclined centre crack ($\beta = 45°$) in an infinite domain with increasing plate dimensions

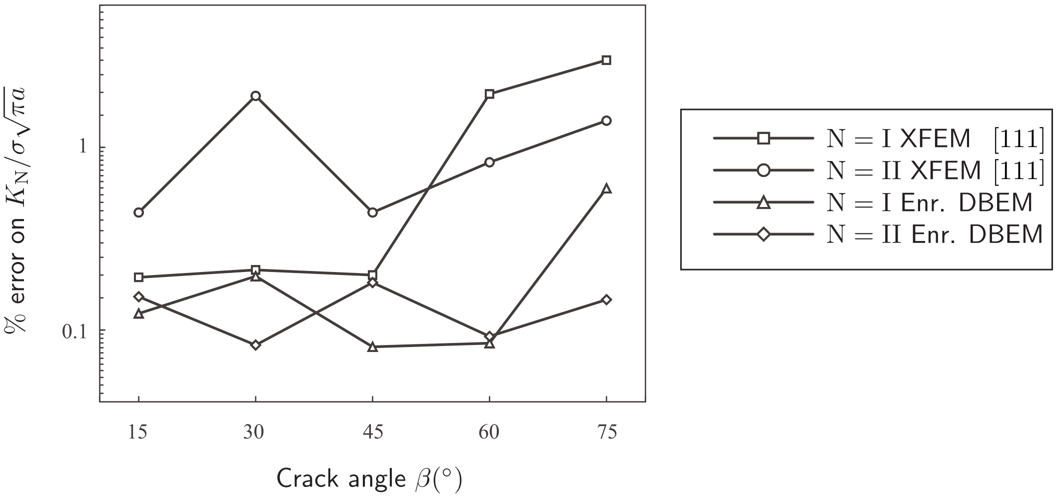

Figure 8.28: XFEM error comparison for infinite plate with inclined crack - four elements per line and $2h = 30mm$

8.4 Curved crack (global enrichment)

Now that several flat crack examples have been used to show the accuracy of the local PUM formulation, our attention now focuses on the application of enrichment to a curved crack since this precludes the use of local enrichment. Instead, it is necessary to use the global enrichment formulation where it was seen in Sec. 7.3.4 that an improvement in accuracy over the unenriched DBEM was seen through the problem of a curved crack within an infinite domain. The following section illustrates some additional results obtained through analysis of the curved crack problem where firstly, comparisons are made with flat crack elements and graded meshes. A comparison is then made between values of J_1 and J_2 obtained through an enriched DBEM analysis and those of a FEM analysis to demonstrate the relative accuracy of the current implementation.

An interesting study which can be carried out on the problem of a curved crack is the change in accuracy which results from the use of flat elements along a curved crack surface (see Fig. 8.29). It may seem completely inappropriate to use flat elements along a curved surface, but noting that analytical expressions can be used for the integrals along flat elements, it becomes clear that the implementation is simplified. For coarse meshes it is expected that large inaccuracies will occur due to the poor approximation of a curve, but as the mesh density increases, this error should decrease to a value of the same order as that for curved elements as the approximation improves. To illustrate the difference, a study was carried out using flat and curved crack elements applied to the same problem as used in Sec. 7.3.4 of a curved crack in an infinite domain. Approximating the problem with a finite plate, the same strategy as used previously was applied, where an equal number of elements are used on each line with no grading (Fig. 7.16a), while the number of elements per line was increased from four to sixteen. J_1 and J_2 were evaluated using the technique described in Sec. 2.6.3 with the integral paths as defined in Fig. 7.15. The results obtained using path four for both flat and curved crack elements (unenriched) are shown in Fig. 8.30 and, to allow for comparison, the results obtained from enriched


(a) Curved elements (b) Flat elements

Figure 8.29: Use of curved and flat elements on curved crack surface

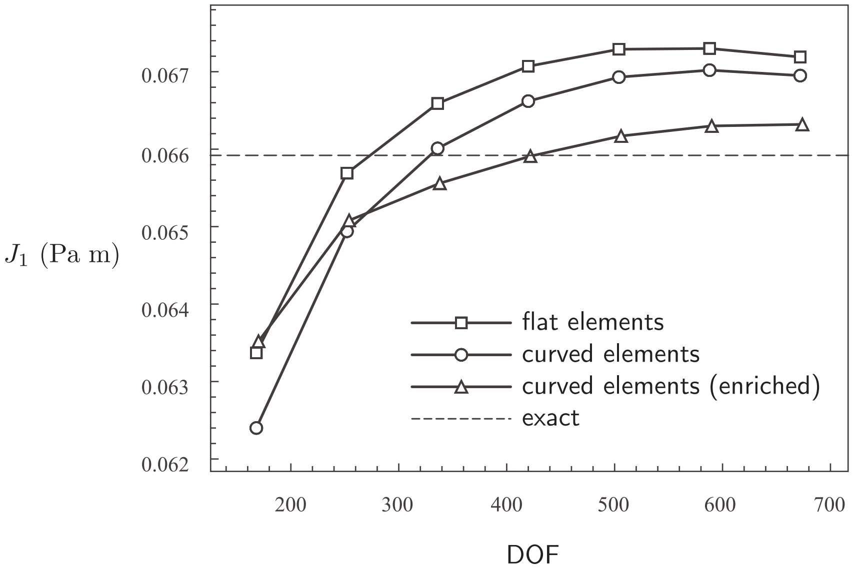

(a) J_1 comparison

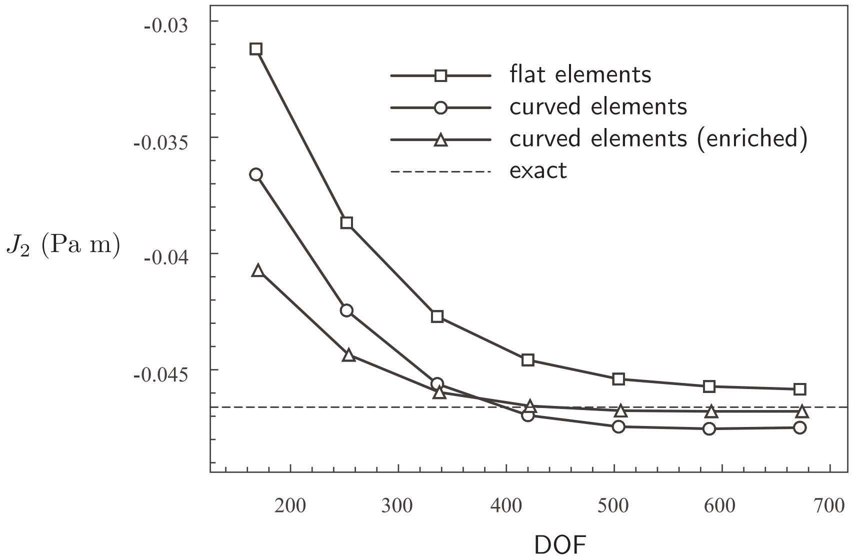

(b) J_2 comparison

Figure 8.30: Comparison of J_k values for curved crack problem with flat and curved crack elements

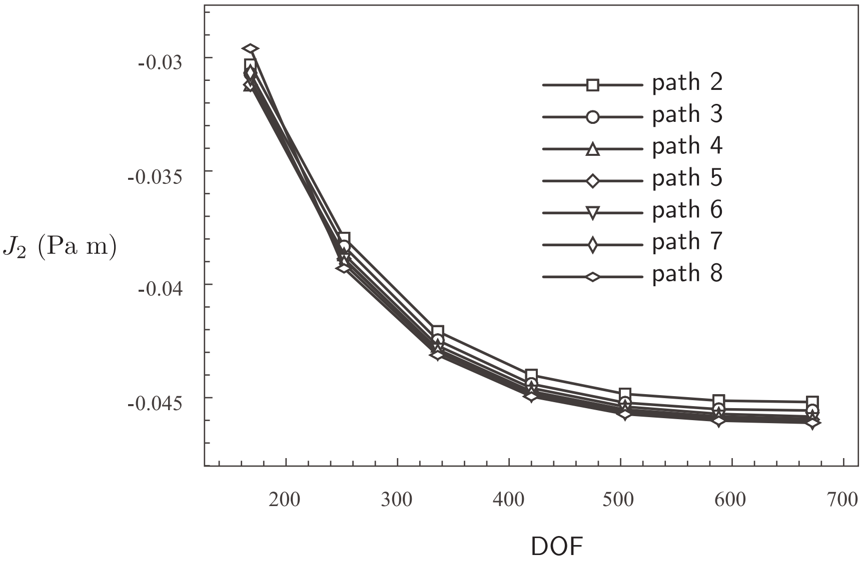

(a) Flat crack elements

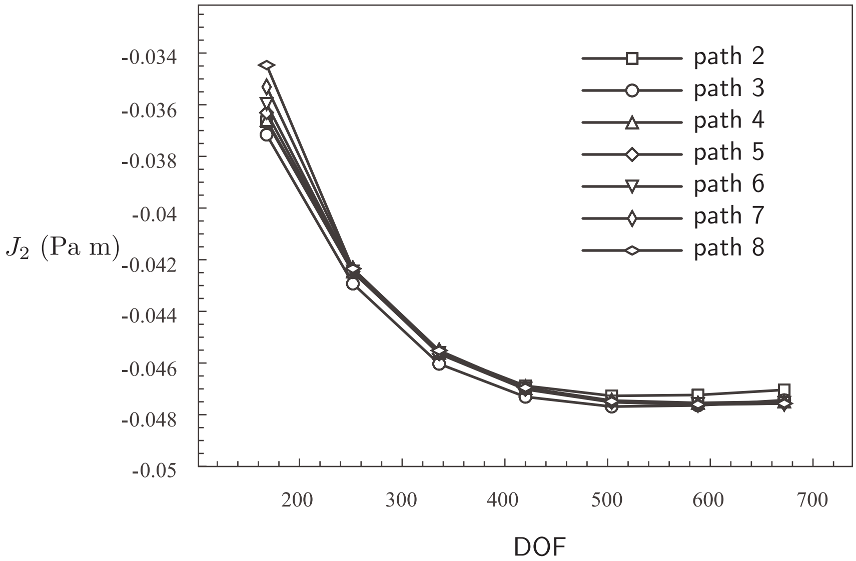

(b) Curved crack elements

Figure 8.31: J_2 path independence for both flat and curved elements applied to curved crack problem

curved elements are also plotted. In addition, to illustrate path independence, the results obtained using paths two to eight for J_2 [5] are shown in Fig. 8.31.

By comparing the relative errors of unenriched curved and flat elements it can be seen, especially for coarse meshes, that the accuracy in J_1 suffers due to the approximation of a curved surface with straight lines. Much of the same is true for the J_2 integrals where a clear improvement in accuracy is seen after introducing enrichment. Interestingly, by observing the unenriched element results for J_2, an improvement in accuracy is realised for coarse meshes by using curved elements over flat elements. But at convergence, where the meshes are so fine that the flat elements very closely approximate a curve, the accuracies are very similar and, in fact, the flat elements give slightly better results. By inspecting the plots illustrating J_2 values for different integration paths (Figs 8.31a and 8.31b), it can be seen that both types of element demonstrate path independence. However, at very coarse meshes, curved elements show a larger difference in values, but this quickly reduces as the number of elements increase. In fact, at higher mesh densities the difference in values is smaller that those obtained using flat elements, and this is seen up to the highest mesh density.

Since all previous analyses used meshes with uniform element spacing, a study was carried out to investigate the effect of including graded elements. This was achieved by carrying out a convergence study where the number of elements per line was increased from four to sixteen. Therefore, the number of elements in both the uniform and graded meshes were equal - Figs 7.16a and 8.32a show the meshes for a uniform mesh and graded mesh with six elements per line. In each, enrichment was applied to crack tip elements. Fig. 8.32b, which illustrates the results for both meshes, shows that an improvement for coarse meshes is seen for the graded mesh while at convergence, the values converge to the same value (as expected). Interestingly, the results for the graded and ungraded meshes converge from different directions while it is expected that both exhibit the same behaviour. The reason for this can be only be speculated and further study is required.

To demonstrate the implementation of the J_2-integral routine (Sec. 2.6.3), Chang and Yeh [113] used the problem of a curved crack in an infinite domain modelled with a fine FEM mesh, graded towards the crack tip. They used the same technique of taking a series of exclusions zones (centred at the crack tip and with radius R) allowing J_2 to be determined using a least-squares routine (Fig. 2.18 and Eqn. 2.80).

---

[5] the results for J_1 show identical trends

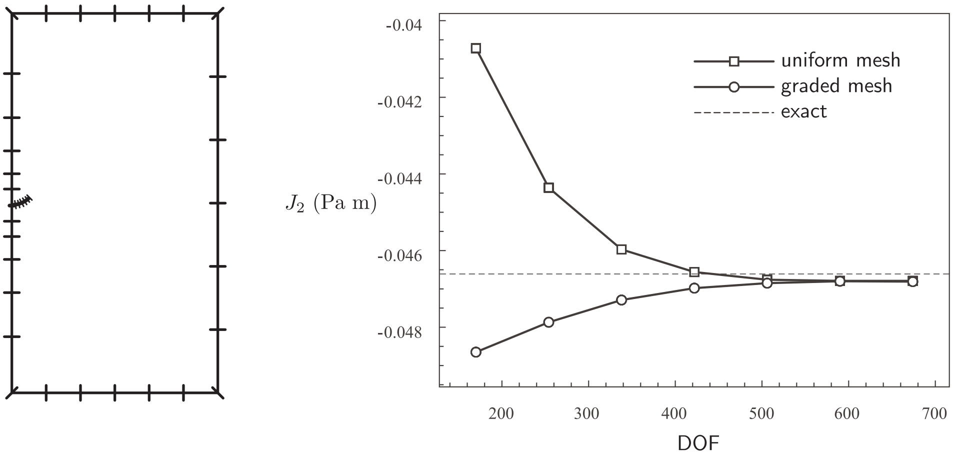

(a) Graded mesh (b) Comparison of uniform and graded mesh J_2 values

Figure 8.32: Graded curved crack analysis - boundary mesh and results

Using exactly the same geometry as for the FEM analysis, a DBEM analysis was carried out with curved elements (unenriched and enriched) and flat elements (unenriched) each with uniform mesh of twelve elements per line (twice the number of elements in Fig. 7.16a). In the enriched analysis, only the crack tip elements were chosen to be enriched since any further increase in enrichment brought little increase in accuracy. The results for each analysis, including the exact solution, are shown in Table 8.3.

Table 8.3: Comparison of J_1 and J_2 values for curved crack in an infinite domain, with % errors in parentheses

	exact[a]	unenriched (flat)	unenriched (curved)	enriched	FEM [113]
J_1	0.06592	0.06729 (2.08)	0.06693 (1.54)	0.06617 (0.38)	0.06684 (1.40)
J_2	-0.04661	-0.04540 (2.60)	-0.04745 (1.81)	-0.04676 (0.32)	-0.04716 (1.18)

---

[a] all values in Pa m

As expected (and also demonstrated in the previous section), the use of curved elements over flat elements gives higher accuracy for both J_1 and J_2 with the results comparable to those obtained using FEM. The use of enrichment, however, gives an even more significant increase in accuracy and it is seen that the percentage errors are more than halved for both values. But the most important result which can be drawn from Table 8.3 is the improvement in accuracy over the FEM results using the enriched DBEM; not only are the results more accurate, but they are obtained using a significantly lower number of degrees of freedom - the enriched DBEM analysis used here exhibited 506 DOF while the FEM analysis, assuming the analysis of [113] used quadratic quadrilateral elements, exhibited ∼3000 DOF.

8.5 Contour integral vs J-integral

All the previous crack examples have almost exclusively used the J-integral to determine SIFs with circular integration paths centred at the crack tip. However, as illustrated in Sec. 2.6.4, an alternative technique commonly known as the contour integral is also available for SIF determination. This sections aims to show, by comparing the results obtained by application of the J-integral and contour integral to an edge crack problem, the differences in SIF accuracy and path independence between each method.

For all tests, the edge crack illustrated in Fig. 8.2a was used with h/w=0.5 and a crack length of a/w=0.5. A reference solution of $K_{\mathrm{I}}/\sigma\sqrt{\pi a}$= 3.010 is given for this problem [109]. To allow a fair comparison between each integral routine, the integration paths defined in Fig. 6.13 were used for both methods with thirty internal points. As before, the number of elements per line was increased from four to twelve (see Fig. 8.2b for an example mesh) where the integral methods were evaluated for both the unenriched and enriched DBEM. Fig. 8.33 illustrates the normalised SIFs obtained using integral path four for each mesh and plots the results for both the unenriched and enriched analyses. A few important comments can be made after inspecting this plot.

Considering the unenriched analyses first, the J-integral demonstrates more accurate results for the first three meshes, but at high mesh densities, the contour integral demonstrates higher accuracies. Once enrichment is introduced, the expected increase in accuracy is seen in both methods with the J-integral showing consistently more accurate results. The contour integral however, actually shows a *decrease* in accuracy as the mesh density is increased and this is most likely attributable to the relatively small integration paths (in comparison to the crack length) at high mesh densities.

In addition, the path-independence of each method was assessed by performing the integral over paths two to eight, where the results for the unenriched and enriched analyses are shown in Figs 8.34 and 8.35 respectively. Dealing with the unenriched results first, both methods show the same erroneous results for paths two and three, and this is due to the close proximity of the internal points to the boundary, as explained in Sec. 7.3.1. For all other paths however, path-independence is demonstrated for both integral methods. In the case of the enriched analyses, the first notable point is the much smaller range of normalised SIFs (y-axis values) due to the high accuracy of the results, but what is most interesting is the obvious increase in value of the SIF between the integral paths of the contour integral method. Ignoring paths two and three, the J-integral demonstrates relatively consistent results between the integral paths while in comparison, the contour integral shows a dependence on the integral path that is even more prominent as the mesh density is increased. It therefore seems that the most sensible choice, particularly for the implementation of the enriched DBEM, is to use the J-integral for the evaluation of SIFs.

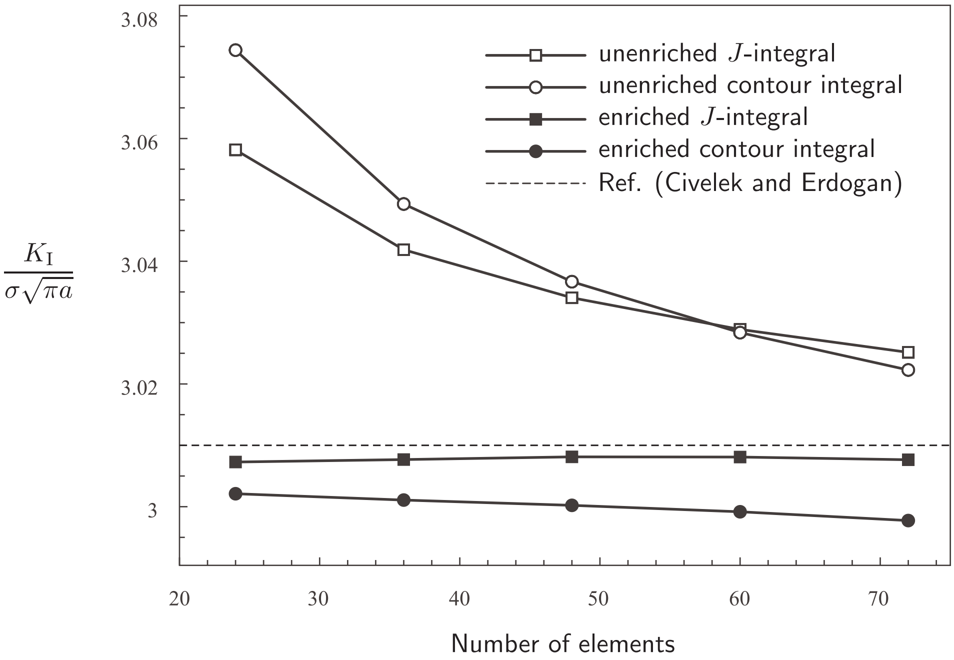

Figure 8.33: Comparison of J-integral and contour integral for edge crack crack problem - integral path four and increasing mesh density

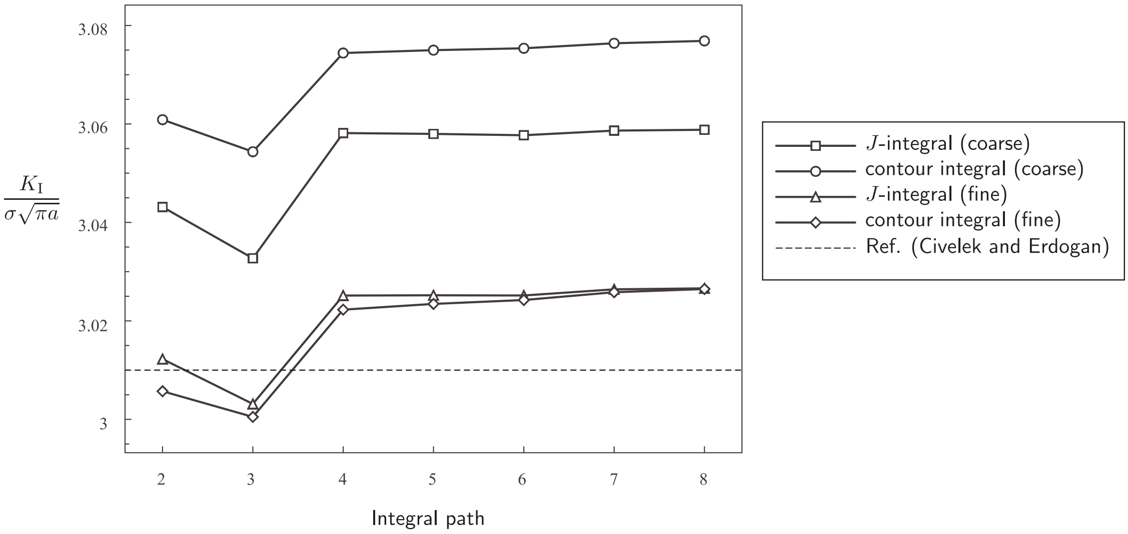

Figure 8.34: Comparison of J-integral and contour integral path independence - unenriched

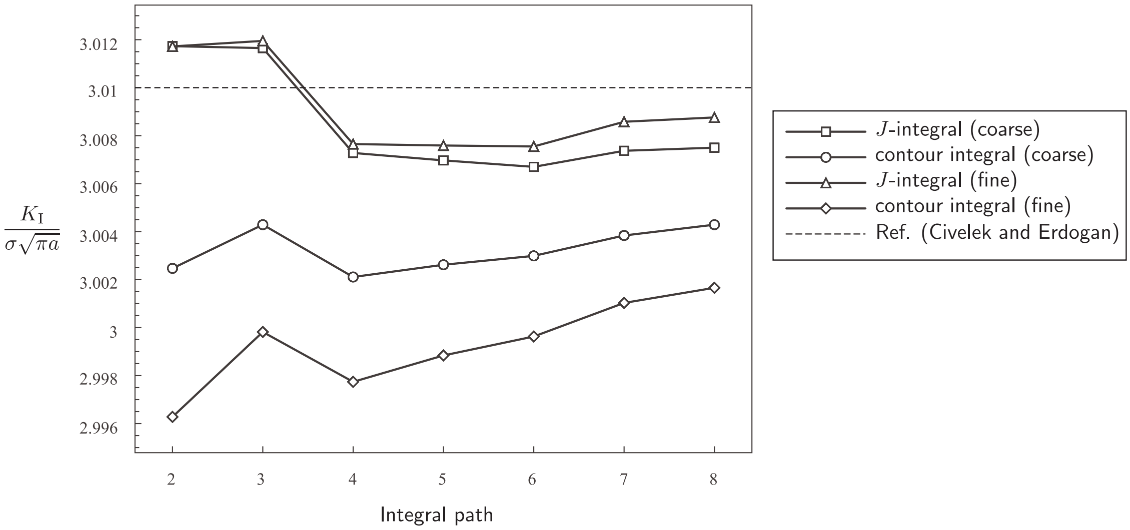

Figure 8.35: Comparison of J-integral and contour integral path independence - using local PUM enrichment

Chapter 9

Conclusions and recommendations for future work

As outlined at the beginning of this thesis, the importance of accuracy in SIFs provides the motivation to formulate numerical methods that can model fracture problems both accurately and efficiently. To achieve this goal, two methods of enriching the BEM/DBEM have been outlined in which the crack tip singularity is captured by using functions derived from crack tip solutions. In the first method of enrichment, termed local PUM enrichment, crack tip basis functions were included in the approximation (by virtue of the PUM) in a manner very similar to the eXtended Finite Element Method. Chapter 6 outlined this procedure where first, the enriched displacement approximation was stated with the additional DOF introduced by enrichment made clear. Once this expression was substituted into the Displacement BIE and Traction BIE, an enriched BEM was introduced capable of modelling cracks with coincident crack surfaces. However, with the introduction of additional local enrichment coefficients, additional equations were required to solve for these additional unknowns and this was realised by using additional collocation points to arrive at a square system. Then, to verify the accuracy of the method and to determine any implications during implementation, the new enriched formulation was applied to a flat crack problem with an exact solution. From this, a few key points were noted, namely:

- By applying enrichment to elements on a flat crack surface, it was seen that the crack tip enrichment basis reduced to one simple function that in turn reduced the number introduced DOF.
- Due to the need to calculate boundary integrals containing crack-tip enrich-

ment functions and the additional need to compute these integrals for collocation at any general point on an element, a general numerical integration scheme was outlined for the evaluation of strongly singular and hypersingular integrals.

- More accurate crack tip displacements were seen in the enriched formulation and, by utilising the J-integral to calculate SIFs, almost an order of magnitude improvement was realised over the unenriched formulation.
- The J-integral path was chosen to start and finish at nodal points on the crack surface where it was found the most accurate results were obtained on paths starting/finishing on elements away from the crack tip.
- Applying a geometrical enrichment strategy suffered from the effect of increasing condition numbers as the mesh density increased. Even with a SVD solver the conditioning of the system sometimes became so poor that no sensible solution could be found. As a result, the recommendation was made to use a topological enrichment strategy, without undue loss of accuracy.
- It was found that the optimum location of the additional collocation points was to place them on enriched elements. It was also shown that the additional points could be placed arbitrarily within these elements (within reason).

This analysis was instrumental in verifying the accuracy of a simple flat crack problem, but in the case of non-flat cracks, the crack-tip enrichment basis is not reduced to a simple, single function (first point above) and therefore the full basis has to be employed. To demonstrate this, the problem of a curved crack within an infinite domain was modelled in which the full crack-tip basis was employed and, due to the increased number of DOF (in comparison to the flat enriched crack), a much larger number of additional collocation points was required. After implementation it was found that the conditioning of the system was affected adversely and the problem was so great that no sensible solution could be obtained. For this reason, another enrichment strategy involving only two global additional degrees of freedom (corresponding to mode I and II fracture) was investigated.

The global enrichment formulation was presented in Chapter 7 in which two forms of the approximation were shown: first, the approximation was given in terms of the global enrichment coefficients $\tilde{K}_{\mathrm{I}}$ and $\tilde{K}_{\mathrm{II}}$ and second, an expression was given which leads to the SIFs K_{I} and K_{I} being output directly. The functions used for enrichment could be interpreted as a combined form of the enrichment basis used in Chapter 6, but in fact they come directly from the first order terms of the Williams expansion. The principle advantage of using the combined enrichment functions is the reduction in the additional DOF over the previous formulation requiring only two additional sets of equations. In addition, rather than using additional collocation points, the global enrichment formulation used additional BIEs, formulated from the crack tip solution that allowed a square system to be formed. In the same manner as in Chapter 6, a flat crack was utilised to evaluate the accuracy of the method where some key results were obtained:

- As before, the enrichment brought about an increase in accuracy in displacements over the unenriched formulation with the cost of only two additional DOF.
- The J-integral was employed to evaluate SIFs where, as before, a vast improvement in accuracy was seen over the unenriched formulation. Likewise, integral paths starting/finishing on elements away from the crack tip yielded the most accurate results.
- To investigate the reason for lower accuracies at paths nearer the crack tip, the numerically calculated J-integral values were plotted against analytical values. It was found that for paths nearer the crack tip numerical integration inaccuracies arose due to nearly singular integrals. However, the accuracy of SIFs using these paths was still very high.
- A comparison was made between SIFs obtained directly from the solution (using the alternative displacement formulation) and those obtained using the J-integral. Much higher accuracy was obtained through the J-integral and, even though a small additional computational cost is introduced, it is recommended that SIFs should be obtained using this technique.
- Importantly, the use of the global enrichment formulation has a much less detrimental effect on the conditioning of the system allowing enrichment to extend beyond crack tip elements bringing an increase in SIF accuracy (in contrast to the previous implementation).

The last point is doubly important, since it not only allows multiple elements to be enriched, but the application of enrichment to curved cracks now becomes possible. To show this, the global enrichment formulation was applied to a curved crack within an infinite domain demonstrating that:

- An improvement in SIF accuracy over the unenriched BEM was seen for the curved crack problem with optimum results obtained by enriching crack tip elements.
- For the enriched implementation, increasing the mesh density brought about an increase in SIF accuracy (as expected), but the results did not converge to the exact values. To explain this, further analysis was carried out in which it was found, due to the use of enrichment functions which are derived from a flat crack, errors are introduced as the curvature increases. However this error was minimal.

Chapter 8 made a direct comparison between the two methods of enrichment while also comparing against the commonly used quarter-point elements. From these results, it was concluded that:

- For both methods of enrichment, approximately an **order of magnitude improvement** over the unenriched DBEM was realised for errors in SIFs.
- The local enrichment formulation exhibited more accurate results than the global enrichment formulation while both methods were seen to show an improvement in accuracy over quarter-point elements.

The local enrichment formulation was applied to a variety of crack geometries (some including multiple enriched crack tips) exhibiting both pure mode I and mixed-mode fracture where in each, improvements in accuracy were seen throughout. But most interestingly, a comparison with the well-known XFEM showed that the results obtained using the present local PUM enrichment strategy compared very favourably. The global enrichment formulation was then compared with a FEM implementation of the curved crack problem where, once again, the accuracy of the results compared very favourably. A final comparison was then made between the J-integral and contour integral where it was shown that the J-integral exhibits higher accuracies in SIFs.

Finally, as is the case with all numerical methods, there is scope for further application and improvement of the method where, without delving into too much detail, a few points can be made:

- An obvious future application of the method is to include a crack propagation procedure where most often, the maximum principal stress criterion is used for determining the crack propagation angle θ_c. If flat propagation steps are

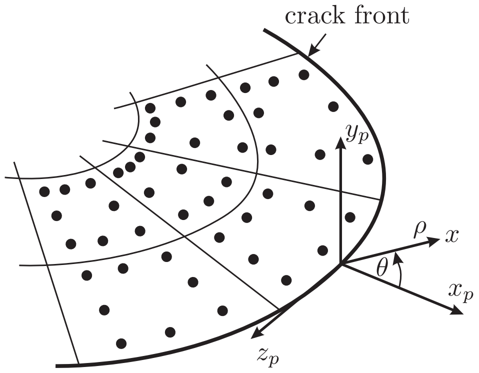

Figure 9.1: Crack tip coordinate system for 3D crack front

used, however, errors are introduced due to the tendency of cracks to follow curved paths. This can be resolved with appropriate routines like that outlined by Portela et al. [114] which uses an iterative procedure with a correction angle to ensure the correct crack path is followed. In addition, a key advantage of using a BEM/DBEM formulation is the ability to include additional elements for each crack propagation step with little difficulty - it is merely a matter of calculating a small number of additional rows and columns (in 3.77) corresponding to the new crack tip elements.

- Two-dimensional fracture problems have been used exclusively in the present work which, for many cases, represent good approximations for a wide variety of practical applications. However, for completely general fracture modelling, the method should be extended to 3D where certain implementation issues need to be overcome:
  - A suitable crack tip coordinate system must be defined such as that used by Sukumar et al. [115] (eg. Fig. 9.1) to allow the crack tip basis functions to be evaluated at an arbitrary point.
  - The fundamental solutions for 3D BEM/DBEM implementation exhibit higher orders of singularity which must be accounted for, but the integration procedure outlined in Sec. 6.2.2 for the evaluation of hypersingular enriched integrals is not limited to 2D and can be applied, with some minor alterations, to 3D kernels.
  - The matrices given by 3.77 are often relatively small for 2D problems (but fully populated), while for the 3D problems the much larger size of the matrices often requires the use of special solvers to give reasonable

runtimes. One such procedure is the ACA routine that has been recently applied to the unenriched DBEM for 3D crack problems [116] and shows encouraging results. Other techniques such as iterative solvers may prove to be beneficial.

- As outlined in Sec. 6.3.4, conditioning may be an issue once enrichment is applied, and the effects encountered in a 3D implementation may even be more severe. For these situations it may be necessary to use preconditioners like that implemented by Bechet et al. [101] for XFEM.

Bibliography

[1] R. Chona, G.R. Irwin, and R.J. Sanford. The influence of specimen size and shape on the singularity-dominated zone. In *Proceedings, 14th National Symposium of Fracture Mechanics*, STP 791, pages I1–I23. American Society for Testing and Materials, 1983.

[2] The comet inquiry. *Flight and Aircaft Engineer*, 66:638–639, 1954.

[3] W. Cohen et al. Report of the court of inquiry into the accidents to comet G-ALYP on 10 January 1954 and comet G-ALYY on 8 April 1954. *Her Majestry Station of Office, London*, 1955.

[4] C.E. Inglis. Stresses in a plate due to the presence of cracks and sharp corners. *Transactions of the Institute of Naval Architects*, 55:219–230, 1913.

[5] A.A. Griffith. The phenomena of rupture and flow in solids. *Phil. Trans. Royal Society*, 221(Series A):163–198, 1921.

[6] M.L. Williams. Stress singularities resulting from various boundary conditions in angular corners of plates in extension. *Journal of Applied Mechanics*, 19:526–528, 1952.

[7] M.L. Williams. On the stress distribution at the base of a stationary crack. *Journal of Applied Mechanics*, 24:109–114, 1957.

[8] H. Tada, P.C. Paris, and G.R. Irwin. *The stress analysis of cracks handbook.* American Society of Mechanical Engineers, 2000.

[9] E. Orowan. Energy of fracture. *Welding Journal, Research Supplement*, 34(3):157s–160s, 1955.

[10] G.R. Irwin. Analysis of stresses and strains near the end of a crack traversing a plate. *Journal of Applied Mechanics*, 24:361–364, 1957.

[11] A.C. Ugural and S.K. Fenster. *Advanced strength and applied elasticity.* Prentice Hall, 4 edition, 2008.

[12] H.M. Westergaard. Bearing pressures and cracks. *Journal of Applied Mechanics*, 6:A49–A53, 1939.

[13] N.I. Muskhelishvili. *Some basic problems of the mathematical theory of elasticity.* Groningen, Noordhoff, 1953.

[14] P. Paris and F. Erdogan. A critical analysis of crack propagation laws. *Journal of Basic Engineering*, 85:528–534, 1963.

[15] S. Li, L. Sun, W. Jia, and Z. Wang. The paris law in metals and ceramics. *Journal of Materials Science Letters*, 15:1493–1495, 1995.

[16] B.L. Karihaloo and Q.Z. Xiao. Accurate determination of the coefficients of elastic crack tip asymptotic field by a hybrid crack element with p-adaptivity. *Engineering Fracture Mechanics*, 68:1609–1630, 2001.

[17] R.J. Sanford. *Principles of Fracture Mechanics.* Prentice Hall, 2003.

[18] B. Gross, J.E. Srawley, and W.F. Brown. Stress intensity factor for a single-edge-notch tension specimen by boundary collocation. *NASA TN D-2395*, 1964.

[19] Y.K. Cheung, C. W. Woo, and Y.H. Wang. Stress intensity factors for a circular arc crack by boundary collocation method. *Engineering Fracture Mechanics*, 34(4):841–849, 1989.

[20] L.E. Hulbert. The numerical solution of two-dimensional problems of the theory of elasticity. *Bulletin 198, Engineering Experiment Station, Ohio State University, Columbus, OH*, 1963.

[21] Y.H. Wang, Y.K. Cheung, and C. W. Woo. The stress intensity factor of a crack emanating form a circular hole in a finite plate by boundary collocation method. *International Journal of Fracture*, 43:97–108, 1990.

[22] O.C. Zienkiewicz and R.L. Taylor. *The Finite Element Method for Solid and Structural Mechanics.* Butterworth-Heinemann, 2005.

[23] P. Tong and T.H.H. Pian. On the convergence of the finite element method for problems with singularity. *International Journal of Solids and Structures*, 9:313–321, 1973.

[24] A. Portela, M.H. Aliabadi, and D.P. Rooke. The dual boundary element method - effective implementation for crack problems. *International Journal for Numerical Methods in Engineering*, 33(6):1269–1287, 1992.

[25] J.O. Watson. Singular boundary elements for the analysis of cracks in plane-strain. *International Journal for Numerical Methods in Engineering*, 38(14):2389–2411, 1995.

[26] T. Belytschko, Y.Y. Lu, and L. Gu. Element-free galerkin methods. *International Journal for Numerical Methods in Engineering*, 37:229–256, 1994.

[27] T. Belytschko, L. Gu, and Y.Y. Lu. Fracture and crack growth by element free galerkin methods. *Modelling and Simulation in Materials Science and Engineering*, 2:519–534, 1994.

[28] T. Belytschko and M. Fleming. Smoothing, enrichment and contact in the element-free Galerkin method. *Computers & Structures*, 71(2):173–195, APR 1999.

[29] José Martínez and José Domínguez. On the use of quarter-point boundary elements for stress intensity factor computations. *International Journal for Numerical Methods in Engineering*, 20:1941–1950, 1984.

[30] J.R. Rice. A path independent integral and approximate analysis of strain concentraion by notches and cracks. *Journal of Applied Mechanics*, 35:379–386, 1968.

[31] H. Ishikawa, H. Kitagawa, and H. Okamura. J integral of a mixed mode crack and its application. *Proc. 3rd Int. Conf. on Mechanical Behaviour of Materials*, 3:447–455, 1980.

[32] P.H. Wen and M.H. Aliabadi. A contour integral for the evaluation of stress intensity factors. *App. Math. Modelling*, 19:450–455, 1995.

[33] M. Stern, E.B. Becker, and R.S. Dunham. A contour integral computation of mixed-mode stress intensity factors. *International Journal of Fracture*, 12(3):359–368, 1976.

[34] N. Miyazaki, T. Ikeda, T. Soda, and T. Muakata. Stress intensity factor analysis of interface crack using boundary element method - application of contour-integral method. *Engineering Fracture Mechanics*, 45(5):559–610, 1993.

[35] M. Gosz and B. Moran. An interaction energy integral method for computation of mixed-mode stress intensity factors along non-planar crack fronts in three dimensions. *Engineering Fracture Mechanics*, 69:299–319, 2002.

[36] J.W. Eischen. An improved method for computing the J_2 integral. *Engineering Fracture Mechanics*, 26(5):691–700, 1987.

[37] J.H. Chang and D.J. Wu. Computation of mixed-mode stress intensity factors for curved cracks in anisotropic elastic solids. *Engineering Fracture Mechanics*, 74:1360–1372, 2007.

[38] E. Betti. *Il nuovo Cimento*, 2, 1872.

[39] M. Gosz, J. Dolbow, and B. Moran. Domain integral formulation for stress intensity factor computation along curved three-dimensional interface cracks. *International Journal of Solids and Structures*, 35(15):1763–1783, 1998.

[40] M.A. Jaswon. Integral equation methods in potential theory - i. *Proc. Roy. Soc. Lond.*, A275:23–32, 1963.

[41] G.T. Symm. Integral equation methods in potential theory - ii. *Proc. Roy. Soc. Lond.*, A275:33–46, 1963.

[42] F.J. Rizzo. An integral equation approach to boundary value problems of classical elastostatics. *Q. Appl. Math.*, 25:83–95, 1967.

[43] T.A. Cruse. Numerical solutions in three dimensional elastostatics. *International Journal of Solids and Structures*, 5:1259–1274, 1969.

[44] J.C. Lachat. *A further development of the boundary integral technique for elastostatics*. PhD thesis, University of Southampton, 1975.

[45] J.C. Lachat and J.O. Watson. Effective numerical treatment of boundary integral equations: a formulation for three dimensional elastostatics. *International Journal for Numerical Methods in Engineering*, 10:991–1005, 1976.

[46] J.J. Pérez-Gavilán and M.H. Aliabadi. A symmetric galerkin formulation and dual reciprocity for 2d elastostatics. *Engineering Analysis With Boundary Elements*, 25:229–235, 2001.

[47] M.H. Aliabadi. *The Boundary Element Method Volume 2 Applications in Solids and Structures.* Wiley, 2002.

[48] D. Nardini and C.A. Brebbia. A new approach to free vibration analysis using boundary elements. *Boundary Element Methods in Engineering*, pages 312–326, 1982.

[49] Lord Kelvin (Thompson W.). Note on the integration of the equations of equilibrium of an elastic solid. *Cambridge and Dublin Mathematical Journal*, 3:87–89, 1848.

[50] T.A. Cruse. Two-dimensional bie fracture mechanics analysis. *App. Math. Modelling*, 2:287–293, 1978.

[51] M.D. Snyder and T.A. Cruse. Boundary-integral equation analysis of crack anisotropic plates. *International Journal of Fracture*, 11:315–328, 1975.

[52] H. Mews. Calculation of stress intensity factors for various crack problems with the boundary element method. In *Proceedings of the 9th International Conference on BEM*, 1987.

[53] L.F. Martha, L.J. Gray, and A.R. Ingraffea. Three-dimensional fracture simulation with a single-domain, direct boundary element formulation. *International Journal for Numerical Methods in Engineering*, 35:1907–1921, 1992.

[54] J.O. Watson. Hermitian cubic boundary elements for plane problems of fracture mechanics. *Res Mechanica*, 4:23–42, 1982.

[55] J. Domínguez and M.P. Ariza. A direct traction bie approach for three-dimensional crack problems. *Engineering Analysis With Boundary Elements*, 24:727–738, 2000.

[56] A.A. Becker. *The Boundary Element Method in Engineering.* McGraw-Hill Book Company, 1992.

[57] X.W. Gao and T.G. Davies. Adaptive integration in elasto-plastic boundary element analysis. *Journal of the Chinese institute of engineers*, 23(3):349–356, 2000.

[58] J.C.F Telles. A self-adaptive co-ordinate transformation for efficient numerical evaluation of general boundary integrals. *International Journal for Numerical Methods in Engineering*, 24:959–973, 1987.

[59] A.J. Wilde, M.H. Aliabadi, and H. Power. Application of a c_0 continuous element to the development of hypersingular integrals. *Communications in Boundary Elements*, 7(3):109–114, 1996.

[60] H.R. Kutt. The numerical evaluation of principal value integrals by finite-part integration. *Numer. Math.*, 24:205–210, 1975.

[61] H.R. Kutt. *Quadrature formula for finite-part integrals.* Technical Report WISK 178, National Reserach Institute for Mathematical Sciences, Pretoria, 1975.

[62] D.F. Paget. The numerical evaluation of hadamard finite-part integrals. *Numer. Math.*, 36:447–453, 1981.

[63] N.I. Ioakimidis. On the gaussian quadrature rule for finite-part integrals with a first-order singularity. *Computer Methods in Applied Mechanics and Engineering*, 2:123–132, 1986.

[64] T.J. Rudolphi. The use of simple solutions in the regularization of hypersingular boundary integral equations. *Mathematical and Computer Modelling*, 15(3-5):269–278, 1991.

[65] K.C. Toh and S. Mukherjee. Hypersingular and finite part integrals in the boundary element method. *International Journal of Solids and Structures*, 31(17):2299–2312, 1994.

[66] L.J. Gray. Evaluation of hypersingular integrals in the boundary element method. *Mathematical and Computer Modelling*, 15(3-5):165–174, 1991.

[67] L.J. Gray and C.S. Soucie. A hermite interpolation algorithm for hypersingular boundary integrals. *International Journal for Numerical Methods in Engineering*, 36(2357-2367), 1993.

[68] V. Sladek and J. Sladek. *Singular integrals in boundary element methods.* Computational Mechanics Publications, 1998.

[69] M. Guiggiani and P. Casalini. Direct computation of cauchy principal value integrals in advanced boundary elements. *International Journal for Numerical Methods in Engineering*, 24:1711–1720, 1987.

[70] M. Guiggiani. Hypersingular formulation for boundary stress evaluation. *Engineering Analysis With Boundary Elements*, 13(2):169–179, 1994.

[71] M. Guiggiani, G. Krishnasamy, T.J. Rudolphi, and F.J. Rizzo. A general algorithm for the numerical-solution of hypersingular boundary integral equations. *Journal of Applied Mechanics-Transactions of the ASME*, 59:604–614, 1992.

[72] M.L. Boas. *Mathematical methods in the physical sciences.* John Wiley & Sons, 1983.

[73] S.K. Chan, I.S. Tuba, and W.K. Wilson. On the finite element method in linear fracture mechanics. *Engineering Fracture Mechanics*, 2:1–17, 1970.

[74] R.D. Henshell and K.G. Shaw. Crack-tip finite elements are unnecessary. *International Journal for Numerical Methods in Engineering*, 9:495–507, 1975.

[75] R.S. Barsoum. On the use of isoparametric finite elements in linear fracture mechanics. *International Journal for Numerical Methods in Engineering*, 10:25–37, 1976.

[76] M.H. Aliabadi and D.P. Rooke. *Numerical Fracture Mechanics.* Computational Mechanics Publications, 1991.

[77] L.P. Harrop. The optimum size of quarter-point crack tip elements. *International Journal for Numerical Methods in Engineering*, 18:1101–1103, 1982.

[78] N.A.B. Yehia and M.S. Shephard. On the effect of quarter-point element size on fracture criteria. *International Journal for Numerical Methods in Engineering*, 21:1911–1924, 1985.

[79] A.R. Ingraffea and C. Manu. Stress-intensity factor computation in three dimensions with quarter-point elements. *International Journal for Numerical Methods in Engineering*, 15:1427–1445, 1980.

[80] Y. Yamada, Y. Ezawa, and I. Nishiguchi. Reconsiderations on singularity or crack tip elements. *International Journal for Numerical Methods in Engineering*, 14:1525–1544, 1979.

[81] J.E. Akin. The generation of elements with singularities. *International Journal for Numerical Methods in Engineering*, 10:1249–1259, 1976.

[82] M. Tanaka and H. Itoh. New crack elements for boundary element analysis of elastostatics considering arbitrary stress singularities. *App. Math. Modelling*, 11:357–363, 1987.

[83] G.T. Symm. Treatment of singularities in the solution of laplace's equation by an integration equation method. *National Physical Laboratory Report NAC31*, 1973.

[84] N. Papamichel and G.T. Symm. Numerical techniques for two-dimensional laplacian problems. *Computer Methods in Applied Mechanics and Engineering*, 6:175–194, 1975.

[85] M.H. Aliabadi, D.P. Rooke, and D.J. Cartwright. An improved boundary element formulation for calculating stress intensity factors: Application to aerospace structures. *Journal of Strain Analysis*, 22:203–207, 1987.

[86] A. Portela, M.H. Aliabadi, and D.P. Rooke. Dual boundary element analysis of cracked plates: singularity subtraction technique. *International Journal Of Fracture*, 55:17–28, 1992.

[87] J.O. Watson. Boundary elements for cracks and notches in three dimensions. *International Journal for Numerical Methods in Engineering*, 65(9):1419–1443, 2006.

[88] A.Y.T. Leung and R.K.L. Su. Mode i crack problems by fractal two level finite element methods. *Engineering Fracture Mechanics*, 48(6):847–856, 1994.

[89] P. Tong, T.H.H. Pian, and S.J. Lasry. A hybrid-element approach to crack problems in plane elasticity. *International Journal for Numerical Methods in Engineering*, 7:297–308, 1973.

[90] Q.Z. Xiao and B.L. Karihaloo. Implementation of hybrid crack element on a general finite element mesh and in combination with xfem. *Computer Methods in Applied Mechanics and Engineering*, 196:1864–1873, 2007.

[91] T. Mura and T. Koya. *Variational methods in mechanics.* Oxford University Press, 1992.

[92] A.J. Fawkes, D.R.J. Owen, and A.R. Luxmoore. An assessment of crack tip singularity models for use with isoparametric elements. *Engineering Fracture Mechanics*, 11:143–159, 1979.

[93] C.A. Brebbia. Critical evaluation of approximate methods in mathematical modelling. In *1st Int. Conf. on Appl. Mathematical Modelling, St. Louis, Missouri*, 1977.

[94] S.E. Benzley. Representation of singularities with isoparametric finite elements. *International Journal for Numerical Methods in Engineering*, 8:537–545, 1974.

[95] I. Babuška and J.M. Melenk. The partition of unity method. *International Journal for Numerical Methods in Engineering*, 40:727–758, 1996.

[96] T. Strouboulis, I. Babuška, and K.L. Copps. The design and analysis of the generalized finite element method. *Computer Methods in Applied Mechanics and Engineering*, 181:43–69, 2000.

[97] T. Strouboulis, K. Copps, and I. Babuška. The generalized finite element method: an example of its implementation and illustration of its performance. *International Journal for Numerical Methods in Engineering*, 47:1401–1417, 2000.

[98] N. Moës, J. Dolbow, and T. Belytschko. A finite element method for crack growth without remeshing. *International Journal for Numerical Methods in Engineering*, 46:131–150, 1999.

[99] T. Belytschko and T. Black. Elastic crack growth in finite elements with minimal remeshing. *International Journal for Numerical Methods in Engineering*, 45:601–620, 1999.

[100] J.E. Dolbow. *An extended finite element method with discontinuous enrichment for applied mechanics.* PhD thesis, Northwestern University, 1999.

[101] E. Bechet, H. Minnebol, N. Moës, and B. Burgardt. Improved implementation and robustness study of the x-fem for stress analysis around cracks. *International Journal for Numerical Methods in Engineering*, 64:1033–1056, 2005.

[102] M. Fleming, Y.A. Chu, B. Moran, and T. Belytschko. Enriched element-free galerkin methods for crack tip fields. *International Journal for Numerical Methods in Engineering*, 40:1483–1504, 1997.

[103] T. Belytschko, Y. Krongauz, M. Fleming, D. Organ, and W.K.S. Liu. Smoothing and accelerated computations in the element free galerkin method. *Journal of Computational and Applied Mathematics*, 74:111–126, 1996.

[104] E. Perrey-Debain, J. Trevelyan, and P. Bettess. New special wave boundary elements for short wave problems. *Communications in Numerical Methods in Engineering*, 18(4):259–268, APR 2002.

[105] N. Sukumar and J.H. Prévost. Modeling quasi-static crack growth with the extended finite element method part i: Computer implementation. *International Journal of Solids and Structures*, pages 7513–7537, 2003.

[106] P. Laborde, J. Pommier, Y. Renard, and M. Salaün. High-order extended finite element method for cracked domains. *International Journal for Numerical Methods in Engineering*, 64:354–381, 2005.

[107] J.R. Berger, A. Karageorghis, and P.A. Martin. Stress intensity factor computation using the method of fundamental solutions: Mixed-mode problems. *International Journal for Numerical Methods in Engineering*, 69:469–483, 2007.

[108] Y. Mi and M.H. Aliabadi. A taylor expansion algorithm for integration of 3d near-singular integrals. *Communications in Numerical Methods in Engineering*, 12:51–52, 1996.

[109] M.B. Civelek and F. Erdogan. Crack problems for a rectangular plate and an infinite strip. *International Journal Of Fracture*, 19(2):139–159, 1982.

[110] W.K. Wilson. *Combined mode fracture.* PhD thesis, University of Pittsburgh, 1969.

[111] Y. Murakami. *Stress intensity factors handbook.* Pergamon, 1987.

[112] S. Bordas, P.V. Nguyen, C. Dunant, H. Nguyen-Dang, and A. Guidoum. An extended finite element library. *International Journal for Numerical Methods in Engineering*, 71(6):703–732, 2007.

[113] J.H. Chang and J.B. Yeh. Calculation of $J2$-integral for 2-d cracks in rubbery materials. *Engineering Fracture Mechanics*, 59(5):683–695, 1998.

[114] A. Portela, M.H. Aliabadi, and D.P. Rooke. Dual boundary element incremental analysis of crack propagation. *Computers & Structures*, 46(2):237–247, 1993.

[115] N. Sukumar, N. Möes, B. Moran, and T. Belytschko. Extended finite element method for three-dimensional crack modelling. *International Journal for Numerical Methods in Engineering*, 48:1549–1570, 2000.

[116] I. Benedetti, A. Milazzo, and M.H. Aliabadi. A fast dual boundary element method for 3d anisotropic crack problems. *International Journal for Numerical Methods in Engineering*, 80:1356–1378, 2009.

[117] G.B. Airy. On the strains in the interior of beams. *Phil. Trans. Royal Society*, 153:49–79, 1863.

[118] Z. Nehari. *Introduction to complex analysis.* Allyn and Bacon, Inc., 1961.

Appendix A

BEM - supplementary material

A.1 Fundamental solutions

A.1.1 Kelvin's fundamental solutions (2D)

The 2D fundamental solutions U_{ij} and T_{ij} are given by Eqns (3.39) and the expressions D_{kij} and S_{kij}, which are used to determine strains and stresses, are written as

$$
\begin{aligned}
D_{kij}(\mathbf{X}', \mathbf{x}) &= \frac{1}{4\pi(1-\nu)r}[(1-2\nu)(r_{,i}\delta_{jk} + r_{,j}\delta_{ki} - r_{,k}\delta_{ij}) + 2r_{,i}r_{,j}r_{,k}] && \text{(A.1.1)} \\
S_{kij}(\mathbf{X}', \mathbf{x}) &= \frac{\mu}{2\pi(1-\nu)r^2}\Bigg\{2\frac{\partial r}{\partial n}[(1-2\nu)\delta_{ij}r_{,k} + \nu(r_{,j}\delta_{ik} + r_{,i}\delta_{jk}) - 4r_{,i}r_{,j}r_{,k}] \\
&\quad +2\nu(n_i r_{,j} r_{,k} + n_j r_{,i} r_{,k}) + (1-2\nu)(2n_k r_{,i} r_{,j} + n_j\delta_{ik} + n_i\delta_{jk}) \\
&\quad -(1-4\nu)n_k\delta_{ij}\Bigg\} && \text{(A.1.2)}
\end{aligned}
$$

A.1.2 Kelvin's fundamental solutions (3D)

The fundamental solution for displacement for a 3D domain is

$$
U_{ij}(\mathbf{X}', \mathbf{x}) = \frac{1}{16\pi\mu(1-\nu)r}\left[(3-4\nu)\delta_{ij} + r_{,i} + r_{,j}\right] \tag{A.1.3}
$$

and the traction fundamental solution

$$
T_{ij}(\mathbf{X}', \mathbf{x}) = -\frac{1}{8\pi(1-\nu)r^2}\left\{\frac{\partial r}{\partial n}\left[(1-2\nu)\delta_{ij} + 3r_{,i}r_{,j} - (1-2\nu)(n_j r_{,i} - n_i r_{,j})\right]\right\} \tag{A.1.4}
$$

A.2 Stresses at boundary points

To calculate the stresses at boundary points it is possible to use the stress boundary equation of (3.59), but this comes at the price of calculating integrals which are strongly singular and hypersingular ($\mathcal{O}(1/r)$ and $\mathcal{O}(1/r^2)$ in 2D). For flat elements it is possible to use analytical expressions (see Sec. 4.4.3) to evaluate these singular terms, but in the general case it is necessary to use special numerical integration routines that can handle these singularities. A much more simple approach is to use the boundary displacements at nodal points which, along with differentiated shape functions, allows the tangential strain to be found. Then, using this strain along with the known values of boundary tractions, boundary stresses can be found with the aid of Hooke's law. This method is not as accurate as the former, but is perfectly adequate for most BEM analyses. First, the unit normal vector **n** and unit tangent vector **m** are defined in Fig. A.1a [1]. The components of the tangent vector are given by

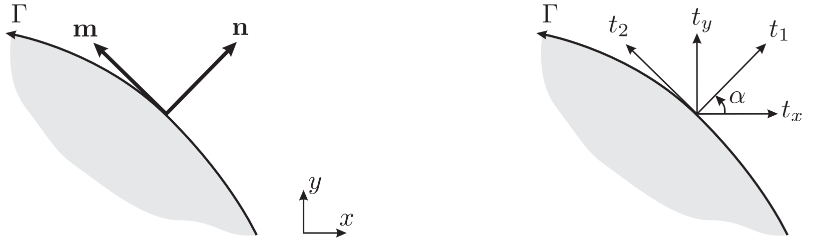

(a) Normal and tangent vectors (b) Traction components for surface stresses

Figure A.1: Calculation of boundary stresses using surface tractions

$$m_i = \frac{1}{J(\xi)}\frac{\mathrm{d}x_i(\xi)}{\mathrm{d}\xi} \quad i = x, y \tag{A.2.5}$$

where the derivatives can be found using the shape functions and nodal coordinates as

$$\frac{\mathrm{d}x_i(\xi)}{\mathrm{d}\xi} = \sum_{a=1}^{3}\frac{\mathrm{d}N_a(\xi)}{\mathrm{d}\xi}x_i^a \tag{A.2.6}$$

(assuming quadratic interpolation). Knowing the tangent components m_i and the displacement components u_i (in the global coordinate system), the tangential displacement is expressed as

$$u_1(\xi) = u_x(\xi)m_x + u_y(\xi)m_y \tag{A.2.7}$$

---

[1] Note that the tangent vector is pointing in the same direction as the boundary coordinate Γ

or, using the nodal displacements with shape function interpolation

$$u_1(\xi) = m_x \sum_{a=1}^{3} N_a(\xi) u_x^a + m_y \sum_{a=1}^{3} N_a(\xi) u_y^a \tag{A.2.8}$$

By differentiating this expression with respect to ξ and using the Jacobian $J(\xi)$, tangential strains can be written as

$$\varepsilon_{11}(\xi) = \frac{1}{J(\xi)} \left\{ m_x \sum_{a=1}^{3} \frac{\mathrm{d}N_a(\xi)}{\mathrm{d}\xi} u_x^a + m_y \sum_{a=1}^{3} \frac{\mathrm{d}N_a(\xi)}{\mathrm{d}\xi} u_y^a \right\} \tag{A.2.9}$$

Our attention now focuses on Fig. A.1b which defines the traction components both in the local coordinate system aligned with the boundary and the global coordinate system (x, y). Denoting the angle between these coordinate systems as α and using the coordinate transformation matrix, the tangential and normal tractions can be found from

$$\begin{bmatrix} t_1 \\ t_2 \end{bmatrix} = \begin{bmatrix} -\sin\alpha & \cos\alpha \\ \cos\alpha & \sin\alpha \end{bmatrix} \begin{bmatrix} t_x \\ t_y \end{bmatrix} \tag{A.2.10}$$

The stress components in the local coordinate system σ_{12} and σ_{22} can then be found simply from

$$\sigma_{22} = t_2 \quad \sigma_{12} = t_1 \tag{A.2.11}$$

The component σ_{11} however, is found using Hooke's law (Eqns 3.10) with the tangential strain ε_{11} and the stress component $\sigma_{22}(= t_2)$ giving

$$\sigma_{11} = \frac{E}{1-\nu^2}\varepsilon_{11} + \frac{\nu}{1-\nu} t_2 \tag{A.2.12}$$

Finally, to obtain stresses in the global coordinate system, these components are transformed using an appropriate transformation matrix to obtain σ_{xx}, σ_{xy} and σ_{yy}

$$\begin{bmatrix} \sigma_{xx} \\ \sigma_{xy} \\ \sigma_{yy} \end{bmatrix} = \begin{bmatrix} \sin^2\alpha & -2\sin\alpha\cos\alpha & \cos^2\alpha \\ -\sin\alpha\cos\alpha & (\cos^2\alpha - \sin^2\alpha) & \sin\alpha\cos\alpha \\ \cos^2\alpha & 2\sin\alpha\cos\alpha & \sin^2\alpha \end{bmatrix} \begin{bmatrix} \sigma_{11} \\ \sigma_{12} \\ \sigma_{22} \end{bmatrix} \tag{A.2.13}$$

A.3 Continuity

A function $f(x)$ is said to possess C^n continuity if $\frac{d^n f}{dx}$ is continuous in value. Imagining a point which joins two curves, we can state:

- C^0 continuity ensures that the curves join at the point

- C^1 continuity ensures that the first derivatives of each curve are equal at the point

- C^2 continuity ensures that the first and second derivatives of each curve are equal at the point

Appendix B

Elastic analysis

B.1 Airy stress function

In order to solve 2D problems in elasticity, the number of unknown quantities is such that eight independent equations are required. These comprise of the two equilibrium equations (Eqn. (3.2)), three strain-displacement equations (Eqn. (3.3)) and the three stress-strain relations (Eqns (3.12)). G.B. Airy [117] instead chose to combine these equations into one function known as the *Airy stress function.* This simplifies the process of finding a solution since it is only the function Φ which now must be found. The function can be used with the semi-inverse method where an Airy stress function is proposed (using *a priori* knowledge of the solution) and the solution is validated by checking against the imposed boundary conditions. For a cartesian coordinate system (x, y) the relations between the Airy stress function Φ and stresses can be written as

$$\sigma_{xx} = \frac{\partial^2 \Phi}{\partial y^2}, \quad \sigma_{yy} = \frac{\partial^2 \Phi}{\partial x^2}, \quad \sigma_{xy} = -\frac{\partial^2 \Phi}{\partial x \partial y} \tag{B.1.1}$$

and likewise for a polar coordinate system (ρ, θ)

$$\sigma_{\rho\rho} = \frac{1}{\rho}\frac{\partial \Phi}{\partial \rho} + \frac{1}{\rho^2}\frac{\partial^2 \Phi}{\partial \theta^2}, \quad \sigma_{\theta\theta} = \frac{\partial^2 \Phi}{\partial \rho^2}, \quad \sigma_{\rho\theta} = -\frac{\partial}{\partial \rho}\left(\frac{1}{\rho}\frac{\partial \Phi}{\partial \theta}\right) \tag{B.1.2}$$

Use of the compatibility equation (Eq. (3.4a)) with (B.1.1) yields the following differential equation

$$\frac{\partial^4 \Phi}{\partial x^4} + 2\frac{\partial^4 \Phi}{\partial x^2 \partial y^2} + \frac{\partial^4 \Phi}{\partial y^4} = 0 \tag{B.1.3}$$

and if we introduce the harmonic operator defined as

$$\nabla^2 = \frac{\partial^2}{\partial x^2} + \frac{\partial^2}{\partial y^2} \tag{B.1.4}$$

or, in polar form

$$\nabla^2 = \left(\frac{\partial^2}{\partial \rho^2} + \frac{1}{\rho}\frac{\partial}{\partial \rho} + \frac{1}{\rho^2}\frac{\partial^2}{\partial \theta^2} \right), \tag{B.1.5}$$

then Eq. (B.1.3) can be written simply as

$$\nabla^4 \Phi = 0 \tag{B.1.6}$$

which is the well-known form of a bi-harmonic equation.

B.2 Complex variables applied to elasticity

The use of complex variables in elasticity, as popularised by Muskhelishvili [13], has been shown to provide solutions to a wide variety of 2D problems. As illustrated in App. B.1, the solution of a problem in elasticity can be reduced to the task of finding a suitable Airy stress function that satisfies the boundary conditions. The complex-variable method also requires that the Airy stress function be satisfied but, as will be shown presently, if the solution can be represented by complex functions and these are shown to be analytic (ie. they satisfy the Cauchy-Riemann equations), then the biharmonic equation is automatically satisfied. If we consider the complex variable z defined as

$$z = x + iy \tag{B.2.7}$$

and define a complex function $Z(z)$ as

$$Z(z) = \mathrm{Re}Z(z) + i\mathrm{Im}Z(z) \tag{B.2.8}$$

then we can use this function as a potential Airy stress function. To explain why this is useful we state the Cauchy-Riemann equations as [118]

$$\frac{\partial \mathrm{Re}Z(z)}{\partial y} = -\frac{\partial \mathrm{Im}Z(z)}{\partial x} \tag{B.2.9a}$$

$$\frac{\partial \mathrm{Im}Z(z)}{\partial y} = -\frac{\partial \mathrm{Re}Z(z)}{\partial x} \tag{B.2.9b}$$

If these conditions are satisfied then the function $Z(z)$ is defined as *analytic* which ensures that the derivative of the function can be evaluated at all points within a domain. Furthermore, if (B.2.9a) is differentiated with respect to y and (B.2.9b) with respect to x and the resulting equations are added, the following can be written

$$\left(\frac{\partial^2}{\partial x^2} + \frac{\partial^2}{\partial y^2}\right) \mathrm{Re}Z(z) = \nabla^2 \mathrm{Re}Z(z) = 0 \tag{B.2.10}$$

Likewise, if we differentiate (B.2.9a) with respect to x and (B.2.9b) with respect to y and sum, a similar expression can be written

$$\left(\frac{\partial^2}{\partial x^2} + \frac{\partial^2}{\partial y^2}\right) \mathrm{Im}Z(z) = \nabla^2 \mathrm{Im}Z(z) = 0 \tag{B.2.11}$$

These expressions show that the real and imaginary parts of an analytic complex function are harmonic functions, and therefore also satisfy the biharmonic equation. Therefore, by simply proving that a complex function is analytic, then it can be inferred that the same function is also a valid Airy stress function that satisfies the biharmonic equation. Furthermore, due to the principle of superposition, if the real and imaginary functions are shown to be valid solutions then the sum of these functions is also a valid solution. These principles are used extensively in the analysis of cracked bodies by Westergaard [12].

Appendix C

Singular integrals

C.1 Definitions

To allow an appropriate choice of integration method for singular boundary integrals to be chosen, it is necessary to provide formal definitions that allows each to be categorised into three types: weakly singular, strongly singular and hypersingular.

- **Weakly singular** integrals are defined as those which *do not* depend on the shape of the exclusion zone (see Fig. 3.6) used in the limiting process.
- **Strongly singular** integrals are defined as those integrals which require a *symmetric* exclusion zone (ie. a semi-circle or hemisphere) in the limiting process.
- **Hypersingular** integrals are those which contain higher orders of singularities than strongly singular integrals.

At first, it seems intuitively wrong that a function which is infinite at a point can be integrated over a certain interval to give a finite result. In fact, it does not matter that the function is infinite at a point, rather, it is the *behaviour* of the function around this singular point that matters. Thus, by considering the limit as an infinitesimal exclusion zone shrinks to zero, the integral can be determined.

C.2 General Telles transformation

The transformation developed by Telles [58] for a singularity lying at a point located at the end of an element was shown in Sec. 4.3.2, but to allow the singular point to lie an any point *within* the element, a more general transformation is required. Denoting the function we wish to integrate over the limits $\xi = -1, 1$ as $f(\xi)$ which contains a weak singularity at ξ' (where $-1 \leq \xi' \leq +1$), then the transformed integral can be written as[1]

$$\int_{-1}^{+1} f\left\{\frac{(\gamma-\gamma')^3+\gamma'(\gamma'^2+3)}{1+3\gamma'^2}\right\}\frac{3(\gamma-\gamma')^2}{1+3\gamma'^2}\,\mathrm{d}\gamma \tag{C.2.1}$$

where γ' is given by

$$\gamma' = \sqrt[3]{\xi'\xi^* + |\xi^*|} + \sqrt[3]{\xi'\xi^* - |\xi^*|} + \xi' \tag{C.2.2}$$

with ξ^* defined as

$$\xi^* = \xi'^2 - 1 \tag{C.2.3}$$

Applying this to the function $\ln|0.3+\xi|$ which contains a weak singularity at $\xi' = -0.3$ (see Fig. C.1a), it is clear that the transformation removes the singularity (Fig. C.1b) and can therefore be evaluated easily using GL quadrature.

C.3 Limiting process for U_{ij} boundary integral

To formulate the BEM, it is necessary to consider the limit of the boundary integrals as the source point $\mathbf{x}'$ approaches the field point $\mathbf{x}$. As described in Sec. 3.1.4, an additional boundary Γ_ε with radius ε (see Fig. 3.6) is included allowing the limit as $\varepsilon \to 0$ to be found. For the integral expression containing U_{ij}, this is written as (3.44) where the first term can be found using an appropriate numerical integration scheme (capable of evaluating a function with a singularity of $\mathcal{O}(\ln(1/r))$ but the second must be considered in greater detail. By substituting in the expression for U_{ij} given by Eq. (3.39a), the integral term over the boundary Γ_ε can be written as

$$\lim_{\varepsilon\to 0}\int_{\Gamma_\varepsilon} \frac{1}{8\pi\mu(1-\nu)}\left\{(3-4\nu)\ln\left(\frac{1}{r}\right)\delta_{ij} + r_{,i}r_{,j}\right\} t_j(\mathbf{x})\,\mathrm{d}\Gamma \tag{C.3.4}$$

Using the polar coordinate system as defined in Fig. C.2, it is possible to express the parameters dependent on r and Γ in terms of the polar coordinates ε and θ. These

---

[1] The transformation shown in [58] in fact contains an error - the corrected version is shown here

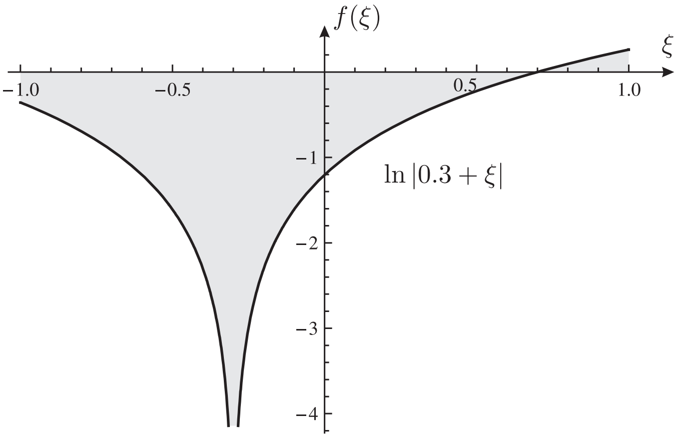

(a) Weakly singular function with $\xi' = -0.3$

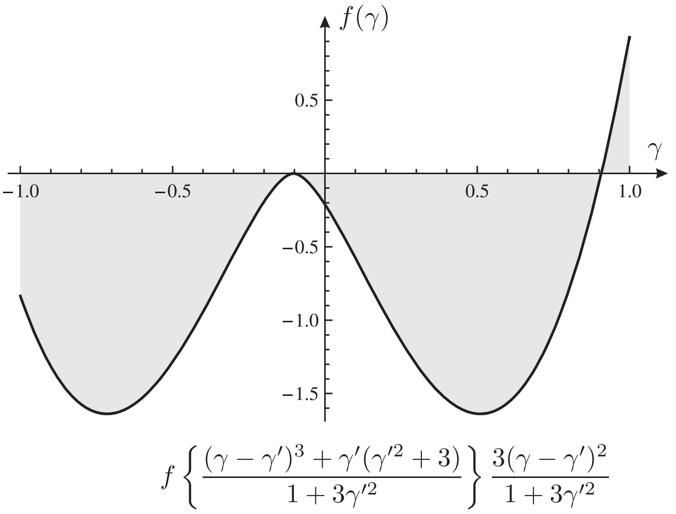

(b) Telles transformation for $\ln|0.3+\xi|$

Figure C.1: General Telles transformation for weakly singular functions

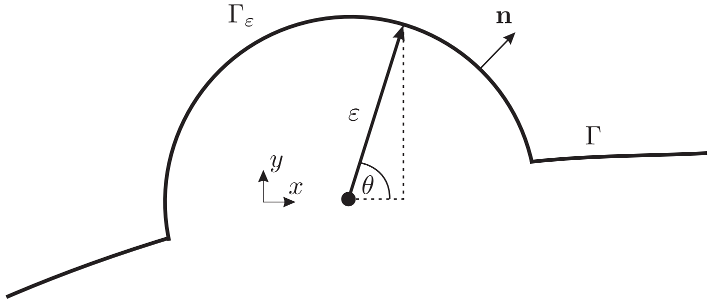

Figure C.2: Semi-circular arc on boundary used for limiting process are written as

$$r = \varepsilon\cos\theta + \varepsilon\sin\theta \tag{C.3.5}$$

$$\mathrm{d}\Gamma_\varepsilon = \varepsilon\mathrm{d}\theta \tag{C.3.6}$$

$$r_{,x} = \cos\theta \qquad r_{,y} = \sin\theta \tag{C.3.7}$$

$$\frac{\partial r}{\partial n} = 1 \tag{C.3.8}$$

where the last expression is true since $r = \varepsilon\mathbf{n}$ and $\mathbf{n}$ is in the same direction as r. Taking the case of $i = x$ and $j = x$ as an example, the above relations can be substituted into Eq. (C.3.4) to give

$$\lim_{\varepsilon\to 0}\int_{\Gamma_\varepsilon}\frac{1}{8\pi\mu(1-\nu)}\left\{(3-4\nu)\ln\left(\frac{1}{\varepsilon(\cos\theta+\sin\theta)}\right)+\cos^2\theta\right\}t_j(\mathbf{x})\,\varepsilon\mathrm{d}\theta \tag{C.3.9}$$

As $\varepsilon \to 0$ the second term of this expression simply equals zero due to the multiplication by ε. The first term however, requires some further manipulation. Considering just the logarithmic term, this can be written using logarithmic rules as

$$\ln\left(\frac{1}{\varepsilon(\cos\theta+\sin\theta)}\right) = \ln\left(\frac{1}{\varepsilon}\right) + \ln\left(\frac{1}{(\cos\theta+\sin\theta)}\right) \tag{C.3.10}$$

Therefore, since the second term will equal zero once multiplied by ε, we are left with the integral

$$C\lim_{\varepsilon\to 0}\int_{\Gamma_\varepsilon}\ln\left(\frac{1}{\varepsilon}\right)t_j(\mathbf{x})\,\varepsilon\mathrm{d}\theta \tag{C.3.11}$$

where C is a constant. Assuming that $t_j(\mathbf{x})$ is non-singular and noting that the logarithmic term does not depend on θ, we are interested in finding

$$\lim_{\varepsilon\to 0}\varepsilon\ln\left(\frac{1}{\varepsilon}\right) \tag{C.3.12}$$

which can be rewritten as

$$\lim_{\varepsilon\to 0}\frac{\ln\left(\frac{1}{\varepsilon}\right)}{\frac{1}{\varepsilon}} \tag{C.3.13}$$

Employing L'Hôpital's rule, which is stated as

$$\lim_{\varepsilon\to c}\frac{f(x)}{g(x)} = \lim_{\varepsilon\to c}\frac{f'(x)}{g'(x)} \tag{C.3.14}$$

Eq. C.3.13 can be expressed as

$$\lim_{\varepsilon \to 0} \frac{\varepsilon}{-\varepsilon^{-2}} = -\varepsilon^3 \tag{C.3.15}$$

$$= 0 \tag{C.3.16}$$

Therefore the entire integral over the boundary Γ_ε is equal to zero for the case $i = j = x$. It is simple to show that this is also the case of each of the other components.

C.4 Limiting process for T_{ij} boundary integral

The limiting process for the boundary integral containing the T_{ij} kernel is carried out in exactly the same manner as in Sec. C.3 by making use of a semi-circular arc with radius ε (Fig. C.2). By evaluating the integral in the limit as $\varepsilon \to 0$, we end up with the desired expression in which the source point $\mathbf{x}'$ lies on the boundary. As described in Sec. 3.1.4, the boundary integral containing the T_{ij} kernel exhibits a jump term α_{ij} (Eq. (3.49)) corresponding to the integral over the portion of the boundary Γ_ε. To evaluate this, the expressions given by Eqns (C.3.5) to (C.3.8) are substituted into the T_{ij} kernel (given by (3.39b) for 2D) where, for illustration, the expression for $i = x$ and $j = x$ is given presently. The jump term α_{xx} can then be written as

$$\alpha_{xx} = -\frac{1}{4\pi(1-\nu)} \lim_{\varepsilon \to 0} \int_{\Gamma_\varepsilon} \frac{1}{\varepsilon} \left[(1-2\nu) + 2r_{,x} r_{,x}\right] \varepsilon \, \mathrm{d}\theta \tag{C.4.17}$$

where, since $n_x = r_{,x}$, the last term in (3.39b) is cancelled. Evaluating this integral over the limits 0 to π and substituting (C.3.7) for $r_{,x}$

$$\begin{aligned} \alpha_{xx} &= -\frac{1}{4\pi(1-\nu)} \int_0^\pi \left[(1-2\nu) + 2\cos^2\theta\right] \, \mathrm{d}\theta \\ &= -\frac{1}{4\pi(1-\nu)} \left[(1-2\nu)\theta + \theta + \frac{1}{2}\sin(2\theta)\right]_0^\pi \\ &= -\frac{1}{2} \end{aligned} \tag{C.4.18}$$

The same procedure can be carried out for different components of i and j to give

$$\alpha_{ij} = -\frac{\delta_{ij}}{2} \tag{C.4.19}$$

C.5 Analytical integration of hypersingular S_{kij} integrals

The implementation of the DBEM is greatly simplified by the use of flat elements along the crack surfaces since analytical expressions can be used for the evaluation of all singular integrals. The expressions for the integration of the singular S_{kij} kernels are given in Sec. 4.4.3, but the details of how the matrix terms are obtained were omitted. For completeness, the derivation of these terms is given here by demonstrating how one of the components is obtained (S_{xxx}) while all others are found in exactly the same fashion. First, the tensor and matrix forms of the integral are written as

$$n_i(\xi') \fint_{-1}^{+1} S_{kij}(\xi', \mathbf{x}(\xi)) N_a(\xi) J(\xi) d\xi \tag{C.5.20}$$

$$= \begin{bmatrix} n'_x & 0 & n'_y & 0 \\ 0 & n'_x & 0 & n'_y \end{bmatrix} \fint_{-1}^{+1} \begin{bmatrix} S_{xxx} & S_{yxx} \\ S_{xxy} & S_{yxy} \\ S_{xyx} & S_{yyx} \\ S_{xyy} & S_{yyy} \end{bmatrix} N_a(\xi) J(\xi)\,\mathrm{d}\xi \tag{C.5.21}$$

Then, by inspecting Fig. C.3, it is possible to write the following expressions for

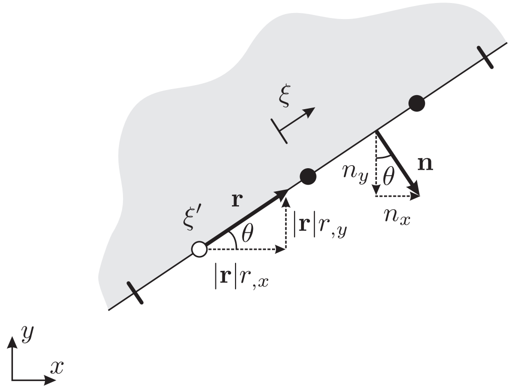

Figure C.3: Relationship between derivatives of r and normal components on a flat element

$r(=|\mathbf{r}|)$, $r_{,x}$, $r_{,y}$ and $\partial r/\partial n$:

$$r = |\xi - \xi'|\frac{l}{2} \tag{C.5.22}$$

$$\cos\theta = \frac{|\mathbf{r}|r_{,x}}{|\mathbf{r}|} = -\frac{n_y}{|\mathbf{n}|} \quad \Rightarrow \quad r_{,x} = -n_y \tag{C.5.23}$$

$$\sin\theta = \frac{|\mathbf{r}|r_{,y}}{|\mathbf{r}|} = \frac{n_x}{|\mathbf{n}|} \quad \Rightarrow \quad r_{,y} = n_x \tag{C.5.24}$$

$$\mathbf{r}.\mathbf{n} = 0 \quad \Rightarrow \quad \frac{\partial r}{\partial n} = 0 \tag{C.5.25}$$

By substituting the above expressions into Eq. A.1.2 with the components $i = j = k = x$, the following simplifications can be made

$$\begin{aligned} S_{xxx} = \frac{\mu}{2\pi(1-\nu)}\frac{1}{(\xi-\xi')^2}\left(\frac{2}{l}\right)^2 \big\{ & 2\nu(n_x n_y^2 + n_x n_y^2) \\ & + (1-2\nu)(2n_x n_y^2 + n_x + n_x) \\ & - (1-4\nu)n_x \big\} \end{aligned} \tag{C.5.26}$$

$$\begin{aligned} = \frac{\mu}{2\pi(1-\nu)}\frac{1}{(\xi-\xi')^2}\left(\frac{2}{l}\right)^2 \big\{ & 4\nu n_x n_y^2 \\ & + 2n_x n_y^2 + 2n_x \\ & - 4\nu n_x n_y^2 - 4\nu n_x \\ & - n_x + 4\nu n_x \big\} \end{aligned} \tag{C.5.27}$$

$$= \frac{\mu}{2\pi(1-\nu)}\frac{1}{(\xi-\xi')^2}\left(\frac{2}{l}\right)^2 \big\{ n_x(2n_y^2+1) \big\} \tag{C.5.28}$$

Noting that the Jacobian is given simply by $l/2$ (where l is the element length), and taking all constants outside of the integral, the integral component S_{xxx} seen in Eq. (C.5.21) is then given by

$$\frac{\mu}{2\pi(1-\nu)} n_x(2n_y^2+1)\left(\frac{2}{l}\right) \fint_{-1}^{+1} \frac{N_a(\xi)}{(\xi-\xi')^2}\,\mathrm{d}\xi \tag{C.5.29}$$

To arrive at exactly the same form as seen in Eq. (4.13), it is a trivial matter of substituting in the relation given by (3.7) to replace μ.

C.6 Subtraction of singularity

C.6.1 Analytical terms

The subtraction of singularity technique that is used for the numerical integration of hypersingular (and strongly singular) terms relies on the analytical integration of certain functions that allow the singular integrand to be regularised. Only the final result was given in Sec. 4.4.4, therefore for completion, the full integration procedure is given here.

The first integral, represented as $\mathcal{I}_{-1}$ (Eq. (4.27)) is integrated analytically to give

$$\begin{aligned}\mathcal{I}_{-1} &= \lim_{\varepsilon\to 0}\left\{ F_{-1}\Big[\ln|\xi-\xi'|\Big]_{-1}^{\xi'-\frac{\varepsilon}{J(\xi')}} + F_{-1}\Big[\ln|\xi-\xi'|\Big]_{\xi'+\frac{\varepsilon}{J(\xi')}}^{+1} \right\} \\ &= \lim_{\varepsilon\to 0}\left\{ F_{-1}\left(\ln\left|\frac{\varepsilon}{J(\xi')}\right| - \ln|-1-\xi'|\right) + F_{-1}\left(\ln|1-\xi'| - \ln\left|\frac{\varepsilon}{J(\xi')}\right|\right) \right\}\end{aligned} \tag{C.6.30}$$

which gives the desired result

$$\mathcal{I}_{-1} = F_{-1}\ln\left|\frac{1-\xi'}{-1-\xi'}\right| \tag{C.6.31}$$

Similarly, $\mathcal{I}_{-2}$ (given by Eq. 4.29) is integrated as

$$\begin{aligned}\mathcal{I}_{-2} &= \lim_{\varepsilon\to 0}\left\{ F_{-2}\left[\frac{-1}{\xi-\xi'}\right]_{-1}^{\xi'-\frac{\varepsilon}{J(\xi')}} + F_{-2}\left[\frac{-1}{\xi-\xi'}\right]_{\xi'+\frac{\varepsilon}{J(\xi')}}^{+1} + N_a(\xi)\frac{b_{kij}(\xi')}{\varepsilon} \right\} \\ &= \lim_{\varepsilon\to 0}\left\{ F_{-2}\left[\frac{-1}{-\varepsilon/J(\xi')} - \frac{-1}{-1-\xi'}\right] + F_{-2}\left[-\frac{-1}{1-\xi'} - \frac{-1}{\varepsilon/J(\xi')}\right] + N_a(\xi)\frac{b_{kij}(\xi')}{\varepsilon} \right\} \\ &= F_{-2}\left[\frac{1}{-1-\xi'} - \frac{1}{1-\xi'}\right] + \lim_{\varepsilon\to 0}\left\{ F_{-2}\left[\frac{2J(\xi')}{\varepsilon}\right] + N_a(\xi)\frac{b_{kij}(\xi')}{\varepsilon} \right\}\end{aligned} \tag{C.6.32}$$

and since the terms within the limit cancel each other (see [70])

$$\mathcal{I}_{-2} = F_{-2}\left[\frac{1}{-1-\xi'} - \frac{1}{1-\xi'}\right] \tag{C.6.33}$$

C.6.2 Power series terms

The procedure outlined by Guiggiani et al. [71] is used to allow the evaluation of hypersingular integrals for cases where analytical expressions cannot be used. The method is valid for 2D and 3D boundary integrals, but for illustration purposes we consider the 2D S_{kij} kernel. All hypersingular integrals involving this term are multiplied by the shape function $N_a(\xi)$ and the Jacobian of transformation $J^n(\xi)$ and, in the case of enriched integrals, the function $\psi_l^u(\xi)$. This can be written as

$$\int_{-1}^{+1} S_{kij}\psi_l^u(\xi)N_a(\xi)J^n(\xi)d\xi \tag{C.6.34}$$

which is of $\mathcal{O}(1/r^2)$ when the source and field point coincide. The method is based on expressing the integrand seen in (C.6.34) in a Taylor series form where definitions are made to simplify later expressions. All the proceeding expressions assume the summation convention for repeated indices.

If the components of the field and source point locations are expressed as x_i and y_i respectively (in keeping with the notation of [69]), then the following Taylor series expansion about the point ξ' can be written

$$\begin{aligned} x_i - y_i &= \left.\frac{dx_i}{d\xi}\right|_{\xi=\xi'}(\xi-\xi') + \left.\frac{d^2x_i}{d\xi^2}\right|_{\xi=\xi'}\frac{(\xi-\xi')^2}{2} + \cdots \\ &= A_i(\xi-\xi') + B_i(\xi-\xi')^2 + \cdots \\ &= A_i\delta + B_i\delta^2 + O(\delta^3), \end{aligned} \tag{C.6.35}$$

which defines the constants A_i and B_i along with the term $\delta := \xi - \xi'$. The constants A and C are also defined as

$$A := \left(\sum_{k=1}^{2} A_k^2\right)^{1/2} \tag{C.6.36}$$

$$C := \sum_{k=1}^{2} A_k B_k \tag{C.6.37}$$

However, to determine A_i and B_i (and therefore A and C), the first and second derivatives about the source point must be found. This is achieved by utilising the relevant shape functions and the nodal coordinates in the following way

$$\frac{dx_i}{d\xi} = \frac{dN_a}{d\xi} x_i^a \tag{C.6.38a}$$

$$\frac{d^2 x_i}{d\xi^2} = \frac{d^2 N_a}{d\xi^2} x_i^a \tag{C.6.38b}$$

Now the derivative $r_{,i}$ can be expressed as

$$\begin{aligned} r_{,i} = \frac{x_i - y_i}{r} &= \frac{A_i}{A} + \left(\frac{B_i}{A} - A_i \frac{A_k B_k}{A^3} \right) \delta + O(\delta^2) \\ &=: d_{i0} + d_{i1}\delta + O(\delta^2) \end{aligned} \tag{C.6.39}$$

while the term $1/r^2$ can also be rewritten as

$$\frac{1}{r^2} = \frac{1}{A^2\delta^2} - \frac{2C}{A^4\delta} + O(1) \tag{C.6.40}$$

$$=: \frac{S_{-2}}{\delta^2} + \frac{S_{-1}}{\delta} + O(1) \tag{C.6.41}$$

It is also useful to express the Jacobian of transformation in terms of its components $J_i(\xi)$ where $J^n(\xi) = \sqrt{J_1(\xi)^2 + J_2(\xi)^2}$ and

$$J_1 = A_2 + 2B_2\delta + O(\delta^2) \tag{C.6.42a}$$

$$J_2 = -A_1 - 2B_1\delta + O(\delta^2) \tag{C.6.42b}$$

As a generalisation, these are written as

$$J_k = J_{k0} + J_{k1}\delta + O(\delta^2) \tag{C.6.43}$$

Finally, we express the shape functions N_a and the enrichment functions ψ_l^u as Taylor expansions

$$\begin{aligned} N_a(\xi) &= N_a(\xi') + \left.\frac{dN_a}{d\xi}\right|_{\xi=\xi'} (\xi - \xi') + \cdots \\ &= N_{a0} + N_{a1}\delta + O(\delta^2) \end{aligned} \tag{C.6.44}$$

and

$$\begin{aligned}\psi_l^u(\xi) &= \psi_l^u(\xi') + \left.\frac{d\psi_l^u}{d\xi}\right|_{\xi=\xi'}(\xi-\xi') + \cdots \\ &= \psi_{l0}^u + \psi_{l1}^u\delta + O(\delta^2).\end{aligned} \tag{C.6.45}$$

The integrand in (C.6.34) can now be expressed as a Taylor series by substituting in expressions (C.6.39), (C.6.40), (C.6.43), (C.6.44) and (C.6.45) while also noting that $J_i = n_i J^n$. By collecting all the terms that contain $1/\delta^2$ and $1/\delta$ where, due to the use of quadratic shape functions, any higher order terms are zero, the following expression can be written for the integrand

$$\begin{aligned}N_a(\xi)S_{kij}\psi_l^u(\xi)J^n(\xi) =& D\Bigg\{\frac{S_{-2}(\xi')N_{a0}h(\xi')\psi_{l0}^u}{\delta^2} \\ &+ \Big[S_{-2}(\xi')\big[N_{a0}h(\xi')\psi_{l1}^u \\ &\quad + \psi_{l0}^u\left(N_{a1}h(\xi') + g(\xi')N_{a0}\right)\big] \\ &\quad + S_{-1}N_{a0}h(\xi')\psi_{l0}^u\Big]/\delta\Bigg\}\end{aligned} \tag{C.6.46}$$

where the constant D is defined as $\mu/2\pi(1-\nu)$, and the terms $h(\xi')$ and $g(\xi')$ are given by

$$\begin{aligned} h(\xi') = {} & 2\nu(J_{i0}d_{j0}d_{k0} + J_{j0}d_{i0}d_{k0}) \\ & + (1-2\nu)(2J_{k0}d_{i0}d_{j0} + J_{j0}\delta_{ik} + J_{i0}\delta_{jk}) \\ & - (1-4\nu)J_{k0}\delta_{ij} \end{aligned} \tag{C.6.47}$$

$$\begin{aligned} g(\xi') = {} & 2(d_{l1}J_{l0} + d_{l0}J_{l1})\big[(1-2\nu)d_{k0}\delta_{ij} \\ & \quad + \nu(d_{j0}\delta_{ik} + d_{i0}\delta_{jk}) - 4d_{i0}d_{j0}d_{k0}\big] \\ & + 2\nu\big[J_{i0}(d_{j1}d_{k0} + d_{j0}d_{k1}) + J_{i1}d_{j0}d_{k0} \\ & \quad + J_{j0}(d_{i1}d_{k0} + d_{i0}d_{k1}) + J_{j1}d_{i0}d_{k0}\big] \\ & + (1-2\nu)\big[2(J_{k1}d_{i0}d_{j0} + J_{k0}(d_{i1}d_{j0} \\ & \quad + d_{i0}d_{j1})) + J_{j1}\delta_{ik} + J_{i1}\delta_{jk}\big] \\ & - (1-4\nu)J_{k1}\delta_{ij} \end{aligned} \tag{C.6.48}$$

where the repeated index in the first two terms in expression (C.6.48) should be noted.

C.7 Analytical expressions for enriched integrals

The enriched BEM outlined in Chapter 6 requires the evaluation of boundary integrals which are both strongly singular and hypersingular and contain crack tip enrichment functions. Since the analytical expressions given by Eqns. (4.11) and (4.16) are only valid for unenriched boundary integrals, the subtraction of singularity technique is used which offers a further advantage of allowing curved elements to be used. However, in the case when flat elements are used along the crack surface (which is often the case) and only the elements adjacent to the crack tip are enriched, it may be possible to use analytical expressions for the enriched singular integrals. This section outlines the analytical expressions that can be used to evaluate the strongly singular and hypersingular enriched integrals for this particular scenario.

The singular integral expressions which we wish to evaluate are those given by (6.4) and (6.6) in which, if the element is flat and adjacent to the crack tip, the enrichment function is given by $\psi_1^u(\xi) = (1 - \xi)^{1/2}$ (for the upper crack surface Γ^{c+}). Treating the integrals in the same manner as in Sec. 4.4.3 where the singular component of the integrand is separated from all other terms and assuming the use of discontinuous shape functions given by Eqns (3.63), the enriched integral expressions are given by

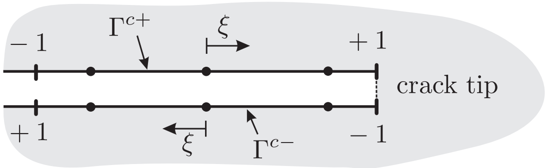

Figure C.4: Local coordinate system for analytical integration for enriched elements

$$I_1^{\Gamma^{c+}}(\xi') = \int_{-1}^{+1} \frac{N_1\sqrt{1-\xi}}{(\xi - \xi')} d\xi = \frac{1}{20}\Bigg(\sqrt{2}[-46 - 45\xi'(\xi' - 2)] + 15\xi'(3\xi' - 4)\sqrt{1-\xi'}\tanh^{-1}\left(\frac{\sqrt{2}}{\sqrt{1-\xi'}}\right)\Bigg) \tag{C.7.49a}$$

$$I_2^{\Gamma^{c+}}(\xi') = \int_{-1}^{+1} \frac{N_2\sqrt{1-\xi}}{(\xi - \xi')} d\xi = -\frac{1}{10}\Bigg(\sqrt{2}[14 + \xi'(30 - 45\xi')] + 5(2 + 3\xi')(3\xi' - 2)\sqrt{1-\xi'}\tanh^{-1}\left(\frac{\sqrt{2}}{\sqrt{1-\xi'}}\right)\Bigg) \tag{C.7.49b}$$

$$I_3^{\Gamma^{c+}}(\xi') = \int_{-1}^{+1} \frac{N_3\sqrt{1-\xi}}{(\xi - \xi')} d\xi = \frac{1}{20}\Bigg(\sqrt{2}[34 - \xi'(45\xi' + 30)] + 15\xi'(3\xi' + 4)\sqrt{1-\xi'}\tanh^{-1}\left(\frac{\sqrt{2}}{\sqrt{1-\xi'}}\right)\Bigg) \tag{C.7.49c}$$

In the case that the element lies on the lower crack surface Γ^{c-} and lies adjacent to the crack tip, the enrichment function is given by $\psi_1^u(\xi) = -(\xi + 1)^{1/2}$. If the nodes on the upper and lower surface are coincident (as in Fig. C.4), then the integrals over the lower enriched element are related to those on the upper element by

$$I_1^{\Gamma^{c-}}(\xi') = I_3^{\Gamma^{c+}}(-\xi') \qquad I_2^{\Gamma^{c-}}(\xi') = I_2^{\Gamma^{c+}}(-\xi') \qquad I_3^{\Gamma^{c-}}(\xi') = I_1^{\Gamma^{c+}}(-\xi') \tag{C.7.50}$$

In a similar fashion, the hypersingular enriched integrals for a flat element on the upper crack surface are given by

$$\begin{aligned}\bar{I}_1^{\Gamma^{c+}}(\xi') = \fint_{-1}^{+1} \frac{N_1\sqrt{1-\xi}}{(\xi-\xi')^2} d\xi = -\frac{3}{8(1+\xi')}\Bigg(&\sqrt{2}(15\xi'^2+2\xi'-8) \\ &+ \frac{(-15\xi'^3+3\xi'^2+14\xi'-4)}{\sqrt{\xi'-1}} \arctan\left(\frac{\sqrt{2}}{\sqrt{\xi'-1}}\right)\Bigg)\end{aligned} \tag{C.7.51a}$$

$$\begin{aligned}\bar{I}_2^{\Gamma^{c+}}(\xi') = \fint_{-1}^{+1} \frac{N_2\sqrt{1-\xi}}{(\xi-\xi')^2} d\xi = -\frac{1}{4(1+\xi')}\Bigg(&\sqrt{2}(-45\xi'^2-24\xi'+16) \\ &+ \frac{(45\xi'^3+9\xi'^2-40\xi'-4)}{\sqrt{\xi'-1}} \arctan\left(\frac{\sqrt{2}}{\sqrt{\xi'-1}}\right)\Bigg)\end{aligned} \tag{C.7.51b}$$

$$\begin{aligned}\bar{I}_3^{\Gamma^{c+}}(\xi') = \fint_{-1}^{+1} \frac{N_3\sqrt{1-\xi}}{(\xi-\xi')^2} d\xi = -\frac{3}{8(1+\xi')}\Bigg(&\sqrt{2}\xi'(15\xi'+14) \\ &+ \frac{(-15\xi'^3-9\xi'^2+10\xi'+4)}{\sqrt{\xi'-1}} \arctan\left(\frac{\sqrt{2}}{\sqrt{\xi'-1}}\right)\Bigg)\end{aligned} \tag{C.7.51c}$$

and, as before,

$$\bar{I}_1^{\Gamma^{c-}}(\xi') = \bar{I}_3^{\Gamma^{c+}}(-\xi') \qquad \bar{I}_2^{\Gamma^{c-}}(\xi') = \bar{I}_2^{\Gamma^{c+}}(-\xi') \qquad \bar{I}_3^{\Gamma^{c-}}(\xi') = \bar{I}_1^{\Gamma^{c+}}(-\xi') \tag{C.7.52}$$

Appendix D

Fracture mechanics - supplementary material

D.1 Crack-tip solutions as fundamental solutions

The use of the crack-tip solution as a weighting function to form additional boundary integral equations requires the analytical expressions for stress around a crack tip to be expressed in terms of tractions. Using $t_i = \sigma_{ij} n_j$ and the stresses given by (2.36), the functions $\psi^t_{\mathrm{I}j}$ and $\psi^t_{\mathrm{II}j}$ used in Eq. (7.12) can be written as

$$\begin{aligned}\psi^t_{\mathrm{I}x} = \frac{1}{\sqrt{2\pi\rho}}\big\{ & n_x \cos(\theta/2)\left[1 - \sin(\theta/2)\sin(3\theta/2)\right] \\ & + n_y \cos(\theta/2)\sin(\theta/2)\cos(3\theta/2)\big\}\end{aligned} \tag{D.1.1a}$$

$$\begin{aligned}\psi^t_{\mathrm{I}y} = \frac{1}{\sqrt{2\pi\rho}}\big\{ & n_x \cos(\theta/2)\sin(\theta/2)\cos(3\theta/2) \\ & + n_y \cos(\theta/2)\left[1 + \sin(\theta/2)\sin(3\theta/2)\right]\big\}\end{aligned} \tag{D.1.1b}$$

$$\begin{aligned}\psi^t_{\mathrm{II}x} = \frac{1}{\sqrt{2\pi\rho}}\big\{ & n_x \sin(\theta/2)\left[2 + \cos(\theta/2)\cos(3\theta/2)\right] \\ & + n_y \cos(\theta/2)\left[1 - \sin(\theta/2)\sin(3\theta/2)\right]\big\}\end{aligned} \tag{D.1.1c}$$

$$\begin{aligned}\psi^t_{\mathrm{II}y} = \frac{1}{\sqrt{2\pi\rho}}\big\{ & n_x \cos(\theta/2)\left[1 - \sin(\theta/2)\sin(3\theta/2)\right] \\ & + n_y \sin(\theta/2)\cos(\theta/2)\sin(3\theta/2)\big\}\end{aligned} \tag{D.1.1d}$$

D.2 Westergaard's complex analysis solution

As outlined in Sec. 2.3, Westergaard used complex variables to arrive at the solution of a crack problem in elasticity. The relations between stresses and the complex functions Z and Y are given by Eqns. (2.31), but for completeness the expressions for strains and displacements are given as

$$E\epsilon_{xx} = (1-\nu)\mathrm{Re}Z - (1+\nu)[y\mathrm{Im}Z' + y\mathrm{Im}Y'] + 2\mathrm{Re}Y \tag{D.2.2a}$$

$$E\epsilon_{yy} = (1-\nu)\mathrm{Re}Z + (1+\nu)[y\mathrm{Im}Z' + y\mathrm{Im}Y'] - 2\nu\mathrm{Re}Y \tag{D.2.2b}$$

$$E\gamma_{xy} = -2(1+\nu)\mathrm{Im}Y - 2(1+\nu)[y\mathrm{Re}Z' + y\mathrm{Re}Y'] \tag{D.2.2c}$$

and

$$Eu_x = (1-\nu)\mathrm{Re}\tilde{Z} - (1+\nu)[y\mathrm{Im}Z + y\mathrm{Im}Y] + 2\mathrm{Re}\tilde{Y} \tag{D.2.3a}$$

$$Eu_y = 2\mathrm{Im}\tilde{Z} - (1+\nu)[y\mathrm{Re}Z + y\mathrm{Re}Y] + (1-\nu)\mathrm{Im}\tilde{Y} \tag{D.2.3b}$$

D.3 J-integral derivation

As described in Sec. 2.6.2 the J-integral is attributed to the work carried out by J. Rice [30] who realised that an energy approach could be taken to evaluate a path integral that is related to the stress intensity factors. By taking any arbitrary integration path around the crack tip - where importantly, this can be positioned to lie away from the singular zone around a crack tip - accurate evaluation of SIFs can be achieved. Since the method is used for numerous examples in the present thesis it is instructive to give a derivation of the integral.

We begin by considering an arbitrary cracked body with area A, boundary Γ,thickness h and subject to arbitrary tractions on non crack-face boundaries as shown in Fig. D.1. It is assumed that the crack faces are traction free. Using this body as a control volume we can consider the change in total energy as the crack progresses by an incremental amount. The total potential energy of the control volume is given by the strain energy W minus the product of tractions and displacements $t_i u_i$ along the boundary Γ (since positive values of tractions and displacements

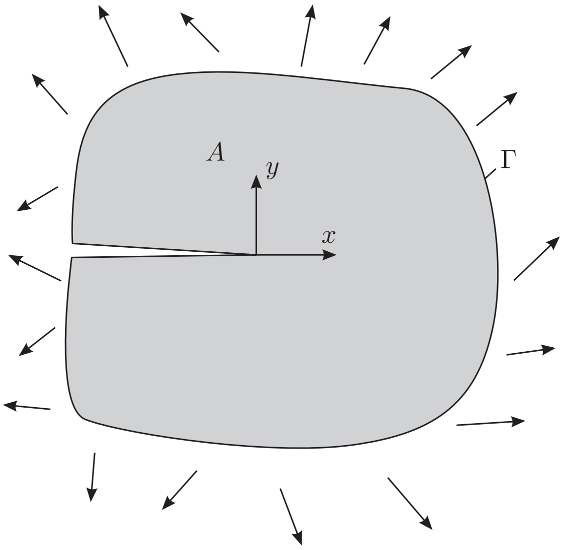

Figure D.1: Cracked body with thickness h subject to arbitrary tractions on non-crack faces

represent energy being removed from the system). This can be written as

$$\Pi = \left\{ \int_A W \mathrm{d}A - \int_\Gamma t_i u_i \mathrm{d}\Gamma \right\} h \tag{D.3.4}$$

But what we are interested in is the change in potential energy which occurs as the crack extends. Therefore, by considering the potential energy release rate (which is covered in Sec. 2.1), and defining the potential energy of the system before and after crack propagation as Π_1 and Π_2 respectively, the following can be written

$$-\frac{\partial \Pi}{\partial A} = -\lim_{\Delta a \to 0} \left(\frac{\Pi_2 - \Pi_1}{h \Delta a} \right) \tag{D.3.5}$$

where by convention, a negative sign has been introduced to make the quantities positive. Equation (D.3.4), which can be written for both states (Γ_1, A_1) and (Γ_2, A_2), is now substituted into D.3.5 to give

$$\begin{aligned} -\frac{\partial \Pi}{\partial A} &= \lim_{\Delta a \to 0} \frac{1}{h \Delta a} \left\{ \left(\int_{A_2} W \mathrm{d}A - \int_{\Gamma_2} t_i u_i \mathrm{d}\Gamma \right) - \left(\int_{A_1} W \mathrm{d}A - \int_{\Gamma_1} t_i u_i \mathrm{d}\Gamma \right) \right\} h \\ &= \lim_{\Delta a \to 0} \frac{1}{\Delta a} \left\{ \int_{A_1 - A_2} W \mathrm{d}A + \int_{\Gamma_2} t_i u_i \mathrm{d}\Gamma - \int_{\Gamma_1} t_i u_i \mathrm{d}\Gamma \right\} \end{aligned} \tag{D.3.6}$$

Since Δa is an infinitesimal quantity that tends to zero, an assumption is made that the displacements between each of the boundaries are related by a linear relationship.

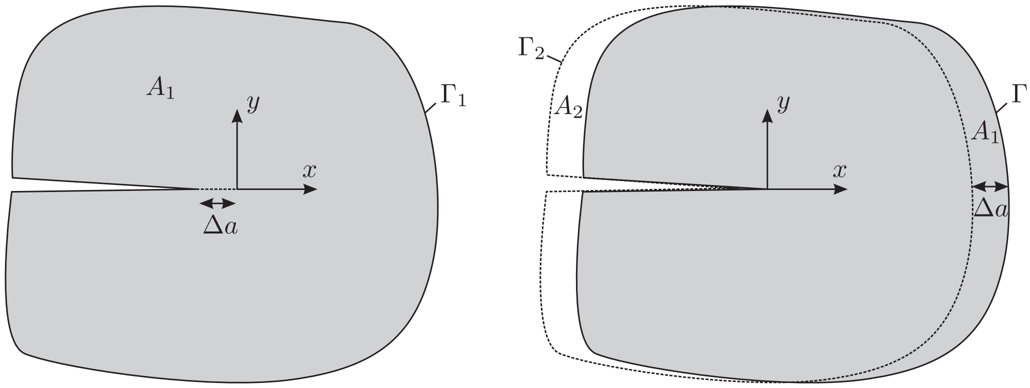

(a) Crack advancement by Δa

(b) Equivalent crack advancement by movement of control volume

Figure D.2: Crack advancement for J-integral definition

If this is true, then by the relationship between strains and displacements, the stresses and tractions must be constant. Knowing this, we can replace the last two terms in (D.3.6) with a single term giving

$$-\frac{\partial \Pi}{\partial A} = \lim_{\Delta a \to 0} \frac{1}{\Delta a} \left\{ \int_{A_1 - A_2} W \mathrm{d}A - \int_{\Gamma} t_i (u_i^1 - u_i^2) \mathrm{d}\Gamma \right\} \tag{D.3.7}$$

where u_i^1 and u_i^2 are the displacements on the boundaries Γ_1 and Γ_2 respectively. In addition, since the boundaries are separated by a horizontal distance Δa (see Fig. D.3), the displacements on each of these boundaries are related by

$$u_i^1 = u_i^2 + \frac{\partial u_i}{\partial x} \tag{D.3.8}$$

where a simple rearrangement and substitution into (D.3.7) gives

$$-\frac{\partial \Pi}{\partial A} = \lim_{\Delta a \to 0} \frac{1}{\Delta a} \left\{ \int_{A_1 - A_2} W \mathrm{d}A - \int_{\Gamma} t_i \frac{\partial u_i}{\partial x} \Delta a \mathrm{d}\Gamma \right\} \tag{D.3.9}$$

By inspecting Fig. D.3 it can be seen that the incremental area dA can be written as $\mathrm{d}A = \Delta a.\mathrm{d}y$ allowing (D.3.9) to be written as

$$-\frac{\partial \Pi}{\partial A} = \lim_{\Delta a \to 0} \frac{1}{\Delta a} \left\{ \int_{\Gamma} W \Delta a \mathrm{d}y - \int_{\Gamma} t_i \frac{\partial u_i}{\partial x} \Delta a \mathrm{d}\Gamma \right\} \tag{D.3.10}$$

then, by defining J as

$$J = -\frac{\partial \Pi}{\partial A} \tag{D.3.11}$$

(D.3.10) can be simplified to give the final expression for the J-integral

$$J = \int_\Gamma \left(W dy - t_i \frac{\partial u_i}{\partial y} \mathrm{d}\Gamma \right) \tag{D.3.12}$$

It is often convenient to express this is a slightly different form by expressing the differential dy in terms of the normal components at the boundary. Using Fig. D.4 it can be shown that d$y = n_x$dΓ allowing (D.3.12) to be rewritten as

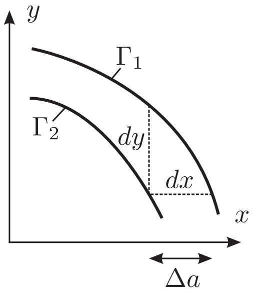

Figure D.3: Incremental quantities between boundaries Γ_1 and Γ_2

$$J = \int_\Gamma \left(W n_x - t_i \frac{\partial u_i}{\partial y} \right) \mathrm{d}\Gamma \tag{D.3.13}$$

In fact to be strictly correct, the above integral is known as the J_1 integral where the J_2 integral can be defined in a similar manner. Using indicial notation these can be written compactly as

$$J_k = \int_\Gamma \left(W n_k - t_i u_{i,k} \right) \mathrm{d}\Gamma, \quad k = 1, 2 \tag{D.3.14}$$

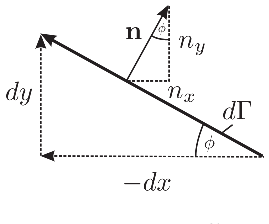

Figure D.4: Relation between normals and differential quantities along J-integral path

D.4 Contour integral auxiliary equations

The use of a contour integral [33] to determine individual stress intensity factors is reliant on the use of appropriate auxiliary equations. Using a cartesian coordinate system (x, y) and the polar crack-tip coordinate system (ρ, θ), the auxiliary displacements are given by

$$u_x^* = \frac{1}{2\mu\sqrt{2\pi\rho}}\{[(1-\kappa)\cos(\theta/2)+\sin\theta\sin(3\theta/2)]c_1 \tag{D.4.15a}$$

$$+[(1+\kappa)\sin(\theta/2)+\sin\theta\cos(3\theta/2)]c_2\} \tag{D.4.15b}$$

$$u_y^* = \frac{1}{2\mu\sqrt{2\pi\rho}}\{[(1+\kappa)\sin(\theta/2)-\sin\theta\cos(3\theta/2)]c_1 \tag{D.4.15c}$$

$$+[(\kappa-1)\cos(\theta/2)+\sin\theta\sin(3\theta/2)]c_2\} \tag{D.4.15d}$$

and the auxiliary stresses

$$\sigma_{xx}^* = \frac{1}{\sqrt{2\pi\rho^3}}\left[\left(\cos(3\theta/2)-\frac{3}{2}\sin\theta\sin(5\theta/2)\right)c_1\right. \tag{D.4.16a}$$

$$\left.+\left(-2\sin(3\theta/2)-\frac{3}{2}\sin\theta\cos(5\theta/2)\right)c_2\right] \tag{D.4.16b}$$

$$\sigma_{yy}^* = \frac{1}{\sqrt{2\pi\rho^3}}\left[\left(\cos(3\theta/2)+\frac{3}{2}\sin\theta\sin(5\theta/2)\right)c_1\right. \tag{D.4.16c}$$

$$\left.+\left(\frac{3}{2}\sin\theta\cos(5\theta/2)\right)c_2\right] \tag{D.4.16d}$$

$$\sigma_{xy}^* = \frac{1}{\sqrt{2\pi\rho^3}}\left[\left(\frac{3}{2}\sin\theta\cos(5\theta/2)\right)c_1\right. \tag{D.4.16e}$$

$$\left.+\left(\cos(3\theta/2)-\frac{3}{2}\sin\theta\cos(5\theta/2)\right)c_2\right]. \tag{D.4.16f}$$

These can be transformed into the required tractions by $t_i = \sigma_{ij}n_j$.

Appendix E

Supplementary results

E.1 Curved crack

To demonstrate path independence of J_1 and J_2 when analysing a curved crack, the results for a variety of integral paths were shown for a series of enriched analyses in Sec. 7.3.4. For completion, the results obtained from a series of unenriched analyses (using the same meshes) are shown presently:

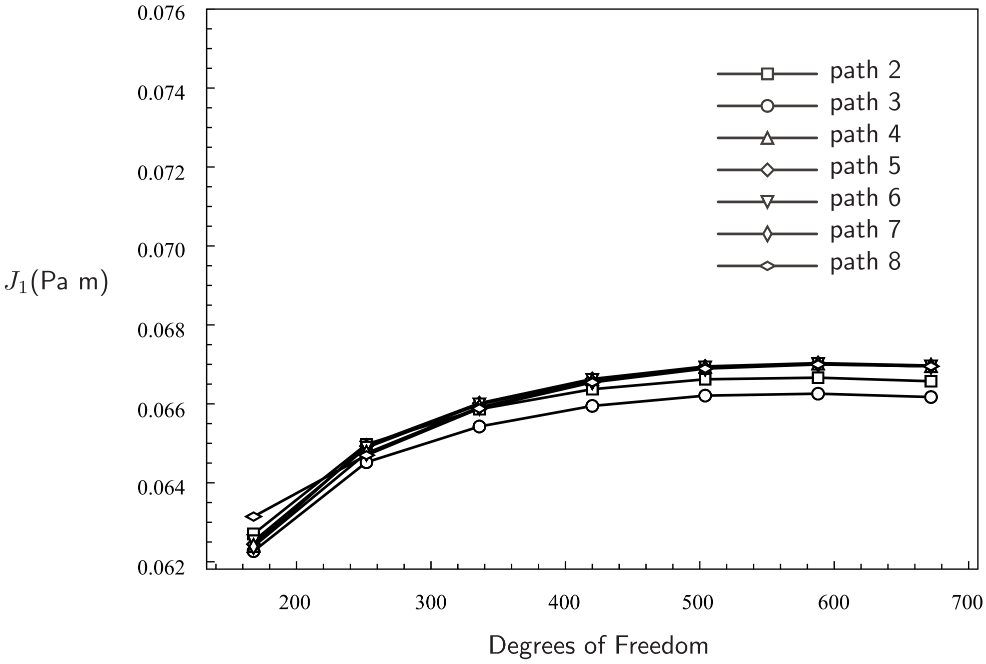

Figure E.1: J_1 path independence for unenriched curved crack analysis

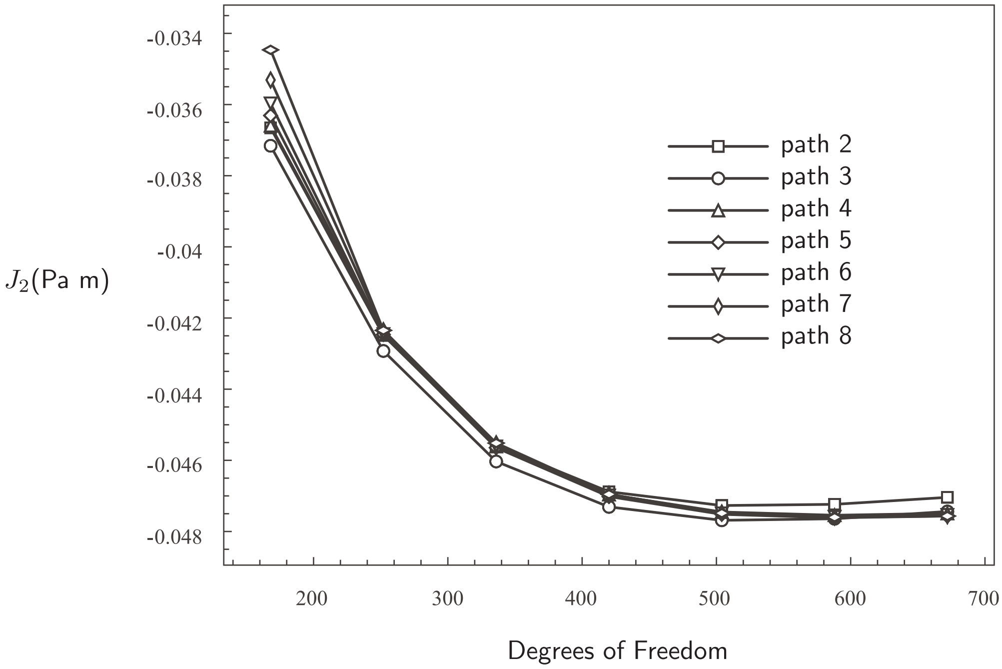

Figure E.2: J_2 path independence for unenriched curved crack analysis

E.2 Inclined edge crack

The ability of the enriched implementation to capture the singularity experienced in a slant edge crack (Fig. 8.15a) was verified in Sec. 8.3.1 where a coarse mesh of four elements per line was used throughout. To provide a reference solution for crack lengths varying from a/w=0.3 to 0.6 and for crack angles β=45° and 62.5°, a more refined mesh of eight elements per line was used (with no element grading) where the results of each are shown in Table E.1. As before, the J-integral with path four was used to determine SIFs.

E.3 Inclined centre crack

In Sec. 8.3.2, the mode I and II SIFs for an inclined centre crack in a finite plate with varying angles of β and a crack length of $a/w = 0.5$ were given. In addition, the results for crack lengths $a/w = 0.2, 0.3, 0.4$ and 0.6 are given presently where Figs E.3 to E.6 illustrate the results for each crack length respectively.

Table E.1: Normalised stress intensity factors for slant edge crack with varying crack angle and crack length - enriched analysis with eight elements per line

	$\beta = 45°$		$\beta = 62.5°$	
a/w	Mode I	Mode II	Mode I	Mode II
0.30	0.884	0.446	1.419	0.338
0.31	0.895	0.451	1.447	0.344
0.32	0.906	0.456	1.476	0.350
0.33	0.918	0.462	1.506	0.355
0.34	0.930	0.468	1.538	0.361
0.35	0.944	0.473	1.571	0.367
0.36	0.958	0.479	1.605	0.374
0.37	0.971	0.486	1.640	0.381
0.38	0.986	0.493	1.677	0.389
0.39	1.001	0.499	1.715	0.397
0.40	1.017	0.505	1.755	0.404
0.41	1.033	0.512	1.797	0.412
0.42	1.050	0.519	1.841	0.420
0.43	1.067	0.526	1.886	0.429
0.44	1.085	0.533	1.934	0.438
0.45	1.103	0.541	1.983	0.447
0.46	1.122	0.548	2.034	0.457
0.47	1.140	0.557	2.088	0.467
0.48	1.160	0.565	2.145	0.477
0.49	1.181	0.573	2.204	0.488
0.50	1.203	0.582	2.264	0.500
0.51	1.225	0.591	2.329	0.511
0.52	1.247	0.600	2.396	0.524
0.53	1.271	0.609	2.467	0.536
0.54	1.295	0.619	2.541	0.549
0.55	1.320	0.629	2.619	0.563
0.56	1.347	0.639	2.701	0.576
0.57	1.373	0.649	2.789	0.591
0.58	1.400	0.661	2.879	0.607
0.59	1.429	0.672	2.974	0.624
0.60	1.458	0.684	3.074	0.643

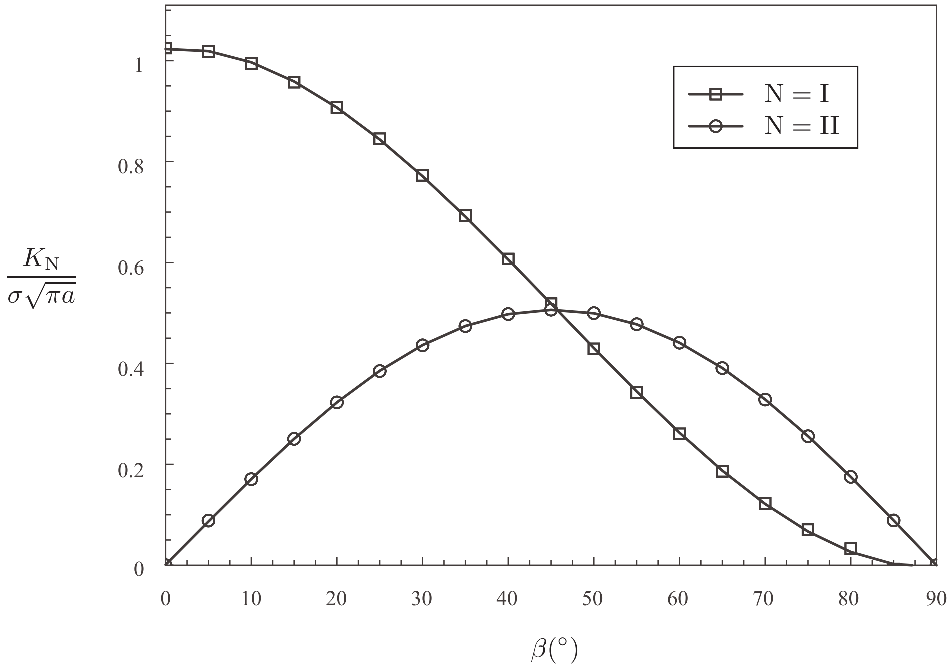

Figure E.3: Normalised SIFs for inclined centre crack with $a/w = 0.2$ and varying crack angle

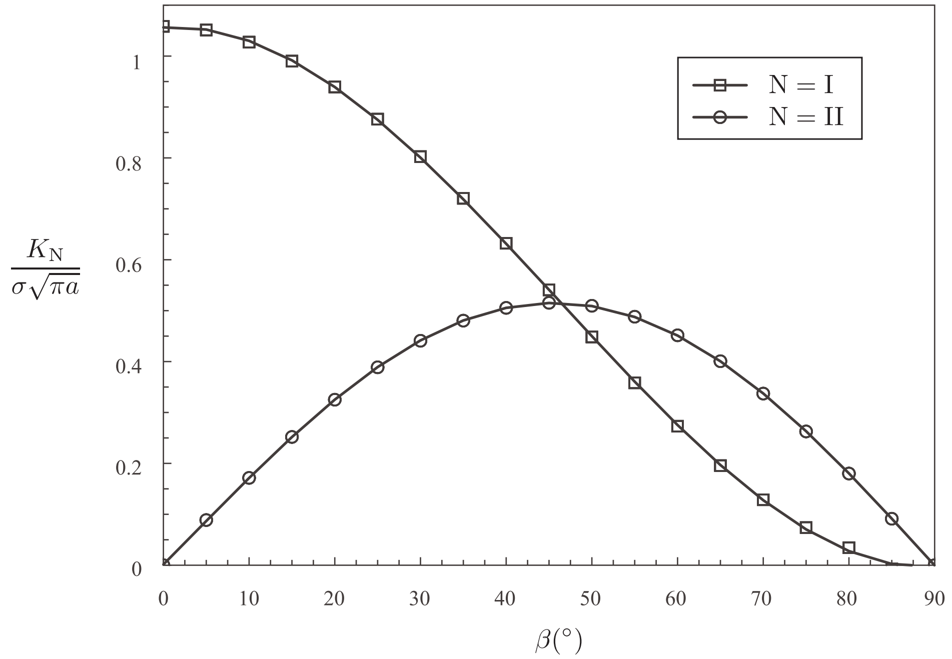

Figure E.4: Normalised SIFs for inclined centre crack with $a/w = 0.3$ and varying crack angle

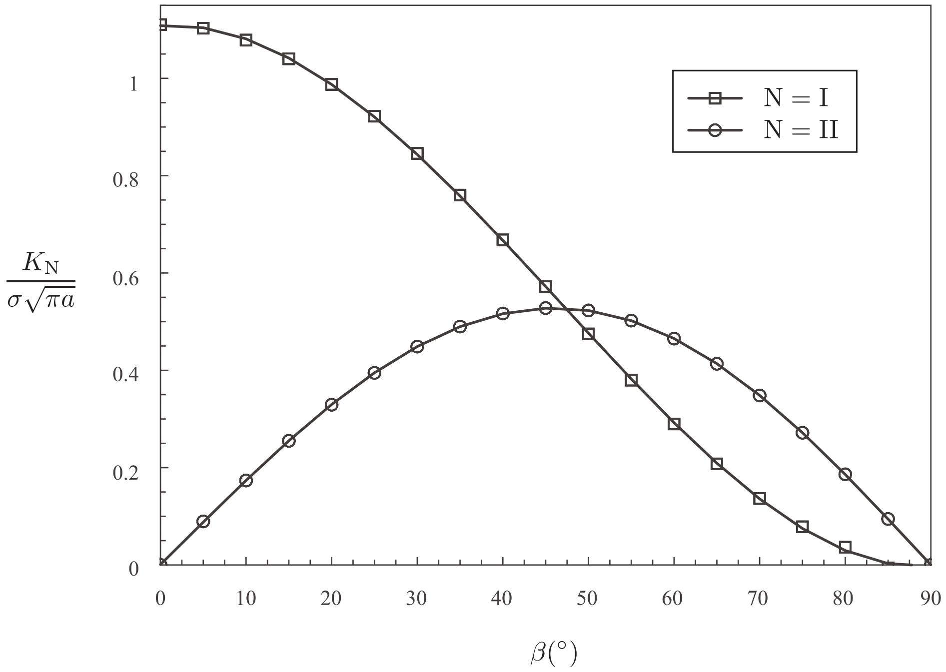

Figure E.5: Normalised SIFs for inclined centre crack with $a/w = 0.4$ and varying crack angle

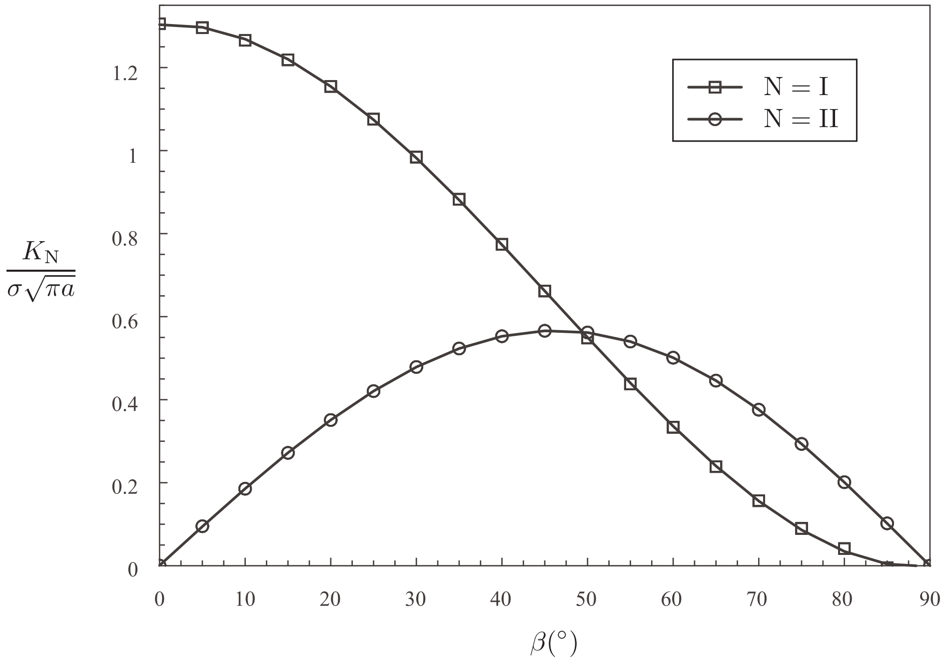

Figure E.6: Normalised SIFs for inclined centre crack with $a/w = 0.6$ and varying crack angle